Mathematical and Stochastic Modelling of Reaction-Diffusion Processes in the Wnt Signalling Pathway

James C. Cavallo

Bachelor of Science, Monash University, 2014
Bachelor of Engineering (with Honours), Monash University, 2014

A thesis submitted for the degree of

Doctor of Philosophy

at Monash University in 2019

School of Mathematical Sciences
Monash University
Melbourne, Australia
2019

Copyright Notice

Abstract

The study of Wnt signalling has attracted significant biological and mathematical attention over the last few decades. Wnt signalling plays a major role in both embryonic development and in disease. The canonical Wnt signalling pathway studied in this thesis heavily influences cell fate and decision making. Classical theoretical studies of the canonical Wnt pathway focus on the regulation of the protein β-catenin by a destruction protein complex containing, among other things, the protein Axin. To effectively study intracellular phenomena such as signalling pathways, mathematical techniques which accurately and efficiently model the underlying reaction-diffusion processes need to be developed.

The mathematical study of reaction-diffusion processes are broadly classified as either deterministic or stochastic. Deterministic models usually assume the scale of the system is sufficiently large, and the effect of stochastic fluctuations are negligible. On the other hand, a stochastic model is usually harder to analyse, but is useful in explaining phenomena which are driven by noise. One of the goals in this thesis is to explore the interface between stochastic and deterministic model properties for use in cell signalling applications.

Two common stochastic model frameworks for modelling reaction-diffusion systems in biology are those developed by Smoluchowski and Doi. The characteristic property of these frameworks is that each molecule is treated as a point diffusing under random Brownian motion. Molecules are said to react at rates which are a function of their relative separation. The greatest challenges limiting the use of these frameworks are the complications which arise from fast-slow kinetics and chemical reversibility. Presented in this thesis is a single formulation for the Doi and Smoluchowski frameworks which extends the classical theory to both high-order and reversible reactions. Applying this new framework to a gold standard Wnt signalling model highlights not just the necessity for stochastic models in biochemical systems, but also for techniques which correctly treat fast and slow chemical processes.

The difference between stochastic and deterministic modelling is further exemplified in this thesis by an investigation of Wnt signalling with Axin2 feedback. The consequence of reducing complex deterministic models of Wnt signalling is that the resulting model can be analytically investigated. This analysis generated a number of directly provable statements about Wnt signalling with feedback from a theoretical perspective. It is shown further that many of these statements are significantly changed when simulating the feedback under stochastic conditions. In some cases, these properties are completely invalidated due to stochastic effects, which arose from studying the equivalent system under well-mixed and spatio-temporal stochastic conditions. These stochastic results are juxtaposed against the analytically-derived deterministic features.

The works in this thesis provides many opportunities to advance the study of both reaction-diffusion processes and the Wnt signalling pathway. The new stochastic framework allows complex systems with fast-slow reactions to be simulated in an efficient manner. The simplified models for Wnt signalling provide new insights into the fundamental behaviour of the pathway.

Declaration

This thesis is an original work of my research and contains no material which has been accepted for the award of any other degree or diploma at any university or equivalent institution and that, to the best of my knowledge and belief, this thesis contains no material previously published or written by another person, except where due reference is made in the text of the thesis.

James Cavallo
23rd August 2019

Publications During Enrolment

The work in this thesis has resulted in two pieces of work: one published article, and one article submitted for publication. Each of these articles were joint work. These two articles form a substantial part of the thesis.

- Chapter 4 is based on the article "Reversible Doi and Smoluchowski Kinetics for High-Order Reactions," *SIAM Journal on Applied Mathematics*, vol. 79, no. 2, pp. 594-618, 2019. This article was joint work with Mark Flegg.

- Chapter 5 is based on the article "Delay-driven oscillations via Axin2 feedback in the Wnt/β-catenin signalling pathway," submitted for publication. This article was joint work with Mark Flegg and Steffen Scholpp from the University of Exeter.

Dedicated to the memory of Charlie Brown,
he was a good duck.
2008 - 2017

Acknowledgements

There are so many people who have helped enhanced my experience through this PhD. Without their support, this thesis would not have come about.

Firstly, thanks to my main supervisor Mark Flegg. At our very first meeting, you managed to excite me about working in mathematical biology, and now, with your help over the last few years, I've made my own contributions to the field. I am thankful that you've allowed me to work on projects that interested me a lot, and were very flexible when I wanted to slightly change the direction of my research. I admire your ability to come up with many amazing ideas, and I feel like this creativity has led me to create a thesis I am proud of.

To my associate supervisor Jen, thanks for your assistance over the years. I am grateful for your willingness to proofread my writing and to provide feedback on my presentations.

To the maths department, thank you for providing as many opportunities to develop my PhD career. From travel funding to regular social events, you've provided more than I expected. I am glad I chose to do my PhD in this school. Special mention to John Chan for listening to my many ideas on how we could improve PhD life, as well as sorting through all the forms I had to fill in.

Throughout my time as a PhD candidate, I have had many co-workers come and go, and each one has provided some sort of help throughout this journey. The mathematics postgraduate community has provided me with endless hours of fun and games which gave me a well-needed break from the hard work of a PhD. In no particular order, I'd like to thank, Amir, Andy, Anurag, Steve, Chloé, Carlos, Joe, Andrew, Damien, Alin, Dana, Jens, Sarah, Ozge, Michael, Angus, Adam, Darcy, Tim, Kevin, Billy, Sophie, Calum, Soheil, Oscar, Abbas, and Kaustav.

I would like to thank my family for providing constant support and encouragement. To my mum Annamaria and sister Laura, when I first brought up the idea of doing a PhD, you both encouraged me to pursue it so I would be doing what I've always loved. To David and Daniel, you've been excellent brothers to me, especially in your abilities to constantly quote The Simpsons with me. To George, I'm grateful that you are part of my family as my brother-in-law. To my little niece Arianna, your cheekiness always brings a smile to my face.

To a lot of people, their pets are considered family to them, and I am of no exception. To little Meowmeow, thanks for being a constant companion to me over the years. I appreciate our morning cuddles as I read a book whilst you fall asleep on my lap, and refuse to move making me strongly consider taking the day off work to spend with you. You are a wonderful cat, and it's hard to remember what life was like without you.

Finally, to my wife Rebecca. We shared this entire PhD journey together and I'm grateful you were there by my side the whole time. I love that we were able to share our excitement and frustrations as we both completed a PhD. Your constant love, support, and encouragement has helped me complete this PhD to the best of my ability. I couldn't have found a better person to spend the rest of my life with.

Contents

Chapter 1

Introduction

1.1 Motivation

The field of mathematical biology has grown rapidly over the last few decades. Just as mathematics has been used to further theoretical understanding in physics and chemistry, it is now common to use mathematics to describe fundamental processes in biology. The greatest advantage of using mathematics to model biological processes is that it can help guide biological experiments, and provides a theoretical framework against which to interpret experimental results. A typical biological experiment can take anywhere from a few days to a few years to complete. Hence careful planning and preparation is a necessity, especially for longer experiments. Mathematics fills in this gap by building models focusing on the fundamental behaviour of a biological process. It is easy to modify parameters in a simulation. Thus once the model is built correctly, many simulations (which can be thought of as mathematical experiments) can be completed in a matter of hours.

The Wnt signalling pathway is a critical cell signalling pathway in multiple animal species (for example, humans, frogs, mice, zebrafish) [1]. The pathway is involved in developmental biology [2] and various diseases including cancer [3]. The study of Wnt signalling is relatively young as the family of Wnt proteins were only discovered in 1982 [4]. Understanding of Wnt was accelerated by a number of biological experiments in the 1990s [5, 6, 7, 8, 9], and the addition of mathematical modelling during the 2000s [10].

There are a large number of different Wnt proteins (approximately 19 can be found in humans) [11]. The three most commonly studied Wnt signalling pathways are: the planar cell polarity pathway [12], the Wnt/Ca^{2+} pathway [13], and the canonical Wnt pathway [14]. This thesis focuses on the canonical Wnt pathway and the underlying diffusion-limited biological reactions that drive this process. In particular, the thesis investigates methods for modelling agent-based stochastic reaction-diffusion processes which may provide unique insights into the behaviour of the pathway.

To effectively simulate the Wnt pathway, it is important to note how the coupling of reaction processes with diffusion can provide unique insights that are not seen in reaction-only models. The following section introduces mathematical methods for modelling chemical reactions, and how these relate to biological pathways. It highlights the typical framework for constructing models which are either deterministic (modelled using ordinary differential equations), or stochastic (modelled using agent-based methods). Diffusion is then briefly introduced, for which spatio-temporal effects are important to accurately model biological systems.

1.2 Aims

By exploring reaction-diffusion processes in the canonical Wnt signalling pathway, this thesis aims to answer the following three questions:

- How can reactions involving more than two molecules be modelled using the current state-of-the-art framework?

- What are the fundamental components of the Wnt signalling pathway which give rise to feedback-driven oscillations? What conditions need to be placed on the interactions between these components for oscillatory behaviour to arise?

- What are the consequences of noise in the Wnt signalling pathway with feedback-driven oscillations?

1.3 Introduction to reaction-diffusion processes

1.3.1 Chemical reactions

Mathematical models of reaction and reaction-diffusion processes focus on describing the rate of change of concentration (or copy number) of each chemical species undergoing a reaction in a system. The rate of reaction is characterised by the reaction rate constant (typically denoted by the letter k, or the capital K used in Chapters 5 and 6), and the order of the reaction. For example, the bimolecular reaction,

$$A + B \xrightarrow{k} C, \tag{1.1}$$

is a reaction that combines/modifies the two reactant molecules A and B to form the product molecule C. As this reaction involves two reactants, it is of order two. The rate of change of the concentrations of the three molecules A, B, and C, can be described by the *law of mass action*, which states, for a well-mixed system, the rate of a chemical reaction is proportional to the product of the concentrations of the reactants. Using this law, the system of ordinary differential equations (ODEs) to describe the change in concentration of A, B, and C are

$$\frac{d[A]}{dt} = -k[A][B], \tag{1.2}$$

$$\frac{d[B]}{dt} = -k[A][B], \tag{1.3}$$

$$\frac{d[C]}{dt} = +k[A][B], \tag{1.4}$$

where the '[ ]' notation describes the concentration of a chemical species. Due to this specific definition of the reaction rate constant, the units for k in a second-order reaction are $1/(\text{Concentration} \times \text{Time})$.

In general, reactions can be of any order. For this reason, determining the rate of reaction is generalised to the following chemical reaction, in which N reactants react together to form M products. A generalized Nth-order reaction is given by,

$$A_1 + A_2 + \ldots + A_N \xrightarrow{k_N^+} P_1 + P_2 + \ldots + P_M, \tag{1.5}$$
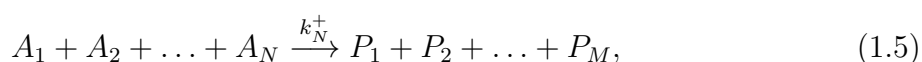
where k_N^+ represents the reaction rate constant for the forward reaction (left-to-right) that is of order N. The subscript for k usually refers to the number of a reaction in a reaction network, whereas for this example, it is used to denote the order of the reaction. The rate for the reaction in (1.5) is calculated by,

$$\text{Rate} = k_N^+ \prod_{i=1}^{N} [A_i]. \tag{1.6}$$

A zeroth-order reaction would mean that $N = 0$, and the product in (1.6) would return the empty product. Thus the rate for a zeroth-order reaction is just the reaction rate constant. The ODE for describing the change in rate of concentration for each molecule A_n and P_m are,

$$\frac{d[A_n]}{dt} = -k_N^+ \prod_{i=1}^{N} [A_i], \qquad\qquad \text{for } n = 1, 2, \ldots, N, \tag{1.7}$$

$$\frac{d[P_m]}{dt} = +k_N^+ \prod_{i=1}^{N} [A_i], \qquad\qquad \text{for } m = 1, 2, \ldots, M. \tag{1.8}$$

The units for the reaction rate constant k_N^+ are $1/(\text{Concentration}^{N-1} \times \text{Time})$. For reaction networks modelled with stochastic methods, it is necessary to convert the concentrations of each molecule $[A_i]$ into copy numbers. This is done by multiplying each concentration by the volume V of the system, to obtain $a_i = [A_i]V$, where the lower-case a_i represents the copy number of the ith chemical species. Substitution of $a_i = [A_i]V$ into (1.6) and simplifying it, yields the stochastic reaction rate,

$$\text{Rate} = \frac{k_N^+}{V^{N-1}} \prod_{i=1}^{N} a_i. \tag{1.9}$$

The units for the stochastic reaction rate constant k_N^+/V^{N-1} are $1/(\text{Copy number}^{N-1} \times \text{Time})$. Note: if a chemical reaction involves N identical species, then the product of copy numbers is determined by reducing the copy number by 1 for each successive repeat, i.e. $A \times (A-1) \times (A-2) \times \ldots \times (A - (N-1))$.

It is common to see in some works that k_N^+/V^{N-1} is rewritten as k_N^+. This is done primarily when working with discrete populations rather than concentrations. Where this is done in this thesis for brevity, it will be noted. Otherwise reaction rate constants k should be interpreted in their 'concentration' form.

In a reaction network, there are multiple reactions occurring. The change in concentration of a chemical species A_n is determined by the summation of the rate of each reaction it is involved in. Equation (1.5) is an example of a single chemical reaction. However in most biological processes, more than one reaction occurs at a time, so instead a reaction network needs to be modelled. To obtain the total rate of change for a single chemical species in a reaction network, it is sufficient to sum the rates of every reaction it is involved in (where it is produced and where it is consumed). This statement can be represented by the general formula,

$$\text{Total rate of change} = \sum \text{Production rates} - \sum \text{Consumption rates.} \tag{1.10}$$

1.3.2 Reaction-diffusion systems

For sparse biological systems, it is not possible to correctly simulate the network using purely the reaction kinetics described in the previous section. This is because the system is no longer well-mixed, therefore the movement of molecules is important in describing the overall change in concentration/copy number. That is, it is no longer enough to state (as in (1.7) for example) that the rate of reaction is proportional to the number of combinations of possible reactants in the system, as this assumes that reactions between each set of reactants has equal likelihood. When considering transport as well as reaction, the proximity of reactants to each other is an important feature which determines the reaction rate. This thesis uses diffusion in the form of Brownian motion to describe the random movement of particles.

The addition of diffusion increases the complexity of modelling biological systems. Macroscopic scale reaction-diffusion systems are typically modelled using partial differential equations (PDEs). However, small systems often use agent-based methods where the exact or approximate location of each molecule is computed, and reactions occur according to a set of rules which are governed by the proximity of individual reactants. A detailed literature review of the methods used to model reaction-diffusion systems, specifically at small scales, is presented in Chapter 3.

1.3.3 Reaction network diagrams

Throughout this thesis, reaction networks will be presented diagrammatically. These diagrams range in complexity from 3 to 17 chemical species, interacting through a host of mass-action reactions. Table 1.1 contains a list of common reaction types written in standard notation and their diagrammatic representation. The rules which govern the diagrammatic notation that will be used in this thesis and summarised in Table 1.1 are as follows. It is assumed that each solid arrow should be interpreted as a single mass-action interaction. Each reaction indicated by an arrow occurs at a rate proportional to the concentrations of each chemical at the base/bases of the arrow, and produces each of the chemicals indicated by the arrow head/heads.

Table 1.1: Pathway diagrams, and the chemical reaction they represent. These diagrams represent the types of reactions that will appear in this thesis. In this table, P represents the product molecule, P_1 and P_2 is used to represent the reaction which produces more than one product, and A, B, C are reactants. The emptyset notation ($\emptyset$) is used to either denote a zero-order reaction (if it is on the left hand side), or a degradation/decay reaction if it is on the right hand side. In the diagram column, an empty space is used in place of the emptyset symbol. Reversible reactions, although they appear as a single motif, should be thought of as two separate reactions.

Diagram	Reaction	Description
	$\emptyset \underset{k^-}{\overset{k^+}{\rightleftharpoons}} P$	Reversible zeroth-order
	$A \underset{k^-}{\overset{k^+}{\rightleftharpoons}} P$	Reversible first-order
	$A \xrightarrow{k} A + P$	First-order signalling
	$A \xrightarrow{k} P_1 + P_2$	First-order dissociation
	$A + B \xrightarrow{k} \emptyset$	Second-order degradation (A and B)
	$A + B \xrightarrow{k} A$	Second-order degradation (B only)
	$A + B \underset{k^-}{\overset{k^+}{\rightleftharpoons}} P$	Reversible second-order
	$A + B + C \underset{k^-}{\overset{k^+}{\rightleftharpoons}} P$	Reversible third-order

1.4 Thesis outline

This thesis consists of 7 chapters, which answers the research questions proposed in the aims.

Chapter 2 is a detailed literature review of different mathematical models for the canonical Wnt signalling pathway. This chapter begins by describing the biological aspects of Wnt signalling, and its importance in both developmental biology and disease development. The highly cited Lee model is introduced, which was one of the first models to comprehensively describe most molecular interactions in the pathway. From this

model, it is shown that there are three separate time-scales which are important to Wnt signalling, first identified by analysis of the Lee model. These separate time-scales will be used to investigate the foundational properties of the Wnt signalling pathway later in Chapter 4. A review of feedback mechanisms associated with Wnt, specifically that of Axin2 production by β-catenin is presented. Three key models are reviewed, the Wawra, Jensen, and Tymchyshyn models. The Tymchyshyn model in particular forms the basis of the new models presented in Chapter 5.

A detailed review of common stochastic modelling algorithms for reaction-diffusion processes is presented in Chapter 3. Each of these stochastic models are important to modelling different biological processes. An overview of commonly used software is presented to the reader if they wish to experiment with some of these algorithms. This leads to a detailed derivation of the Gillespie stochastic simulation algorithm (SSA), an algorithm commonly used in modelling reaction-diffusion processes. The popular Smoluchowski kinetics is introduced, and a review of the frameworks which build upon Smoluchowski's work is presented. This chapter concludes with an overview of the Smoldyn software, one of the most commonly cited software to model reaction-diffusion processes.

The research presented in Chapter 4 extends the Smoluchowski kinetic framework to reversible Nth-order reactions. The research combines the kinetics of four different approaches, into a single coherent framework. This new framework is used to alter the Smoldyn algorithm such that reversible Nth-order reactions can be simulated. The new model and algorithm is tested by simulating basic second-, third-, and fourth-order reactions. It is then applied to the classical canonical Wnt signalling pathway without feedback. The original model is simulated, and it is shown to give inaccurate results, due to a fundamental problem in Smoluchowski kinetics. It is shown that replacing two bimolecular reactions in the Lee model with a single trimolecular reaction eliminates this problem.

The Axin2 feedback loop in the canonical Wnt signalling pathway is researched in Chapter 5. In this chapter, existing Axin2 feedback models are simplified as much as possible, without altering the key behaviour of the model. This simplification produces two models: (1) the implicit-delay model, and (2) the explicit-delay model. The implicit-delay model is a pathway of four species described by a system of ordinary differential equations, whilst the explicit-delay model is a pathway of three species described by a system of delay differential equations. The models are simple enough such that analytical conditions for stability of the pathway are derived and discussed for their biological implications. By examining the differences in the two models, interesting mathematical observations are made and discussed.

In Chapter 6, the simplified models created in Chapter 5, are simulated stochastically using the methods of Chapters 3 and 4. This is done in order to determine when and if the region of parameters which induce oscillations is changed under stochastic conditions. The reactions in the implicit-delay model defined in Chapter 5 are modelled using both the Gillespie SSA, and the Smoldyn algorithm to simulate what happens when a spatial component is introduced into this model. Various spatio-temporal noise-related effects on the Wnt signalling pathway are presented and discussed.

The thesis concludes with Chapter 7. The last chapter summarises the main results from the thesis, and uses this to motivate new open research problems.

Chapter 2

Review of Wnt signalling pathway models

Throughout this chapter, there are a large number of proteins with long names. In any equations written for these proteins, their names are abbreviated or replaced with a symbol. All of these abbreviations and symbols are contained in Table 2.1. Refer to this table throughout the chapter to be reminded what each symbol stands for.

2.1 The canonical Wnt signalling pathway

The Wnt signalling pathways are important processes in developmental biology [2], and for its role in cancer development [3]. Molecularly, Wnts constitute a family of evolutionary conserved glycoproteins encoded by 19 genes in humans, which interact with 10 different Wnt receptors and seven-transmembrane spanning Frizzled (Fzd) proteins [11]. After the Wnt ligands bind to these receptors, they form ligand-receptor complexes, which include specific co-receptors to activate various downstream pathways [15] such as the Wnt/PCP pathway [12], the Wnt/Ca^{2+} pathway [13], and the canonical Wnt/β-catenin signalling pathway [14], the latter of which is studied in this thesis.

The canonical Wnt pathway is heavily involved in the regulation of gene transcription [16]. Studies have shown the pathway influences cell proliferation [17], differentiation [18], migration [19], cell-fate specification [20], and axis patterning [21]. These processes are commonly studied in humans [22], Xenopus (a genus of frogs) [23], and Drosophila (a genus of flies) [24].

Study of the canonical Wnt pathway has helped highlight a link between the pathway and various diseases such as bone disease and cancer [25, 26]. Wnt was initially identified in its activation of the breast cancer gene in mice [4], and then its role in human colon cancer [27]. Often these types of cancers are characterised by elevated levels of β-catenin, a protein responsible for rapid cell division and cell migration [28]. Mutations in this pathway can mis-regulate these processes and lead to cancer development [5].

The canonical pathway has the following main functions: the formation of a destruction complex responsible for regulating β-catenin, the dissociation of destruction complex in the presence of an inhibitory Wnt receptor complex, and the translocation of β-catenin into the nucleus to induce cellular responses.

The destruction complex in the canonical Wnt pathway is responsible for regulation of β-catenin [29, 6]. The destruction complex is composed of the scaffolding proteins: adenomatous polyposis coli (APC) [30], Axin [7], glycogen synthase kinase 3β (GSK3β) [31], protein phosphatase 2A (PP2A) [32], and casein kinase 1α (CK1) [33]. Within this

Table 2.1: List of common notation used throughout this thesis.

Notation	Description
A	Axin
A_m	mAxin2 RNA
Ap	APC
Ap/A	APC/Axin
Ax_2	Axin2
B	β-catenin
B/Ap	β-catenin/APC
B/DC	β-catenin/Destruction complex
$B/G/A$	β-catenin/GSK3β/Axin
B/T	β-catenin/TCF
C	Destruction complex
C_1	β-catenin/Destruction complex
C_2	Receptor complex/Destruction complex
D_a	Activated Dishevelled
D_i	Inactive Dishevelled
DC	Destruction Complex (APC/Axin/GSK3β)
DK	DKK1 (dickkopf inhibitor 1)
G	GSK3β
G/A	GSK3β/Axin
k_i	Reaction rate constant for reaction i
k^+	Forward reaction rate constant
k^-	Reverse reaction rate constant
L	LRP5/6 co-receptor
L/A	LRP5/6 co-receptor/Axin
R	Receptor complex
T	TCF (Transcription Factor)
$\mathcal{W}$	Wnt
$X*$	Phosphorylated protein or complex

complex, APC and Axin are phosphorylated by the presence of bound GSK3β and CK1 [34, 8]. This allows the complex to bind to and phosphorylate β-catenin [35]. Phosphorylated β-catenin is released from this complex, and then targeted for degradation [36].

Activation of the Wnt section of the pathway starts with Wnt ligands binding to Fzd receptors [37] and its co-receptor, the low-density lipoprotein receptor-related protein 5/6 (LRP5/6) [38]. The subsequent formation of a Wnt-Fzd-LRP5/6 complex [39] leads to the recruitment of the destruction complex to the plasma membrane. In the Wnt-ON state, LRP5/6 is phosphorylated leading to inactivation of GSK3β and blockage of β-catenin phosphorylation and thereby stabilization of β-catenin [9, 40]. The stabilized β-catenin can then accumulate in the nucleus where it interacts with TCF/LEF and activates Wnt-dependent target gene expression [41]. Wnt signalling regulates the level of the Axin proteins at several steps, with Axin2 being a major transcriptional target of the β-catenin/TCF complex [42]. Activation of Axin2 induces β-catenin degradation [43].

Therefore, Axin2 functions as a negative feedback pathway regulating Wnt signalling [44].

The final main process in the canonical pathway is the translocation of β-catenin into the nucleus [45, 46]. This typically occurs by its binding with transcription factor (TCF) [47]. β-catenin can then influence various cellular processes. However, in the absence of a Wnt receptor complex, β-catenin is rapidly phosphorylated and degraded by the destruction complex. This continuous depletion prevents translocation of β-catenin to the nucleus.

Recently, experiments have illuminated much of the uncertainty that once shrouded the manner by which Wnt receptor complexes interact with β-catenin regulation. A mechanism has been suggested through which endocytosis (a process describing a protein that is brought into a cell) may facilitate β-catenin signal activation [48]. In this process, Dishevelled (Dvl) [49] serves as a hub protein which interacts with several Wnt signalling components [50] and the endocytic machinery. After Wnt binds to its receptors Fzd and LRP5/6, the β-catenin destruction complex re-localises to the cell membrane for de-activation. To do so, Dvl binds to the Fzd receptor and to Axin to form a polymeric structure – the so-called Dvl-Axin scaffold [51], which recruits more activated Fzd-LRP5/6 proteins to the Wnt signalosome (the collection of Wnt proteins involved in the canonical Wnt pathway). Intracellularly, Dvl and Axin provide the structural scaffold for the other components of the β-catenin destruction complex. In parallel, Dvl interacts with the $\mu 2$ subunit of the Clathrin-mediated endocytic complex AP2 [52, 53]. Dvl binds to one end of the elongated C-terminal domain of AP2$\mu 2$ to induce the formation of Clathrin-coated pits. Interference of Dvl2-AP2$\mu 2$ binding leads to the degradation of the Dvl-Axin scaffold and blocks the formation and endocytosis of the Wnt signalosome [54] together with the destruction complex. After endocytosis, the Dvl-Axin scaffold is stabilised, and maintains the platform for Wnt signalosome function [55]. Lack of AP2 might lead to conformational changes of Dvl [56] and Axin [57] leading to inactivation of the bound β-catenin destruction complex [54]. This mechanism ensures continuous inhibition of the destruction complex by *deactivation* rather than *dissociation* as proposed by Lee *et al.* [58]. This deactivation mechanism forms the basis for the models developed in Chapter 5.

Advancements in the understanding and development of the Wnt signalling pathway has been heavily influenced by mathematical models [10]. Section 2.2 explores how the main mathematical models for Wnt were constructed, and how these models influence the scientific discovery of the Wnt mechanism.

2.2 Modelling the canonical Wnt signalling pathway

From this point on, notation is introduced to simplify the protein names down to only a few letters. Refer back to Table 2.1 to see a summary of all notation used in this chapter. Where possible, notation is kept as similar to what is used in the paper (for example the numbering of reactions in Lee *et al.*).

2.2.1 Lee model

A 2003 paper by Lee *et al.* has been treated as the mainstay Wnt signalling pathway amongst biologists and modellers [58]. The paper was the first to comprehensively describe major molecular interactions in the pathway, in an attempt to understand how the concentration of β-catenin is affected by the presence of a Wnt signal. The paper was based on and calibrated against a mixture of new and previous experimental data [40].

The Lee model represents Wnt signalling with 15 proteins and 17 reaction processes. These processes are a combination of binding, dissociation, phosphorylation, dephosphorylation, production, and degradation. The pathway is presented in Figure 2.1. There are three main steps to this pathway: (1) the formation of destruction complex, (2) the degradation of β-catenin through the destruction core cycle, and (3) the inhibition of the destruction complex in the presence of Wnt.

The destruction complex is made up of the three scaffolding proteins, APC (Ap), Axin (A), and GSK3β (G). The Lee model describes the formation of destruction complex occurring in three sequential steps: (1) the binding of APC with Axin to form APC/Axin (Ap/A) (Reaction 7), (2) the binding of APC/Axin with GSK3β to form APC/Axin/GSK3β (DC) (Reaction 6), and (3) the phosphorylation of APC and Axin by GSK3β to form APC*/Axin*/GSK3β (DC*) (Reaction 4 and 5). Each of these processes can also occur in reverse. Of note in the Lee model is that there is no turnover of APC or GSK3β, but there is turnover of Axin (Reaction 13). A main finding from the Xenopus data used by the authors is that Axin exists at significantly lower concentrations compared to APC and GSK3β (0.2 nM compared to 100 nM). This supports the assumption that APC and GSK3β are conserved in this pathway. However, in other cell lines, Axin is much less sparse [1].

The β-catenin (B) protein is degraded via the destruction core cycle in three steps: it first binds to the phosphorylated destruction complex (B/DC*) (Reaction 8), which can go in reverse. This complex then phosphorylates β-catenin (B*/DC*) (Reaction 9). Phosphorylated β-catenin (B*) is released from the complex (Reaction 10) before degrading (Reaction 11). DC* is then returned, in which it can bind with more β-catenin and repeat the process. The constant replenishment of DC* and its low concentration levels implies that β-catenin phosphorylation is highly sensitive to destruction complex. The Lee model also includes the turnover of β-catenin (Reaction 12).

Lee *et al.* acknowledge in their paper that the binding of Wnt to Frizzled receptors, and the activation of Dishevelled is poorly defined. They simplify this process by assuming in the presence of a Wnt signal ($\mathcal{W}$), inactive Dishevelled (D_i) is activated (Reaction 1 and 2). The activated Dishevelled (D_a) then dissociates the unphosphorylated destruction complex (Reaction 3). The rate of this dissociation can effectively be treated as constant, as D_a is not consumed in the reaction, and D_a reaches a steady state early in simulations (see Figure 2.2). The models developed in Chapters 4 and 5 treat this reaction rate as constant, ignoring the transient behaviour of switching Wnt on and off.

The Lee model includes other proteins and binding steps not directly influential to the destruction core cycle, but important for the pathway overall as they sequester signalling components. This includes the binding of β-catenin to TCF to form β-catenin/TCF (B/T) (Reaction 14), and the binding of β-catenin to APC to form β-catenin/APC (B/Ap) (Reaction 15). The former is important for Axin2 feedback models.

The reaction pathway in Figure 2.1 can be described by the system of 15 ODEs,
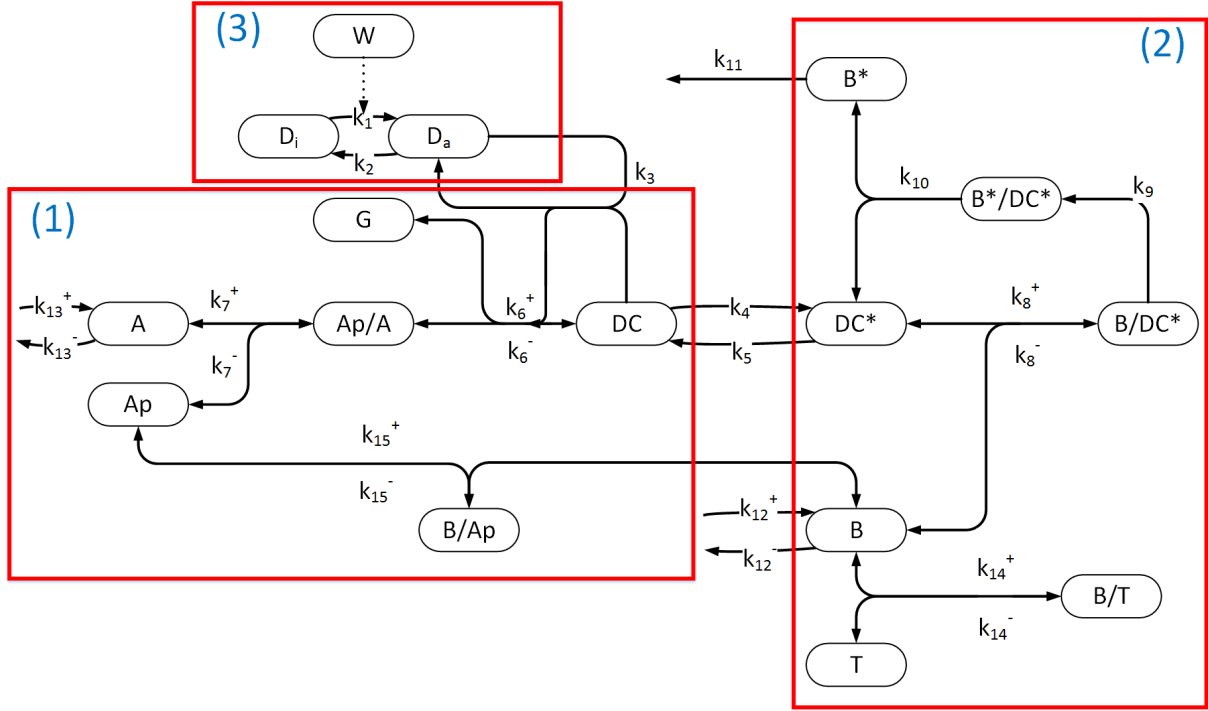
Figure 2.1: The Lee model for the Wnt signalling pathway. The three main parts to this model are encapsulated within the three red rectangles. These parts include (1) the formation of destruction complex (DC), (2) the phosphorylation and regulation of β-catenin (B), and (3) the activation of Dishevelled (D_i to D_a) by a Wnt ($\mathcal{W}$) signal.

$$\frac{d[D_i]}{dt} = -v_1 + v_2, \tag{2.1}$$

$$\frac{d[D_a]}{dt} = v_1 - v_2, \tag{2.2}$$

$$\frac{d[DC^*]}{dt} = v_4 - v_5 - v_8 + v_{10}, \tag{2.3}$$

$$\frac{d[DC]}{dt} = -v_3 - v_4 + v_5 + v_6, \tag{2.4}$$

$$\frac{d[G]}{dt} = v_3 - v_6, \tag{2.5}$$

$$\frac{d[Ap/A]}{dt} = v_3 - v_6 + v_7, \tag{2.6}$$

$$\frac{d[Ap]}{dt} = -v_7 - v_{15}, \tag{2.7}$$

$$\frac{d[B/DC^*]}{dt} = v_8 - v_9, \tag{2.8}$$

$$\frac{d[B^*/DC^*]}{dt} = v_9 - v_{10}, \tag{2.9}$$

$$\frac{d[B^*]}{dt} = v_{10} - v_{11}, \tag{2.10}$$

$$\frac{d[B]}{dt} = v_{12} - v_8 - v_{14} - v_{15}, \tag{2.11}$$

$$\frac{d[A]}{dt} = v_{13} - v_7, \tag{2.12}$$

$$\frac{d[T]}{dt} = -v_{14}, \tag{2.13}$$

$$\frac{d[B/T]}{dt} = v_{14}, \tag{2.14}$$

$$\frac{d[B/Ap]}{dt} = v_{15}, \tag{2.15}$$

where each v_i is a flux related to reaction i, described by,

$$v_1 = k_1[\mathcal{W}][D_i],$$
$$v_2 = k_2[D_a],$$
$$v_3 = k_3[D_a][DC],$$
$$v_4 = k_4[DC],$$
$$v_5 = k_5[DC^*],$$
$$v_6 = k_6^+[G][Ap/A] - k_6^-[DC],$$
$$v_7 = k_7^+[Ap][A] - k_7^-[Ap/A],$$
$$v_8 = k_8^+[B][DC^*] - k_8^-[B^*/DC^*],$$

$$v_9 = k_9[B/DC^*],$$
$$v_{10} = k_{10}[B^*/DC^*],$$
$$v_{11} = k_{11}[B^*],$$
$$v_{12} = k_{12}^+ - k_{12}^-[B],$$
$$v_{13} = k_{13}^+ - k_{13}^-[A],$$
$$v_{14} = k_{14}^+[B][T] - k_{14}^-[B/T],$$
$$v_{15} = k_{15}^+[B][Ap] - k_{15}^-[B/Ap].$$

The fluxes in v_7, v_8, v_{14}, and v_{15} are assumed by Lee *et al.* to reach pseudo-equilibrium rapidly. The Lee model makes use of these assumptions to reduce the number of ODEs. However, here these assumptions will not be used, and instead the forward reaction rate constants are set to $k_i^+ = 100$. In using values smaller than 100, the results obtained will differ to that of Lee *et al.*, mostly due to a computational issue in solving the system of ODEs where the reverse reaction is significantly larger than the forward reaction. Without a large value for k_i^+, the forward reaction will never be seen. This is then multiplied by their corresponding dissociation constant K_i to obtain the back reaction rate constant k_i^-. The calibrated parameters used by Lee *et al.* to simulate the model are found in Table 2.2.

Table 2.2: Parameters for the Lee model.

	Parameter	Value	Units
Conservation quantities	Dsh^0	100	nM
	APC^0	100	nM
	TCF^0	15	nM
	$\text{GSK3}\beta^0$	50	nM
Dissociation constants	K_7	50	nM
	K_8	120	nM
	K_{14}	30	nM
	K_{15}	1200	nM
Rate constants	k_1	0.1818	min^{-1}
	k_2	1.818×10^{-2}	min^{-1}
	k_3	0.05	$\text{nM}^{-1}\,\text{min}^{-1}$
	k_4	0.2667	min^{-1}
	k_5	0.1333	min^{-1}
	k_6^+	9.091×10^{-2}	$\text{nM}^{-1}\,\text{min}^{-1}$
	k_6^-	0.909	min^{-1}
	k_9	206	min^{-1}
	k_{10}	206	min^{-1}
	k_{11}	0.417	min^{-1}
	k_{12}^+	0.423	$\text{nM}\,\text{min}^{-1}$
	k_{12}^-	2.489×10^{-4}	min^{-1}
	k_{13}^+	8.22×10^{-5}	$\text{nM}\,\text{min}^{-1}$
	k_{13}^-	0.167	min^{-1}

The model is simulated using the following approach. The system starts at the corresponding steady state for when Wnt is in its off state ($[\mathcal{W}] = 0$). At $t = 0$, Wnt is turned on ($[\mathcal{W}] = 1$), and the simulation runs until $t = 2000$ minutes, allowing it to reach a new steady state. At $t = 2000$ minutes, Wnt is turned off again, and run until $t = 4000$ minutes so it can return to its original state. This simulation demonstrates how well Wnt can transition between the two states, which provides an insight into how the key components of the pathway operate. Figure 2.2 demonstrates how the change in destruction complex compared to the change in β-catenin clearly operate on different time-scales. This statement was confirmed in a future paper by Mirams *et al.* which is explored in Section 2.2.2, for which the Lee model operates on not two distinct time-scales, but on three [59].

Interestingly, the time it takes for the first switch to reach steady state is noticeably longer than the time it takes for the second switch. This phenomenon can be explained by noticing how sensitive β-catenin is to a small change in destruction complex. Given a slight increase in destruction complex at $t = 2000$ minutes, β-catenin starts to rapidly degrade and reaches steady state at around the same time as destruction complex. However for the first $2,000$ minutes, despite the shorter time for destruction complex to reach steady state, it takes a while for β-catenin to respond even though it is no longer rapidly degraded. This is because the natural degradation of β-catenin (k_{12}^-) operates on a longer time-scale than to the phosphorylation of β-catenin via destruction complex (as demonstrated in the next section). Hence it takes longer for β-catenin to reach steady state.
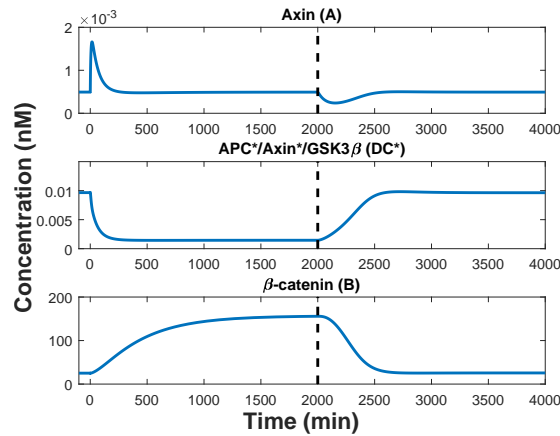
Figure 2.2: Time evolution of solutions to the Lee model (2.1) to (2.15) as the Wnt state is changed from the off ($[\mathcal{W}] = 0$) state to the on ($[\mathcal{W}] = 1$) state at time $t = 0$ minutes. The parameters used are those listed in Table 2.2 with forward rate parameters set to 100 for k_7^+, k_8^+, k_{14}^+, and k_{15}^+. The Wnt state is then turned off ($[\mathcal{W}] = 0$) again at time $t = 2000$ minutes (denoted by a dashed line at $t = 2000$). The system smoothly moves between the off and on states reaching steady state in approximately $2,000$ minutes.

The Lee model was calibrated to experimental data in transition from on to off (see Figure 2.3). These experiments and simulation investigated how β-catenin would degrade in response to four changes compared to (a) an initial reference state. These include: (b) the addition of 0.2 nM of Axin, (c) addition of $1,000$ nM of activated Dishevelled, (d) inhibition of GSK3β, and (e) the addition of $1,000$ nM of TCF. In comparison to the reference state, the addition of Axin rapidly degraded β-catenin, whilst the other three methods slowed down the degradation of β-catenin in similar ways. The simulations in Figure 2.3 suggest that adding TCF or inhibiting GSK3β were more effective in preventing

β-catenin degradation than the addition of activated Dishevelled. This statement matches experimental data [9]. This suggests that Wnt helps decrease β-catenin degradation, however it does not completely prevent it from being phosphorylated through the core destruction cycle. Meanwhile inhibition of GSK3β suggests that it significantly decreases the concentration of destruction complex. The addition of TCF suggests that all the β-catenin binds to TCF and is therefore protected from destruction complex.

The final claim from Lee *et al.* is that Axin exists in very small concentrations (relative to the other components of destruction complex APC and GSK3β), and is therefore the limiting factor in determining how β-catenin is phosphorylated via the core destruction cycle. This can be seen in Figure 2.3 by comparing simulation (a) and (b) together. Addition of a small amount of Axin results in a significantly faster degradation of β-catenin. This further supports that Axin is the limiting component in how the destruction complex forms. This claim is supported by comparing the model to experimental results [58]. However, it was later found that this key behaviour only exists in Xenopus oocytes (the type of cells used in Lee *et al.*'s experiments), and that this claim does not easily extend to other animals, in particular mammalian cells [1].
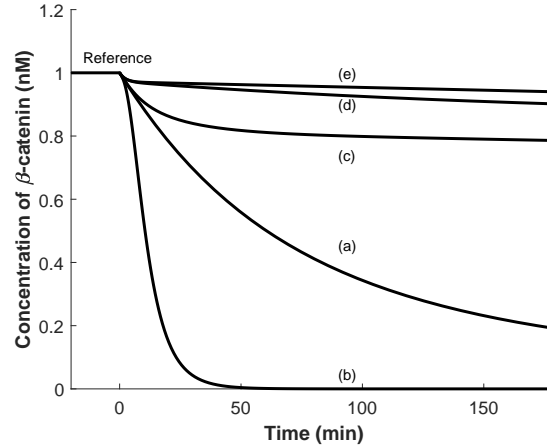
Figure 2.3: Simulations of β-catenin degradation where β-catenin and Axin influx are set to zero ($k_{12}^+ = 0$, $k_{13}^+ = 0$). For $t < 0$, the system is at steady state with $[\mathcal{W}] = 0$. At $t = 0$, k_{12}^+ and k_{13}^+ are set to 0. (a) Reference case where no changes were made. (b) Addition of 0.2 nM of Axin. (c) Addition of 1,000 nM of activated Dishevelled and $k_2 = 0$. (d) Inhibition of GSK3β by setting k_4 and k_9 to zero. (e) Addition of 1,000 nM of TCF.

2.2.2 The multiple time-scales of the Wnt signalling pathway

A paper by Mirams *et al.* investigated how different sections of the Lee model operated on different time-scales [59]. The paper reduced the ODE system from 15 components down to six [60], and then completed a systematic analysis to support the claim that the Lee model operates on three distinct time-scales.

To reproduce the results from Mirams, the first step is to non-dimensionalise the reduced ODE system in (2.1) to (2.15). Time is scaled by $1/k_5$, and the 6 chemical species are scaled as in Table 2.3.

Table 2.3: Mirams model variables and scaling for the six key components in the model.

Dimensional	Dimensionless	Scaling	Description
D_a	X_1	$1/\text{Dsh}^0$	Dishevelled (active)
DC	X_2	k_5/k_{13}^+	APC/Axin/GSK3β
B^*/DC^*	X_3	k_5/k_{13}^+	β-catenin*/APC*/Axin*/GSK3β
A	X_4	k_5/k_{13}^+	Axin
DC^*	X_5	k_5/k_{13}^+	APC*/Axin*/GSK3β
B	X_6	$1/K_{14}$	β-catenin

The resulting dimensionless ODEs which are obtained from the original Lee model in (2.1) to (2.15) are,

$$\frac{dX_1}{dt} = k_1'[\mathcal{W}](1 - X_1) - k_2'X_1, \tag{2.16}$$

$$\frac{dX_2}{dt} = -(k_3'X_1 + k_4' + k_6^{'-})X_2 + X_5 + \frac{k_6^{'+}X_4}{1 + K_{14}'X_6}, \tag{2.17}$$

$$\frac{dX_3}{dt} = k_9'X_5X_6 - k_{10}'X_3, \tag{2.18}$$

$$\frac{dX_4}{dt} = \frac{\left(k_3'X_1 + k_6^{'-}\right)X_2 - \left(\dfrac{k_6^{'+}}{1 + K_{14}'X_6} + k_{13}^{'-}\right)X_4 + 1 + \dfrac{dX_6}{dt}\dfrac{K_7'K_{14}'X_4}{(1 + K_{14}'X_6)^2}}{1 + \dfrac{K_7'}{1 + K_{14}'X_6}}, \tag{2.19}$$

$$\frac{dX_5}{dt} = \frac{\Psi(X_2, X_3, X_5, X_6)\Phi(X_5, X_6) - X_5K_8'\left(k_{12}^{'+} - K_{14}'X_5X_6 - k_{12}^{'-}X_6\right)}{(1 + K_8'X_6)\,\Phi(X_5, X_6) - k_{13}^{'+}X_5}, \tag{2.20}$$

$$\frac{dX_6}{dt} = \frac{k_{13}^{'+}X_6\Psi(X_2, X_3, X_5, X_6) - (1 + K_8'X_6)\left(k_{12}^{'+} - K_{13}'X_5X_6 - k_{12}^{'-}X_6\right)}{k_{13}^{'+}K_8'X_5X_6 - (1 + K_8'X_6)\,\Phi(X_5, X_6)}, \tag{2.21}$$

where

$$\Psi(X_2, X_3, X_5, X_6) = k_4'X_2 + k_{10}'X_3 - X_5 - k_9'X_5X_6 \tag{2.22}$$

$$\Phi(X_5, X_6) = 1 + k_6^{'+}k_{13}^{'+}X_5 + \frac{\text{TCF}^0}{(1 + X_6)^2} + \frac{\text{APC}^0}{(1 + K_{14}'X_6)^2}. \tag{2.23}$$

By scaling each species, the reaction rate (and dissociation) constants change as well. These scaled rates are represented as k' or K'. The constants k_1, k_2, k_4, k_6^-, k_{10}, k_{11}, k_{12}^-, and k_{13}^- are all scaled (divided) by k_5. The other constants are scaled as $k_3' = \text{Dsh}^0k_3/k_5$, $k_6^{'+} = k_6^+\text{GSK3}^0\text{APC}^0/(K_7k_5)$, $k_9' = k_9K_{14}/(k_5K_8)$, $k_{12}^{'+} = k_{12}^+/(k_5K_{14})$, $k_{13}^{'+} = k_{13}^+/(k_5K_8)$, $K_{13}' = k_9k_{13}^{'+}/k_5$, $K_7' = \text{APC}^0/K_7$, $K_8' = K_{14}/K_8$, and $K_{14}' = K_{14}/K_{15}$.

Results of the solutions to (2.16) to (2.21) are shown in Figure 2.4 for which the system starts at steady state with Wnt off ($[\mathcal{W}] = 0$), then it is turned on ($[\mathcal{W}] = 1$) at $t = 0$ until it reaches steady state, then Wnt is turned off again and run until it returns to the original steady state. From this figure, it is more clear that the turnover of β-catenin (X_6) operates on a longer time-scale than the other components. Although it is not immediately clear if active destruction complex and β-catenin- bound destruction complex (X_5 and X_3 respectively) operate on a shorter time-scale than the remaining three components. This becomes clearer when noticing that the reaction rate constants

k_9' and k_{10}', which helps bind and phosphorylates β-catenin, are about 100 times larger than all other constants, suggesting that the phosphorylation of β-catenin via the core destruction cycle is rapid in comparison to the turnover rate of β-catenin.
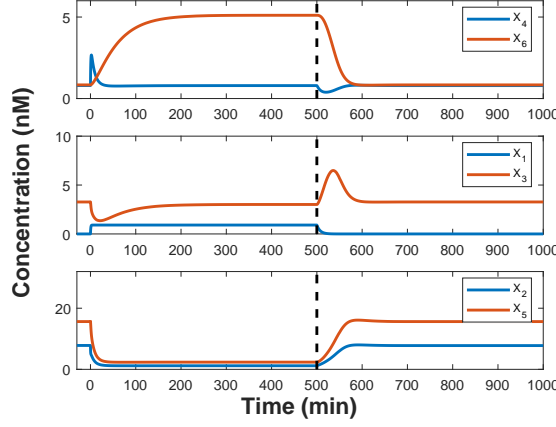
Figure 2.4: Simulations of the dimensionless versions of the Lee model (2.16) to (2.21). For $t < 0$, the system is at steady state when $[\mathcal{W}] = 0$. The parameters used are scaled versions of the parameters in Table 2.2. The rate constants k_1, k_2, k_4, k_6^-, k_{10}, k_{11}, k_{12}^-, and k_{13}^- are all scaled (divided) by k_5. The other constants are scaled as $k_3' = \mathrm{Dsh}^0 k_3/k_5$, $k_6'^+ = k_6^+ \mathrm{GSK3}^0 \mathrm{APC}^0/(K_7 k_5)$, $k_9' = k_9 K_{14}/(k_5 K_8)$, $k_{12}'^+ = k_{12}^+/(k_5 K_{14})$, $k_{13}'^+ = k_{13}^+/(k_5 K_8)$, $K_{13}' = k_9 k_{13}'^+/k_5$, $K_7' = \mathrm{APC}^0/K_7$, $K_8' = K_{14}/K_8$, and $K_{14}' = K_{14}/K_{15}$. For $0 < t < 500$, Wnt is turned on ($[\mathcal{W}] = 1$) and allowed to reach steady state. At $t = 500$ (denoted by a dashed line), Wnt is turned off ($[\mathcal{W}] = 0$), and the system returns to its original steady state.

To determine the three time-scales that the Wnt pathway operates on, Mirams introduced the parameter $\varepsilon = k_{12}'^- = 1.93 \times 10^{-3}$, using this to scale the six dimensionless ODEs. This parameter scales the other reaction rate constants onto a similar level. The parameters that change are $\hat{k}_9 = \varepsilon^1 k_9'$, $\hat{k}_{10} = \varepsilon^1 k_{10}'$, $\hat{k}_{12}^+ = \varepsilon^{-1} k_{12}'^+$, $\hat{k}_{13}^+ = \varepsilon^{-2} k_{13}'^+$, $\hat{K}_{13} = \varepsilon^{-1} K_{13}'$, and $\hat{K}_{14} = \varepsilon^{-1} K_{14}'$. All other constants remain unchanged, and are relabelled as $\hat{k}_i = k_i'$ for the ith reaction rate (or dissociation) constant. Making these substitutions, the dimensionless ODEs (2.16) to (2.21) become,

$$\frac{dX_1}{dt} = \hat{k}_1 \hat{\mathcal{W}}(1 - X_1) - \hat{k}_2 X_1, \tag{2.24}$$

$$\frac{dX_2}{dt} = -(\hat{k}_3 X_1 + \hat{k}_4 + \hat{k}_6^-)X_2 + X_5 + \hat{k}_6^+ \frac{X_4}{1 + \varepsilon \hat{K}_{14} X_6}, \tag{2.25}$$

$$\varepsilon \frac{dX_3}{dt} = \hat{k}_9 X_5 X_6 - \hat{k}_{10} X_3, \tag{2.26}$$

$$\frac{dX_4}{dt} = \frac{(\hat{k}_3 X_1 + \hat{k}_6^-)X_2 - (\hat{k}_6^+ + \hat{k}_{13}^-)X_4 + 1}{1 + \hat{K}_7}, \tag{2.27}$$

$$\varepsilon \frac{dX_5}{dt} = -\frac{(\hat{k}_9 X_5 X_6 - \hat{k}_{10} X_3)}{1 + \hat{K}_8 X_6} + \varepsilon \frac{\hat{k}_4 X_2 - X_5}{1 + \hat{K}_8 X_6}, \tag{2.28}$$

$$\frac{1}{\varepsilon} \frac{dX_6}{dt} = (\hat{k}_{12}^+ - \hat{K}_{13} X_5 X_6 - X_6) - \frac{\hat{k}_{13}^+ X_6}{1 + \hat{K}_8 X_6}(\hat{k}_9 X_5 X_6 - \hat{k}_{10} X_3), \tag{2.29}$$

where the three time-scales are determined by the ε^1, ε^0, and ε^{-1} coefficients in front of the various time derivatives.

$O(\varepsilon)$: Short time-scales - Rapid phosphorylation of β-catenin via the core destruction cycle

Equations (2.26) and (2.28) operate on a short time-scale, that is to say they reach pseudo-equilibrium rapidly. These reactions relate to the phosphorylation of β-catenin and its release from DC*. It is this time-scale which provides further evidence of how efficiently destruction complex can regulate β-catenin, and why in the presence of Wnt, a small decrease in destruction complex results in a large increase of β-catenin. Future models of Wnt, explored throughout the rest of this chapter and in Chapters 4 and 5, all take into account the speed of this reaction as a fundamental assumption.

$O(1)$: Medium time-scales - Formation of destruction complex

Before destruction complex can phosphorylate β-catenin, it first needs to form from its scaffolding proteins, Axin, APC, and GSK3β. Mirams considers the speed at which this forms to be on a medium time-scale. Realistically, these reactions occur on the order of minutes in experiments, and therefore can appear to be "quick". However relative to the processes in Section 2.2.2, these reactions are 'medium' in speed.

For the Mirams model, the components Dishevelled, destruction complex, and Axin all operate on this scale (see (2.24), (2.25) and (2.27)). Interestingly, Dishevelled works on time-scales of the same order as destruction complex and Axin, which means that changes to Wnt can result in observable changes in destruction complex and Axin.

The reactions in this time-scale become important in building microscopic stochastic simulations for the Wnt pathway (see Chapter 3). Specifically, the rate of destruction complex formation causes an issue in utilising Smoluchowski kinetics (see Section 3.5.4). This issue is addressed in Chapter 4.

$O(\varepsilon^{-1})$: Long time-scale - Degradation of free β-catenin

The longest characteristic time-scale refers to the degradation of β-catenin via both the natural degradation and proteasomal removal. The degradation of β-catenin rate constant, $k_{13} = 2.57 \times 10^{-4}$ min^{-1} is approximately $1,000$ times smaller than any other first order reaction rate constant in the Lee model. This suggests why in a system with Wnt on ($[\mathcal{W}] = 1$), β-catenin takes a while before reaching steady state, as its steady state depends mostly upon the influx of β-catenin (k_{12}^+) and the degradation (k_{12}^-) when destruction complex is mostly inhibited. The same cannot be said for when Wnt goes from the on state to the off state. The second part of Figure 2.4 ($t > 500$), shows a rapid decrease in the concentration of β-catenin, which can be explained by the increase of destruction complex on the medium time-scale, causing the rapid phosphorylation of β-catenin on the short time-scale, making it appear that the degradation of β-catenin occurs on a scale smaller than the long time-scale.

2.3 Models of canonical Wnt signalling with Axin2 feedback

2.3.1 Introduction to oscillating signalling pathways

Oscillatory behaviour in developmental biology is a commonly studied biological phenomena. In cellular signalling, three important oscillating pathways are those involving

Notch [61], fibroblast growth factors (FGF) [62], and Wnt [63]. These three oscillating pathways can be coupled together to form what is called the segmentation clock [64], a complicated gene network which coordinates somitogenesis with a clock-like periodicity. The three pathways are linked together by the nucleus of a cell which allows the pathway to have crosstalk. This crosstalk has been studied extensively through experiments and mathematical models [65, 66, 67]. Chapter 5 focuses on the Axin2 feedback loop in the Wnt oscillating pathway, therefore the models presented in this section will focus on Wnt independent of Notch and FGF. Linking the proposed models in Chapter 5 with the Notch and FGF signalling network could form the basis of future work.

It has been demonstrated that the canonical Wnt pathway exhibits oscillatory behaviour, and this is explained through the presence of a negative feedback loop involving Axin2. Research has shown that β-catenin and the β-catenin/TCF complex, when it has translocated into the nucleus, can induce the production of the Axin2 protein [44], which is a negative regulator of β-catenin. Higher levels of Axin lead to higher levels of destruction complex, which results in larger regulation of β-catenin. The decrease in β-catenin then decreases Axin2. This negative feedback loop can then repeat resulting in observed oscillatory behaviour.

There has been considerable mathematical interest into the Axin2 feedback loop. Initial models based on the Lee model were complex, and required the use of mathematical heuristics to obtain reasonable results. Recent modelling approaches are significantly simpler and less computationally expensive. The following sections highlight the changes in modelling the feedback loop, and how variations in the modelling has led to new insights into the Wnt signalling pathway.

2.3.2 Wawra model

The model by Wawra *et al.* extends the Lee model by introducing two negative feedback loops [68]. The first of these introduces Axin2 (Ax_2), a protein that is produced in the presence of β-catenin, which then increases the production of Axin. The second loop, uses dickkopf inhibitor 1 (DK) [69], also produced in the presence of β-catenin, which inhibits the ability of Dishevelled to dissociate the destruction complex [70]. The reaction pathway for this model is shown in Figure 2.5. The new species and reactions are highlighted in red, to distinguish that these are added to the Lee model.
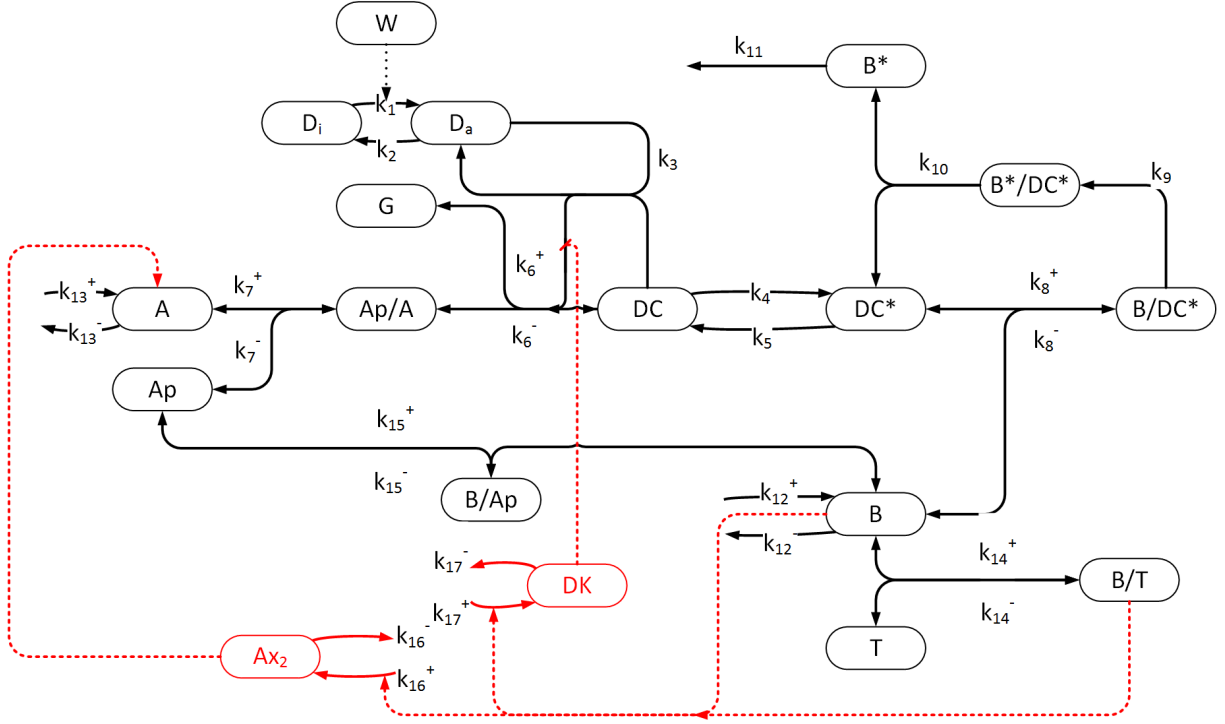
Figure 2.5: The Wawra model for describing the Axin2 (Ax_2) and dickkopf inhibitor 1 (DK) feedback loops in the Wnt signalling pathway. This model extends that of Lee *et al.* by introducing the feedback reactions and components in red. Synthesis of Ax_2 and DK is accelerated by a β-catenin and β-catenin/TCF signal. Ax_2 then up-regulates Axin (A). DK inhibits the effect D_a has on dissociating the destruction complex (DC). This inhibition is represented by a "/".

The Wawra model uses the ordinary differential equations from the Lee model, and adds two components (and their reactions) to it. The Wawra model introduces time delays which converts the ODEs into delay differential equations (DDEs). The Lee model equations that differ in the Wawra model are listed below. These equations are,

$$\frac{d[DC]}{dt} = -\mathbf{v}_3 - v_4 + v_5 + v_6, \tag{2.30}$$

$$\frac{d[G]}{dt} = \mathbf{v}_3 - v_6, \tag{2.31}$$

$$\frac{d[Ap/A]}{dt} = \mathbf{v}_3 - v_6 + v_7, \tag{2.32}$$

$$\frac{d[A]}{dt} = -v_7 + \mathbf{v}_{13}, \tag{2.33}$$

$$\frac{d[Ax_2]}{dt} = \mathbf{v}_{16}, \tag{2.34}$$

$$\frac{d[DK]}{dt} = \mathbf{v}_{17}, \tag{2.35}$$

Each bolded flux $\mathbf{v}_i$ (which differ from the Lee model in Section 2.2.1) is equal to,

$$\mathbf{v}_3 = k_3[D_a][DC]\left(1 - \frac{[DK](t - T_{p,DK} - T_{diff,DK}) - DK^{\mathcal{W}=0}}{DK^{\mathcal{W}=1} - DK^{\mathcal{W}=0}}v_{3,inh}\right), \qquad (2.36)$$

$$\mathbf{v}_{13} = k_{13}^+ - k_{13}^- + a[Ax_2](t - T_{p,Ax_2}), \qquad (2.37)$$

$$\mathbf{v}_{16} = bh^+([B](t - T_{r,Ax_2}) + [B/T](t - T_{r,Ax_2}), \theta, m) + l - c[Ax_2], \qquad (2.38)$$

$$\mathbf{v}_{17} = bh^+([B](t - T_{r,DK}) + [B/T](t - T_{r,DK}), \theta, m) + l - c[DK], \qquad (2.39)$$

where $\mathbf{v}_3$, $\mathbf{v}_{13}$, $\mathbf{v}_{16}$, and $\mathbf{v}_{17}$ have time delays. The flux in $\mathbf{v}_{16}$ and $\mathbf{v}_{17}$ utilises the Hill function,

$$h^+(X, \theta, m) = \frac{X^m}{X^m + \theta^m}. \qquad (2.40)$$

Hill functions are generally found in modelling gene networks, and Wawra finds that they work well in describing the Axin2 feedback loop in the Wnt/β-catenin pathway. The new parameters used by Wawra *et al.* for these DDEs are listed in Table 2.4.

Table 2.4: Parameters for the Wawra model.

	Parameter	Value	Units
Rate constants	c	0.23	min^{-1}
Synthesis fluxes	k_{13}^+	7.4×10^{-5}	nM min^{-1}
Delays	T_{r,Ax_2}	33.45	min
	T_{p,Ax_2}	7	min
	$T_{r,DK}$	8.22	min
	$T_{p,DK}$	2.26	min
	$T_{diff,DK}$	30	min
Hill function	θ	111.7	nM
	m	5	dimensionless
Translation Rate	a	4.5	min^{-1}
Other constants	$DK^{\mathcal{W}=0}$	1.827×10^{-6}	nM
	$DK^{\mathcal{W}=1}$	1.644×10^{-5}	nM
	l	4.129×10^{-7}	nM min^{-1}
	b	3.831×10^{-6}	nM min^{-1}
	$v_{3,inh}$	0.5	dimensionless

The Wawra model is a complex process and difficult to reproduce for the following reasons. The most prominent reason is that it uses delay differential equations. These have the added complexity of needing to keep track of the systems history. Additionally, stiff DDEs (which is the case for oscillatory systems), generally cause computational issues with typical solvers. Combining this with the fact the Wawra model is a system of 17 differential equations further increases the computational cost to simulate the model. Sections 2.3.3 and 2.3.4 overcome this computational problem by using a simplified Wnt model that incorporates the removal of destruction complex instead of it dissociating into its scaffolding proteins [71, 72].

The purpose of the Wawra *et al.* paper was to investigate how Axin2 feedback and dickkopf inhibitor 1 feedback affected oscillations in β-catenin, and to attempt to computationally determine how sensitive these oscillations are to these two feedback components.

The results implied that both processes are needed to induce oscillations, as Axin2 affects the concentration of destruction complex, whilst dickkopf inhibitor 1 affects how well Dishevelled can deconstruct the destruction complex.

The paper provided one of the first mathematical insights into oscillations of β-catenin. Even though the results are difficult to analyse, they do provide enough information to warrant further investigation. For example, it is not clear if Axin2 or dickkopf inhibitor 1 feedback is a dominating mechanism, or if both are required to modulate the systems.

2.3.3 Jensen model

A paper by Jensen *et al.* [71] further explores the negative feedback loop created by Axin2. However the model moves away from the heuristic and complex detail of the Lee and Wawra models, simplifying the process to 8 components (see Figure 2.6). The Jensen model differs to that in Wawra *et al.* as it uses a Wnt deactivator type process which removes destruction complex from the system, instead of just dissociating it like the Wawra model. This change in how Wnt operates is highlighted in red in Figure 2.6.
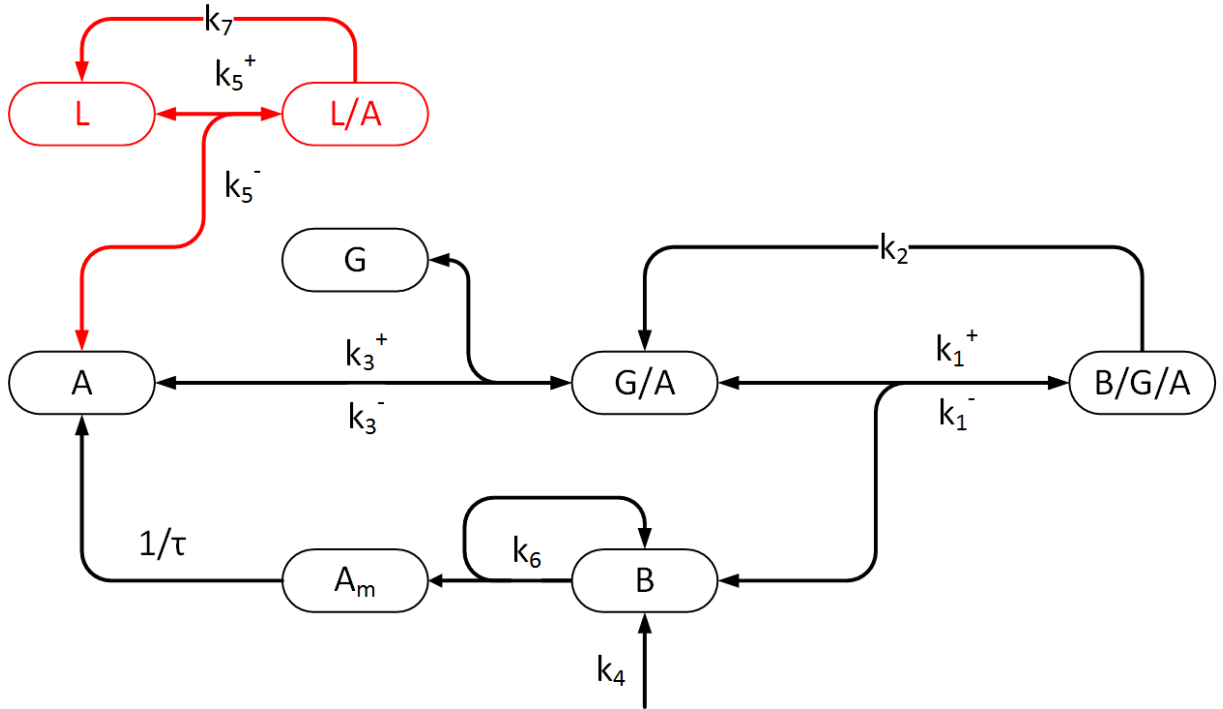
Figure 2.6: The Jensen model for describing the Axin2 feedback loop. Reactions and components that differ to the Lee model are highlighted in red. Central to this process is the deactivation of Axin (A) by a Wnt receptor complex represented by LRP5/6 (L). This process helps degrade Axin at a varying rate, which is essential for inducing oscillations in β-catenin.

The Jensen model has 8 ODEs (8 chemical species) that describe 15 reactions. These

ODEs are,

$$\frac{d[B/G/A]}{dt} = k_1^+[B][G/A] - k_1^-[B/G/A] - k_2[B/G/A], \tag{2.41}$$

$$\frac{d[G/A]}{dt} = k_3^+[G][A] - k_3^-[G/A] - k_1^+[B][G/A] + k_1^-[B/G/A] + k_2[B/G/A], \tag{2.42}$$

$$\frac{d[B]}{dt} = k_4 - k_1^+[B][G/A] + k_1^-[B/G/A], \tag{2.43}$$

$$\frac{d[G]}{dt} = -k_3^+[G][A] + k_3^-[G/A], \tag{2.44}$$

$$\frac{d[A]}{dt} = -k_3^+[G][A] + k_3^-[G/A] + k_7[A_m] - k_5^+[A][L] + k_5^-[L/A], \tag{2.45}$$

$$\frac{d[A_m]}{dt} = k_6[B]^2 - 1/\tau_{Am}[A_m], \tag{2.46}$$

$$\frac{d[L/A]}{dt} = k_5^+[A][L] - k_5^-[L/A] - k_7[L/A], \tag{2.47}$$

$$\frac{d[L]}{dt} = -k_5^+[A][L] + k_5^-[L/A] + k_7[L/A], \tag{2.48}$$

where $B/G/A$ is the complex (β-catenin/GSK3β/Axin), G/A is the GSK3β/Axin complex, B is β-catenin, G is GSK3β, A is Axin, A_m is Axin2 mRNA, L is LRP5/6, and L/A is the Axin/LRP5/6 complex. The parameters for these ODEs are listed in Table 2.5.

Table 2.5: Parameters for the Jensen model.

Parameter	Value	Units
k_1^+	0.1	nM^{-1} min^{-1}
k_1^-	7	min^{-1}
k_2	200	min^{-1}
k_3^+	0.2	nM^{-1} min^{-1}
k_3^-	1.2	min^{-1}
k_4	0.4	nM min^{-1}
k_5^+	10	nM^{-1} min^{-1}
k_5^-	0.08	min^{-1}
k_6	0.7	nM^{-1} min^{-1}
k_7	0.7	min^{-1}
τ_{Am}	40	min
k_8	0.1	min^{-1}

The model is simulated in Figure 2.7 using parameter values from Table 2.5, and setting the initial concentrations to zero for all components except GSK3β and LRP5/6, which are both set to 50 nM. From this figure, it is clear that all 8 components demonstrate oscillatory behaviour.
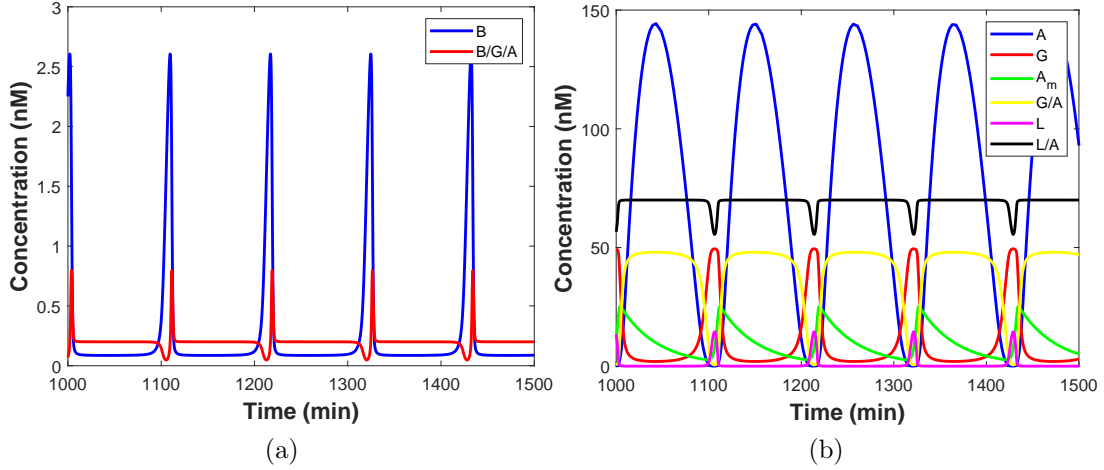
Figure 2.7: (a) Simulated results for β-catenin (B) and destruction complex ($B/G/A$). (b) Simulated results for Axin (A), GSK3β (G), Axin2 mRNA (A_m), GSK3β/Axin (G/A), LRP5/6 (L), Axin/LRP5/6 (L/A). Simulations are run until 1,500 minutes, and plotted from $t = 1,000$ to $t = 1,500$ minutes to skip past any initial transient behaviour. The concentration of destruction complex (B/G/A) has been multiplied by 100 to make the results comparable to β-catenin for plotting purposes.

There are three key differences that the Jensen model exhibits compared to the Wawra model:

1. The model uses Wnt as a deactivator of destruction complex instead of a deconstructor,

2. The system contains 8 ODEs using only zero, first, and second order reactions,

3. The system treats delays by dividing Axin2 mRNA by an exponentially distributed average time delay τ. This effectively reduces the rate at which Axin2 mRNA degrades.

Statement (1) means that the pathway needed to describe oscillations is much simpler than that of the Wawra model. Statement (2) makes it easier to perform a stability analysis and thus gain a deeper insight into the fundamental mechanisms. Statement (3) means that the system can be solved easily using many of the available ODE solvers, and can be solved in a short amount of time. This also means Jensen *et al.* were able to run many simulations exploring how oscillations are affected by different parameter sets.

According to Jensen *et al.*, the two important parameters for determining if oscillations are induced are $D_{B/G/A}$ and $D_{G/A}$, both of which are dissociation constants of destruction complex and the GSK3β/Axin2 complex,

$$D_{B/G/A} = \frac{k_1^-}{k_1^+}, \tag{2.49}$$

$$D_{G/A} = \frac{k_3^-}{k_3^+}. \tag{2.50}$$

To determine how these parameters affect the appearance of oscillations, simulations are run where the ratios $D_{B/G/A}$ and $D_{G/A}$ are both varied from 1 to 1,000. The amplitude and the period between oscillations (if any) of Axin2 are plotted as a heat map in Figure 2.8

to show how the variation in these two parameters affect the oscillations. Jensen *et al.* created other heat maps, but claimed that this is the best one as it provides such a large domain for which these pairs of parameters can be chosen from.
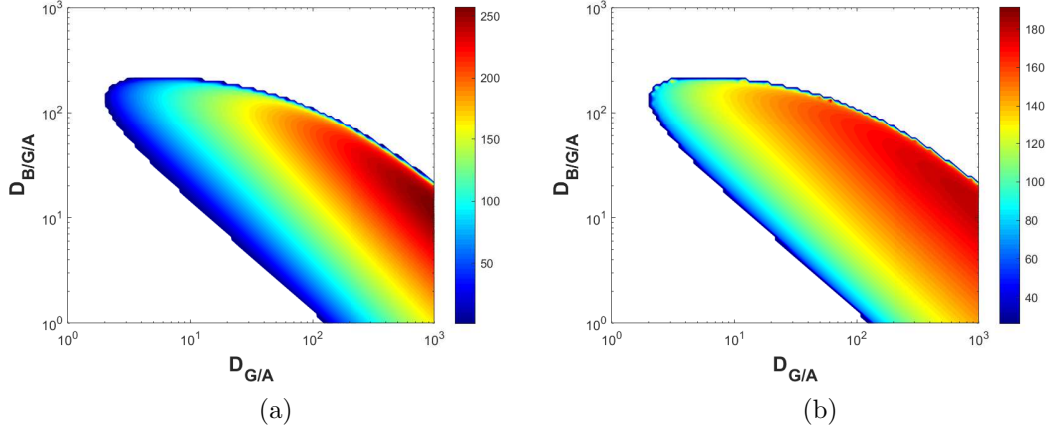
Figure 2.8: Two heat maps demonstrating the region for which oscillations occur for different parameter choices of $D_{B/G/A}$ and $D_{G/A}$ in the Jensen model. These maps plot the magnitude of the amplitude (a), and the period (b) of each oscillation of Axin2 (A). Amplitude is calculated as the average difference between the maximum and minimum values of Axin2, whilst period is computed as the average time between each peak of Axin2.

The results of the paper suggested that the following conditions are necessary to induce oscillations:

1. There must be an Axin2 feedback loop, in which β-catenin produces Axin2.

2. There must be a saturated degradation of Axin2 via the Wnt receptor complex, which inadvertently causes a time delay for which the Axin2 complex can then degrade β-catenin.

3. There is a lower limit for Wnt, and that the LRP5/6 complex must be greater than this limit.

2.3.4 Tymchyshyn model

A paper by Tymchyshyn and Kwiatkowska [72] used stochastic modelling techniques [73, 74] to explore how oscillations of β-catenin occur in the presence of a high and low Wnt stimulus. This model used only 6 components, focusing on Axin, β-catenin, and the Wnt receptor complex. Reactions for the Tymchyshyn model are presented in Figure 2.9.
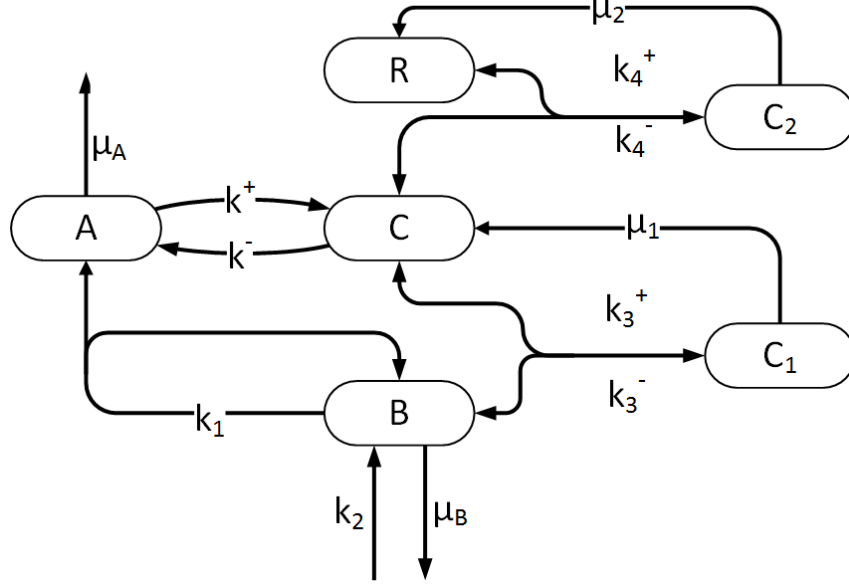
Figure 2.9: The Tymchyshyn model for describing the Axin2 feedback loop in the Wnt signalling pathway. Here, A represents Axin, B is β-catenin, C is active destruction complex, R is the Wnt receptor complex, C_1 is the B/C complex, and C_2 is the R/C complex. This model treats the total concentration of R as constant. The removal of C after binding with R is rapid. This demonstrates that the rate of removal of C is significantly faster than the phosphorylation of B by C.

The Tymchyshyn paper does not list the differential equations used to model the process deterministically, so these have been derived based on reactions and rate constants listed in their code [72]. This model contains 6 components, and a total of 15 reactions. The equivalent ODE system is,

$$\frac{d[A]}{dt} = k_1[B] - \mu_A[A] - k^+[A] + k^-[C], \tag{2.51}$$

$$\frac{d[B]}{dt} = k_2 - k_3^+[B][C] + k_3^-[C_1] - \mu_B[B], \tag{2.52}$$

$$\frac{d[C]}{dt} = -k_3^+[B][C] + (k_3^- + \mu_1)[C_1] + k^+[A] - k^-[C] - k_4^+[R][C] + k_4^-[C_2], \tag{2.53}$$

$$\frac{d[R]}{dt} = -k_4^+[R][C] + (k_4^- + \mu_2)[C_2], \tag{2.54}$$

$$\frac{d[C_1]}{dt} = k_3^+[B][C] - (k_3^- + \mu_1)[C_1], \tag{2.55}$$

$$\frac{d[C_2]}{dt} = k_4^+[R][C] - (k_4^- + \mu_2)[C_2], \tag{2.56}$$

where the parameters are listed in Table 2.6.

Table 2.6: Parameters for the Tymchyshyn model.

Parameter	Value	Units
k_1	0.012	nM^{-1} min^{-1}
k_2	0.423	min^{-1}
k_3^+	1	nM^{-1} min^{-1}
k_3^-	0.1	min^{-1}
k_4^+	100	nM min^{-1}
k_4^-	0.01	min^{-1}
k^+	0.05	nM^{-1} min^{-1}
k^-	0.025	min^{-1}
μ_1	0.5	nM^{-1} min^{-1}
μ_2	0.008	min^{-1}
μ_A	0.0167	min
μ_B	0.001	min

To reproduce the results from Tymchyshyn *et al.*, simulations are run using a high Wnt stimulus ($R_{\text{total}} = 10$ nM), and low Wnt stimulus ($R_{\text{total}} = 2$ nM), where the deterministic solution is overlapped with the stochastic simulation (see Figure 2.10). The stochastic simulation uses the Gillespie SSA [75] (see Section 3.4.1) in lieu of the π-calculus algorithm used by the authors. For the high Wnt case, the stochastic and deterministic solutions match closely with only minor discrepancies between the models. For the low Wnt case, periodic spiking is observed in the stochastic simulation, whilst the deterministic solution reaches steady state. Although the paper does not analyse this spiking in detail, the results most resemble the phenomenon called *self-induced stochastic resonance* [76, 77]. This behaviour is explored in further detail in Chapter 6.
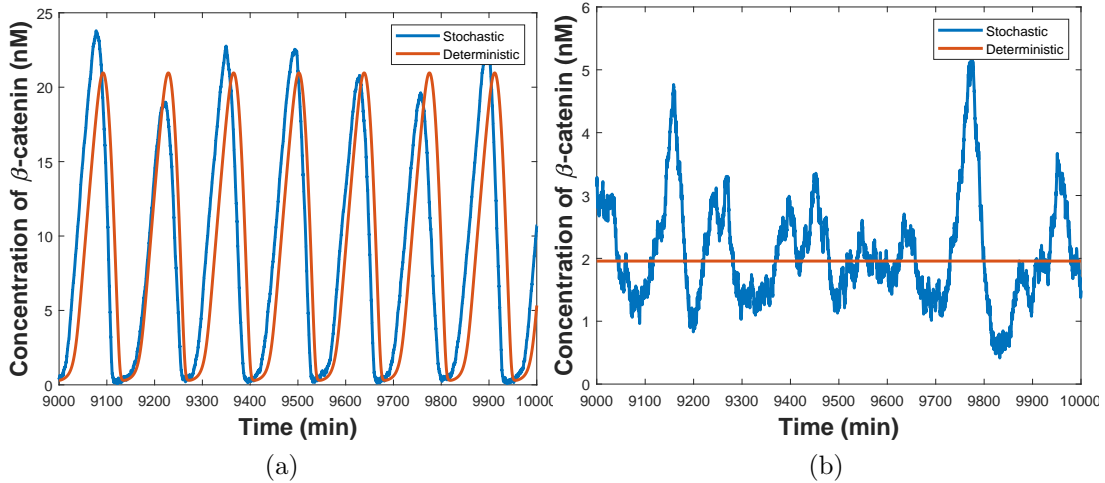
Figure 2.10: Comparison of stochastic simulations of the Tymchyshyn model for (a) high Wnt case ($R_{\text{total}} = 10$ nM) and (b) low Wnt case ($R_{\text{total}} = 2$ nM), using the Gillespie SSA, and plotted against its deterministic solution. The high Wnt case demonstrates oscillations both stochastically and deterministically, which match well. The low Wnt case only oscillates for the stochastic simulation.

2.4 Conclusion

In this chapter, common mathematical models for Wnt signalling were reviewed, and the key behaviours of each model were highlighted. The Lee model, being one of the first models to comprehensively describe most molecular interactions in the pathway, has provided an excellent basis for which future models were built on. In particular, the work by Mirams *et al.* showed how the Lee model operates on three distinct time-scales. This means the pathway has slow, fast, and very fast reactions. This difference in reaction speeds for Wnt is simulated in Section 4.5, where the model is used to highlight a fundamental problem when modelling the pathway stochastically.

The Axin2 feedback models developed by Wawra, Jensen, and Tymchyshyn, showed how the Lee model with feedback can be simplified. The Wawra model was a highly complex model that can be difficult to use to induce oscillations. The Jensen and Tymchyshyn models both showed that if the model is simplified, and is simulated using Wnt as a deactivator-type process, then it is significantly easier to induce oscillations, which leads to deeper analysis into how these oscillations occur. However, these models were still too complex to develop analytical relationships to determine the exact conditions for oscillations. This problem is solved by the models created in Chapter 5, for which the Jensen and Tymchyshyn models are simplified down to four components.

Chapter 3

Stochastic modelling of reaction-diffusion processes in biology

3.1 Introduction to stochastic reaction-diffusion systems

For many biological systems, it is insufficient to model reactions using only deterministic approaches such as ordinary or partial differential equations. For example, systems with low concentrations (low population/copy numbers) often require consideration of how these particles stochastically interact with each other, and where these particles are located in space. To accurately include these characteristics, a model is required which resolves the trajectories and interactions of individual agents which constitute the system. In the most common case of reaction-diffusion systems, the exact type of modelling approach used depends upon a number of factors, mainly the concentration of each agent, and the volume of the system. The former of these factors affects the computational cost-accuracy trade off for reactions whilst the latter affects that of diffusive processes. In short, the characteristic scales of the system determine the type of model which is most appropriate.

For this chapter, the following three spatial scales in order of decreasing scale will be considered: macro-, meso-, and micro-scale models. Typically, macro-scale models are used for volumes and copy numbers large enough such that a concentration can be defined. Meso-scale models are used for systems with a small volume and copy numbers smaller than macro-scale models. Micro-scale models operate on a similar (but usually smaller) scale than meso-scale models, but at the point where the actual positions of particles are required. Scales smaller than this include molecular, atomic, and quantum scales, which are not of interest to this thesis.

This chapter begins with a general description of algorithms for reaction-diffusion processes, and the commonly used software to simulate these systems. Following on from that, a detailed discussion about meso-scale models, and the so-called Gillespie algorithm will be presented. Attention is then turned to micro-scale systems, with an emphasis on using Smoluchowski kinetics (and the frameworks that extend Smoluchowski's work) to model reaction-diffusion systems for irreversible reactions of any order, and reversible reactions up to order two. The chapter concludes with a detailed description of the Smoldyn program, and its underlying mathematics and algorithms. It shall be noted here

that discussion in this literature review will be limited to systems which ignore crowding effects.

3.2 Overview of algorithms and software for reaction-diffusion processes

In this section, a general description of algorithms for reaction-diffusion processes is presented alongside a quick overview of the main software used to model these systems. For a non-mathematical modeller who only needs to simulate a system under a particular set of parameters, the algorithms and software presented in this section are self-contained and user friendly. The actual algorithms and mathematical basis on which each software is built is only of interest to those who need to write their own algorithms. For this reason, the software and algorithms are presented first, then Sections 3.4 and 3.5 explain the underlying methods in detail.

Algorithms used to simulate reaction-diffusion systems can be classified into two main categories:

- Fixed time-step algorithms, and

- Event-driven algorithms.

The first of these algorithms, evolves the system from some current time t to a future time $t + \Delta t$ at a fixed or predetermined time-step Δt. Within this small time window, any reaction or diffusive processes that occur are carried out. The system is updated, and the process is repeated until the simulation reaches a pre-defined end time.

Event-driven algorithms, work by skipping ahead to the next reactive or diffusive 'event', thereby eliminating all the time-steps in between in which nothing happens. This type of algorithm works best for smaller systems in which the likelihood of there being a lot of time where nothing occurs is high. Typically the event-driven algorithms are exact kinetics whilst fixed time-step algorithms are efficient but suffer from inaccuracies which often disappear as $\Delta t \to 0$.

3.2.1 Algorithms for reaction-only processes

For a deterministic (typically macro-scale) system, reaction-only processes are frequently simulated by solving a dynamical system of ordinary differential equations (ODEs). ODE models are very widely used due to their ease of construction and well-known numerical solution algorithms. However, when attempting to simulate this process stochastically, different methods are required.

The most intuitive way to introduce stochasticity and discreteness into these systems is to define a fixed time-step Δt and set the discrete copy numbers for each chemical species. At each time-step, assuming mass action kinetics, the modeller checks to see if a reaction occurs. The probability that a reaction happens at each time-step is equal to the product of the reaction rate constant, the population numbers of all molecules involved in the reaction, and the time-step Δt. For example, the bimolecular reaction $A + B \xrightarrow{k} P$ occurs with probability $P_{\Delta t} = k \Delta t A(t) B(t)$, where $A(t)$, $B(t)$ represents the population number of A and B at time t.

There are two major limitations of using a fixed time-step to simulate reactions, (1) the time-step Δt needs to be small enough such that one reaction occurs at a time, and

(2) if the time-step is too small, then the computational time will be too high. Therefore a balance between accuracy and computational speed needs to be determined when using fixed time-step methods.

Daniel Gillespie [75] proposed a solution to this problem by realising that for small systems, there is a lot of time between reactions in which nothing happens. Rather than calculate all of these time-steps, it was proposed to skip ahead to the next reaction event, which would maintain the accuracy, but significantly reduced the computational time. The method that resulted is now referred to as the Gillespie stochastic simulation algorithm (SSA). This algorithm is explained in detail in Section 3.4.1.

A major drawback of the Gillespie SSA is that if the system is large enough, then the average time-step will be quite small, resulting in a very large computation time. To bypass this, Daniel Gillespie introduced the τ-leaping method which approximates the Gillespie SSA to speed up computational time with acceptable losses in accuracy [78].

3.2.2 Algorithms for reaction-diffusion processes

The coupling of diffusion with reactive processes significantly increases the complexity and computational power required in comparison to reaction-only algorithms. The meso-scale and micro-scale models to be introduced in Sections 3.4 and 3.5 work on the basis that molecules in a bimolecular reaction need to be 'close' to each other to react. For meso-scale models on a lattice, the two particles need to be in the same compartment. For micro-scale models, particles react based on their separation, and for other more complex models, their energy. These conditions mean that any algorithm needs to be designed to efficiently check how far apart molecules are, and whether they can react with each other.

For meso-scale models, molecules diffuse by jumping into their neighbouring compartments. This 'jumping' can be thought of as a reaction, where particles diffuse to the next compartment at a rate proportional to their diffusion constant. Treating diffusion like a reaction allows the use of event-driven algorithms like the Gillespie SSA for meso-scale models (see Section 3.4.1).

Micro-scale models unfortunately do not lend themselves to event-driven algorithms quite easily. Particles on the micro-scale scale move about freely, and interact with each other through collisions. A lot of the software used to model these systems utilise a fixed time-step [79, 80, 81]. Recent work has been focused on how micro-scale reaction-diffusion systems can be more efficiently modelled using an event-driven algorithm [82, 83, 84].

3.2.3 Software for meso-scale models

Common software to model meso-scale reaction-diffusion systems include StochKit2 [85], URDME [86], CRDME [87], MesoRD [88], and StochSS [89].

StochKit2 is typically used for modelling systems with reactions-only and does not consider diffusive processes. The main algorithms used by the program include the Gillespie SSA [75], and the τ-leaping method [78]. A major advantage to StochKit2 is it automatically chooses the best algorithm to use based on the system to simulate, thus resulting in faster computational speeds at the required accuracy.

For simulating reaction-diffusion systems on a lattice structure, URDME, CRDME, and MesoRD would all be appropriate choices. MesoRD simulates systems on a typical lattice using the Next Subvolume Method [90]. URDME (Unstructured Reaction-Diffusion Master Equation) looks at modelling systems on arbitrary meshes. CRDME (Convergent Reaction-Diffusion Master Equation) reduces the compartmental size small enough such

that each compartment includes only a single particle. Bimolecular reactions are then resolved by checking for molecules in neighbouring compartments. This reduction significantly decreases the computational time as there are now less combinations of pairs of molecules to check for.

3.2.4 Software for micro-scale models

Micro-scale models as defined in this thesis involve particles moving freely in continuous space, and reacting when they collide. In comparison to on-lattice meso-scale models, the diffusion of particles is limited by the size of the time-step used, as opposed to the physical size of a compartment in a lattice for fixed time-step micro-scale models. Small time-steps must be used, otherwise it becomes possible for particles to pass through each other and not react, artificially reducing the effective reaction radius at the scale of the whole system. This is a major computational issue with micro-scale models; use a time-step too small and the simulation takes too long to complete, or use a large time-step which sacrifices accuracy.

The Smoldyn program [81] solves the problem of speed and accuracy by implementing an algorithm that adjusts the condition which defines a reaction event based on the time-step selected. This lets the user set a larger time-step, whilst still maintaining a high level of accuracy. The Smoldyn algorithm will be the focus of Section 3.6.

The MCell program [79, 80] pre-dates Smoldyn, and for a while was one of the most commonly used software for micro-scale models. This has since changed, as Smoldyn has been repeatedly optimised to provide far superior computational speed whilst maintaining accuracy [91, 92, 93]. Where MCell lacks in computational speed, it makes up for by having an excellent graphical interface using the program CellBlender [94].

The eGFRD program (enhanced Green's Function Reaction Dynamics) utilises an event-driven algorithm for modelling micro-scale systems [82, 83, 84]. For lattice-models, event-driven algorithms are simple to implement, as each compartment acts as a boundary to each particle, and therefore particles can only react with reactants inside that compartment, or they can diffuse to the next compartment. Micro-scale models do not lend themselves as well to event-driven algorithms, as the distance between each diffusive step is microscopically small and limited by the time-step used in Brownian dynamics [95]. The eGFRD program solves this problem, by placing protective spheres around each particle, or a pair of particles that could react. For each sphere, the time it takes until both the next reaction and diffusive step (escaping the protective sphere) is calculated, and stored in an ordered list. The algorithm then moves through the list one event at a time, executing the events, and updating the overall system based on the event outcome. Although event-driven algorithms in general are quicker to compute than fixed time-step methods, it has been shown recently that the eGFRD program has issues for systems with more than 10,000 molecules due to significant computational resources required to adapt dynamically to the events simulated [96].

3.2.5 Hybrid-scale models

There have been various successful attempts at combining the algorithms across macro-, meso-, and micro-scale frameworks into so-called hybrid models. Hybrid models aim to increase the computational speed of simulations, by allowing the system to be modelled on different scales. The rules for combining the scales depends upon each model. This thesis does not go into detail into how the models are constructed. Instead, common

hybrid models for each combination of scale is presented.

An algorithm that combines macro- and meso-scale models is the pseudo-compartment method [97]. PDE-assisted Brownian dynamics is used to couple the macro-scale with micro-scale models [98]. Meso- and micro-scale models can be combined using the two-regime method [99], the adaptive two-regime method [100], the compartment-placement method [101], and the ghost cell method [102].

The Smoldyn algorithm has recently been updated to simulate hybrid models that combine meso- and micro-scale models [103]. Other software packages describing the combination of meso- and micro-scale models include Virtual Cell [104], and the hybrid model developed by Klann *et al.* [105]. Smoldyn claims that its hybrid simulations are faster and more accurate [103], hence it is suggested to choose that software over the others.

3.3   Macro-scale models

Macro-scale models are typically used for any large-volume system in which the number of molecules present is usually in the order of over 1 million (however that is not to say meso- and micro-scale models cannot model 1 million molecules), and the stochastic interactions between individual molecules are not important, but instead only the expected macro-scale distribution of reactants is of interest. Systems of this type are modelled with the reaction-diffusion PDE,

$$\frac{\partial \mathbf{u}}{\partial t} = D\nabla^2 \mathbf{u} + \mathbf{R}(\mathbf{u}), \tag{3.1}$$

in which $\mathbf{u}(\mathbf{x}, t)$ describes the concentration of molecules with position $\mathbf{x}$ at time t, D is the diffusion constant, ∇^2 is the Laplacian with respect to spatial coordinates $\mathbf{x}$, and $\mathbf{R}(\mathbf{u})$ describes any reaction terms, and is often non-linear. The advantage of using (3.1) is that there is an extensive literature describing analytical and numerical methods to efficiently solve systems of this type. This equation can even be extended to include stochastic behaviour implicitly by introducing noise terms and turning it into a stochastic partial differential equation (SPDE). The details for the PDE literature will not be explained as this is outside the scope for this thesis.

3.4   Meso-scale models

One of the major limitations of macro-scale methods is that they do not capture stochastic effects of individual events very well. One way to address this problem with minimal computational cost, is to model the movement and reaction of individual molecules on a lattice. There are various ways to model reaction-diffusion processes on a lattice [106].

The focus of this section is on what would be considered the simplest approach to meso-scale models (using a regular lattice), and how to simulate it using a Gillespie algorithm [75]. Refer back to Section 3.2.3 for a discussion of more advanced algorithms and software that make use of more complex lattice structures.

For meso-scale models simulated on a one-dimensional regular lattice, the following approach is taken.

1. Construct a one-dimensional lattice with length L and divide it into K compartments. Each compartment has length $h = L/K$.

2. Initialize the distribution of particles by assigning them to lattice compartments.

3. If required, define on which part of the lattice particles may enter or leave the system.

4. At each time-step (Δt), particles jump into a neighbouring compartment with probability $D\Delta t/h^2$.

5. Particles in each compartment may react on their own, or react with another particle inside that lattice. The probability of these reactions are computed by multiplying the associated reaction rate constant with the product of the copy numbers of each reactant and the time-step Δt.

6. The algorithm returns to step 4 until a desired end in the simulation.

This method approximates particles into a local environment and allows each particle to interact with other particles in the local neighbourhood. However, this method is limited by how small each compartment can be. As the compartment size is decreased, the computational complexity increases but accuracy increases. There is a lower limit to the compartmental size, at which the parameter h is small enough, causing the probability of reaction to be greater than 1 irrespective of how small the time-step is (that is the compartmental effective reaction rate goes to infinity) [107]. If resolution beyond this critical level is required, it is necessary to use the micro-scale models discussed in Section 3.5. However some of the methods presented in Section 3.2.3, in particular convergent reaction-diffusion master equation (CRDME) [87], can be used accurately at any compartmental size. This effectively allows accurate simulations of reaction-diffusion systems without massively increasing the computational cost associated with micro-scale models.

3.4.1 Gillespie stochastic simulation algorithm (SSA)

Event-driven algorithms are commonly used in stochastic modelling at the meso-scale generally because they run fast without compromising on accuracy. One of the most widely used algorithms for meso-scale reaction-diffusion processes was proposed by Daniel Gillespie [75]. The key characteristic of this algorithm is that it calculates the time until the next event happens (whether it be a reaction or diffusion step), jumps ahead to this time, updates this one event only, and then updates the event propensities/rates. This type of algorithm is most beneficial to small systems that react slowly, as there would be a large time gap in between events occurring. However for larger systems with fast reactions, the time between events is significantly smaller, therefore increasing the computational cost of using this approach.

The Gillespie SSA can be used for reaction-only, diffusion-only, or for reaction-diffusion processes. To model diffusion via the Gillespie SSA, it is necessary for the system to be defined on a lattice, such that each particle can transfer across compartments.

Reaction processes

The Gillespie SSA for a reactive system is;

1. Generate two random numbers r_1, r_2 uniformly distributed in the interval (0,1).

2. For each reaction, calculate the mass action propensity,

$$\alpha_i = k_i \prod_{j=1}^{N_i} A_j(t), \tag{3.2}$$

where α_i is the propensity for the ith reaction, k_i is the reaction rate constant, N_i is the number of reactants for the ith reaction, and $A_j(t)$ represents the number of molecules at time t for the jth reactant. Note that this equation is slightly different if the same reactant is utilised more than once in the reaction. For example, in a bimolecular reaction involving two A molecules, the propensity is calculated as $A * (A - 1)$ instead of A^2.

3. Compute the total propensity,

$$\alpha = \sum_{i=1}^{m} \alpha_i, \tag{3.3}$$

where m is the total number of reaction events in the system.

4. Calculate the time τ until the next reaction using the inverse transform sampling relation,

$$\tau = \frac{1}{\alpha} \log(r_1^{-1}). \tag{3.4}$$

5. Determine which reaction occurs by finding i that satisfies,

$$\frac{1}{\alpha} \sum_{j=0}^{i-1} \alpha_j \leqslant r_2 < \frac{1}{\alpha} \sum_{j=0}^{i} \alpha_j, \tag{3.5}$$

where $\alpha_0 = 0$. Update the copy numbers for each species based on reaction i, then advance time from t to $t + \tau$. Repeat steps (1-5) until the time reaches the end of the simulation.

In practice, the speed of the algorithm can be improved by updating step 2 after the reaction event in step 5. By knowing what reaction has happened, the user can then update only the propensities that will change, that is the ones which include the reactants and products of the reaction event. This type of process resembles the "next-reaction method" [108].

Diffusion processes

The Gillespie SSA can be applied to diffusion processes, by treating each diffusion step as a reaction-like event. The algorithm for diffusion is described in one dimension on a regular lattice for a single species, however the method can easily be extended to 2 or 3 dimensions, for irregular lattices, and for multiple species.

Given a 1-dimensional domain of length L, divide the domain into K compartments of length $h = L/K$. Let $A_i(t)$ denote the number of molecules in compartment i at time t. Let the diffusion rate constant be $d = D/h^2$. Each diffusion step is denoted as the set of reactions,

$$A_1 \underset{d}{\overset{d}{\rightleftarrows}} A_2 \underset{d}{\overset{d}{\rightleftarrows}} \ldots \underset{d}{\overset{d}{\rightleftarrows}} A_K, \tag{3.6}$$

where $A_i \xrightarrow{d} A_{i+1}$ represents a jump of one molecule to the right, and $A_i \xleftarrow{d} A_{i+1}$ is a jump of one molecule to the left. With these definitions, the Gillespie SSA for diffusion processes is as follows,

1. Generate two random numbers r_1, r_2 uniformly distributed in the interval (0,1).

2. For each compartment, calculate the propensity,

$$\alpha_i = A_i(t)d, \tag{3.7}$$

   where α_i is the propensity for the ith diffusion event, and $A_i(t)$ is the number of molecules in compartment i at time t.

3. Compute the total propensity,

$$\alpha = \sum_{i=1}^{K-1} \alpha_i + \sum_{i=2}^{K} \alpha_i, \tag{3.8}$$

   as each molecule can jump to the compartment to the left or right (except for the two end compartments).

4. Calculate the time τ until the next reaction by,

$$\tau = \frac{1}{\alpha} \log(r_1^{-1}). \tag{3.9}$$

5. Determine if a jump to the left or right occurs.

   (a) If $r_2 < \sum_{i=1}^{K-1} \alpha_i$, a jump to the right occurs. Therefore an i is found which satisfies,

$$\frac{1}{\alpha} \sum_{j=1}^{i-1} \alpha_j \leqslant r_2 < \frac{1}{\alpha} \sum_{j=1}^{i} \alpha_j. \tag{3.10}$$

   Update $A_i(t)$ and $A_{i+1}(t)$ by decreasing and increasing them by 1 respectively.

   (b) Else if $r_2 \geqslant \sum_{i=1}^{K-1} \alpha_i$, a jump to the left occurs. Therefore an i is found which satisfies,

$$\frac{1}{\alpha} \left(\sum_{j=1}^{K-1} \alpha_j + \sum_{j=2}^{i-1} \alpha_j \right) \leqslant r_2 < \frac{1}{\alpha} \left(\sum_{j=1}^{K-1} \alpha_j + \sum_{j=2}^{i} \alpha_j \right). \tag{3.11}$$

   Update $A_i(t)$ and $A_{i+1}(t)$ by increasing and decreasing them by 1 respectively.

6. Advance time from t to $t + \tau$, and then repeat steps (1-7) until the desired end of the simulation.

Reaction-diffusion processes

The Gillespie SSA for reaction-diffusion processes combines the previous two algorithms, where the time until the next reaction or diffusion event is computed, and which event occurs is determined. However, there is now the added complication of needing to know which compartment each molecule is in, which increases the computational power for any reactions involving more than one molecule. This increases the complexity of computing the propensity for bimolecular reactions.

This thesis uses the Gillespie SSA for comparison purposes only and does not contribute to the development of associated methods, therefore the detailed algorithm is not included. Instead, the reader is referred back to the software presented in Section 3.2.3 for background on software for reaction-diffusion systems.

3.5 Micro-scale models

For the purposes of this thesis, a micro-scale model is defined as a model which considers individual biological molecules (proteins, enzymes, DNA, etc.) as point particles with no intrinsic three-dimensional form, and how each biological molecule moves and interacts with each other. There are models which operate on even smaller scales (molecular, atomic, quantum scales) whereby intra-molecular properties are considered, however these are not of interest to this thesis as they are typically limited to only a very small number of molecules.

In Chapter 4, diffusion is modelled using Brownian motion of individual molecules [109], and reactions are modelled using the framework derived by Marian von Smoluchowski [110]. This framework is then used again in Chapter 6 to model feedback loops in the Wnt signalling pathway.

3.5.1 Brownian motion

In 1827, Robert Brown observed the supposedly random motion of pollen particles suspended in water [109]. This type of random motion has since been referred to as Brownian motion. A particle undergoing Brownian motion is one that is suspended in some solvent, and is constantly bombarded by solvent particles, which makes the particle appear to move erratically.

Mathematically, Brownian motion is usually described by the Wiener process,

$$d\mathbf{X}_t = \sqrt{2D}d\mathbf{W}_t, \tag{3.12}$$

where $\mathbf{X}_t$ is the trajectory of a particle in three dimensions, $\mathbf{W}_t$ is a three-dimensional Wiener process, and D is the diffusion constant for the particle studied. The corresponding Fokker-Planck equation [111, 112] for the probability density function p of $\mathbf{X}_t$ is,

$$\frac{\partial}{\partial t}p(\mathbf{x}, t) = D\nabla^2 p(\mathbf{x}, t), \quad t > 0 \tag{3.13}$$

which corresponds to the PDE for diffusion, and the lower-case $\mathbf{x}$ represents the position of a particle in three-dimensional space. For simulation purposes, the Wiener process in (3.12) is integrated from t to $t+\Delta t$ using Ito calculus [113] to give the Brownian dynamics,

$$\mathbf{X}(t + \Delta t) = \mathbf{X}(t) + \sqrt{2D\Delta t}\boldsymbol{\xi}, \tag{3.14}$$

where Δt is the time-step, and $\boldsymbol{\xi}$ is a vector of normally distributed random numbers with zero mean and unit variance that differs for each particle and each dimension. This equation indicates how a new position $\mathbf{X}(t + \Delta t)$ is randomly calculated based on the previous position $\mathbf{X}(t)$ in the absence of any interactions with boundaries of reactants. These Brownian dynamics are explored further in Section 3.6.

3.5.2 Zero- and First-order reactions

Zero-order reactions

A zero-order reaction is one which takes the chemical notation,

$$\emptyset \xrightarrow{k_0} P, \tag{3.15}$$

in which the products P (of which there can be more than one product) are randomly generated at an average rate of k_0 molecules per unit time, and either placed at a pre-determined location, or placed randomly inside the domain. The empty set symbol ($\emptyset$) denotes that the molecules are produced from nothing according to the model. In reality, this would not be physically possible. Therefore in the context of modelling reaction-diffusion systems, the $\emptyset$ represents either molecules that flow into the system, or molecules produced from some other molecule that is not of interest to the overall process. When a zero-order reaction occurs in a micro-scale model, the initial position of products P will depend on the context of the reaction, but is often placed randomly inside the domain.

First-order reactions

First-order reactions take the form,

$$A \xrightarrow{k_1} P, \tag{3.16}$$

where the products P can also be replaced by $\emptyset$ (denoting a decay reaction). In micro-scale models, when a first-order reaction takes places, the molecules P are placed at the location of the reactant molecule A.

3.5.3 An important note about bimolecular and higher-order reactions

In the case of bimolecular reactions (and in fact any reaction involving more than one reactant), a rule which defines when a reaction will occur between local reactants should be defined. The rule needs to be matched to the reaction kinetics being modelled.

For the meso-scale models described in Sections 3.2.3 and 3.4, molecules had to be within the same compartment. In the case of micro-scale models, the 'closeness' now depends on the actual relative distance between two or more molecules, and thus requires a more rigorous mathematical explanation than what is given by meso-scale models. To model this 'closeness', the simplest definition for bimolecular reactions is just the Euclidean separation of the reactants. The following sections explain the work of Smoluchowski (and the models built on this framework) where 'closeness' is the separation of the molecules for a bimolecular reaction, and then show how these ideas extend to higher-order reactions. In Chapter 4, this will be extended further to apply to reversible higher-order reactions.

3.5.4 Smoluchowski kinetics for bimolecular reactions

Smoluchowski kinetics are based on the model developed by Marian von Smoluchowski in 1916 [110]. Smoluchowski was originally motivated to develop these ideas to describe the rate at which two diffusing, hard, spheres come into contact, for example, in more traditional systems of particles in a fluid. Smoluchowski made a note that this result would be useful for modelling chemical reactions, which certainly proved to be the case. Classical Smoluchowski kinetics is applied to bimolecular reactions,

$$A + B \xrightarrow{k} P, \tag{3.17}$$
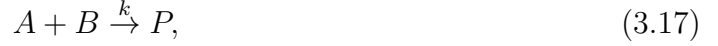
where k is the reaction rate constant, and P represents the product molecules.

Smoluchowski kinetics is defined by imposing that around any one point reactant A, there is a sphere with radius ρ (called the binding radius). According to the Smoluchowski framework for modelling a reaction, when the reactant B diffuses onto the surface of this sphere, then A and B undergo a reaction. This process is represented diagrammatically in Figure 3.1.
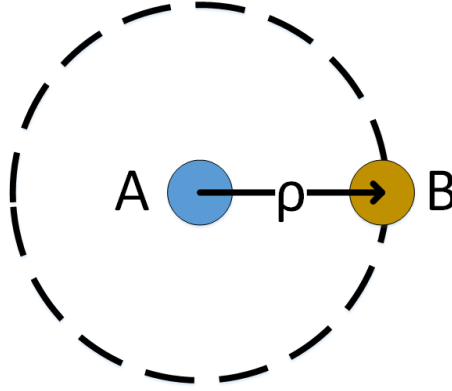
Figure 3.1: Smoluchowski radius for bimolecular reactions. A sphere is placed around the molecule A, with radius equal to the binding radius ρ. When a molecule of B diffuses onto the surface of this sphere, then A and B react.

The following derivation determines the size of the binding radius ρ in relation to the reaction rate constant k and the diffusion constants D_A, D_B. Let A and B be two diffusing molecules whose positions are $\mathbf{X}_A(t)$, $\mathbf{X}_B(t)$, with diffusion constants D_A and D_B respectively. Both A and B diffuse with Brownian dynamics. Let $\mathbf{R}(t) = \mathbf{X}_B(t) - \mathbf{X}_A(t)$ be the separation between the coordinates for A and B. This separation in a micro-scale model is determined by (3.14),

$$\mathbf{R}(t + \Delta t) = \mathbf{R}(t) + (\sqrt{2D_B\Delta t}\boldsymbol{\xi}_B - \sqrt{2D_A\Delta t}\boldsymbol{\xi}_A). \tag{3.18}$$

As both $\boldsymbol{\xi}_A$ and $\boldsymbol{\xi}_B$ are vectors of independent normally distributed random numbers with zero mean, their difference is also a vector of normally distributed random numbers with zero mean, and variance equal to the sum of the variances. Therefore (3.18) becomes,

$$\mathbf{R}(t + \Delta t) = \mathbf{R}(t) + \sqrt{2(D_A + D_B)\Delta t}\boldsymbol{\xi}. \tag{3.19}$$

The Fokker-Planck equation for (3.19) is,

$$\frac{\partial P(\mathbf{r}, t)}{\partial t} = (D_A + D_B)\nabla^2 P(\mathbf{r}, t), \tag{3.20}$$

where $P(\mathbf{r}, t)$ is the joint cumulative distribution function that at time t, the separation between molecule A and B is $\mathbf{r}$ and has yet to react. If the initial separation $\mathbf{r}(0)$ is uniformly distributed and external boundaries are neglected, the system is spherically symmetric. Letting $\|\mathbf{r}\| = r$, (3.20) becomes (in a spherical coordinate system),

$$\frac{\partial p(r,t)}{\partial t} = (D_A + D_B) \frac{1}{r^2} \frac{\partial}{\partial r} \left(r^2 \frac{\partial p(r,t)}{\partial r} \right), \tag{3.21}$$

where the lower-case $p(r, t)$ is a cumulative distribution function. Smoluchowski investigates (3.21) at pseudo-steady state (ignoring any transient effects on small time-scales and assuming that boundaries are at $r \to \infty$), reducing (3.21) to the ODE,

$$\frac{d^2 p}{dr^2} + \frac{2}{r} \frac{dp}{dr} = 0. \tag{3.22}$$

For this ODE, there are two boundary conditions. The first is that a reaction occurs instantaneously on the surface of a sphere with radius $r = \rho$. This means $p(\rho) = 0$, which implies that $p = 0$ also for $r \leqslant \rho$. The second condition is $p(r) \to 1$ as $r \to \infty$. This condition represents that if B is far enough away from A, then they cannot react together. Solving (3.22) and applying the boundary conditions gives the cumulative distribution function,

$$p(r) = 1 - \frac{\rho}{r}, \quad \text{for } r \geqslant \rho. \tag{3.23}$$

To relate ρ to the reaction rate constant k, the diffusive flux over the sphere with radius ρ is computed by the relation,

$$k = 4\pi \rho^2 (D_A + D_B) \frac{dp}{dr} \bigg|_{r=\rho}. \tag{3.24}$$

Substitution of (3.23) into (3.24), and evaluating the derivative at $r = \rho$ gives the Smoluchowski relation,

$$k = 4\pi \rho (D_A + D_B). \tag{3.25}$$

To use (3.25) to simulate a model, the reaction rate constant k and the diffusion constants D_A and D_B are usually taken from experimental values. Substitution of these constants into (3.25) gives the size of the binding radius ρ. Molecules in the system will diffuse via Brownian dynamics, and react whenever a molecule of B diffuses onto the surface of the sphere of radius ρ placed around A.

3.5.5 The Collins-Kimball model

The Smoluchowski kinetics in the previous section makes the assumption that a bimolecular reaction will occur instantaneously once the two reactants come into contact. This condition can be mathematically represented as an absorbing boundary, where the surface of the sphere placed around the molecule A will absorb a molecule of B that diffuses onto the surface. This type of assumption makes the reaction diffusion-limited, where the rate at which the reaction will occur is limited by how quickly the molecules diffuse to each other.

The Collins-Kimball model analyses Smoluchowski kinetics, and modifies it such that reactions become activation-limited instead [114]. This is achieved by changing the boundary at the binding radius ρ, from

$$p(\rho) = 0, \tag{3.26}$$

for the Smoluchowski case, to the Collins-Kimball boundary condition,

$$\left.\frac{dp(r)}{dr}\right|_{r=\rho} = \frac{kp(\rho)}{D}. \tag{3.27}$$

This provides an alternative way to resolve bimolecular reactions. However for simulations, determining if two molecules react together under this condition is more computationally intensive than the Smoluchowski approach [81]. For this reason, this thesis will not focus on the Collins-Kimball model.

3.5.6 Doi kinetics for generalized bimolecular reactions

Under the Smoluchowski framework, molecules react instantly once they are within a distance ρ of each other. In reality, Smoluchowski kinetics could be considered simplistic since molecules are likely to collide with each other multiple times before undergoing a reaction, if they were to react at all.

Masao Doi proposed modifying Smoluchowski kinetics to say that when two molecules come into contact, they react at a rate proportional to some constant λ [115]. A visual representation of this is shown in Figure 3.2. This allows the molecules to pass through each other, and it is possible for the two molecules to come into 'contact' but not react. This framework allows a very simple way to model two molecules colliding with each other before reacting (or not reacting).
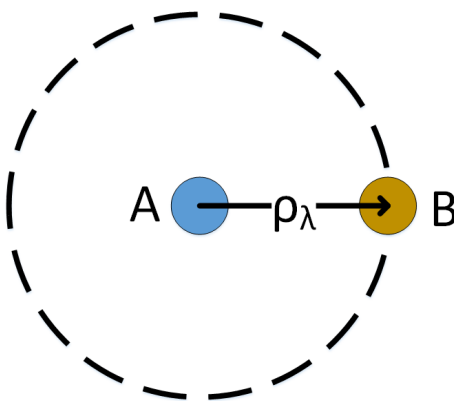
Figure 3.2: The Doi model for bimolecular reactions. The binding radius now depends on some constant rate λ. When a molecule of B diffuses into the sphere around A, there is a probability less than 1 that the two molecules react. Under this framework, it is entirely possible for B to diffuse completely through this sphere without reacting with A.

To build Doi's model, the assertion is that when a molecule of B comes within the sphere with binding radius ρ_λ placed around the molecule A, they react at a constant rate equal to λ. Note, this also means the Doi model reduces to Smoluchowski kinetics if $\lambda \to \infty$ (i.e. the reaction is instantaneous). In fixed time-step simulations, the two molecules react with probability $P_\lambda = \lambda \Delta t$, where Δt is the time-step. To obtain the

ODEs for this model, (3.21) is used, where the PDE is split into two regions, the first for $r \leqslant \rho_\lambda$ which is the region in which a reaction occurs, and the second for $r > \rho_\lambda$. In pseudo-steady state, the resulting ODEs are analogous to (3.22), and are,

$$0 = (D_A + D_B)\left(\frac{d^2p}{dr^2} + \frac{2}{r}\frac{dp}{dr}\right) - \lambda p, \qquad \text{for } r \leqslant \rho_\lambda, \qquad (3.28)$$

$$0 = (D_A + D_B)\left(\frac{d^2p}{dr^2} + \frac{2}{r}\frac{dp}{dr}\right), \qquad \text{for } r > \rho_\lambda. \qquad (3.29)$$

Solving these two ODEs gives the general solutions,

$$p(r) = \frac{a_1}{r}\sinh(r\beta) + \frac{a_2}{r}\cosh(r\beta), \qquad \text{for } r \leqslant \rho_\lambda, \qquad (3.30)$$

$$p(r) = a_3 + \frac{a_4}{r}, \qquad \text{for } r > \rho_\lambda, \qquad (3.31)$$

where the constant $\beta = \sqrt{\lambda/(D_A + D_B)}$ is introduced to simplify the notation. Given that there are now two ODEs, two additional conditions are introduced in order to solve both equations. The condition $\lim_{r\to\infty} p(r) = 1$ remains. As the reaction at $r = \rho$ is no longer instantaneous, the condition $p(\rho) = 0$ is removed. Instead, $p(r)$ and $p'(r)$ are both continuous at $r = \rho$, and that $p(r)$ is finite at $r = 0$. Imposing these four conditions gives the solutions,

$$p(r) = \frac{\sinh(r\beta)}{r\beta\cosh(\rho_\lambda\beta)}, \qquad \text{for } r \leqslant \rho_\lambda, \qquad (3.32)$$

$$p(r) = 1 - \frac{\rho_\lambda}{r} + \frac{\tanh(\rho_\lambda\beta)}{r\beta}, \qquad \text{for } r > \rho_\lambda. \qquad (3.33)$$

To relate ρ_λ to the reaction rate constant k, the diffusive flux over the sphere with radius ρ_λ is calculated by,

$$k = 4\pi(D_A + D_B)\rho_\lambda^2 \frac{dp}{dr}\bigg|_{r=\rho_\lambda}. \qquad (3.34)$$

Substitution of (3.32) or (3.33) into (3.34) and evaluating it gives the Doi relation,

$$k = 4\pi(D_A + D_B)\left[\rho_\lambda - \sqrt{\frac{D_A + D_B}{\lambda}}\tanh\left(\rho_\lambda\sqrt{\frac{\lambda}{D_A + D_B}}\right)\right]. \qquad (3.35)$$

As expected, the limit $\lambda \to \infty$ sends the 'tanh' term to zero faster than $\sqrt{(D_A + D_B)/\lambda}$, and returns the Smoluchowski result in (3.25), where $\rho = \lim_{\lambda\to\infty}\rho_\lambda$.

3.5.7 Lipková kinetics for reversible bimolecular reactions

For this section, complications arising from a reversible bimolecular reaction will be discussed. A reversible bimolecular reaction takes the form,

$$A + B \underset{k^-}{\overset{k^+}{\rightleftharpoons}} P. \qquad (3.36)$$

Extending Smoluchowski kinetics to reversible reactions brings in the added problem of what to do with the reverse reaction. When the product molecule P undergo the reverse

reaction and the reactants A and B return, a reasonable question to ask is, where should these molecules be placed? A natural thought is to place all the molecules at the centre of mass of the product molecule P. If this is done, then by the Smoluchowski model, these two molecules are within the binding radius ρ, and therefore must instantaneously react to form the product again. With this rule, the reverse reaction effectively never happens, therefore Smoluchowski kinetics does not work for reversible reactions. However, this is not an issue with Doi kinetics.

A paper by Lipková *et al.* develops reversible reaction kinetics under a Doi regime (which can reduce to a Smoluchowski framework) [116]. When the reverse reaction occurs, the Lipková model places the two molecules at a distance σ from each other. This σ is referred to as the unbinding radius. Under a Smoluchowski framework, the unbinding radius σ must be larger than the binding radius ρ. For the Doi regime, the relative sizes of the two radii is irrelevant. When the product molecule P dissociates into the reactant molecules A and B, the molecule B is placed randomly on the surface of a sphere with radius σ around A such that the centre of mass of A and B is equal to the position of the centre of mass of product molecule P.

In the Lipková model, the new dimensionless parameter α is introduced, where $\alpha = \sigma/\rho_\lambda$ is the ratio between the unbinding and binding radius. The derivation of the Lipková model is split into two sections, one where $\alpha > 1$, and the other where $\alpha \leqslant 1$. An advantage to the first case is that a modeller can utilise either the Smoluchowski or Doi framework unlike the second case where only a Doi framework can be used. An advantage to the second case is that one can take $\alpha \to 0$, which helps reduce the number of parameters needed to simulate a reversible reaction. A visual representation of both cases is shown in Figure 3.3.

(a)   (b)
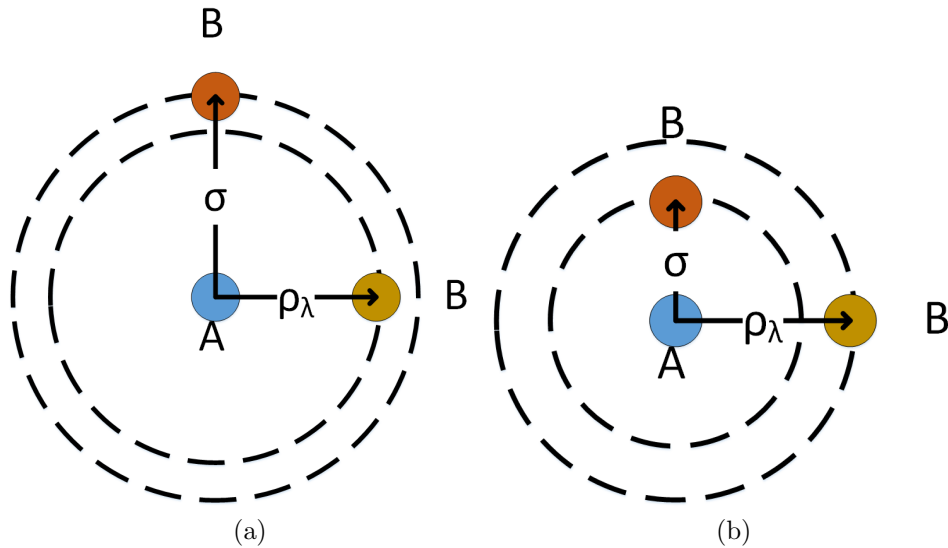
Figure 3.3: The two cases for the Lipková model. The first case (a), is when $\alpha > 1$, that is to say the unbinding radius is larger than the binding radius. The second case (b), is the opposite, that is $\alpha \leqslant 1$.

The reverse reaction rate constant k^- is independent of the binding and unbinding radius

In the Lipková model, the binding (ρ_λ) and unbinding (σ) radius are only related to the forward reaction rate constant k^+, and not the reverse reaction rate constant k^-. The

Lipková model is built to describe how far the two reactants have to be to react together (binding), and how close they can be when they are produced by the reverse reaction (unbinding). These rules are in place to ensure the micro-scale rates correctly match the macro-scale reaction rate constant k^+. They are only in place to match k^+, hence ρ_λ and σ will only be related to k^+ in this model, and for all future models involving reversible reactions (see Chapter 4).

The reverse reaction rate constant is included in the Lipková model in the same way that first-order reactions are treated. At a particular time t, the product molecule P can dissociate with probability $P_{\text{rev}} = 1 - \exp(-k^-\Delta t)$.

Case $\alpha > 1$

For this case, there are two ODEs, one in the region for which the forward reaction occurs, and the other for outside this region, which is where the reverse reaction happens. The ODEs for the cumulative distribution function $p(r)$ is derived in the same way as (3.28) and (3.29) with the addition of a point source at $r = \sigma$ to the reverse reaction. The ODEs are,

$$(D_A + D_B)\left(\frac{d^2p}{dr^2} + \frac{2}{r}\frac{dp}{dr}\right) - \lambda p = 0, \quad \text{for } r \leqslant \rho_\lambda, \tag{3.37}$$

$$(D_A + D_B)\left(\frac{d^2p}{dr^2} + \frac{2}{r}\frac{dp}{dr}\right) + Q(r - \sigma) = 0, \quad \text{for } r > \rho_\lambda, \tag{3.38}$$

where Q is a placeholder function that behaves like a Dirac delta function (molecules from the reverse reaction are placed at exactly σ away from the origin), and p is a cumulative distribution function describing the probability of finding a molecule of B at a distance less than r from a molecule of A. The ODEs are nondimensionalised by the following variables,

$$\beta = \rho_\lambda\sqrt{\frac{\lambda}{D_A + D_B}}, \quad \kappa = \frac{k^+}{\rho_\lambda(D_A + D_B)}, \quad r' = \frac{r}{\rho_\lambda}. \tag{3.39}$$

For brevity's sake, r' will be rewritten as r. By introducing these parameters, (3.37) and (3.38) become,

$$\frac{d^2p}{dr^2} + \frac{2}{r}\frac{dp}{dr} - \beta^2 p = 0, \quad \text{for } r \leqslant 1, \tag{3.40}$$

$$\frac{d^2p}{dr^2} + \frac{2}{r}\frac{dp}{dr} + \frac{\kappa}{4\pi\alpha^2}\delta(r - \alpha) = 0, \quad \text{for } r > 1, \tag{3.41}$$

where $\delta(r - \alpha)$ is the Dirac delta function centred at $r = \alpha$. To solve these ODEs, the following four conditions are defined: $p(r)$ is finite at the origin, $p(r)$ and its derivative are continuous at $r = 1$, and as $r \to \infty$, $p(r) \to 1$. Using these conditions, the solution to (3.40) and (3.41) are,

$$p(r) = \frac{4\pi\alpha + \kappa}{4\pi\alpha\beta\cosh(\beta)}\frac{\sinh(\beta r)}{r}, \quad \text{for } r \leqslant 1, \tag{3.42}$$

$$p(r) = \frac{4\pi\alpha + \kappa}{4\pi\alpha}\left(1 - \frac{1}{r} + \frac{\tanh(\beta)}{\beta r}\right) - \frac{\kappa H\left[r - \alpha\right](r - \alpha)}{4\pi r\alpha}, \quad \text{for } r > 1, \tag{3.43}$$

where $H[r - \alpha]$ is the Heaviside step function. To relate ρ_λ and σ to the dimensionless forward reaction rate constant κ, the diffusive flux through a dimensionless sphere with radius 1 is computed by,

$$\kappa = 4\pi \frac{dp}{dr}\bigg|_{r=1}. \tag{3.44}$$

Substitution of (3.42) or (3.43) into (3.44) and evaluating gives the first Lipková relation,

$$\kappa = \frac{4\pi\alpha(\beta - \tanh(\beta))}{\beta\alpha - \beta + \tanh(\beta)}. \tag{3.45}$$

Redimensionalising (3.45) whilst keeping the β variable, gives the full dimensional Lipková relation,

$$k^+ = \frac{4\pi\rho_\lambda\sigma(D_A + D_B)\left(\beta - \tanh\left(\beta\right)\right)}{\beta(\sigma - \rho_\lambda) + \rho_\lambda \tanh\left(\beta\right)}. \tag{3.46}$$

Taking the limit $\sigma \to \infty$ for (3.46) yields the Doi relation in (3.35). In this limit, the reverse reaction does not recombine without diffusing from outside the boundary layer near the reaction radius, and therefore is indistinguishable from a forward reaction in a well-mixed environment. A well-mixed environment is one where the distribution of molecules appear to be similar across the entire domain.

Case $\alpha \leqslant 1$

By having both the forward and reverse reaction occur inside the sphere with binding radius ρ_λ, the ODEs in (3.40) and (3.41) are replaced with the single ODE in dimensionless form,

$$\frac{d^2p}{dr^2} + \frac{2}{r}\frac{dp}{dr} - \beta^2 p + \frac{\kappa\delta(r - \alpha)}{4\pi\alpha^2} = 0, \quad \text{for } r \leqslant 1. \tag{3.47}$$

As both the forward and reverse reaction are within the binding radius ρ_λ, then there is no diffusive flux for $r > 1$ in steady-state. This means that $p(r) = 1$ for $r \geqslant 1$. The extra condition that $p(r)$ must be finite at the origin gives the solution,

$$p(r) = \frac{4\pi\alpha\beta + \kappa\sinh(\beta - \beta\alpha)}{4\pi\alpha\beta\sinh(\beta)}\frac{\sinh(\beta r)}{r} - \frac{\kappa H[r - \alpha]\sinh(\beta r - \beta\alpha)}{4\pi\alpha\beta r}. \tag{3.48}$$

Differentiating (3.48), and enforcing $p'(1) = 0$, yields the second Lipková relation,

$$\kappa = \frac{4\pi\alpha(\beta - \tanh(\beta))}{\cosh(\beta - \beta\alpha)(\tanh(\beta) - \tanh(\beta - \beta\alpha))}. \tag{3.49}$$

Redimensionalising (3.49) but keeping the dimensionless β variable for the sake of brevity yields the full form,

$$k^+ = \frac{4\pi\sigma(D_A + D_B)\left(\beta - \tanh\left(\beta\right)\right)}{\cosh\left((\rho_\lambda - \sigma)\frac{\beta}{\rho_\lambda}\right)\left(\tanh\left(\beta\right) - \tanh\left((\rho_\lambda - \sigma)\frac{\beta}{\rho_\lambda}\right)\right)}. \tag{3.50}$$

Geminate recombination

When it comes to reversible reactions, there is the added complication of geminate recombination [81, 117]. A geminate recombination event occurs when molecule P dissociates into molecules A and B, and those same two molecules recombine some nominally small time after, but before the molecules diffuse apart. When it comes to simulating reversible reactions, it is advisable to reduce the probability of geminate recombination, otherwise the overheads of simulations will be significantly higher [117].

Let Φ be the probability of geminate recombination, and $\pi(r)$ be the probability density that newly created molecules A and B from the same dissociation reaction, react again before having a chance to diffuse away from each other. Of all forward reactions that occur, a fraction Φ are geminate reactions. To derive the ODEs for $\pi(r)$, it is noted that the probability of finding $\pi(r)$ is determined by summation of the flux of geminate reactions with the rate of reaction of non-geminate reactions. That is to say,

$$0 = \frac{d^2\pi}{dr^2} + \frac{2}{r}\frac{d\pi}{dr} + \beta^2(1 - \pi(r)), \qquad \text{for } r \leqslant 1, \qquad (3.51)$$

$$0 = \frac{d^2\pi}{dr^2} + \frac{2}{r}\frac{d\pi}{dr}, \qquad \text{for } r > 1. \qquad (3.52)$$

These ODEs can be derived using an approach found in Chapter 3 of Berg's book [113]. As $r \to \infty$, the two molecules A and B are far enough away from each other that it is impossible for them to recombine, hence the probability is equal to zero. The additional constraints are that $\pi(r)$ is finite at the origin, and it is continuous (including its derivative) at $r = 1$. Solving (3.51) and (3.52) subject to these boundary conditions gives the solutions,

$$\pi(r) = 1 - \frac{\sinh(r\beta)}{r\beta\cosh(\beta)}, \qquad \text{for } r \leqslant 1, \qquad (3.53)$$

$$\pi(r) = \frac{\beta - \tanh(\beta)}{r\beta}, \qquad \text{for } r > 1. \qquad (3.54)$$

In dimensionless variables, when the reverse reaction occurs, A and B are placed a distance α away from each other. The probability of geminate recombination is then defined as $\Phi = \pi(\alpha)$. This gives the probabilities,

$$\Phi = 1 - \frac{\sinh(\alpha\beta)}{\alpha\beta\cosh(\beta)}, \qquad \text{for } \alpha \leqslant 1, \qquad (3.55)$$

$$\Phi = \frac{\beta - \tanh(\beta)}{\alpha\beta}, \qquad \text{for } \alpha > 1. \qquad (3.56)$$

In the case of an instantaneous forward reaction ($\beta \to \infty$), (3.56) reduces to,

$$\Phi = \frac{1}{\alpha}. \qquad (3.57)$$

3.5.8 Higher-order kinetics

Given Smoluchowski (and Doi) kinetics have been developed for irreversible and reversible bimolecular reactions, a natural question to ask is, how do these kinetics extend to trimolecular reactions and even higher-order reactions? This section focuses on developing the kinetics required to model the irreversible reaction,

$$A_1 + A_2 + \ldots + A_N \xrightarrow{k^+} P, \qquad (3.58)$$

where each A_i represents the ith reactant in a reaction involving N reactants.

The main problem with developing kinetics for higher-order reactions, is to properly define what 'closeness' means. For example, let there be three molecules, A, B, C, undergoing a trimolecular reaction. If a sphere of radius ρ is placed around the molecule A (as done for Smoluchowski kinetics), then a reaction occurs when B and C both come into contact with this sphere (similar to the bimolecular case). This rule says nothing about how far B and C are from each other. Furthermore, the probability that these two events would occur simultaneously is infinitesimally small. On the other hand, if they are on complete opposite ends of that sphere, then it is likely that they are too far apart from each other and should not react. At the same time, it is unclear how to calculate the size of this sphere, as it needs to relate to the trimolecular reaction rate constant.

3.5.9 Flegg kinetics for higher-order reactions

The recent work of Flegg [118] produced a generalised result that allows one to model a reaction involving any number of reactants under a Smoluchowski framework. However this work was not extended to *reversible* reactions of any order. This is addressed in Chapter 4.

Flegg resolves the problem of 'closeness' by first changing the distance metric into Jacobi vectors (usually used in N-body problems). Jacobi vectors are then related together in a Pythagorean way. The size of the binding radius ρ, is then related back to this new distance metric.

Transformation to Jacobi coordinates

For the N-molecular reaction defined in (3.58), the coordinates of each species A_i is denoted by $\mathbf{x}_i$. This represents the Cartesian position of each molecule in 3-dimensional space. Each coordinate undergoes the linear transformation,

$$\boldsymbol{\eta}_i = \sum_{j=1}^{N} M_{ij}\mathbf{x}_j, \qquad (3.59)$$

where M_{ij} represents the matrix transformation coefficients calculated in (3.60), and $\boldsymbol{\eta}_i$ represents the displacement of molecule i from the weighted average position of the previous $(i-1)$ molecules. Here, $\boldsymbol{\eta}$ represents the Jacobi coordinates (separation vectors). M_{ij} is chosen such that $\boldsymbol{\eta}$ evolves according to linear diffusion,

$$\sum_{i=1}^{N} D_i M_{ij} M_{ik} = 0, \qquad (3.60)$$

for each $j \neq k$. This condition is met when the weighted average position is defined by the centre of diffusion using,

$$\overline{\mathbf{x}}_i = \frac{\sum_{j=1}^{i} \mathbf{x}_j D_j^{-1}}{\sum_{m=1}^{i} D_m^{-1}}. \qquad (3.61)$$

With this, the separation vectors are now defined as,

$$\boldsymbol{\eta}_1 = \overline{\mathbf{x}}_N, \qquad (3.62)$$

$$\boldsymbol{\eta}_i = \mathbf{x}_i - \overline{\mathbf{x}}_{i-1}, \qquad (3.63)$$

where $\boldsymbol{\eta}_1$ defines the weighted average position for all N molecules. The transformation in (3.59) that represents (3.62) and (3.63) is described by a matrix M with elements,

$$M_{ij} = \begin{cases} D_j^{-1}\left[\sum_{m=1}^{N} D_m^{-1}\right]^{-1}, & i = 1, \\ -D_j^{-1}\left[\sum_{m=1}^{i-1} D_m^{-1}\right]^{-1}, & j < i, \quad i > 1, \\ 1, & j = i, \quad i > 1, \\ 0, & j > i, \quad i > 1. \end{cases} \tag{3.64}$$

Kinetics for irreversible N-molecular reactions

To derive the kinetics for an irreversible N-molecular reaction, P is defined to be the joint cumulative distribution function of finding a combination of reactant molecules with positions $\mathbf{x}_1, \mathbf{x}_2, \ldots, \mathbf{x}_N$ that are yet to react. P is governed by the diffusion equation,

$$\frac{\partial P(\mathbf{x},t)}{\partial t} = \left[\sum_{i=1}^{N} D_i \nabla_i^2\right] P(\mathbf{x},t), \tag{3.65}$$

where ∇_i^2 is the Laplacian operator for each position $\mathbf{x}_i$. Transforming this system into Jacobi coordinates (see (3.62) and (3.63)), then (3.65) becomes,

$$\frac{\partial P_{\boldsymbol{\eta}_i}(\boldsymbol{\eta_i},t)}{\partial t} = \left[\sum_{i=1}^{N} \hat{D}_i \hat{\nabla}_i^2\right] P_{\boldsymbol{\eta}_i}(\boldsymbol{\eta_i},t), \tag{3.66}$$

where the ^ notation denotes which symbols relate to the transformed Jacobi coordinates, and,

$$\hat{D}_i = \sum_{j=1}^{N} D_j M_{ij}^2 = \begin{cases} \overline{D}_N, & i = 1, \\ D_i + \overline{D}_{i-1}, & i > 1, \end{cases} \tag{3.67}$$

where $\overline{D}_N$ is the diffusion constant for the centre of diffusion of N molecules given by,

$$\overline{D}_N = \frac{1}{\sum_{i=1}^{N} D_i^{-1}}. \tag{3.68}$$

Equation (3.66) is defined over all $\boldsymbol{\eta}$, however $\boldsymbol{\eta}_1$ represents the average weighted position of all N molecules, and does not describe the 'closeness' of the molecules. For a well-mixed system that is arbitrarily large, the cumulative distribution function $P_{\boldsymbol{\eta}}$ is independent of $\boldsymbol{\eta}_1$. Integrating (3.66) over the whole domain reduces the dimensionality down and becomes,

$$\frac{\partial P(\boldsymbol{\eta},t)}{\partial t} = \left[\sum_{i=2}^{N} \hat{D}_i \hat{\nabla}_i^2\right] P(\boldsymbol{\eta},t), \tag{3.69}$$

where $P(\boldsymbol{\eta},t)$ represents the cumulative distribution function of finding a set of molecules within a set proximity range that have yet to react. This dimensionality reduction is analogous to using the moving frame in regards to the bimolecular problem.

What is left to describe is the condition for which the reaction of N molecules occurs. To do this, Flegg defines the reactive boundary to be,

$$\mathcal{P}_N^2 = \Delta_N \sum_{i=2}^{N} \frac{\|\boldsymbol{\eta}_i\|^2}{\hat{D}_i} \leqslant \rho^2, \tag{3.70}$$
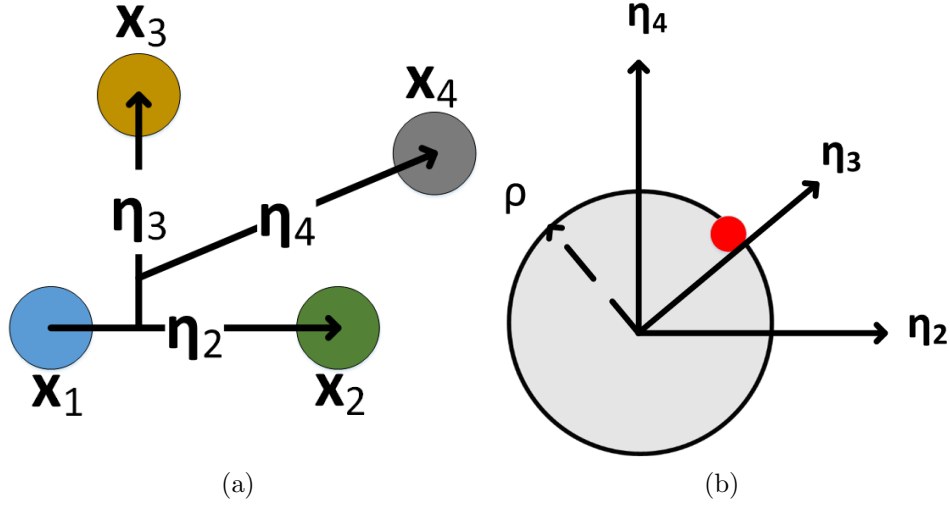
Figure 3.4: (a) A physical representation of how the Jacobi vectors ($\boldsymbol{\eta}$) are constructed relative to four molecules. (b) The red point represents the proximity of four molecules moving in $3(N-1)$-dimensional space ($N = 4$). A reaction occurs when the proximity of four molecules moves to within the hypersphere with radius ρ.

where

$$\Delta_N = \frac{\Sigma_{i=1}^N D_i^{-1}}{\Sigma_{1 \leqslant m < i \leqslant N}(D_i D_m)^{-1}}, \tag{3.71}$$

$$\tag{3.72}$$

is a diffusion parameter that scales (3.70) such that it is a distance metric, and the $1 \leqslant m < i \leqslant N$ notation refers to finding all combinations of m and i such that m is less than i, and both are less than N. The symbol $\mathcal{P}_N$ denotes what is to be known as the proximity of N molecules, and describes the overall separation of all molecules from each other in a concise way which is well suited to determining the reaction kinetics. A physical representation of the binding proximity ρ for N molecules is shown in Figure 3.4.

To relate the reaction rate constant k^+ to the binding proximity ρ, (3.65) is taken to pseudo-steady state assuming a Doi-like reaction at rate λ inside the reaction proximity to yield the following two PDEs,

$$0 = \hat{\nabla}^2 P - \lambda P, \qquad\qquad \text{for } \mathcal{P}_N \leqslant \rho, \tag{3.73}$$

$$0 = \hat{\nabla}^2 P, \qquad\qquad \text{for } \mathcal{P}_N > \rho, \tag{3.74}$$

where the first equation is in the proximity region for which the reaction occurs. Equations (3.73) and (3.74) are nondimensionalised using the following dimensionless quantities,

$$r = \sqrt{\frac{\Delta_N}{\rho^2} \sum_{i=2}^N \frac{\|\boldsymbol{\eta}_i\|^2}{\hat{D}_i}}, \quad \beta = \rho\sqrt{\frac{\lambda}{\Delta_N}}, \quad \kappa = \frac{k^+}{\Delta_N \mathcal{D} \rho^{2\mu}}, \quad \mu = \frac{3N-5}{2}, \tag{3.75}$$

where,

$$\mathcal{D} = \prod_{i=2}^N \left(\frac{\hat{D}_i}{\Delta_N}\right)^{3/2}. \tag{3.76}$$

Applying the dimensionless relationships converts (3.73) and (3.74) to,

$$0 = \frac{d^2p}{dr^2} + \frac{(2\mu+1)}{r}\frac{dp}{dr} - \beta^2 p, \qquad \text{for } r \leqslant 1, \qquad (3.77)$$

$$0 = \frac{d^2p}{dr^2} + \frac{(2\mu+1)}{r}\frac{dp}{dr}, \qquad \text{for } r > 1. \qquad (3.78)$$

Solving both of these ODEs yields the general solutions,

$$p(r) = \frac{a_1}{r^\mu} I_\mu(r\beta) + \frac{a_2}{r^\mu} K_\mu(r\beta), \qquad \text{for } r \leqslant 1, \qquad (3.79)$$

$$p(r) = a_3 + \frac{a_4}{r^{2\mu}}, \qquad \text{for } r > 1, \qquad (3.80)$$

where I_μ and K_μ are the modified Bessel functions of the first and second kind respectively both with order μ. The conditions that $p(r)$ must be finite at the origin, is continuous at $r = 1$ including its derivative, and as $r \to \infty$, $p(r) \to 1$, will be used to find the constants. Using these, the solutions are,

$$p(r) = \frac{4\mu}{2\mu I_\mu(\beta) + \beta\left(I_{\mu-1}(\beta) + I_{\mu+1}(\beta)\right)} \frac{I_\mu(r\beta)}{r^\mu}, \qquad \text{for } r \leqslant 1, \qquad (3.81)$$

$$p(r) = 1 - \frac{1}{r^{2\mu}} \frac{\mu I_\mu(\beta) - \beta\left(I_{\mu-1}(\beta) + I_{\mu+1}(\beta)\right)}{\mu I_\mu(\beta) + \beta\left(I_{\mu-1}(\beta) + I_{\mu+1}(\beta)\right)}, \qquad \text{for } r > 1. \qquad (3.82)$$

To relate ρ to k^+, the flux of the cumulative distribution function $p(r)$ over the surface of the hypersphere with radius 1 is calculated by,

$$\frac{k^+}{\Delta_N \mathcal{D} \rho^{2\mu}} = S_{2(\mu+1)} \left.\frac{dp}{dr}\right|_{r=1}, \qquad (3.83)$$

where $S_m = m\pi^{m/2}/\Gamma(m/2 + 1)$ represents the surface area of an m-dimensional hypersphere, and Γ is the Gamma function. Evaluating (3.83) by substituting (3.81) or (3.82) gives the irreversible N-molecular Doi kinetics,

$$k^+ = \frac{4\pi^{\mu+1} \mathcal{D} \Delta_N \rho^{2\mu}}{\Gamma(\mu)} \Phi_\mu(\beta), \qquad (3.84)$$

where,

$$\Phi_\mu(\beta) = 1 - \frac{4\mu I_\mu(\beta)}{\beta[I_{\mu-1}(\beta) + I_{\mu+1}(\beta)] + 2\mu I_\mu(\beta)}. \qquad (3.85)$$

To obtain the Smoluchowski version of (3.84), the limit $\beta \to \infty$ ($\lambda \to \infty$) is taken resulting in $\Phi_\mu(\beta) \to 1$, and gives,

$$k^+ = \frac{4\pi^{\mu+1} \mathcal{D} \Delta_N \rho^{2\mu}}{\Gamma(\mu)}. \qquad (3.86)$$

For the bimolecular case ($N = 2$), then $\mu = 1/2$, and (3.86) reduces to the Smoluchowski relation,

$$k^+ = 4\pi\rho(D_A + D_B). \qquad (3.87)$$

3.6 The Smoldyn algorithm

Smoldyn is a widely popular software which allows modellers to simulate micro-scale reaction-diffusion processes using a finite time-step algorithm. The Smoldyn algorithm allows for simulation of the following main processes: diffusion, surface interactions, zero-order reactions, first-order reactions, and bimolecular reactions. The order for which Smoldyn updates these events for a single time-step is shown in Figure 3.5.

The Smoldyn algorithm does not simulate reactions involving more than two molecules (trimolecular and above). It is often proposed that higher-order reactions can simply be formed using a series of bimolecular reactions. In the case of micro-scale models, this is not accurate. This will be explored further in Chapter 4. In this section is a detailed description of the Smoldyn algorithms. These algorithms are then extended and generalised where necessary in Chapter 4 to be able to simulate reversible reactions of any order under a Doi or Smoluchowski regime.
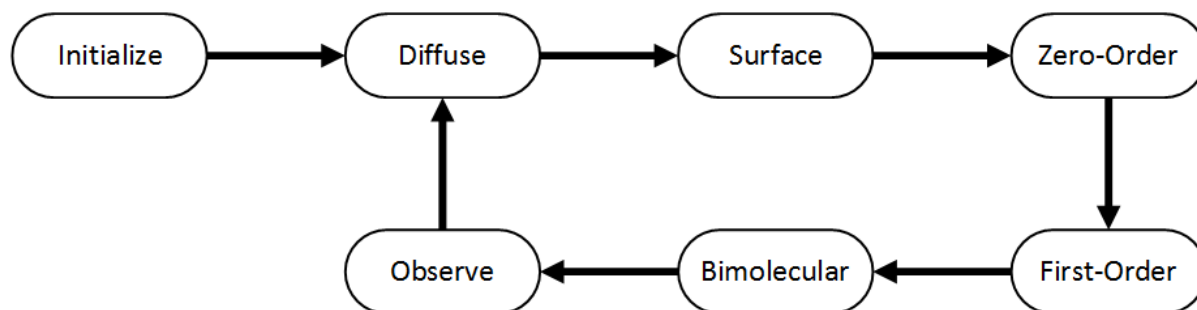
Figure 3.5: A flowchart depicting the processes in the Smoldyn algorithm, and the order for which it progresses through various events in each time-step. Once the system is initialized, it enters a loop, where the particles diffuse, any surface interactions are resolved, then zero-, first- and second-order reactions are computed in that order. Changes to the system are recorded, and it then goes through the loop again until it reaches the end of the simulation.

Diffusion with Brownian dynamics

In the micro-scale framework, there are many ways to simulate diffusion. Smoldyn utilises Brownian Dynamics [95], the numerical approximation to Brownian motion, which has a very simple implementation. Equation (3.14) is rewritten here explicitly for a molecule with position (X, Y, Z) as

$$X(t + \Delta t) = X(t) + \sqrt{2D\Delta t}\xi_1, \tag{3.88}$$

$$Y(t + \Delta t) = Y(t) + \sqrt{2D\Delta t}\xi_2, \tag{3.89}$$

$$Z(t + \Delta t) = Z(t) + \sqrt{2D\Delta t}\xi_3, \tag{3.90}$$

where each ξ is sampled from the normal distribution with zero mean and unit variance at each time-step for each molecule and each dimension it moves in.

Surface interactions

Smoldyn considers three possible surface interactions,

1. Reflecting boundary,

2. Periodic boundary,

3. Absorbing boundary.

For reflecting boundaries, the particle is treated like light reflecting off a mirror. From time t to $t + \Delta t$, the particle is assumed to have a straight line trajectory, and if this hits the boundary, then it reflects and continues its trajectory until it reaches it new position. Note that if Δt is small enough, a smooth boundary can be considered locally flat, which is why this works also on curved boundaries.

For periodic boundaries, the system is treated as if it had no boundary, and instead the particle wraps around the domain. Physically this would be similar to particles diffusing on the surface of a torus in which once they have diffused a complete rotation around the torus, it ends up in its original position. To calculate the new position for a particle under periodic boundary conditions in one-dimension, the domain goes from 0 to L. If a particle with position X moves a distance a, and if $X + a > L$, then the particle wraps around to the start, and has new position $X + a - L$. This method can be extended to multiple dimensions.

For absorbing boundaries, if a particle diffuses to outside the domain, then that particle is said to have been absorbed and is removed from the system. For large time-steps, it is possible that the trajectory of the particle passes through the boundary before arriving at a final position which is still in the domain. That is the particle still exists in the system, when it should have been absorbed. To correct this problem, Smoldyn has the option to calculate the probability that a particle crossed the boundary in between t and $t + \Delta t$, and if it did, the particle is absorbed.

Zero-order reactions

Recalling the zero-order reaction,

$$\emptyset \xrightarrow{k_0} P, \tag{3.91}$$

where k_0 is the reaction rate constant for a zero-order reaction and P is the product molecule. The rate at which molecules are produced in a zero-order reaction is independent of the concentration of any molecules in the system. Hence for each time-step Δt, an average of $k_0 \Delta t$ molecules of P are produced. For a stochastic simulation, this actual number of molecules produced changes at each time-step. To handle this, Smoldyn samples the number of molecules to add at each time-step from a Poisson distribution. Specifically, the probability P_0 that exactly j molecules of P are produced in a single time-step is calculated by,

$$P_0(j) = \frac{(k_0 \Delta t)^j \exp(-k_0 \Delta t)}{j!}. \tag{3.92}$$

First-order reactions

Recalling the first-order reaction,

$$A \xrightarrow{k_1} P, \tag{3.93}$$

where k_1 is the first-order reaction rate constant, and P may be a product molecule, or it is $\emptyset$ denoting that a molecule has decayed. The probability that a molecule undergoes a first-order reaction in a single time-step Δt is calculated by $P_1 = 1 - \exp(-k_1 \Delta t)$. The reactant molecule A is then either decayed, or replaced with the product molecule P, which is placed at the exact location of A.

Irreversible bimolecular reactions

Recalling the irreversible bimolecular reaction,

$$A + B \xrightarrow{k^+} P, \tag{3.94}$$

where A and B are two molecules that react with each other at a rate proportional to the reaction rate constant k^+. Smoldyn uses the binding radius ρ defined by Smoluchowski, hence the namesake SMOLuchowski DYNamics. The Smoluchowski relation for instantaneous irreversible bimolecular reactions is restated here as,

$$k^+ = 4\pi\rho(D_A + D_B), \tag{3.95}$$

where D_A and D_B are the diffusion constants for molecules A and B respectively. The use of Smoluchowski kinetics in this form makes the assumption that $\Delta t \to 0$. However, for an actual simulation, Δt is finite. This causes a problem, where in a single time-step from t to $t + \Delta t$, it is possible for a molecule of B to pass through the binding radius around A, and finish at a point outside of this binding radius. This results in molecules A and B still in the system, when they no longer should be, producing results with artificially smaller reaction rates. Smoldyn addresses this problem by increasing the size of ρ as Δt increases, that is there is a corrected binding radius $\rho_{\Delta t}$ such that $\rho_{\Delta t} > \rho$ for all $\Delta t > 0$. In the limit as $\Delta t \to 0$, then $\rho_{\Delta t} \to \rho$. For brevity's sake, this section will use ρ in place of $\rho_{\Delta t}$. The precise correction to ρ required for a finite time-step Δt is not so straightforward. The following steps need to be completed,

1. Generate a lookup table that relates k^+ to the parameter $s = \frac{\sqrt{2(D_A + D_B)\Delta t}}{\rho}$, which is the dimensionless root mean square (RMS) separation change in a time-step relative to the reaction radius.

2. Use an inverted iterative scheme to find ρ based on a particular choice of k^+ and Δt.

The bulk of the work is in first generating the lookup table, however the table only needs to be generated once, and then it can be used for many other simulations (Smoldyn actually stores this table into the software so it does not need to be recalculated). The table is generated by starting with the reaction-diffusion PDE,

$$\frac{\partial g}{\partial t} = \frac{D}{r^2} \frac{\partial}{\partial r}\left(r^2 \frac{\partial g}{\partial r}\right), \tag{3.96}$$

where $g(r, t)$ is called the *radial distribution function* (RDF). To generate the lookup table, let $s = \exp(\delta)$, where $-3 \leqslant \delta \leqslant 3$ sampled at regular intervals usually separated by 0.1. The PDE (3.96) can be solved using Green's functions, where between t_i and $t_{i+1} = t_i + \Delta t$, the solution $g(r)$ is found by iterating through,

$$g_{i+1}(r) = \int_0^\infty 4\pi r'^2 \Psi(r, r', s) g_i(r') dr'. \tag{3.97}$$

Here g_i and g_{i+1} is used to denote the RDF at time t and $t + \Delta t$ respectively. The function $\Psi(r, r', s)$ is,

$$\Psi(r, r', s) = \frac{1}{4\pi r r'}\left[G_s(r - r') + G_s(r + r')\right], \tag{3.98}$$

$$\text{where } G_s(c) = \frac{1}{s\sqrt{2\pi}}\exp(-\frac{c^2}{2s^2}), \tag{3.99}$$

is the Green's function for diffusion in radial coordinates. To reduce the time it takes to solve (3.97) and to simplify the calculation, the trapezoidal method is used to approximate the integral from $0 \leqslant r \leqslant R$, where R is far enough away from the reaction boundary at $r = 1$ (R is usually set to 10), and the rest of the integral is calculated by approximating $g_i(r) = 1 + \dfrac{a_i}{r}$, where a_i is a parameter fitted from the last 10% of the RDF in $0 \leqslant r \leqslant R$. Equation (3.97) is integrated in the external region $r > R$ analytically to yield,

$$4\pi R s^2 \Psi(r, R, s) + \frac{1}{2}(e_- + e_+) + \frac{a_i}{2r}(e_- - e_+), \tag{3.100}$$

$$\text{where } e_\pm = erfc\left(\frac{R \pm r}{s\sqrt{2}}\right). \tag{3.101}$$

Finally, at each time-step, the reduced reaction rate is calculated by,

$$\frac{k_i \Delta t}{\rho^3} = \int_0^1 4\pi r^2 g_i(r) dr, \tag{3.102}$$

which computes the reduced reaction rate over the region in which the bimolecular reaction occurs ($0 \leqslant r \leqslant 1$).

The Smoldyn algorithm can be summarised as,

1. Initialize $\delta = -3$ and set $s = \exp(\delta)$. Set $g(r, 0) = g_0(r) = 1$.

2. Diffuse molecules by calculating (3.97).

3. React molecules by calculating reduced reaction rate with (3.102).

4. Set $g(r) = 0$ for $0 \leqslant r \leqslant 1$.

5. Repeat steps 2-4 until the difference between successive k values is less than $1/10^5$.

6. Store the value of the reduced reaction rate k corresponding to the value of s.

7. Increment δ by 0.1, and repeat steps 1-6 until $\delta = 3$.

The stored values of the reduced reaction rate k and the parameter s now form a lookup table. This lookup table only needs to be generated once in the Smoldyn algorithm (and in fact is already loaded in the Smoldyn software).

Before the table can be used, the case of when $\delta < -3$ and $\delta > 3$ need to be considered. For these cases, it is not worth calculating k using the above algorithm. Instead these cases converge to exact simple equations of the form,

$$\frac{k \Delta t}{\rho^3} = 2\pi s^2, \qquad\qquad \text{for } s < \exp(-3), \tag{3.103}$$

$$\frac{k \Delta t}{\rho^3} = \frac{4\pi}{3}, \qquad\qquad \text{for } s > \exp(3), \tag{3.104}$$

where (3.103) is the Smoluchowski relation for small Δt whilst (3.104) assumes each time-step is large enough that the distribution of particles inside the reaction radius is well-mixed and equal everywhere to the constant distribution as $r \to \infty$.

Given that there is now a table and equations for all values of s, the table can be inverted to find ρ given a particular choice of k and Δt. This inversion process is carried out using a *root bracketing algorithm* (see [81]). Theoretically, this new value of ρ (for a

large time-step) should provide the same results as the ρ from Smoluchowski (for a small time-step). If this is the case, then the larger time-step would run much faster, and is better to use. In reality, there still needs to be a balance of accuracy against speed, so the larger time-step may not produce highly accurate results since the reaction becomes rate-limited instead of diffusion-limited, but it does allow a complicated simulation to be completed in a much faster time. To that extent, Smoldyn actually does an excellent job at getting accurate results for larger time-steps, and this explains its widespread utility in scientific and mathematical research.

Reversible bimolecular reactions

Smoldyn can also simulate reversible bimolecular reactions. Let $\alpha = \sigma/\rho$ be the ratio between the unbinding and binding radius. The algorithm in the previous section to generate the lookup table is only modified slightly. After the reaction in step 4 ($g(r)$ set to 0 for $0 \leqslant r \leqslant 1$), a diffused delta function $\Psi(r, \sigma, s)$ is added to $g(r)$. Given a particular choice of k^+, α, and Δt, the lookup table is inverted to solve for ρ and σ.

3.7 Conclusion

The main focus of this chapter was to provide a detailed overview of how Smoluchowski kinetics can simulate reaction-diffusion processes on a microscopic scale. Smoluchowski and Doi kinetics are used to simulate irreversible bimolecular reactions. Lipková *et al.* extended this work to reversible bimolecular reactions. Flegg took Smoluchowski and Doi's approach, extending it to irreversible Nth-order reactions. This leads to the question, how can these kinetics be generalized into one singular framework capable of modelling reversible N-molecular reactions? Naturally this leads to the next question, how does the Smoldyn algorithm need to be modified such that it can simulate reversible N-molecular reactions? These two questions are researched in Chapter 4.
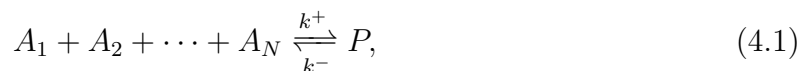
Chapter 4

Reversible Doi and Smoluchowski kinetics for high-order reactions

4.1   Introduction

Smoluchowski kinetics has undergone an extensive evolutionary process since its creation over 100 years ago. The kinetics, originally describing the contact rate of two diffusing spheres [110], has since been applied to modelling reaction-diffusion processes for biological systems [81]. Masao Doi extended the kinetics to simulate the repeated collision of molecules before they react [115]. This framework was expanded to model bimolecular reactions that can go in reverse [116]. Most recently, the kinetics described the irreversible reaction of more than two molecules [118].

The continuous development of these kinetics has championed one of the last works by Marian von Smoluchowski [110]. However, there is still one missing piece with these kinetics, that is how can they be used to describe reversible reactions involving any number of molecules under a Doi regime?

The focus of this chapter is on developing the Doi (and subsequently Smoluchowski) kinetics for the following chemical reaction of N molecules at the scale of individual molecules,

$$A_1 + A_2 + \cdots + A_N \underset{k^-}{\overset{k^+}{\rightleftharpoons}} P, \tag{4.1}$$

where k^+ and k^- are the reaction rate constants for the forward and reverse reaction respectively, A_i is the ith chemical reactant, and P is the product of the reaction of N molecules [119].

To derive the kinetics for (4.1), the notation in this chapter will closely follow that of Lipková *et al.* and Flegg, where the reversible bimolecular reaction frameworks in Lipková *et al.* [116] are extended to higher-order reactions in the framework of Flegg [118]. A lot of the notation was introduced in Sections 3.5.7 and 3.5.9, however it is reintroduced here to remind the reader.

To begin with, a particular set of N reactants in the system of molecules is identified. At any moment in time these N reactants can either be in the bound state P or in the dissociated state. In the dissociated state, the positions of the N molecules (one of each reactant species A_i) in space is denoted by $\mathbf{x}_i$ for $i = 1, \ldots, N$ with diffusion constants D_i respectively. For higher-order reactions, it is useful to transform the problem of the reacting system to 'proximity' coordinates $\boldsymbol{\eta}_i$ (analogous to a scaled Jacobi coordinate

system) rather than particle coordinates $\mathbf{x}_i$. These coordinates are,

$$\boldsymbol{\eta}_i = \sqrt{\frac{\Delta_N}{\hat{D}_i}}\left(\mathbf{x}_i - \overline{\mathbf{x}}_{i-1}\right), \quad \text{for } i = 2, \ldots, N \tag{4.2}$$

$$\text{where } \overline{\mathbf{x}}_\mathbf{i} = \frac{\sum_{j=1}^i \mathbf{x}_\mathbf{j} D_j^{-1}}{\sum_{m=1}^i D_m^{-1}}, \tag{4.3}$$

$$\hat{D}_i = D_i + \overline{D}_{i-1}, \tag{4.4}$$

$$\Delta_N = \frac{\Sigma_{i=1}^N D_i^{-1}}{\Sigma_{1 \leqslant m < i \leqslant N}(D_i D_m)^{-1}}, \tag{4.5}$$

$$\overline{D}_i = \frac{1}{\Sigma_{m=1}^i D_m^{-1}}, \quad \text{and} \tag{4.6}$$

$$\mathcal{D} = \prod_{i=2}^N \left(\frac{\hat{D}_i}{\Delta_N}\right)^{3/2}. \tag{4.7}$$

The sum in the denominator of (4.5) is taken for all integer combinations of i and m where i is strictly greater than m. The variable $\overline{\mathbf{x}}_{i-1}$ represents the centre of diffusion of the previous $(i-1)$ molecules (that is, the molecules of A_1 through A_{i-1} inclusive) [118]. Jacobi coordinates are usually constructed using the centres of mass. The centre of diffusion is calculated in the same way as the centre of mass but instead of weighting with mass the inverse diffusion constants of the respective point particles are used instead (4.3). The advantage of using diffusion-based Jacobi coordinates is that under this transformation to the system, the Laplacian remains unchanged whilst at the same time the vectors $\boldsymbol{\eta}_i$ for $i = 2, \ldots, N$ are measures of the point separations rather than their absolute positions in space. The scaling of $\sqrt{\Delta_N/\hat{D}_i}$ for each of the proximity vectors in (4.2) mean that the resultant diffusion of the set of reactants in proximity space is isotropic and symmetry may then be exploited. The vectors $\boldsymbol{\eta}_i$ for $i = 2, \ldots, N$ describe the relative positions of the molecules in space and are shown diagrammatically without their scaling in Figure 4.1a.

The measure of 'closeness' is called the proximity for the N molecules $\mathcal{P}_N$ [118]. This proximity is,

$$\mathcal{P}_N = \left[\sum_{i=2}^N \|\boldsymbol{\eta}_i\|^2\right]^{1/2}. \tag{4.8}$$

A higher-order reaction (or even a bimolecular reaction) occurs when the proximity of N reactants falls within a critical distance ρ. That is, when

$$\mathcal{P}_N < \rho. \tag{4.9}$$

The reaction parameter ρ, often referred to as the binding radius, is ubiquitous throughout the various reaction frameworks discussed in Chapter 3, and is determined by the macroscopic reaction rate constant k^+. Throughout this chapter, ρ shall be referred to as the *binding proximity*, as it is a parameter that operates in $3(N-1)$ dimensional space. The two-dimensional projection of ρ for a 3-particle system is shown visually in Figure 4.1b. The projection into the two-dimensional plane is dependent on the angle between the position vectors and the diffusion constants of the model.
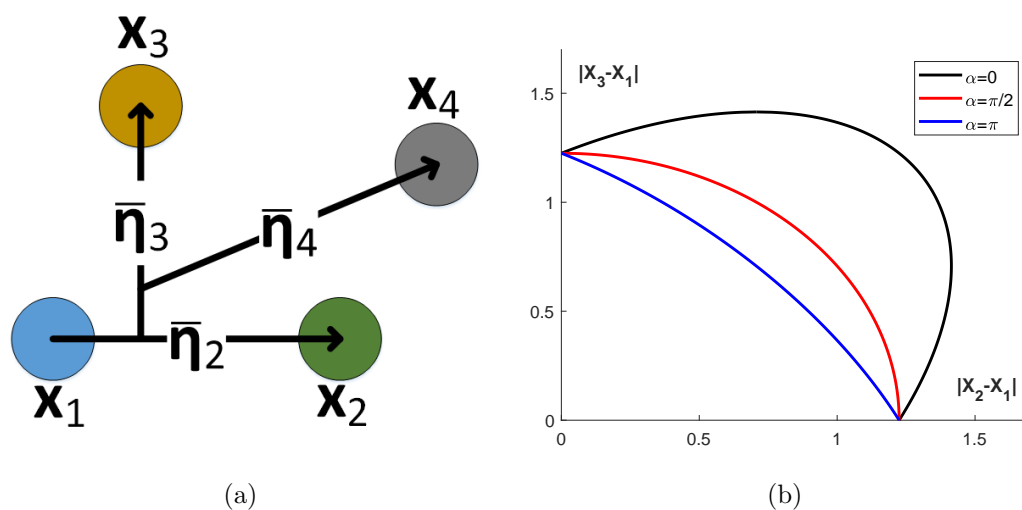
(a)   (b)

Figure 4.1: (a) Unscaled proximity coordinates $\overline{\boldsymbol{\eta}}_i = \boldsymbol{\eta}_i \sqrt{\hat{D}_i / \Delta_N}$ in relation to molecule positions in space $\mathbf{x}_i$ for a 4-molecule system of reactants. (b) Plot of the 2-D projection of how far $\mathbf{x}_2$ and $\mathbf{x}_3$ can be from $\mathbf{x}_1$, given the angle α, which is the angle between the vectors $\mathbf{x}_2 - \mathbf{x}_1$ and $\mathbf{x}_3 - \mathbf{x}_1$. This plot is centred around $\mathbf{x}_1$. The diffusion constants and the reaction proximity ρ are set to 1. Each curve is part of the ellipse with equation $\|\mathbf{x}_2\|^2 + \|\mathbf{x}_3\|^2 - \|\mathbf{x}_2\|\|\mathbf{x}_3\| \cos(\alpha) = 3/2$, where the three α angles are chosen as 0, $\pi/2$, and π. For $\alpha = \pi$, $\mathbf{x}_2$ and $\mathbf{x}_3$ are at their furthest point away from each other, hence they need to be much closer to $\mathbf{x}_1$ to satisfy the reaction condition (4.8). For $\alpha = 0$ (black curve), $\mathbf{x}_2$ and $\mathbf{x}_3$ are the closest to each other that they can be, therefore allowing the molecules to be further away from $\mathbf{x}_1$ and still satisfy (4.8).

When the reaction goes in reverse, the resulting N molecules are placed a proximity at exactly the critical distance σ. That is, when

$$\mathcal{P}_N = \sigma. \tag{4.10}$$

To derive the kinetics for this reaction, a similar approach to the derivations in Section 3.5 is executed. Specifically, the methods used in the derivation of Flegg kinetics (Section 3.5.8) and Lipková kinetics (Section 3.5.7) are combined together.

Similar to the Lipková approach, the problem is split up into two cases: the case when the ratio $\alpha > 1$, and the case where $\alpha \leqslant 1$ (reminder that $\alpha = \sigma/\rho$). The probability of geminate recombination ϕ is derived for both cases, and it is shown how they can be used to assist in choosing the parameters for numerical simulations. The algorithm to simulate these kinetics is developed by extending the Smoldyn algorithm to reversible N-molecular reactions. This is then applied to a theoretical example to check the method works for the simplest bimolecular, trimolecular, and quadmolecular reaction. Finally, this stochastic simulation is applied to the Lee model of the Wnt signalling pathway, highlighting how the model fails, and how it can be fixed by modifying the model to include a trimolecular reaction.

4.2 Reaction kinetics for reversible N-molecular reactions

To model reversible reactions involving N reactants, the parameter α, used in the Lipková *et al.* paper [116], is reintroduced here as,

$$\alpha = \frac{\sigma}{\rho}. \tag{4.11}$$

As a reminder, α is the ratio of the unbinding proximity σ to the binding proximity ρ. In simpler terms, α demonstrates how far away the reactants produced by a reverse reaction are placed (with relative separation equal to σ) in comparison to the reactants combining together (within the binding proximity ρ) for the forward reaction of (4.1).

It is important to note that the unbinding radius σ in this case is a parameter to control the rate of the *forward* reaction (and not the reverse reaction). This appears to be counter-intuitive, as it is only introduced when modelling reversible reactions. This is because, under pseudo-steady state conditions where particles unbind at a distance σ and rate k^-, the forward reaction rate which includes geminate recombination and bulk interactions should remain k^+, and this is dependent on carefully determining the correct diffusion-controlled relationship between σ and ρ. Since the presence of geminate recombination increases the net forward reaction rate, the reaction radii ρ is smaller than its irreversible counterpart. If α is large, then the reversible reaction is initialised so that the forward reactants are effectively placed 'in bulk' and geminate recombination probability goes to zero. In this case, ρ is expected to reduce to the irreversible case (as will be demonstrated in general in this section, and was demonstrated for bimolecular reactions by Lipková *et al.* [116])

The implementation of the unbinding radius is as follows. At an exponentially distributed time with rate k^-, P unbinds into $A_1, \ldots, A_N$. A uniformly distributed random direction in $[3(N-1)]$-dimensional proximity coordinates (as defined by (4.2)) is chosen and the N molecules are initialized with a proximity of σ in that direction.

In the Doi framework, it is possible to set $\sigma \leqslant \rho$ and still balance the reverse and forward reactions (which is obviously not possible in the Smoluchowski framework). Thus, the results of the analysis will be presented separately depending on whether or not $\alpha > 1$ or $\alpha \leqslant 1$ in the Doi framework. Specifically, it will be shown the relationships between k^+, σ and ρ which keep (1) the *net* forward reaction rate at k^+ times the concentration of reactants in the bulk and (2) the forward and reverse reactions in pseudo-equilibrium. The derivation for these relations are in Sections 4.2.1 and 4.2.2. The two cases are shown diagrammatically in Figure 4.2 (for the case of $N = 3$).
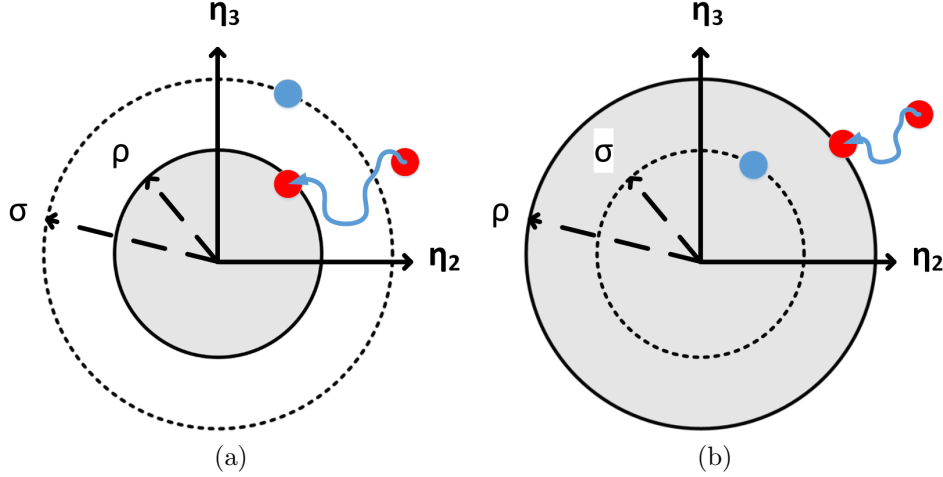
Figure 4.2: Two-dimensional projection of proximity coordinates for a set of three reactants undergoing a reversible third order reaction shown for cases in which (a) $\alpha > 1$ and (b) $\alpha \leqslant 1$. The red point indicates a possible set of three reactants moving within the coordinate system. When the proximity is less than ρ, a reaction may occur between these reactants which removes the state from the system. The region in which the reaction may occur is shaded in gray and is determined by the forward reaction rate k^+ and σ. At a rate k^-, for each reacted product P in the system, a set of three reactants is initialized with P at their centre of diffusion such that their proximity is exactly σ. This corresponds to somewhere, randomly sampled, from the dotted manifold. An example of one of these initiated reactant triplets is portrayed in blue in each case. This newly initiated set of reactants then either diffuse away from the reaction region in gray or reacts shortly after being initialized (geminate recombination).

4.2.1 Case $\alpha > 1$

Here the kinetic rate equation for a Nth order reversible reaction under the Doi regime is derived. Let P be a joint cumulative distribution function that describes the probability of finding a combination of reactant molecules with positions $\mathbf{x}_1, \mathbf{x}_2, \ldots \mathbf{x}_N$ that have yet to react. This function satisfies,

$$\frac{\partial P(\mathbf{x}, t)}{\partial t} = \left[\sum_{i=1}^{N} D_i \nabla_i^2 \right] P(\mathbf{x}, t). \tag{4.12}$$

Equation (4.12) is transformed into proximity coordinates by (4.2) and the domain is split into two regions; the region inside the binding proximity (3.70) and the region outside it. Inside the binding proximity, a sink at a rate λ is added. It is assumed that the reversible reaction occurs at some rate at a proximity of σ outside of the reaction radius. A pseudo steady-state is assumed. In steady state the cumulative distribution function in the proximity space for a set of reactants is described by the PDEs,

$$0 = \hat{\nabla}^2 P - \lambda P, \qquad \qquad \text{for } \mathcal{P}_N \leqslant \rho, \tag{4.13}$$

$$0 = \hat{\nabla}^2 P + Q(\mathcal{P}_N - \sigma), \qquad \qquad \text{for } \mathcal{P}_N > \rho, \tag{4.14}$$

where $\hat{\nabla}^2$ is the full $3(N-1)$ dimensional Laplacian and $Q(\mathcal{P}_N - \sigma)$ is a Dirac-like distribution describing the creation of molecules from the reverse reaction at a proximity

σ from the origin. It may seem important at this stage to enforce that the rate of production described by Q is dependent on k^- and the probability of being in the bound state, but this is not important. This is because for any rate of production at a proximity σ, the production rate is balanced with a forward reaction rate of k^+; the rate k^- just determines the rate particles should be generated at σ in steady state, but it should not affect the calculation of k^+ as it relates to σ. To analyse these PDEs, the following dimensionless quantities are introduced,

$$r = \sqrt{\sum_{i=2}^{N} \frac{\|\boldsymbol{\eta}_i\|^2}{\rho^2}}, \quad \beta = \rho\sqrt{\frac{\lambda}{\Delta_N}}, \quad \kappa = \frac{k^+}{\Delta_N \mathcal{D}\rho^{2\mu}}, \quad \mu = \frac{(3N-5)}{2}. \tag{4.15}$$

In the processes of transforming (4.12) into (4.13) and (4.14), the scaling Jacobian $\mathcal{D}$ is introduced, and a normalization factor Δ_N, which depend on the diffusion constants of the system of particles. Due to the symmetry of the problem, (4.13) and (4.14) produce the following two ODEs for $p(r)$ (the dimensionless cumulative distribution function P in its radial proximity coordinate),

$$0 = \frac{d^2 p}{dr^2} + \frac{(2\mu+1)}{r} \frac{dp}{dr} - \beta^2 p, \qquad \text{for } r \leqslant 1, \tag{4.16}$$

$$0 = \frac{d^2 p}{dr^2} + \frac{(2\mu+1)}{r} \frac{dp}{dr} + \omega\delta(r-\alpha), \qquad \text{for } r > 1, \tag{4.17}$$

where ω describes the non-dimensional nominal rate of creation of molecules at $r = \alpha$ (which becomes inconsequential after balancing this rate with the flux over the boundary $r = 1$) and $\delta(r-\alpha)$ is the Dirac delta function. The following conditions are implemented: that $p(r)$ remains bounded at $r = 0$, is continuous and differentiable at $r = 1$, and in the limit that $r \to \infty$, $p(r) \to 1$ which represents the dimensionless cumulative distribution function of molecules far enough away from the origin. The parameter ω is eliminated by noting that at equilibrium, the rate of molecules created by the reverse reaction is equal to the rate at which molecules are consumed in the forward reaction. Additionally, the dimensionless forward reaction rate constant κ is equal to the total flux of the cumulative distribution function over the unit hypersphere at $r = 1$. Combining these two statements gives

$$\kappa = S_{2(\mu+1)}\omega\alpha^{2\mu+1} = S_{2(\mu+1)} \frac{dp}{dr}\bigg|_{r=1}, \tag{4.18}$$

where S_m is the surface area of a unit m-dimensional hypersphere calculated by $S_m = m\pi^{m/2}/\Gamma(m/2+1)$, where Γ is the gamma function with respect to the argument $(m/2+1)$. Solving (4.16) and (4.17) with the appropriate boundary conditions gives,

$$p(r) = 2\mu\left(1 + \frac{\omega\alpha}{2\mu}\right)\frac{1}{\beta I'_\mu(\beta) + \mu I_\mu(\beta)}\left(\frac{I_\mu(r\beta)}{r^\mu}\right), \quad \text{for } r \leqslant 1, \tag{4.19}$$

$$p(r) = \left(1 - \frac{1}{r^{2\mu}}\right)\left(1 + \frac{\omega\alpha}{2\mu}\right)\frac{\beta I'_\mu(\beta) - \mu I_\mu(\beta)}{\beta I'_\mu(\beta) + \mu I_\mu(\beta)}$$
$$- \frac{\omega\alpha H(r-\alpha)}{2\mu}\left(1 - \left(\frac{\alpha}{r}\right)^{2\mu}\right), \quad \text{for } r > 1, \tag{4.20}$$

where H is the Heaviside step function, I is the modified Bessel function of the first kind and $I'_\mu(\beta)$ is the derivative of $I_\mu(r\beta)$ with respect to r and evaluated at $r = 1$. This relation is equal to $I'_\mu(\beta) = [I_{\mu-1}(\beta) + I_{\mu+1}(\beta)]/2$. Insertion of (4.19) or (4.20) into (4.18) gives

$$\kappa = \frac{4\pi^{\mu+1}\alpha^{2\mu}\Phi_\mu(\beta)}{\Gamma(\mu)\left(\alpha^{2\mu} - \Phi_\mu(\beta)\right)}, \tag{4.21}$$

where

$$\Phi_\mu(\beta) = 1 - \frac{4\mu I_\mu(\beta)}{\beta[I_{\mu-1}(\beta) + I_{\mu+1}(\beta)] + 2\mu I_\mu(\beta)}. \tag{4.22}$$

Redimensionalising (4.21) gives the new kinetics,

$$k^+ = \frac{4\pi^{\mu+1}\mathcal{D}\Delta_N\rho^{2\mu}\sigma^{2\mu}\Phi_\mu(\beta)}{\Gamma(\mu)\left[\sigma^{2\mu} - \rho^{2\mu}\Phi_\mu(\beta)\right]}. \tag{4.23}$$

Special cases of this relation can be derived by taking appropriate limits. For the case of $\alpha > 1$, the Smoluchowski regime is valid, and the relationship between k^+, ρ, and σ is derived by simply taking the limit $\lambda \to \infty$ ($\beta \to \infty$) to give,

$$k^+ = \frac{4\pi^{\mu+1}\mathcal{D}\Delta_N\rho^{2\mu}\sigma^{2\mu}}{\Gamma(\mu)(\sigma^{2\mu} - \rho^{2\mu})}. \tag{4.24}$$

The irreversible rate is derived from initializing reversible reactions at $\sigma \to \infty$. As $\sigma \to \infty$, (4.23) and (4.24) agree with (3.84) and (3.86) as expected. It is important to note that one cannot simply take the limit $k^- \to 0$ to go from reversible to irreversible regimes since this violates the assumption that $k^- = O(1)$. With such slow reversible reactions, a pseudo-steady state cannot be assumed and other more detailed methods are required (or in many circumstances with k^- small one can just assume that the reaction is irreversible and/or simply place initialized reactants far from the reaction radius).

If the forward reaction is bimolecular, substitution of $N = 2$ into (4.23) reduces the relation to (noting that when $N = 2$, $\mu = 1/2$ and Φ_μ reduces to include hyperbolic trigonometric functions),

$$k^+ = \frac{4\pi\sigma\hat{D}_2\left(\rho\sqrt{\dfrac{\lambda}{\hat{D}_2}} - \tanh\left(\rho\sqrt{\dfrac{\lambda}{\hat{D}_2}}\right)\right)}{\sigma\sqrt{\dfrac{\lambda}{\hat{D}_2}} - \rho\sqrt{\dfrac{\lambda}{\hat{D}_2}} + \tanh\left(\rho\sqrt{\dfrac{\lambda}{\hat{D}_2}}\right)}, \tag{4.25}$$

which is the same as (3.46), albeit written in a different form.

The famous Smoluchowski result $k^+ = 4\pi(D_A + D_B)\rho$ is recovered from (4.23) by taking the series of limits $\sigma \to \infty$ and $\lambda \to \infty$, and then setting $N = 2$.

4.2.2 Case $\alpha \leqslant 1$

This section focuses on the derivation for the reaction kinetics for a Nth order reversible reaction in which the unbinding proximity is smaller than the binding proximity (i.e. $\alpha \leqslant 1$). In this case the ODEs (4.16) and (4.17) have to be replaced with the single ODE,

$$\frac{d^2p}{dr^2} + \frac{(2\mu + 1)}{r}\frac{dp}{dr} - \beta^2 p + \frac{\kappa}{S_{2(\mu+1)}\alpha^{2\mu+1}}\delta(r - \alpha) = 0, \quad \text{for } r \leqslant 1. \tag{4.26}$$

As the reactions occur within $r \leqslant 1$, there is no diffusive flux (since the system in steady state) for $r > 1$. Hence the scaled cumulative distribution function $p(r)$ is constant and equal to 1 for $r > 1$. The general solution to (4.26) is

$$
p(r) = \frac{c_1}{r^\mu} I_\mu(r\beta) + \frac{c_2}{r^\mu} K_\mu(r\beta)
$$
$$
- \frac{\kappa}{(r\alpha)^\mu S_{2(\mu+1)}} f(r, \alpha) \left[K_\mu(\alpha\beta) I_\mu(r\beta) - I_\mu(\alpha\beta) K_\mu(r\beta) \right], \quad (4.27)
$$

where K_μ is the modified Bessel function of the second kind and

$$
f(r, \alpha) = (2H[r-1] - 1) H [\alpha - rH[1-r] - H[r-1]] \times
$$
$$
H \left[-\alpha + H[1-r] + rH[r-1] \right]. \quad (4.28)
$$

As there is no diffusive flux at $r = 1$, then $\left. \dfrac{dp}{dr} \right|_{r=1} = 0$ and $p(1) = 1$. Applying these conditions to (4.27) gives

$$
\kappa = \frac{2\pi^{\mu+1} \alpha^\mu \beta^2 I_{\mu+1}(\beta)}{I_\mu(\alpha\beta) \Gamma(\mu+1)}. \quad (4.29)
$$

In this case reactants are generated with a proximity σ less than ρ, and immediately after being initialized, they satisfy the binding condition (4.9). As such, a Smoluchowski framework cannot be used here. Thus the Doi framework is exclusively considered here. In this case, in dimensionalised form,

$$
k^+ = \frac{2\pi^{\mu+1} \mathcal{D} \sigma^\mu \rho^{2+\mu} \lambda I_{\mu+1}(\beta)}{I_\mu \left(\sigma\sqrt{\dfrac{\lambda}{\Delta_N}} \right) \Gamma(\mu+1)}. \quad (4.30)
$$

The most logical advantage in using the case $\alpha \leqslant 1$ is it allows for placement of reactants to be on top of each other (in the location of the original product P) when the reverse reaction occurs. This significantly simplifies the implementation of the reverse reaction in practical problems. The forward reaction rate can be determined in this case by taking $\alpha \to 0$. In this limit, (4.30) becomes

$$
k^+ = (2\pi)^{\mu+1} \mathcal{D} \rho^{2+\mu} \lambda \beta^{-\mu} I_{\mu+1}(\beta). \quad (4.31)
$$

Whilst this equation is easy to implement, it may not be ultimately desirable due to the high expected frequency of geminate recombination which slows the computational time of practical simulations significantly. In the next section, the geminate recombination probability is derived. One of the other important reasons for knowing this probability as a function of model parameters is because it allows a modeller to answer the question of 'how large should σ be such that the forward rate of reaction is determined by the irreversible relationship?'. In other words, if the assumptions of pseudo-steady state are relaxed, how does geminate recombination go to zero as σ gets large resulting in decreased coupling of the forward and reverse processes?

4.2.3 Geminate recombination

Let ϕ be the probability of geminate recombination, β is the dimensionless Doi reaction rate, and $\pi(r)$ the probability that newly created molecules $A_1, A_2, \cdots, A_N$ formed from

the dissociation of P with a proximity of $\mathcal{P}_N = r$ react again before diffusing away (that is the separation of molecules $r \to \infty$). Of all forward reactions that occur, a fraction ϕ of them are geminate reactions. To calculate the probability $\pi(r)$, the fraction of non-geminate reactions $(1 - \phi)$, and the rate (β^2) that they undergo a reaction needs to be known. Using a method similar to Berg [113] and Lipková [116], the resultant ODEs are,

$$0 = \frac{d^2\pi(r)}{dr^2} + \frac{(2\mu + 1)}{r}\frac{d\pi(r)}{dr} + \beta^2(1 - \pi(r)), \qquad \text{for } r \leqslant 1, \qquad (4.32)$$

$$0 = \frac{d^2\pi(r)}{dr^2} + \frac{(2\mu + 1)}{r}\frac{d\pi(r)}{dr}, \qquad \text{for } r > 1, \qquad (4.33)$$

where the right hand term of (4.32) describes the rate at which molecules that have yet to combine will recombine, whilst (4.33) does not have a term as this is outside the region for the forward reaction. Solving these two ODEs gives the general solutions

$$\pi(r) = a_1 \frac{I_\mu(r\beta)}{r^\mu} + a_2 \frac{K_\mu(r\beta)}{r^\mu} + 1, \qquad \text{for } r \leqslant 1, \qquad (4.34)$$

$$\pi(r) = a_3 + \frac{a_4}{r^{2\mu}}, \qquad \text{for } r > 1. \qquad (4.35)$$

$\pi(r)$ has constraints that it exists at the origin, is continuous at $r = 1$ including its derivative, and that as $r \to \infty$, $p(r) \to 0$. In dimensionless variables, when the reverse reaction happens, the separation of particles is equal to α. Implementing the above conditions and defining $\phi = \pi(\alpha)$ yields the probability of geminate recombination,

$$\phi = 1 - \frac{4\mu I_\mu(\alpha\beta)}{\alpha^\mu \left[\beta I_{\mu-1}(\beta) + 2\mu I_\mu(\beta) + \beta I_{\mu+1}(\beta)\right]}, \qquad \text{for } \alpha \leqslant 1, \qquad (4.36)$$

$$\phi = \frac{\left[\beta I_{\mu-1}(\beta) - 2\mu I_\mu(\beta) + \beta I_{\mu+1}(\beta)\right]}{\alpha^{2\mu} \left[\beta I_{\mu-1}(\beta) + 2\mu I_\mu(\beta) + \beta I_{\mu+1}(\beta)\right]}, \qquad \text{for } \alpha > 1. \qquad (4.37)$$

In the Smoluchowski limit $(\beta \to \infty)$, then $\phi = 1$ for $\alpha \leqslant 1$ (as expected, geminate recombination is inevitable), and for $\alpha > 1$, $\phi = \alpha^{-2\mu}$, which agrees in the bimolecular case of $\phi = 1/\alpha$ as published by Andrews and Bray [81].

Returning to the Doi framework, in the case when $\alpha \to 0$ $(\sigma \to 0)$ discussed in Section 4.2.2, (4.36) reduces to

$$\phi = 1 - \frac{4\mu\beta^\mu}{2^\mu\Gamma(\mu + 1)\left[\beta I_{\mu-1}(\beta) + 2\mu I_\mu(\beta) + \beta I_{\mu+1}(\beta)\right]}. \qquad (4.38)$$

As previously discussed, whilst setting $\alpha = 0$ has benefits for numerical implementation, it can lead to high computational overhead because of the suboptimal geminate recombination probability. To keep ϕ small in the case of $\alpha = 0$, set $\beta = \beta_c \ll 1$ and take the first order Taylor expansion of (4.31) and (4.38) to obtain,

$$\phi \approx \frac{\beta_c^2}{4\mu}, \quad \text{and} \quad k^+ \approx \frac{\pi^{\mu+1}\Delta_N \mathcal{D}\rho^{2\mu}\beta_c^2}{\Gamma(\mu + 2)}. \qquad (4.39)$$

Combining the two equations in (4.39) together alongside the Flegg kinetics in (3.86) gives,

$$\phi = \frac{k^+\Gamma(\mu)(\mu + 1)}{4\pi^{\mu+1}\Delta_N \mathcal{D}\rho^{2\mu}} = \frac{\rho_s^{2\mu}}{\rho^{2\mu}}(\mu + 1), \qquad (4.40)$$

where ρ_s is the binding proximity for the irreversible case in (3.86). This new relation is based on the kinetics if the reaction was irreversible, in comparison to the reversible reaction kinetics.

The final thing to note about the geminate recombination probability in the case of $\alpha > 1$ is that ϕ falls away at a rate of $\alpha^{-2\mu}$. In terms of reaction order this is α^{3N-5}. The implication is that convergence of k^+ as defined in the reversible case to the irreversible case is much faster as σ gets large when the reactions are higher-order reactions. The advantage of using higher-order reactions in this case is that one can effectively use the $\sigma \to \infty$ limiting case more easily without sacrificing the accuracy of the simulation. As previously discussed, taking the limit $\sigma \to \infty$ means that forward and reverse reaction rates are not coupled by geminate recombination which allows for a relaxation of the pseudo-steady state assumption.

4.2.4 Selecting free parameters

For irreversible Doi reactions, there are two parameters to determine λ and ρ. Equation (3.84) determines one parameter, so at most there is one free parameter to calculate. Often the choice is determined by setting either $\rho = \rho_{\mathrm{mol}}$ (the molecular radius) for more heuristically 'realistic' simulations or $\lambda \to \infty$ for more simplistic implementation. For reversible Doi reactions, there are three parameters to determine, λ, ρ, and σ. Finding a suitable value for σ is complicated by the introduction of the probability of geminate recombination ϕ.

In both the Doi and Smoluchowski frameworks, $\phi \propto \alpha^{-2\mu}$, where $\alpha = \sigma/\rho > 1$. Choosing α (by appropriately choosing σ sufficiently large) such that ϕ is kept low has a number of benefits. Firstly, it means that simulations will not need to track a large number of superfluous geminate recombination events. Secondly, the reaction rate k^+ more accurately approximates the irreversible rate and therefore the simulations are more robust to relaxations in the pseudo-steady state assumption.

Choosing parameters in order to keep ϕ small depends on the application. Of course, setting σ to be so large that reactants initialized in the domain of the problem are well-mixed will lead accurately to irreversible forward reaction rates, however at the cost of losing the spatial heterogeneity of these reactants required in many applications. Ideally, one should choose σ large enough such that k^+ in the reversible case is approximately the irreversible case. Based on (4.23), this is achieved for $\sigma \ll \rho \Phi_\mu(\beta)^{1/(2\mu)}$ where ρ is the irreversible reaction radius. To what extent is 'much less than' here depends on the order of the reaction N as discussed in the previous section (since $\phi \propto \alpha^{-2\mu}$). Once σ is chosen, the other parameters ρ and λ may be chosen.

In some applications, taking a large σ is just not practical. In these situations, one might choose to minimize the complexity of the numerical simulations by simply setting $\alpha = 0$ and choosing β to be small as described in Section 4.2.3.

4.3 Development of Smoldyn-based algorithm for reversible N-molecular reactions

The modelling of chemical reactions can be broken down into three main steps: diffusion of the particles, forward reaction of N molecules, and a reversible reaction. Diffusion is modelled with Brownian dynamics as dictated by the Euler-Maruyama method [95]. The forward reaction occurs with probability, $P_\lambda = \lambda \Delta t$ whenever N reactants meet the

reaction proximity condition in (4.9). If $P_\lambda = 1$, then the reaction occurs instantly, i.e. the reaction is in the Smoluchowski regime. For the reverse reaction, each molecule can dissociate with probability, $P_{\text{rev}} \approx 1 - \exp(-k^-\Delta t)$.

The simulation proceeds by the following 3 steps in each time-step,

1. If one of each of the molecules A_1 to A_N are within the binding proximity ρ, then generate a random number r_1 uniformly distributed in the interval $(0, 1)$. If $r_1 < P_\lambda$, then the forward reaction occurs. A molecule of P is placed such that it is located at the centre of diffusion of the N reacting molecules.

2. For each molecule of P, generate a random number r_2 uniformly distributed in the interval $(0, 1)$. If $r_2 < P_{\text{rev}}$, then the reverse reaction occurs. The molecules A_1 to A_N are placed randomly on the surface of a $3(N-1)$-dimensional hypersphere with radius σ such that their centre of diffusion is equal to the dissociating molecule P.

3. Use Brownian dynamics to update the position of every molecule.

In the event that $\Delta t \to 0$, then the Smoluchowski results derived in this chapter are sufficient to use in a simulation. This method utilizes a finite time-step, as done in the Smoldyn program [81]. This algorithm was extended by Flegg to work for irreversible N-molecular reactions [118]. For numerical purposes, the size of the reaction proximities, ρ and σ are modified based on the time-step and the choice of λ. For larger time-steps and smaller λ, the reaction proximity increases. This modification effectively allows a modeller to use a higher time-step without compromising on accuracy.

The algorithms to generate a lookup table relating the reaction rate constant k^+ to the reaction proximity ρ, and to find ρ from this lookup table, as well as a numerical algorithm to calculate the probability of geminate recombination are detailed in the following sections.

4.3.1 Generating a finite time-step lookup table relating ρ to k^+ for a reversible Nth order reaction

A lookup table allows one to choose an appropriate reaction proximity ρ based on the reaction rate constant k^+ and the time-step Δt. The cumulative distribution function $g(r, \tau)$ is defined to behave like a time-dependent analogue of the distribution $p(r)$ in between time-steps. Creating a source term at $r = \alpha$ for the reverse reaction gives the reaction-diffusion PDE,

$$\frac{\partial g}{\partial \tau} = \frac{1}{r^{2\mu+1}} \frac{\partial}{\partial r} \left(r^{2\mu+1} \frac{\partial g}{\partial r} \right) + \frac{\kappa \delta(r - \alpha)}{S_{2(\mu+1)} \alpha^{2\mu+1}}. \tag{4.41}$$

The time-step is nondimensionalised by $\Delta t = \rho^2 \Delta \tau / \Delta_N$. For even values of N, analytic Green's functions can be used to solve (4.41) and give an integral equation relating $g(r, \tau + \Delta \tau)$ and $g(r, \tau)$. For odd values of N this cannot easily be done analytically, which means (4.41) must be solved numerically. This is done by implementing a forward-time central-space (FTCS) finite difference scheme.

To ease the restrictions on the time-step, the parameter s' is introduced where $s' = \frac{\sqrt{2\Delta_N \Delta t}}{\rho} = \sqrt{2\Delta\tau}$. For the sake of generating a table, let $s' = \exp(\delta)$, where s' has a range $\exp(-3) \leqslant s' \leqslant \exp(3)$ and the values of δ typically increase by 0.2. The table

generated from the proceeding steps will store dimensionless reduced reaction rate $\mathcal{K}$ with each value of s' where,

$$\mathcal{K} = \kappa \Delta \tau = \frac{k^+ \Delta t}{\mathcal{D} \rho^{2\mu+2}} = \lim_{\tau \to \infty} P_\lambda \int_0^1 S_{2(\mu+1)} r^{2\mu+1} G(r) dr, \qquad (4.42)$$

and $G(r)$ is the steady distribution $g(r, \tau)$ that is generated by iterating a numerical solution of (4.41) from τ to $\tau + \Delta \tau$. Before each iteration, the $g(r, \tau)$ distribution is reduced by a factor $(1 - P_\lambda)$ for $r < 1$ to simulate removal by forward reaction.

The following iterative scheme is implemented to generate the table.

1. Set values for P_λ and α. Set $\delta = -3$. δ increases at each iteration until it reaches $\delta = 3$. For $\alpha \leqslant 1$, the order is reversed, δ begins at 3 and decreases until it reaches -3 or $\mathcal{K} \to \infty$. Set $s' = \exp(\delta)$.

2. Initialize $g(r, 0) = g_0(r, 0) = 1$ for $0 < r < R$. R is chosen to be sufficiently far from the reacting proximity at $r = 1$. It is found that choosing R to be the greater of $\lceil \alpha \rceil$ or 2 is good enough. Values of r are separated by ensuring $\Delta r \ll \Delta \tau$.

3. Diffusion simulated by numerically solving the homogeneous part of (4.41) from $\tau = 0$ to $\tau = \Delta \tau$. Boundary conditions are implemented by letting $g(r) = 1$ for $r > \alpha$. If $\alpha \leqslant 1$, then $g(r) = 1$ for $r > 1$. At the origin, a zero derivative boundary condition is implemented.

4. The reduced rate of reaction $\mathcal{K}$ is computed by (4.42).

5. The forward reaction depletes the cumulative distribution function for $r \leqslant 1$ for the next iteration of g by setting $g(r, 0) = g_{i+1}(r, 0) = (1 - P_\lambda) g_i(r, \Delta \tau)$ in this region, but leaving the distribution unchanged elsewhere.

6. The back reaction is incorporated by adding

$$f(r) = \omega \delta(r - \alpha) = \frac{P_\lambda}{\alpha^{2\mu+1}} \delta(r - \alpha) \int_0^1 r^{2\mu+1} g_i(r, \Delta \tau) dr \qquad (4.43)$$

to the function $g_{i+1}(r, 0)$.

7. Repeat steps (2) through (6) iterating g_i each time. If consecutive $\mathcal{K}$ differ by more than 1 part in 10^5, the scheme undergoes another iteration by repeating steps (4) to (7) using the new initial distribution $g_{i+1}(r, 0)$. Otherwise, take $g_i(r, \Delta \tau) = G(r)$ and the corresponding reaction rate constant from (4.42) is stored in a table.

8. For $\alpha > 1$, increase δ by 0.2. If $\alpha \leqslant 1$, decrease δ by 0.2. Repeat steps (2) to (8).

9. If required, repeat the entire algorithm for different values of P_λ and α.

4.3.2 Finding ρ from the lookup table

With the lookup table generated in Section 4.3.1, a second iterative scheme is used to determine the value of ρ to be used in a simulation. The table in Section 4.3.1 is generated for values of s' in the range $\exp(-3) \leqslant s' \leqslant \exp(3)$. Within this range, $\mathcal{K}$ is found by the lookup table. Outside of this range, other formulas are used.

For $s' > \exp(3)$, approximate $G(r) = 1$ for all r, τ, and

$$\mathcal{K} = \frac{P_\lambda \pi^{\mu+1}}{\Gamma(\mu+2)}. \tag{4.44}$$

For $s' < \exp(-3)$, the Smoluchowski results from Section 4.2 can be used. The time-step Δt is approximated by a differential dt and if $\alpha > 1$, then

$$\mathcal{K} = \frac{2s'^2 \pi^{\mu+1} \alpha^{2\mu} \Phi_\mu(\beta)}{\Gamma(\mu)\left[\alpha^{2\mu} - \Phi_\mu(\beta)\right]}. \tag{4.45}$$

In the case where $P_\lambda = 1$, then (4.45) reduces to

$$\mathcal{K} = \frac{2s'^2 \pi^{\mu+1} \alpha^{2\mu}}{\Gamma(\mu)\left(\alpha^{2\mu} - 1\right)}. \tag{4.46}$$

If $\alpha \leqslant 1$, then substitute the related equation into (4.42) to get

$$\mathcal{K} = \frac{s'^2 \alpha^\mu \pi^{\mu+1} \beta^2 I_{\mu+1}(\beta)}{I_\mu(\alpha\beta)\Gamma(\mu+1)}. \tag{4.47}$$

In the special case of $\alpha = 0$, then

$$\mathcal{K} = 2^\mu s'^2 \pi^{\mu+1} \beta^{-\mu} \rho^{2+\mu} \lambda I_{\mu+1}(\beta). \tag{4.48}$$

The binding proximity ρ can then be found by following the root bracketing algorithm used by Andrews and Bray [81], and Flegg [118]. Evaluations of $\mathcal{K}$ in this algorithm are given by a table (in the suitable range of s') or by the formulas presented in this section. In the case that $P_\lambda \ll 1$ and $\alpha > 1$, then it is advisable to tabulate $s' \in [\exp(-6), \exp(0)]$ instead of $s' \in [\exp(-3), \exp(3)]$.

4.3.3 Numerical probability of geminate recombination

After using the methods in Sections 4.3.1 and 4.3.2 to calculate the binding proximity given a particular pair of values of α and P_λ, the resulting values can be validated by comparing them to the probability of geminate recombination. Given the choice of α, P_λ and s', these values are accepted if the probability of geminate recombination, ϕ, is significantly less than 1.

To calculate this probability, a modification of the method from Lipková *et al.* is presented [116]. From Lipková *et al.*, $p(r)$ is the probability that a newly formed molecule reacts with its newly formed partner before escaping to infinity. The function $p(r)$ satisfies the equation

$$p(r) = P_\lambda \int_0^1 K(r, r', s)dr' + (1 - P_\lambda) \int_0^1 K(r, r', s)p(r')dr'$$
$$+ \int_1^\infty K(r, r', s)p(r')dr', \quad (4.49)$$

where $K(r, r', s)$ is the Green's function solution to

$$\frac{\partial g}{\partial \tau} = \frac{1}{r^{2\mu+1}} \frac{\partial}{\partial r}\left(r^{2\mu+1}\frac{\partial g}{\partial r}\right), \tag{4.50}$$
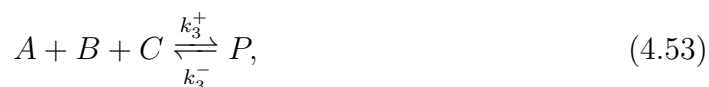
where (4.49) has the boundary condition that $p(r) \to 0$ as $r \to \infty$. The probability of geminate recombination is then given as $\phi = p(\alpha)$. Given that a Green's function cannot easily be found for higher-order reactions, the PDE is solved numerically instead. At each time-step, the PDE is solved numerically from $r = 0$ to $r = R$, where R is far enough away from $r = \alpha$. Then $p(r)$ in the range $0 \leqslant r \leqslant 1$ is replaced with

$$p_{i+1}(r) = P_\lambda + (1 - P_\lambda)p_i(r), \quad \text{for } 0 \leqslant r \leqslant 1, \tag{4.51}$$

where i refers to the ith iteration of solving the PDE. The iterations terminate when the difference between $p_{i+1}(\alpha)$ and $p_i(\alpha)$ are less than 1 part in 10^5. After solving this, if ϕ is too high, then choose either a higher value of α, or a lower value of P_λ, then repeat the method in Sections 4.3.1 and 4.3.2 to find the required value of ρ.

4.4 Theoretical simulations

Here, the accuracy of higher-order reversible reactions is tested by comparing examples of $N = 2$, $N = 3$ and $N = 4$ molecular reactions. The three independent chemical systems start from steady state, and are run to determine how well they remain at steady state. These three examples represent the reactions,

$$A + B \underset{k_2^-}{\overset{k_2^+}{\rightleftharpoons}} P, \tag{4.52}$$

$$A + B + C \underset{k_3^-}{\overset{k_3^+}{\rightleftharpoons}} P, \tag{4.53}$$

$$A + B + C + D \underset{k_4^-}{\overset{k_4^+}{\rightleftharpoons}} P, \tag{4.54}$$

where P represents some product molecule.

4.4.1 Definitions of parameters for theoretical simulations

For each simulation, k_i^- and k_i^+ is designed in such a way that the expected number of reactant and product molecules at steady state would be 25. Nominal (dimensionless) values for diffusion constants are set to $D_A = D_B = D_C = D_D = D_P = 1$, and a domain which was a unit cube with periodic boundary conditions (so as not to introduce any boundary effects) was chosen. The initial copy numbers of A, B, C, D, and P are set to their expected values of 25, and are uniformly distributed throughout the domain. The dimensionless rate constants for each of the systems $k_2^+ = 3.2$, $k_2^- = 80$, $k_3^+ = 0.0032$, $k_3^- = 2$, $k_4^+ = 1.28 \times 10^{-5}$, $k_4^- = 0.2$ were set. For these simulations, a Doi regime is used, by setting $\lambda = 10^4$, and $\Delta t = 10^{-5}$.

4.4.2 Results of theoretical simulations

The steady state distribution (defined at long times - specifically $t = 100$) for each chemical system is displayed in Figure 4.3 juxtaposed with known well-mixed copy number distributions for P (see Section 4.4.3 for the derivation).
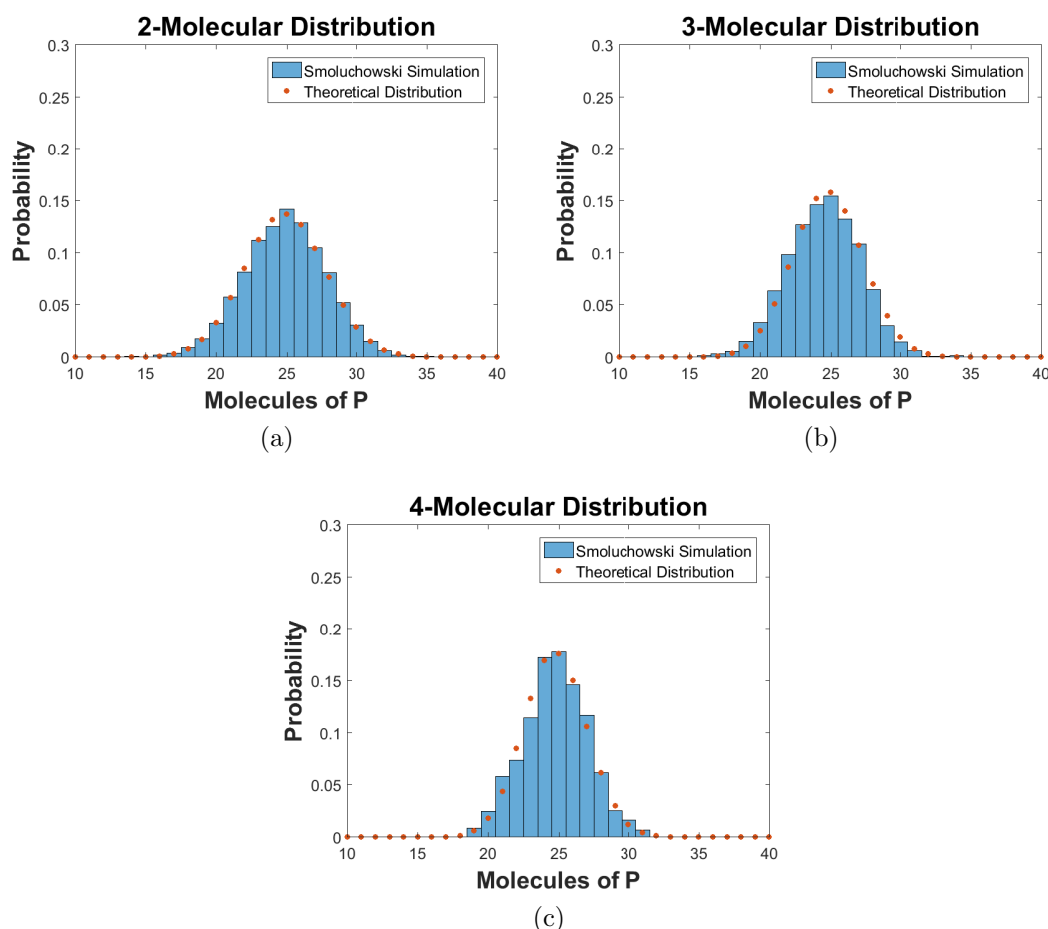
Figure 4.3: The distribution of copy numbers for the production of product molecule P in each of the steady state reversible systems overlapped with the theoretical distributions (4.59). (a) Bimolecular system (4.52) with Kullback-Leibler divergence of 8.938×10^{-4}, (b) Trimolecular system (4.53) with Kullback-Leibler divergence of 0.0113, and (c) Fourth-order molecular system (4.54) with Kullback-Leibler divergence of 0.011. The steady state distribution (assumed after a dimensionless time period of $t = 100$) with time-step $\Delta t = 10^{-5}$ is plotted as blue bars. The theoretical distributions are plotted as red points.

Increasing the order of the reaction increases the computational time for each simulation. For these simulations, custom MATLAB code was used. The computational time for each simulation was recorded. For the bimolecular reaction, it took $1,422$ seconds, the trimolecular reaction took $2,211$ seconds, and the quadmolecular reaction took $7,242$ seconds to complete. As expected, the computational time increases as the order of reaction increases. The main reason for this is because at each time-step, each combination of reactant molecules need to be checked to see if they are within the binding proximity. Increasing the order of reaction increases the number of combinations of molecules to check. One way to reduce the computational time is to implement computer science techniques to speed up the algorithm, and to increase the CPU speed. This could be done by following a similar method to the Smoldyn program designed to run on a graphics processing unit [93].

4.4.3 Chemical master equation derivation for N-molecular reactions

The theoretical steady state distributions in Figure 4.3 are found from the steady state of the associated chemical master equation for each system. This equation is derived as follows. Begin with the the general chemical reaction,

$$A_1 + A_2 + \cdots + A_N \underset{k^-}{\overset{k^+}{\rightleftharpoons}} P. \tag{4.55}$$

The results in this section were completed such that each of the reactants and products will always have the same copy number. Hence let $A_i(t) = n$ for all $i = 1, 2, \ldots, N$. Define p_n to be the probability that there are n molecules each of $A_i(t)$ at time t. The associated master equation for (4.55) is,

$$\frac{dp_n}{dt} = -k^+ n^N p_n + k^+ (n+1)^N p_{n+1} + k^- \left[N_T - (n-1) \right] p_{n-1} - k^- (N_T - n) p_n, \tag{4.56}$$

where N is the order of the reaction, and N_T is the maximum possible number of molecules of $A_i(t)$. Taking the steady state distribution,

$$p_1 = \frac{k^-}{k^+} N_T p_0, \tag{4.57}$$

$$p_{n+1} = \frac{(k^+ n^N + k^- (N_T - n)) p_n - k^- (N_T - (n-1)) p_{n-1}}{k^+ (n+1)^N}. \tag{4.58}$$

The solution of this recurrence formula is,

$$p_n = \binom{N_T}{n} \left(\frac{k^-}{k^+} \right)^n \frac{p_0}{(n!)^{N-1}}, \tag{4.59}$$

where $N_T = 50$ is the maximum number of product molecules possible in each of the simulations in Figure 4.3, N is the order of the reaction, and p_n is the probability that there are n molecules of the product at steady state. The constant p_0 is a normalization constant such that $\sum_{n=0}^{N_T} p_n = 1$.

4.4.4 Comparison of theoretical simulations to steady state distributions

The distributions (4.59) (also plotted in Figure 4.3) start similar to a binomial distribution for $N = 2$ and become progressively narrower as the reaction order increases. This is a property of the fact that when the system fluctuates to have fewer (or more) than expected P molecules, the rate at which the system attempts to correct this is not proportional to the deviation away from the expected value because the forward reaction rate is proportional to $(N_T - n)^N$. There is very strong agreement between the simulations and the theoretical distributions calculated by the Kullback-Leibler divergence for each distribution [120].

4.5 Stochastic Doi model of the Wnt signalling pathway

Here a stochastic microscopic model is developed for the Wnt signalling pathway using the proposed simulation framework of this chapter. It is unclear how Wnt (and its target

protein, β-catenin) give rise to a vast array of different cellular outcomes. It has been suggested that noise-induced effects and/or positive feedback of negative regulators may play a role in determining dynamic β-catenin concentrations in cells but to date, no molecular-based stochastic model has been proposed [68].

In modelling the Wnt pathway, the erroneous outcomes that may result in modelling some biological phenomena using only bimolecular reactions in a microscopic framework is highlighted.

### 4.5.1 From the Lee model to a modified Wnt model

The presentation of the model is as follows; first the reader is reintroduced to the Lee model [58]. As the model was fully discussed in Section 2.2.1, this section will just recap the main processes and behaviour of the Lee model. From here, the Lee model is stripped back to isolate the main β-catenin regulation cycle. The 'modified' Wnt model is simulated using the Gillespie SSA (see Section 3.4.1 for details of the algorithm). Importantly, the modified Wnt model (as with the Lee model on which it is based) considers chemical reactions to be sequences of bimolecular reactions. It will be shown that, because of the presence of fast time-scales in the model, a microscopic Smoluchowski simulation of the modified Wnt system yields completely non-physical results. Interpreting the fast reaction using a trimolecular reaction allows for a more accurate simulation and in the process of constructing the model, it is noted that β-catenin levels may be subject to significant stochastic focusing which may raise the β-catenin levels if the protein Axin is in short supply (as is the case with Xenopus oocytes).

The Lee model contains 15 protein species which undergo a total of 17 possible zero-, first-, and second-order reactions [58]. The full Lee ODE model is presented diagrammatically in Figure 4.4a, alongside the 'modified' Wnt model in Figure 4.4b, and the 'modified' trimolecular Wnt model in Figure 4.4c. The main components of the pathway to be studied in this chapter include the formation of destruction complex (DC) from its constituent proteins, the turnover of β-catenin (B) through natural production and degradation, the rapid phosphorylation of β-catenin by destruction complex (DC*), and the influence of Wnt ($\mathcal{W}$) and Dishevelled (D_i, D_a) on dissociating the destruction complex.

4.5.2 A modified Wnt model

In this chapter, the components of the full Lee model which are stripped back in the modified model are shown in boxes in Figure 4.4a. The remaining modified model is shown in Figure 4.4b. The model is fully reduced to use a trimolecular reaction in Figure 4.4c. Details of how this model reduction is achieved through quasi-steady state assumptions is detailed in Section 4.5.3. The omissions of the modified Wnt model are justified here:

1. It is assumed the activation of Dishevelled in the presence of the Wnt protein reaches equilibrium instantly. This is a significant simplification since the delay caused by waiting for Dishevelled activation or deactivation can be important. This assumption is made because Dishevelled activation/deactivation simply delays changes in the core B regulation cycle and this is mathematically uninteresting to the underlying mechanism being modelled. The modified Wnt model assumes the dissociation rate of DC* is constant (but dependent on the binary states of Wnt being on or off). If Wnt is switched from on to off (or vice versa), then the rate of dissociation of the DC complex is instantaneously changed to match the Lee model in the case
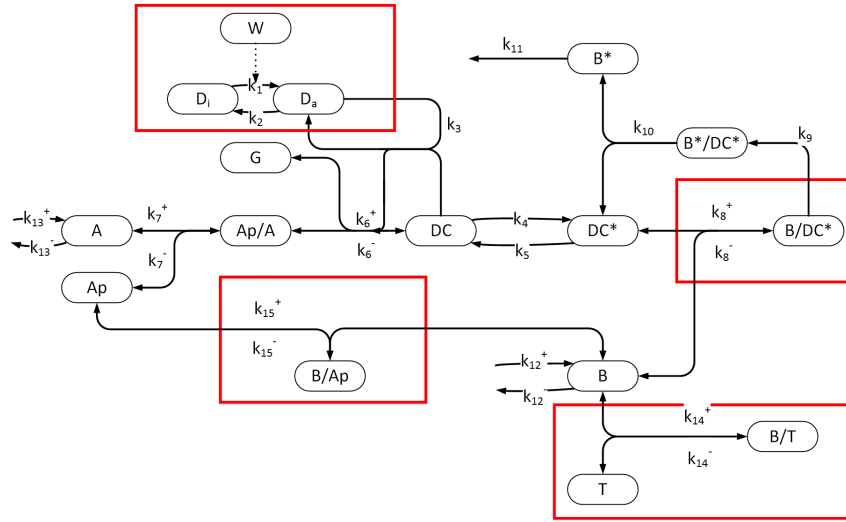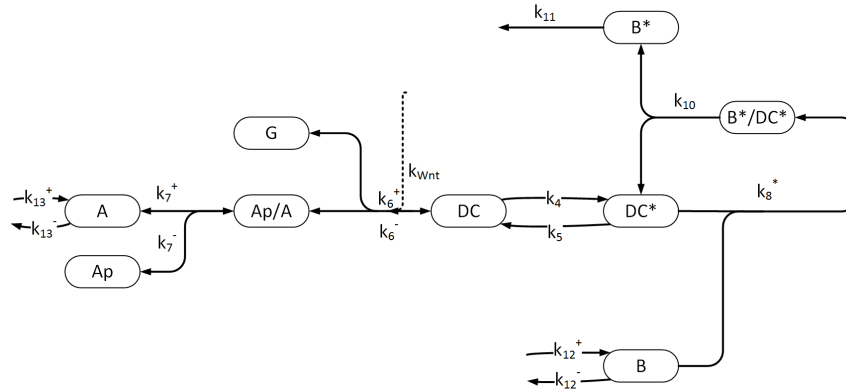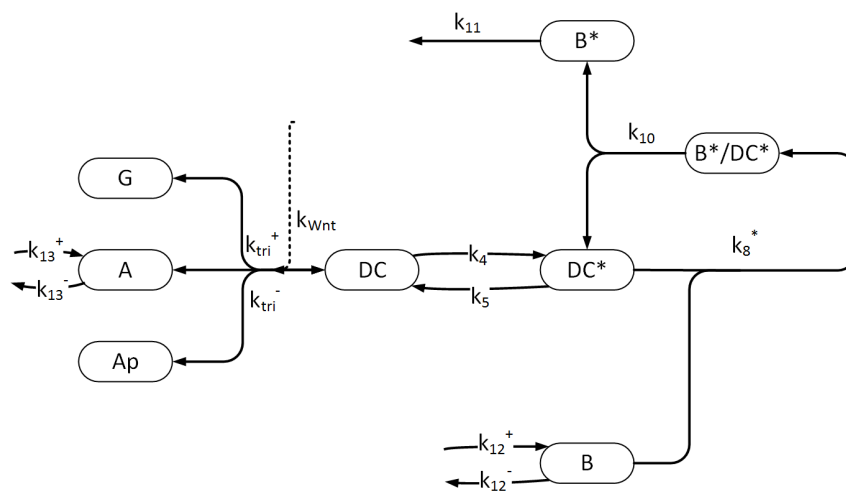
Figure 4.4: (a) Lee model with proteins to be removed enclosed within red boxes. (b) Modified Lee model. (c) Modified Lee model using a trimolecular reaction for DC formation.

where activated Dishevelled (D_a) and inactivated Dishevelled (D_i) reach instantaneous equilibrium. Thus, Wnt and Dishevelled are not explicitly present in the modified model but the effects of these chemical species are modelled through the changing of parameter k_6^- (the dissociation rate of DC).

2. It is assumed phosphorylation of B bound to the destruction complex is rapid, therefore the effective binding rate of B to DC* is modified (reduced) to appropriately reflect this change. The intermediate B/DC* complex simply adds a delay to the degradation of B, therefore it is effectively modelled by delaying the association of B with DC*.

3. The association of B/APC and B/TCF is excluded from the simulation. This was done mostly for numerical efficiency but also because these reactions in the model affect B only through a sequestration effect. Such an effect is experienced by other (unmodelled) binding events such as B to surface proteins. This model does not necessitate any of these stabilizing protein complexes which have a passive role in B regulation and are uninteresting to the underlying regulatory process being modelled here.

4.5.3 Reduction of the Lee model for Wnt signalling

In this section, the following notation is reintroduced. D_i is inactive Dishevelled, D_a is activated Dishevelled, $\mathcal{W}$ is Wnt, Ap is APC, A is Axin, G is GSK3β, Ap/A is APC/Axin, DC is APC/Axin/GSK3β, DC* is APC*/Axin*/GSK3β, B is β-catenin, B/DC* is β-catenin/APC*/Axin*/GSK3β, and B*/DC* is β-catenin*/APC*/Axin*/GSK3β. The values for each reaction rate constant, k_i are presented in Table 4.1.

The dissociation of destruction complex by Dishevelled is treated as a constant rate

To simplify the effect of $\mathcal{W}$ on DC, take the ODE for D_a to be at equilibrium,

$$\frac{d[D_a]}{dt} = k_1[\mathcal{W}][D_i] - k_2[D_a] = 0. \tag{4.60}$$

By adding the total concentration of Dishevelled, $\text{Dsh}^0 = [D_i] + [D_a]$, then the steady state concentration of $[D_a]$ reduces to,

$$[D_a] = \frac{k_1[\mathcal{W}]\text{Dsh}^0}{k_1[\mathcal{W}] + k_2}. \tag{4.61}$$

The binding and subsequent phosphorylation of β-catenin with destruction complex is combined into a single step

To simplify B/DC*, let its corresponding ODE reach equilibrium,

$$\frac{d[B/DC^*]}{dt} = k_8^+[B][DC^*] - k_8^-[B/DC^*] - k_9[B/DC^*] = 0. \tag{4.62}$$

This in turn gives,

$$[B/DC^*] = \frac{k_8^+[B][DC^*]}{k_8^- + k_9}. \tag{4.63}$$

The ODEs for DC* and B^*/DC^* are (ignoring other reactions),

$$\frac{d[\text{DC}^*]}{dt} = -k_8^+[B][\text{DC}^*] + k_8^-[B/\text{DC}^*] + k_{10}[B^*/\text{DC}^*], \tag{4.64}$$

$$\frac{d[B^*/\text{DC}^*]}{dt} = k_9[B/\text{DC}^*] - k_{10}[B^*/\text{DC}^*]. \tag{4.65}$$

Substitution of (4.63) into (4.64) and (4.65) gives,

$$\frac{d[\text{DC}^*]}{dt} = -[B][\text{DC}^*]\left(k_8^+ - \frac{k_8^+ k_8^-}{k_8^- + k_9}\right) + k_{10}[B^*/\text{DC}^*], \tag{4.66}$$

$$\frac{d[B^*/\text{DC}^*]}{dt} = [B][\text{DC}^*]\left(k_8^+ - \frac{k_8^+ k_8^-}{k_8^- + k_9}\right) - k_{10}[B^*/\text{DC}^*]. \tag{4.67}$$

This is simplified by saying that $\overline{k}_8^+$ is the modified reaction rate constant for Reaction 8, and is given by,

$$\overline{k}_8^+ = \left(k_8^+ - \frac{k_8^+ k_8^-}{k_8^- + k_9}\right). \tag{4.68}$$

Formation of destruction complex is converted into a single trimolecular reaction

To convert the formation of DC into a single trimolecular reaction, then the ODE for Ap/A needs to be taken at equilibrium,

$$\frac{d[\text{Ap/A}]}{dt} = k_7^+[\text{Ap}][\text{A}] - k_7^-[\text{Ap/A}] - k_6^+[\text{Ap/A}][\text{G}] + [\text{DC}](k_6^- + k_3[\text{D}_a]) = 0. \tag{4.69}$$

At equilibrium,

$$[\text{Ap/A}] = \frac{k_7^+[\text{Ap}][\text{A}] + [\text{DC}](k_6^- + k_3[\text{D}_a])}{k_7^- + k_6^+[\text{G}]}. \tag{4.70}$$

The ODE for DC (ignoring the phosphorylation/dephosphorylation reactions) is,

$$\frac{d[\text{DC}]}{dt} = k_6^+[\text{Ap/A}][\text{G}] - [\text{DC}](k_6^- + k_3[\text{D}_a]), \tag{4.71}$$

Inserting (4.70) and (4.61) into (4.71) gives,

$$\frac{d[\text{DC}]}{dt} = \frac{k_6^+ k_7^+[\text{Ap}][\text{A}][\text{G}]}{k_7^- + k_6^+ \text{G}^0} - [\text{DC}]\left(k_6^- + \frac{k_1 k_3[\mathcal{W}]\text{Dsh}^0}{k_1[\mathcal{W}] + k_2}\right)\left(\frac{k_7^-}{k_7^- + k_6^+ \text{G}^0}\right), \tag{4.72}$$

where G^0 is the total concentration of GSK3β. The trimolecular rates are therefore,

$$k_{\text{Tri}}^+ = \frac{k_6^+ k_7^+}{k_7^- + k_6^+ \text{G}^0}, \quad k_{\text{Tri}}^- = \frac{k_6^- k_7^-}{k_7^- + k_6^+ \text{G}^0}, \quad k_{\text{Wnt}} = \left(\frac{k_1 k_3[\mathcal{W}]\text{Dsh}^0}{k_1[\mathcal{W}] + k_2}\right)\left(\frac{k_7^-}{k_7^- + k_6^+ \text{G}^0}\right), \tag{4.73}$$

where k_{Tri}^+, k_{Tri}^-, and k_{Wnt}, are the trimolecular reaction rate constants for the forward reaction, back reaction, and the increase to the back reaction rate in the presence of Wnt respectively. Equation (4.72) is rewritten using the notation in (4.73) to give,

$$\frac{d[\text{DC}]}{dt} = k_{\text{Tri}}^+[\text{Ap}][\text{A}][\text{G}] - (k_{\text{Tri}}^- + k_{\text{Wnt}})[\text{DC}]. \tag{4.74}$$

The parameters taken from the Lee model, and the new parameters calculated in this section, are summarized in Table 4.1.

Table 4.1: Reaction rate constant parameters as used in the Lee model and the modified model. A parameter not used in one of the models will be labelled N/A for not applicable.

Reaction Rate Constant	Units	Lee Model	Modified Model
k_1	min^{-1}	0.182	N/A
k_2	min^{-1}	1.82×10^{-2}	N/A
k_3	$\text{nM}^{-1}\text{min}^{-1}$	5×10^{-2}	N/A
k_4	min^{-1}	0.267	0.267
k_5	min^{-1}	0.133	0.133
k_6^+	$\text{nM}^{-1}\text{min}^{-1}$	9.09×10^{-2}	N/A
k_6^-	min^{-1}	0.909	N/A
K_7	nM	50	N/A
K_8	nM	120	N/A
k_9	min^{-1}	206	N/A
k_{10}	min^{-1}	206	206
k_{11}	min^{-1}	0.417	0.417
k_{12}^+	nM min^{-1}	0.423	0.423
k_{12}^-	min^{-1}	2.57×10^{-4}	2.57×10^{-4}
k_{13}^+	nM min^{-1}	8.22×10^{-5}	8.22×10^{-5}
k_{13}^-	min^{-1}	0.167	0.167
k_{Tri}^+	$\text{nM}^{-2}\text{min}^{-1}$	N/A	1.802×10^{-4}
k_{Tri}^-	min^{-1}	N/A	0.0901
k_{Wnt}	min^{-1}	N/A	0.451
$\overline{k}_8^+$	$\text{nM}^{-1}\text{min}^{-1}$	N/A	1.717
k_7^+	$\text{nM}^{-1}\text{min}^{-1}$	N/A	1.0×10^{-2}
k_7^-	min^{-1}	N/A	0.5
k_8^+	$\text{nM}^{-1}\text{min}^{-1}$	N/A	$100,000$
k_8^-	min^{-1}	N/A	$12,000,000$

4.5.4 A stochastic model from the modified Wnt model

To build a stochastic Wnt model, a spatial domain is introduced, and diffusion is used as a mechanism for molecular transport. It is assumed that proteins diffuse at a constant rate for all molecules where $D = 10^{-6}$ mm^2/s is used as it is a typical diffusion constant for proteins [81]. Furthermore, the concentration of each protein needs to be converted into a population number. This is achieved by multiplying the concentration by the cell volume (V). The Lee model uses Xenopus eggs which has a typical cell diameter of 1 mm, (a cell volume of 4.2 mm^3) [121]. Since Xenopus eggs are substantially larger than most cells, using the whole cell volume would mean there are on the order of 100 billion molecules to simulate. A cubic sub-volume with one millionth the volume of the whole cell is used, specifically a volume of size $V = 4.2 \times 10^{-6}$ mm^3 which reduces the approximate (expected) total population size to under 800,000. The initial copy numbers for each species is listed in Table 4.2. On the boundaries of a cube, periodic boundary

conditions are used.

Table 4.2: Initial populations of each protein

Protein	Ap	A	Ap/A	G	DC	DC*	B	B/DC*	B*
Size	223,745	1	2	126,124	2	4	385,941	5	2,321

Importantly, the reduction in the domain volume means that the expected copy number of Axin (a core component of DC) is just 1. Careful consideration in this situation has been taken to ensure that fluctuations in DC concentration on this spatial scale occur mainly from reactions (on the time-scale of $1/k_6^- \sim 60$ s) rather than from loss of spatio-temporal fluctuations which would ordinarily be derived from diffusive transport between sub-volumes of the oocyte (on the time-scale of $V^{2/3}/D \sim 250$ s).

To simulate the molecules and reactions in the modified Wnt model, a Doi regime is chosen for the simulations with $P_\lambda = 0.1$, $\alpha = 1.5$ and $\Delta t = 5 \times 10^{-5}$ min. The simulations are run until a maximum time of 800 minutes. The simulation models the transition from Wnt-on to Wnt-off by initializing molecular copy numbers to expected values according to the steady state of the ODE system with k_6^- in the 'on' state. In principle, the simulation models the transition from high expected B copy numbers ($\sim 386,000$) to low expected B copy numbers ($\sim 73,000$) as determined by the mean-field ODE system. As shall be seen, this is not the case.

The Smoluchowski version of the modified Wnt model is compared to the model simulated using the Gillespie SSA. The Gillespie SSA used in these simulations only take into account the reaction events. The volume for the Gillespie SSA is kept as $V = 4.2 \times 10^{-6}$ mm^3, and the mean of 100 Gillespie simulations are plotted alongside the Smoluchowski simulation in Figure 4.5

4.5.5 Failure of the modified Lee model and simulation of bi-molecular reactions

Figure 4.5 compares the stochastic bimolecular simulation (Smoluchowski model) with another stochastic simulation modelled using the Gillespie SSA [75]. In Figure 4.5b, it is observed that initially the B does not seem to degrade as fast as it should but then ends at a steady 'Wnt-off' state which is significantly less than the Gillespie model predicts. As shall be seen later, the initial behaviour of B can be explained as a consequence of noise in the system. The late (under prediction) of the Smoluchowski simulation, however, can be explained by erroneous simulation of DC assembly using serialized bimolecular reactions.
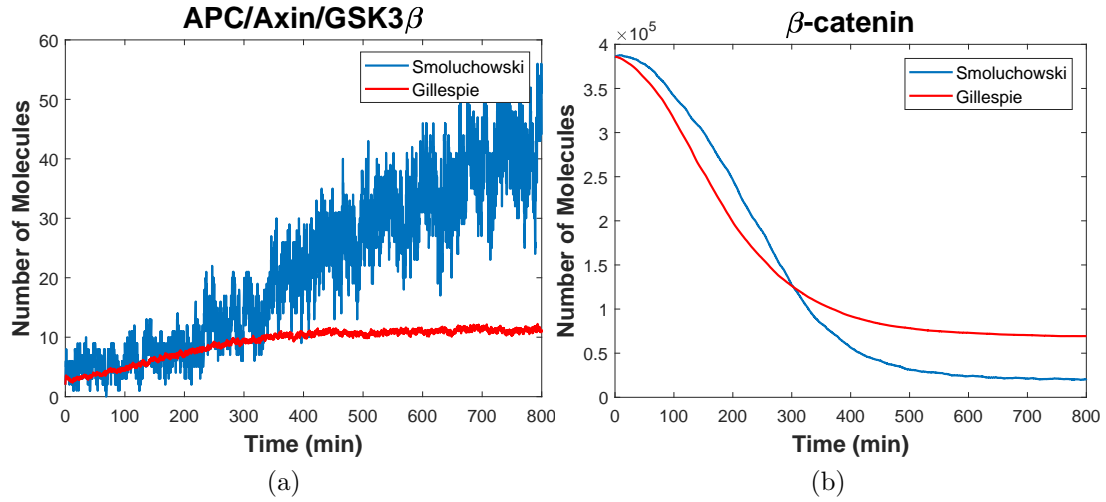
Figure 4.5: Results of the modified Lee model through comparison of the Smoluchowski (blue curve) and Gillespie (red curve) models for (a) destruction complex, and (b) β-catenin levels. The Smoluchowski model runs for 800 minutes using a time-step $\Delta t = 5 \times 10^{-5}$ min. For the Gillespie model, the average results of 100 simulations are plotted. The models agree for the first 200 minutes at which point the number of APC/Axin/GSK3β begin to increase. As a result, the degradation of β-catenin sharply increases and reaches a lower than expected steady state.

In Figure 4.5a, it is clear that the reason for low B copy numbers in the Wnt-off state are due to significantly inflated DC copy numbers. This phenomenon can be explained by the fact that reaction radii are determined by assuming that they are small and pseudo-steady flux is achieved quickly. In the case of APC/Axin complex binding with GSK3β to form the destruction complex, the reaction radius is large (due to the high affinity of GSK3β for APC/Axin) and thus the forward rate (the formation of DC) is unphysically inflated.

The simulations can be visualized with the use of Figure 4.6 which breaks the bimolecular formation of DC into two stages. When APC and Axin combine to form APC/Axin, the binding radius for the following reaction is large and is created at a single instance in time (this is shown in Figure 4.6 with the sudden materialization of point 4). Since Reaction 6 is rapid, the instant that APC/Axin is created, it finds local GSK3β to bind with. Thus, the forward reaction is not 'fast', it is 'instantaneous' and this throws the balance in favour of the DC assembly when compared with the first order (fast) dissociation of APC/Axin into its constituents (the reverse Reaction 7). Despite the number of DC molecules only increasing by 30 (in the simulations), it causes B to degrade by an extra 50,000 molecules (see Figure 4.5b). This is because the system is highly sensitive to DC, which are efficient regulators of B.
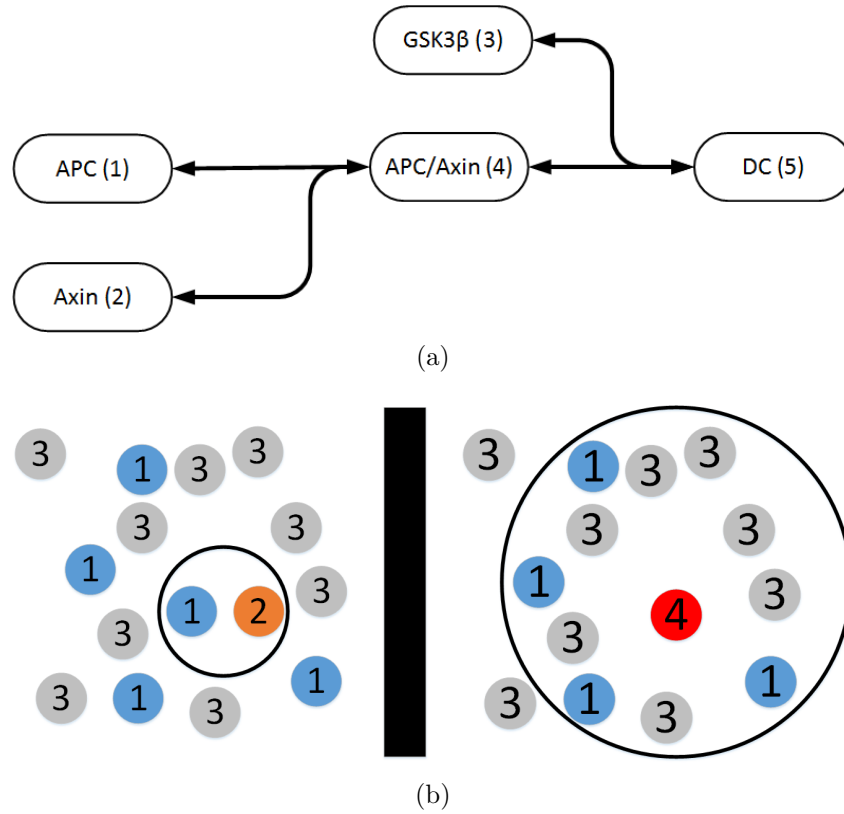
(a)

(b)

Figure 4.6: (a) The pathway for the formation of DC. (b) State of the system when an APC molecule (1) is about to combine with an Axin molecule (2) to form an APC/Axin complex (4). The APC/Axin complex (4) then looks for a GSK3β molecule (3) to combine with. Notice how multiple GSK3β molecules are encompassed within the binding radius. This makes the second reaction effectively instantaneous, leading to a larger than expected amount of DC.

4.5.6 Modified Wnt model using a trimolecular reaction

Due to the rapid decay of APC/Axin, it is possible to show that the Gillespie model reduces to a trimolecular reversible reaction whereby molecules Axin, APC and GSK3β combine to form DC in a single step.

To ensure that there are no fundamental changes to the model, the Gillespie SSA for both the bimolecular and trimolecular interpretations of DC assembly are compared. Figure 4.7 demonstrates that (aside from early transient behaviour) the two Gillespie models are very similar. This validates the use of a trimolecular model in place of the bimolecular model.
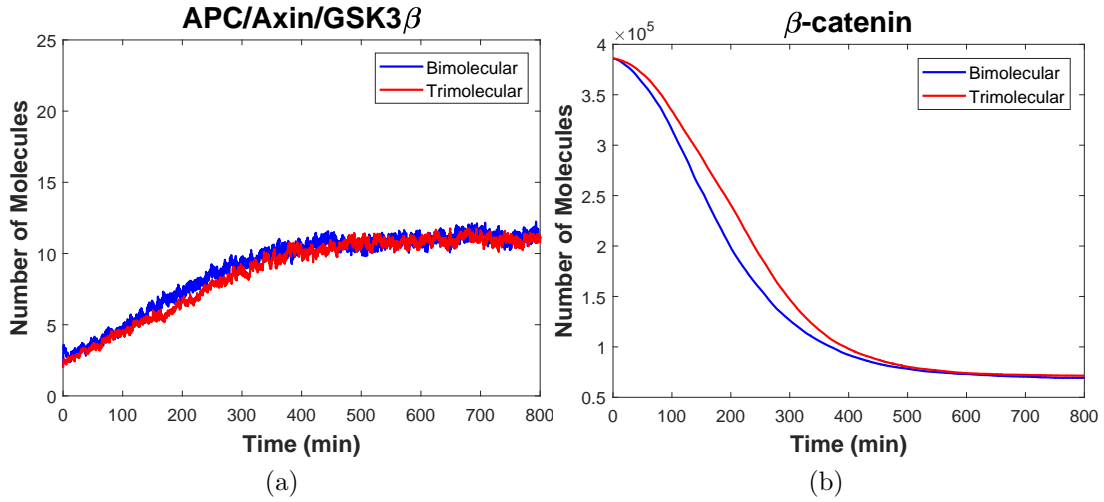
Figure 4.7: Comparison of the modified Wnt model against a model using a trimolecular reaction for the formation of destruction complex. The amount of (a) destruction complex, and (b), β-catenin levels are plotted. The blue line represents the modified bimolecular model, whilst the red line represents the modified trimolecular model. Both are modelled using the Gillespie SSA. Initially there is a small difference between the two models, however the models still reach the same steady state.

Using the reversible trimolecular technique proposed in this chapter, the trimolecular modified model is simulated against its equivalent Gillespie model using simulation parameters $P_\lambda = 0.1$, $\alpha = 1.5$ and $\Delta t = 5 \times 10^{-5}$ min. The simulations are run until a maximum time of 800 minutes and are plotted in Figure 4.8.
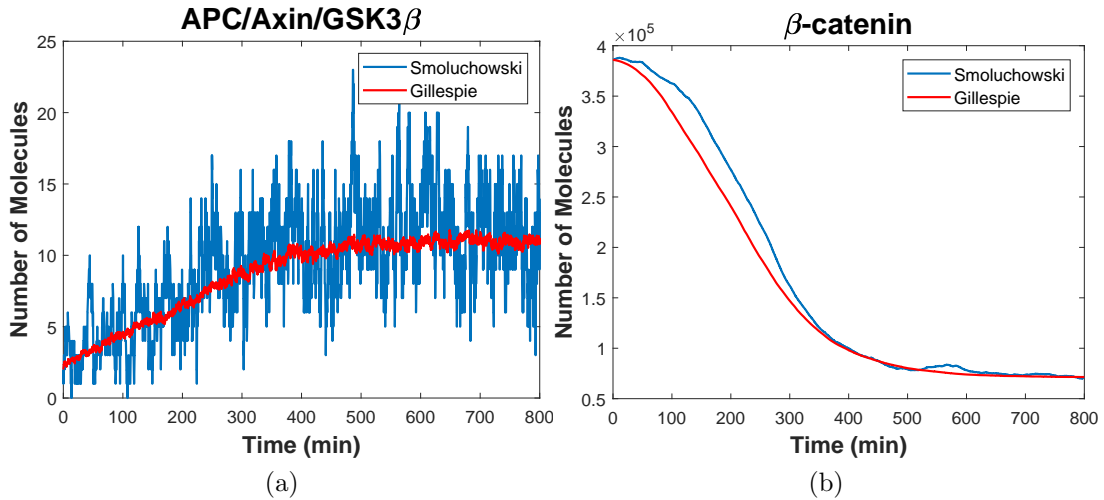

Figure 4.8: Results of the modified Wnt model (using a trimolecular reaction) through comparison of the Smoluchowski (blue curve) and Gillespie (red curve) models for (a) destruction complex, and (b) β-catenin levels. The Smoluchowski model runs for 800 minutes using a time-step $\Delta t = 5 \times 10^{-5}$ min. For the Gillespie model, the average results of 100 simulations are plotted.

Immediately, it can be seen in Figure 4.8a that the issue with unbalanced assembly of DC is no longer a problem with the trimolecular interpretation of this process. On the other hand, B levels do not respond as expected to Wnt switching off. There still seems

to be a period of B over-prediction in the simulation. The discrepancy diminishes nearly to zero by about 400 minutes into the transition from the on state to off state.

The over-prediction of B in the Smoluchowski model is driven by the high asymmetric noise in DC levels in the Wnt-on state. In the Wnt-off state the DC concentration levels are high enough that a symmetric distribution around the mean is expected and the ODE correctly predicts level of B. This is known as stochastic focusing and is a bi-product of intrinsic noise often overlooked by ODE models (not a computational error) [122, 123].

Stochastic focusing occurring within the core destruction cycle can be verified by isolating the cycle, and fixing the DC copy numbers by decoupling it from constant assembly and dissociation into APC, Axin and GSK3β. The 'first' reduced core cycle model is,

$$\text{DC*} + B \rightarrow B\text{*/DC*}, \tag{4.75}$$

$$B\text{*/DC*} \rightarrow \text{DC*}, \tag{4.76}$$

$$\emptyset \rightleftharpoons B. \tag{4.77}$$
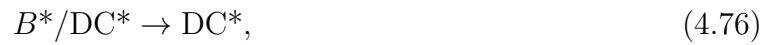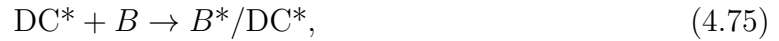
This first reduced core cycle model ignores DC fluctuations which is hypothesized as the cause of increased B copy numbers.

In a second reduced core cycle model, the model is fully reduced to the model without stochastic focusing in [122] by replacing (4.75) and (4.76) with the reaction $\text{DC*} + B \rightarrow \text{DC*}$ (with a combined forward reaction rate to compensate).

Simulations are run in Figure 4.9 where the system starts at steady state with Wnt-on, and Wnt remains on. This is to determine how well each model remains at steady state. Four simulations are plotted in Figure 4.9. The trimolecular Smoluchowski model for Wnt is plotted alongside the expected steady state determined by solving the associated system of ODEs, and alongside the two reduced core cycle models.

As predicted, in the reduced core models the level of B does not deviate from the steady state. The simulation of the first reduced core cycle model shows a slight decrease in B which remains within 10% of the expected steady state and can be explained by the fact that the steady state copy number for DC in this model was not a whole number and had to be rounded up to accommodate the discrete model of DCs. The fact that B deviation from the ODE seems to be dependent on not only low DC concentrations in the Wnt-on regime but also temporal fluctuations in DC copy number is strong evidence that stochastic focusing may play a significant role in B levels.
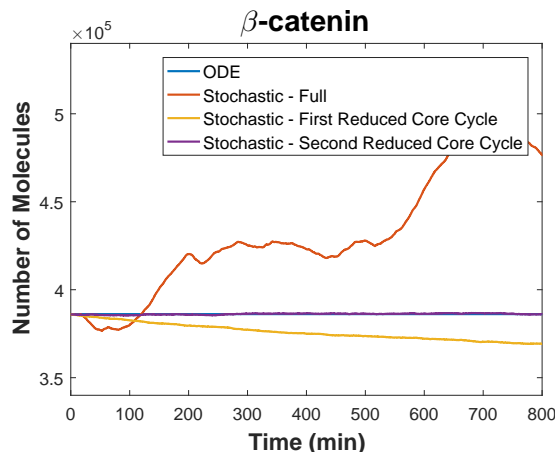
Figure 4.9: Simulations with Wnt turned on demonstrating the inclusion of stochastic focusing. The blue curve (hidden underneath the purple curve), is the expected steady state from the ODE model. Given the model already starts at steady state with $[\mathcal{W}] = 0$, it will remain at steady state (and theoretically so will the stochastic models). The red curve corresponds to the full model in the case that Wnt is turned on ($[\mathcal{W}] = 1$). The orange curve models the reactions in (4.75) to (4.77) only. The purple curve uses the same model as the orange curve, except DC* is kept constant throughout.

4.6 Conclusion

In this chapter, Doi – and by extension – Smoluchowski theory of diffusion-limited inter-actions has been extended to incorporate reversible reactions of any order. It was shown that the theory for reversible reactions developed by Lipková *et al.* [116] is easily extended to higher dimensions under the theoretical framework of Flegg [118]. By utilizing the Doi model, there were two potential strategies that could be used to choose parameters for simulating reactions, one where molecules which result from a reverse reaction are placed outside the reaction radius ($\alpha > 1$), and one which reactants are placed inside the reaction radius ($\alpha \leqslant 1$). By considering both the probability of geminate recombination and the simplicity of implementation, the consequences and limitations of these strategies were discussed.

In the validation of the methodologies, it was first shown that it can be used to recover analytically derived predictable steady states. Then a classical model for Wnt signalling was used to demonstrate the usefulness of the higher-order reaction methodology [58]. This was done by first demonstrating that in the case of fast bimolecular catalytic reactions, the Doi (and Smoluchowski) frameworks may be inappropriate and inaccurate. Secondly, a reduced form of the classical model was simulated to demonstrate that the methodology can be used for running accurate individual particle-based simulations of real complex systems, and in the process, identify new stochastic effects which may not be a feature of more coarse-grained approaches.

Chapter 5

Delay-driven oscillations via Axin2 feedback in the Wnt/β-catenin signalling pathway

5.1   Introduction

The Lee model proposed a comprehensive theoretical model of cytosolic β-catenin regulation and the role of Wnt signalling in this [58]. Whilst there is some clarity in the understanding of the β-catenin regulation cycle, the way in which Wnt and its receptor complex interferes with this cycle precisely is still being studied. Lee *et al.* assumed that the action of Wnt was to activate Dishevelled, which in turn increased the dissociation rate of the enzyme GSK3β from the destruction complex scaffolding proteins APC and Axin. Conceded by the authors in 2003, the signal propagation from the Wnt ligand to the destruction complex was 'poorly understood'.

Recent experiments have illuminated much of the uncertainty that once shrouded the manner by which Wnt receptor complexes interact with β-catenin regulation [48]. Section 2.1 explored experimental models in which a Wnt receptor complex *deactivates* destruction complex rather than *dissociating* it. These experiments led to the mathematical models in Section 2.3 for which the Jensen [71] and Tymchyshyn [72] models support the induction of sustained oscillations through deactivation processes.

The difference in outcome between deactivation and dissociation mechanisms might seem trivial when considering the overall effect on β-catenin levels. However, it is demonstrated in this chapter that it is not as trivial as may first appear since significant differences in the asymptotic stability of β-catenin levels is observed between these two models when negative feedback is considered.

Multiple feedback loops have been identified in reference to Wnt signalling, and there have been various attempts to develop mathematical models for these. The most studied feedback loop acknowledges that Axin2 is a target for β-catenin/TCF regulated transcription [44, 27]. As a component of the destruction complex, β-catenin/TCF regulated Axin2 transcription represents a negative feedback for Wnt signalling.

The main Axin2 feedback models from Section 2.3 are summarised again in the following paragraphs. Each paragraph gives a brief overview into each model's unique behaviour, any mathematical and computational limitations, and the models advantages and disadvantages. Each of these models influence the construction of the new models developed in this chapter.

Oscillations in Wnt signalling have been observed experimentally and studied for its

relationship to oscillations in other pathways [124]. Theoretically oscillations can be generated for the Lee model with the inclusion of Axin2 *and* DKK1 [68]. It was shown by Wawra *et al.* that the inclusion of heuristically defined Hill's function kinetics, and the use of delay differential equations can induce oscillations [68]. This work constituted a purely numerical investigation due to the model complexity (a system of 17 ordinary and delay differential equations), which made it impossible to fully analyse the conditions for the oscillatory behaviour.

Considering *only* the Axin2 feedback mechanism, Tymchyshyn *et al.* were able to show that a stochastic model of Wnt signalling was capable of inducing oscillatory behaviour [72] . This model reduces the Wnt pathway to 6-components. Characteristic of the Tymchyshyn model is the treatment of the Wnt receptor complex as a deactivator (rather than dissociator) of the destruction complex which is in line with recent experimental observations. The Tymchyshyn model used stochastic π-calculus techniques [74] via the BioSPI simulation platform [73] to investigate how their model behaves stochastically. They run two types of simulations, one in which there is a high Wnt stimulus, and the other for a low Wnt stimulus, and they compare this to the deterministic solution. For the high Wnt stimulus case, both the stochastic and deterministic solutions show sustained oscillatory behaviour. However for the low Wnt stimulus case, the deterministic solution does not exhibit any oscillations, but the stochastic simulation has periodic spiking. It is not established by Tymchyshyn *et al.* if the oscillatory behaviour of their model is stochastically induced, or if it is a property of the underlying dynamical system since their analysis is achieved through numerical experiments alone. This oscillatory behaviour forms the basis for Chapter 6 in which Gillespie and Smoldyn simulations are computed to determine how these stochastic oscillations arise.

By investigating a Wnt oscillator model for somitogenesis, Jensen *et al.* were able to create an ODE model that exhibits oscillatory behaviour [71]. They present a simplified version of the Wnt pathway (using 8 components), and provide parameter regimes for when oscillations are induced. One key finding from this paper included the qualitative condition necessary to produce oscillations: that a high concentration of β-catenin can promote Axin2 mRNA such that deactivation of Axin2 by the receptor complex reaches saturation [65]. The model uses non-linear kinetic feedback terms, and is a system of ODEs with sufficient complexity that analytical investigation is not possible. The conditions for oscillatory behaviour in their model are explored by numerical experimentation in the parameter space, as is the case in all of these modelling attempts.

In this chapter, an investigation into the detail of the theoretical conditions for sustained oscillations in Wnt signalling is conducted. This is completed by first constructing a deterministic dynamical model based on recent findings, and reducing this model to exhibit its fundamental features and structure. The models focus on the Axin2 feedback mechanism.

It is first demonstrated that a simple model of Wnt signalling whereby the Wnt receptor complex dissociates the destruction complex into active components (reminiscent of the Lee model), will not exhibit sustained oscillatory behaviour observed in experiments under any parameter regime.

Since Axin2 is upregulated by β-catenin-moderated transcription, it is uncertain how best this process should be modelled, specifically how should the intrinsic temporal feedback delay be incorporated into the model. Two separate models are investigated and compared in which feedback delay is implemented (1) implicitly with an intermediate chemical species, and (2) explicitly using delay differential equations. The condition for asymptotic instability of the static steady state which drive the system into sustained

oscillations for model type (1) and model type (2) is solved analytically, with the key features determined from this. These relationships give deep insight into the Wnt signalling pathway structure. Importantly, it will be proved that the Wnt-dependent deactivation rate of Axin needs to be above a threshold amount compared with the rate of Axin degradation of β-catenin for sustained oscillations.

It will be shown that the delay in feedback is a necessary characteristic of the system driving sustained oscillations, and that oscillations occur in all cases within a single finite window of Wnt signal strengths. The width of this window changes with the parameters of the system in a well-defined way. It will be shown numerically how the amplitude and period of the resultant sustained oscillations depends significantly on the parameters of the model. These kinds of theoretical insights explain (in a mathematically rigorous way) why some cells respond differently to different levels of Wnt stimulus compared with other cells.

5.2 Models

Wnt signalling in this chapter is modelled at a very fundamental level, focusing on the key underlying structure of the model on the time-scale of the whole signalling process. Since the focus is on the key Axin2 feedback mechanism, the following chemical species are included in each of the models; Axin (A), β-catenin (B), active destruction complex (C), and Wnt-bound (activated) receptor complex (R). For brevity's sake, the [ ] notation that represents the concentration of a species is dropped.

5.2.1 The reduction of the Tymchyshyn model to its base structure

The model of Tymchyshyn *et al.* (first reviewed in Section 2.3.4) forms the basis of the deactivation models in this chapter. The model is presented in Figure 5.1. Notice that this model includes two intermediate protein complexes B/C (C_1) and R/C (C_2), which are formed by binding of each of the two indicated proteins.
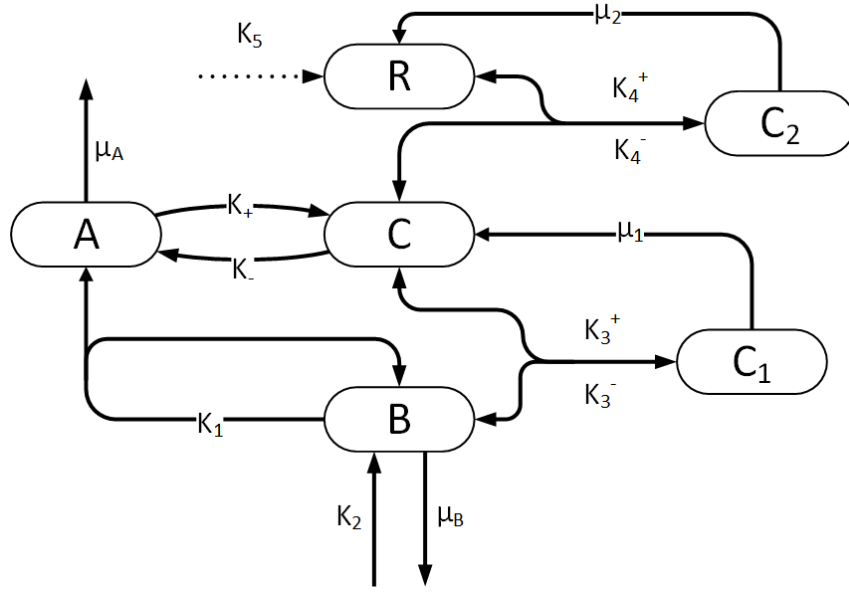
Figure 5.1: Tymchyshyn *et al.* model using 6 components. This model is the same as that reviewed in Figure 2.9, except with the addition of the dotted reaction involving the rate constant k_5. This rate is not part of the Tymchyshyn model, but is used for the models developed throughout this chapter.

This model contains 6 components and a total of 12 reactions. The ODEs are,

$$\frac{dA}{dt} = k_1 B - \mu_A A - k^+ A + k^- C, \tag{5.1}$$

$$\frac{dB}{dt} = k_2 - k_3^+ BC + k_3^- C_1 - \mu_B B, \tag{5.2}$$

$$\frac{dC}{dt} = -k_3^+ BC + (k_3^- + \mu_1)C_1 + k^+ A - k^- C - k_4^+ RC + k_4^- C_2, \tag{5.3}$$

$$\frac{dR}{dt} = -k_4^+ RC + (k_4^- + \mu_2)C_2, \tag{5.4}$$

$$\frac{dC_1}{dt} = k_3^+ BC - (k_3^- + \mu_1)C_1, \tag{5.5}$$

$$\frac{dC_2}{dt} = k_4^+ RC - (k_4^- + \mu_2)C_2, \tag{5.6}$$

The first assumption is that phosphorylation and removal of β-catenin via the destruction complex (denoted by the rate μ_1) is efficient when compared to other possible fates for the temporary complex C_1 [59]. Without scaling time, it is clear from (5.5) that $C_1 = O(\mu_1^{-1})$ and a pseudo-steady state $\mu_1 C_1 = k_3^+ BC$ is concluded by looking at dominant balances in (5.5). This algebraic relation negates the need for (5.5) and terms such as $k_3^- C_1$ in other equations vanish to leading order.

The second modification applied to the Tymchyshyn model reflects the assumption that receptor complex is dynamic during Wnt signalling, not conserved as in the Tymchyshyn model [48]. Based on recent findings outlined in Section 5.1, it is assumed that receptor complex is formed at a rate k_5 which is dependent on receptor and co-receptor turnover rates and supply of Wnt signal. In the process of deactivating the destruction complex, the receptor complex is itself deactivated (sent to the proteasome). By making the assumption that the deactivation process is rapid once a binding of R and C is

achieved, it is clear from a dominant balance of (5.6) that $k_4^- C_2$ may be neglected to leading order.

The third assumption is that β-catenin degradation is dominated by Axin-mediated ubiquitination. Therefore it is assumed that μ_B is small and can be neglected from the model.

The fourth assumption is much the same as the third. It assumes that the removal of Axin under Wnt stimulus is dominated by deactivation via the Wnt receptor signalosome. Thus, it assumes that μ_A is small and can be neglected. This is not the case, however, in the deconstructor models inspired by Lee *et al.*. In the deconstructor models, Axin is not removed at all by receptors and natural decay of Axin μ_A is non-zero (it is chosen such that A, B and C have the same steady state concentrations as the deactivator models).

Finally, during Wnt signalling, it is assumed that an active destruction complex is much more likely to be removed via Wnt receptor deactivation (a dominant feature of the model) than by spontaneous dephosphorylation or dissociation of the destruction complex. Therefore the activation of A is approximated to be irreversible ($k^- = 0$). The exception to this is of course the deconstructor model of Wnt signalling (for example, the Lee model) which postulates that active Wnt receptor complex acts by increasing k^- to non-trivial values.

For the models in this chapter, the rate constants are relabelled as $k_3^+ = K_3$, $k_4^+ = K_4$, $k_5 = K_5$, and $k^\pm = K_\pm$. The deconstructor and deactivator models, are shown in Figure 5.2. In this figure, the black and blue reactions represent the deconstructor model, whilst the black and red reactions represent the deactivator model. In the following sections, the four models depicted in this figure are explored; the deconstructor model, the implicit-delay deactivator model, the zero-delay deactivator model, and the explicit-delay deactivator model.
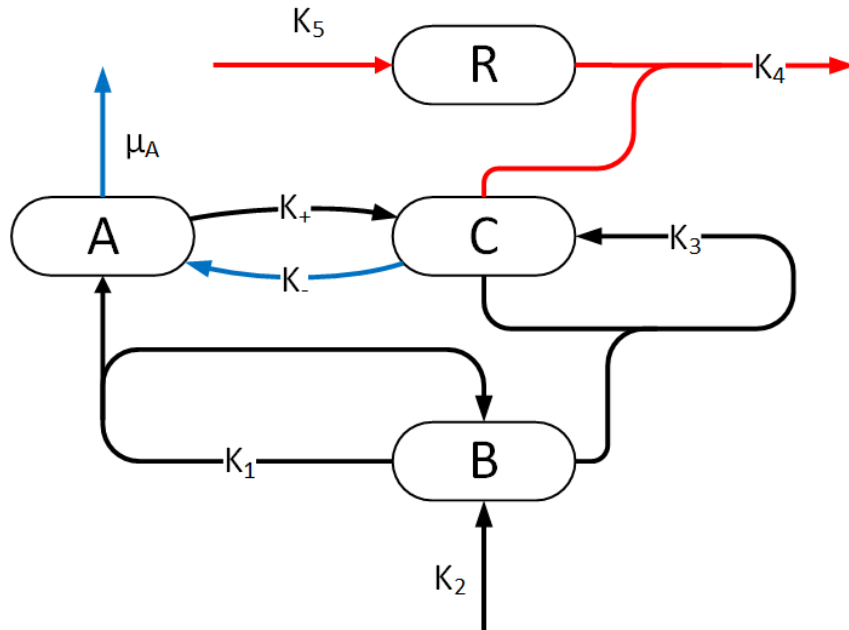

Figure 5.2: The reduced version of the Tymchyshyn model. Reactions in black represent the base model. Adding the reactions in blue to the base model produces the deconstructor model. Alternatively, adding the red reactions to the base gives the deactivator model.

5.2.2 The deconstructor model

This section begins with an exploration of the deconstructor model which focuses on the key components of the Lee model. The parameter K_- is used to encapsulate the deconstruction of the destruction complex (C) in the presence of a Wnt stimulus. To balance the system, the parameter μ_A is retained, although it is assumed that this will be negligible for future models.

In Figure 5.3, a diagram of the key interactions which form the signalling network is presented for the deconstructor model. Importantly, in the deconstructor model, it is assumed that activated receptor complex interacts with destruction complex and deconstructs it into its components without affecting the concentration of the receptor complex and therefore, the receptor complex dynamics is decoupled from the network and considered to reach a steady state which depends on the supply of Wnt stimulus (transient solutions are not considered in this chapter). Thus, the receptor complex (R) is assumed to indirectly govern the reaction rate given by K_-. As shall be demonstrated for this simple system, irrespective of the efficacy of the effect of Wnt stimulation (the value of K_-), sustained oscillating solutions cannot be generated without adding complexity to the model (that is, the base structure of this system does not easily lend itself to sustained oscillatory behaviour).
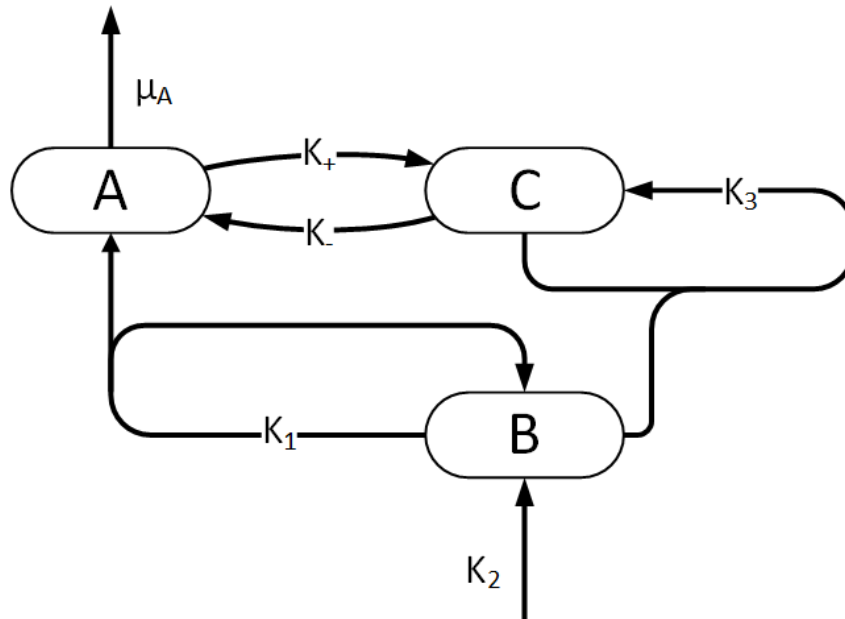

Figure 5.3: The deconstructor model is a reduced version of the Lee model. The effect of Wnt in deconstructing the destruction complex (C) is summarised within the rate constant K_-. In comparison to the deactivation model (see Figure 5.4), this deconstructor model includes removal of Axin (A) through degradation at a rate proportional to μ_A (to stop unbounded production of Axin in the absence of removal by Wnt).

The deconstructor model is the following system of three ordinary differential equations

(ODEs),

$$\frac{dA}{dt} = K_1 B - (K_+ + \mu_A)A + K_- C, \tag{5.7}$$

$$\frac{dB}{dt} = K_2 - K_3 BC, \tag{5.8}$$

$$\frac{dC}{dt} = K_+ A - K_- C, \tag{5.9}$$

Stability analysis of deconstructor Wnt mechanisms

Here it is proved that the Wnt receptor mechanism which deconstructs the destruction complex (such as that of Lee *et al.*) cannot maintain sustained oscillatory behaviour under Axin feedback in the simplified model. The deconstructor Wnt mechanism activates Dishevelled which then breaks the destruction complex into its scaffolding proteins (APC, Axin, and GSK3β). These scaffolding proteins are not removed from the system, therefore they can recombine to form the destruction complex. The focus here will be on the long time stability of the systems steady state under Wnt stimulation, so that the deconstruction rate can be considered as some constant K_- which depends on the concentration of Wnt as well as other properties of the cell and relevant proteins.

Let $d\mathbf{X}/dt = \mathbf{F}(\mathbf{X})$, where $\mathbf{X} = (A, B, C)$, and $\mathbf{F}$ represents the RHS of (5.7) to (5.9). Let the steady state $\mathbf{X}_0$ be such that $\mathbf{F}(\mathbf{X}_0) = \mathbf{0}$ in which all chemical species are non-negative. Denote the steady state to be $\mathbf{X}_0 = (A_0, B_0, C_0)$. The steady state concentrations are uniquely defined as,

$$A_0 = \left(\frac{K_1 K_2 K_-}{K_3 \mu_A K_+}\right)^{1/2}, \quad B_0 = \left(\frac{K_2 \mu_A K_-}{K_1 K_3 K_+}\right)^{1/2}, \quad C_0 = \left(\frac{K_1 K_2 K_+}{K_3 \mu_A K_-}\right)^{1/2}. \tag{5.10}$$

Linearisation around this steady state $\mathbf{X} = \mathbf{X}_0 + \boldsymbol{\epsilon}$ where $0 < |\boldsymbol{\epsilon}| \ll 1$ reduces the model to $d\boldsymbol{\epsilon}/dt = \mathbf{J_F}(\mathbf{X}_0)\boldsymbol{\epsilon} + O(|\boldsymbol{\epsilon}|^2)$, where $\mathbf{J_F}(\mathbf{X}_0)$ is the Jacobian of the RHS of (5.7) to (5.9) evaluated at $\mathbf{X}_0$. Stability around this steady state is therefore predicated on all of the real parts of the eigenvalues of $\mathbf{J_F}(\mathbf{X}_0)$ being less than 0. The eigenvalues λ of $\mathbf{J_F}(\mathbf{X}_0)$ are given by

$$|\mathbf{J_F}(\mathbf{X}_0) - \lambda \mathbf{I}| = \begin{vmatrix} -K_+ - \mu_A - \lambda & K_1 & K_- \\ 0 & -K_3 C_0 - \lambda & -K_3 B_0 \\ K_+ & 0 & -K_- - \lambda \end{vmatrix} = 0, \tag{5.11}$$

which yields the auxiliary equation $D(\lambda) = \lambda^3 + a\lambda^2 + b\lambda + c = 0$, where

$$a = \mu_A + K_+ + K_- + K_3 C_0, \tag{5.12}$$
$$b = \mu_A K_- + K_3 C_0 (\mu_A + K_+ + K_-), \tag{5.13}$$
$$c = K_1 K_3 K_+ B_0 + \mu_A K_3 K_- C_0. \tag{5.14}$$

The Routh-Hurwitz criteria for a third order polynomial states that $D(\lambda) = 0$ will have roots which lie entirely in the left half plane - meaning the steady state is asymptotically stable - if and only if (1) the coefficients a, b, and c are all positive and (2) $(ab - c) > 0$. Condition (1) is met since all parameters are assumed positive and thus a, b, and c are all sums of positive numbers. Condition (2) is met by inspection since each of the two terms in c appear as terms in the product ab, which has many other (unbalanced) positive terms. This analysis demonstrates that the introduction of Axin feedback into a simple model of Wnt which features a deconstruction role for the Wnt receptor complex will not, under any parameter regime, lead to an asymptotically unstable steady state and thus sustained oscillations.

5.2.3 The implicit-delay deactivator model

A deactivator model, one in which Wnt receptor complex (R) deactivates destruction complex, is based on the mechanism for Wnt signalling at the receptor level first described in Section 2.1. In the Wnt-on situation, Wnt ligand is bound to Fzd receptor and its co-receptor LRP6. Activation of this receptor complex leads to Ap2-dependent recruitment of the β-catenin destruction complex to the plasma membrane. In particular, Dvl binds to Fzd and Axin to LRP6 and thus, ensures signalosome formation at the cytoplasmic membrane and tight association with the destruction complex. Subsequent internalization of the Wnt signalosome is mediated by the interaction of Dvl with Ap2μ2 and leads to the sequestration of Dvl, Axin, CK1, GSK3β, and β-catenin in cytoplasmic aggregates – the inactive β-catenin destruction complex. The ligand-receptor complex is routed to late endosomes for degradation or recycling, whereas the β-catenin destruction complex is kept inactive. The degradation of Wnt and the deactivation of Axin (destruction complex) results in a co-removal of these species from the system and is described in the model to occur at some rate K_4. Subsequently, the destruction complex becomes activated again by, for example, phosphorylation of Axin. However this occurs on comparatively very long time-scales and is not a significant process in the Wnt-on state.

In this model, as opposed to the deconstructor model, receptor complex is supplied at some rate K_5. This rate is determined by the Wnt stimulus, but also other factors such as the cell-type and expression levels of Fzd receptors, co-receptors (for example from the LRP family), and/or promoters such as R-spondin. The receptor complex binds to active destruction complex, and then removes both itself and destruction complex from the system.

The implicit-delay model is presented diagrammatically in Figure 5.4. This model is a system of four ordinary differential equations (ODEs),

$$\frac{dA}{dt} = K_1 B - K_+ A, \tag{5.15}$$

$$\frac{dB}{dt} = K_2 - K_3 BC, \tag{5.16}$$

$$\frac{dC}{dt} = K_+ A - K_4 CR, \tag{5.17}$$
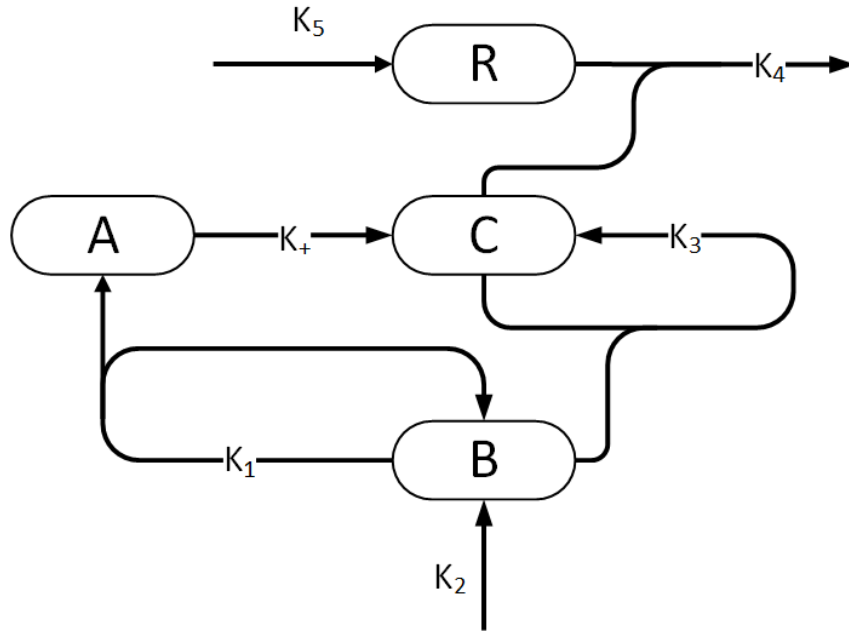
$$\frac{dR}{dt} = K_5 - K_4 CR. \tag{5.18}$$

Figure 5.4: The implicit-delay deactivator model. This model contains four chemical species that can be modelled using ODEs. Key to this model is the deactivation of destruction complex (C) by removal with the receptor complex (R), and the delay in production of (C) by the intermediate production and conversion of Axin (A).

A simulation of this model is plotted in Figure 5.5 which produces sustained oscillations in β-catenin. This simulation shows that there is indeed at least one set of parameters for which the system sustains oscillations. The exact conditions to determine what set of parameters cause the steady state to become asymptotically unstable and instigate sustained oscillations will be researched in Section 5.3.2.
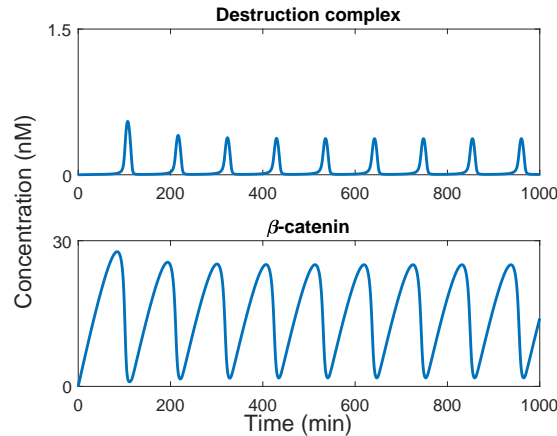

Figure 5.5: Implicit-delay deactivator model with rate constants $K_1 = 0.012$ min^{-1}, $K_2 = 0.423$ nM min^{-1}, $K_3 = 1$ nM^{-1} min^{-1}, $K_+ = 0.1$ min^{-1}, $K_4 = 10$ nM^{-1} min^{-1}, and $K_5 = 0.18$ nM min^{-1}. These rate constants are taken from the model in Tymchyshyn *et al.* [72]. This set of rate constants show that there is at least one case in which sustained oscillations are induced.

In this model, there is a delay in the feedback mechanism between β-catenin (B) and destruction complex (C). This delay is modelled implicitly by the necessity of β-catenin

(B) to produce, first, inactive Axin (A). It was found that if this delay is not present in the system (for example, if it is assumed that β-catenin (B) produces destruction complex (C) directly), the system behaves very differently and does not have the potential to result in sustained oscillations. This fact is proved in Section 5.2.4 by taking the limit of this model as $K_+ \to \infty$. Part of this delay in the feedback could be thought to occur due to the time taken for transcription of Axin. Section 5.2.5 will describe a separate model in which the delay is made explicit using a delayed differential equation.

5.2.4 The zero-delay deactivator model

The implicit-delay model from the previous section simplifies the pathway to four components, so a natural question to ask is, can sustained oscillations be generated by a simpler model? The first attempt to answer this question is to note that Axin (A) seemingly has a small contribution to the overall system. It is produced by β-catenin and subsequently converted into activated Axin. This suggests the implicit-delay model can be simplified by letting destruction complex (C) be produced directly from β-catenin (B). In doing so, the new pathway is shown in Figure 5.6.
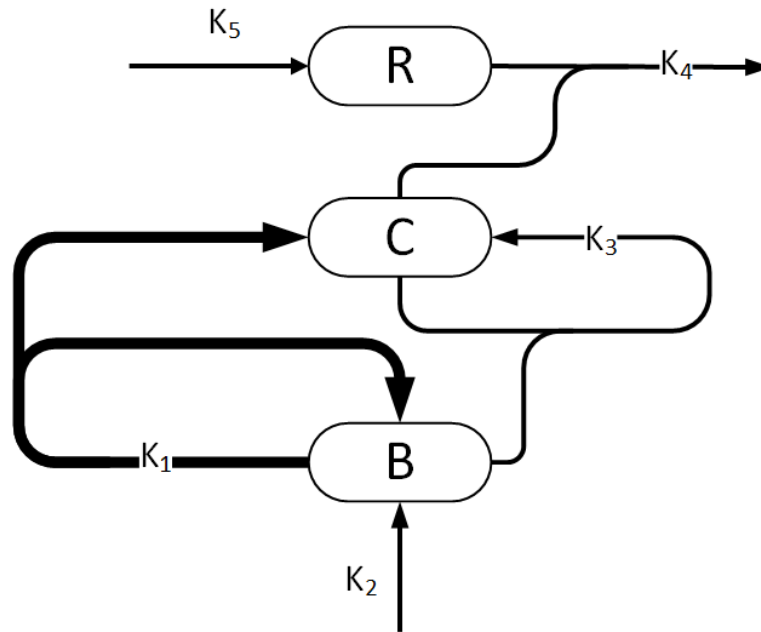

Figure 5.6: The zero-delay deactivator model with three chemical species. This model does not include Axin (A), and instead directly produces destruction complex (C). The thick line with rate constant K_1 denotes that this is treated as a fixed time delay for the explicit-delay model in Section 5.2.5.

This pathway has the following system of ODEs,

$$\frac{dB}{dt} = K_2 - K_3 BC, \tag{5.19}$$

$$\frac{dC}{dt} = K_1 B - K_4 CR, \tag{5.20}$$

$$\frac{dR}{dt} = K_5 - K_4 CR. \tag{5.21}$$

Stability analysis of deactivator Wnt models with no feedback delay

Here it is mathematically proved that a non-zero delay is necessary in the Axin feedback mechanism of a deactivator Wnt model in order to produce sustained oscillations. The unique steady states of (5.19) to (5.21) are,

$$B_0 = \frac{K_5}{K_1}, \quad C_0 = \frac{K_1 K_2}{K_3 K_5}, \quad R_0 = \frac{K_3 K_5 K_5}{K_1 K_2 K_4}. \tag{5.22}$$

Following an identical analysis methodology from the previous section, the auxiliary equation $D(\lambda) = \lambda^3 + a\lambda^2 + b\lambda + c = 0$ is computed, where,

$$a = K_3 C_0 + K_4 C_0 + K_4 R_0, \tag{5.23}$$
$$b = K_3 K_4 C_0 R_0 + K_3 K_4 C_0 C_0 + K_1 K_3 B_0, \tag{5.24}$$
$$c = K_1 K_3 K_4 C_0 B_0. \tag{5.25}$$

Checking the Routh-Hurwitz criteria, similar to Section 5.2.2, it is noted that (1) a, b, and c are all positive as the system parameters are positive, and (2) $(ab - c) > 0$ since the second term of a multiplied by the third term of b is c, and thus c only cancels part of ab. Therefore the eigenvalues of the Jacobian for this system all lie in the left half plane and the steady state is asymptotically stable - and unable to sustain oscillations irrespective of the other model parameters.

Importance of a delay in deactivator models

Going from an implicit-delay deactivator model to a zero-delay model, the sustained oscillations have disappeared, and it was proved that a zero-delay model will never have sustained oscillations. This suggests that a delay is vital to inducing sustained oscillations, and it is shown in the next section that adding a fixed time delay to the zero-delay model allows the system to oscillate again. Before moving to the next model, the implicit-delay model is graphically investigated to provide a hint as to how a system of three differential equations can still oscillate.

In Figure 5.7, all four components (A, B, C, R) are plotted, by first scaling each component by its corresponding maximum concentration, then overlapping A and B on the one plot, with C and R on the other plot. In the first plot, it is seen that A always lags B, which demonstrates that there is a slight delay in producing A from B.
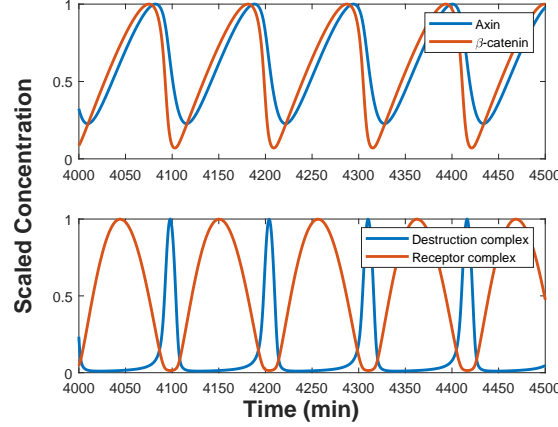
Figure 5.7: Scaled plots of the implicit-delay deactivator model with Axin (A) and β-catenin (B) in the top plot, and destruction complex (C) with receptor complex (R) in the bottom plot. The simulations uses rate constants $K_1 = 0.012$ min^{-1}, $K_2 = 0.423$ nM min^{-1}, $K_3 = 1$ nM^{-1} min^{-1}, $K_+ = 0.1$ min^{-1}, $K_4 = 10$ nM^{-1} min^{-1}, and $K_5 = 0.18$ nM min^{-1}.

In comparing C to R, it can be seen that they appear to be inversely proportional to each other. Also, the time at which C spikes seems to line up well with the trough of B. This suggests that at this trough, the gap between A and B is wider because of the increase in C.

5.2.5 The explicit-delay deactivator model

An important feature which can determine the existence of sustained oscillating solutions for the implicit-delay deactivator model is the existence of a delay in the feedback from β-catenin to destruction complex. In the previous model, it was shown that in the absence of this delay, the system is always asymptotically stable, hence a delay is required in these models. Previously it was assumed that this delay can be modelled implicitly by the inclusion of an intermediate species (which one can think of as inactive Axin or perhaps Axin mRNA). In practice, it is not clear that this delay should be modelled in this manner. The transcription processes has many steps and works like a machine to produce Axin proteins after some period of delay. It may therefore be argued that an equally appropriate model is for the β-catenin dependent upregulation of destruction complex to occur after some fixed, explicit, delay.

To build the explicit-delay deactivator model, the model from Section 5.2.4 is used, and where a time delay τ is introduced into the reaction $B \xrightarrow{K_1} B + C$. The ODEs now become the delay differential equations (DDEs),

$$\frac{dB}{dt} = K_2 - K_3 BC, \tag{5.26}$$

$$\frac{dC}{dt} = K_1 B(t - \tau) - K_4 CR, \tag{5.27}$$

$$\frac{dR}{dt} = K_5 - K_4 CR. \tag{5.28}$$

To compare the explicit- and implicit-delay models, τ is required to be set to $\tau \equiv 1/K_+$. One simulation is plotted using $\tau = 1/0.1 = 10$ min in Figure 5.8, and it can be seen that sustained oscillations are induced which are similar, but slightly different to the implicit-delay model from Figure 5.5. Whilst under this condition ($\tau = 1/K_+$), the explicit- and

implicit-delay models are not identical, it is simple to prove (see Section 5.3.3) that under this condition the two models share the same steady state (of which there is always only one), and under limiting conditions this steady state shares similar conditions for stability (see Section 5.3.1).
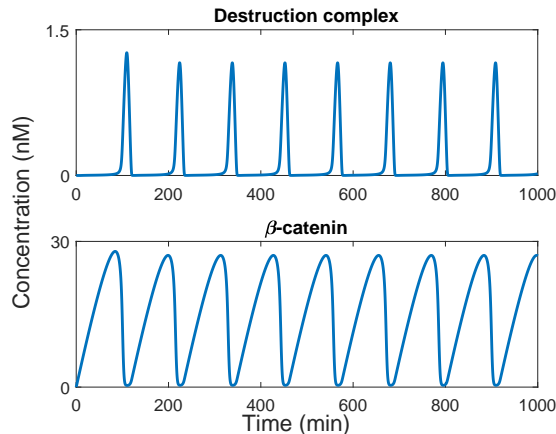

Figure 5.8: Plot of the evolution of destruction complex and β-catenin in the explicit-delay deactivator model. The simulation uses parameters $K_1 = 0.012$ min^{-1}, $K_2 = 0.423$ nM min^{-1}, $K_3 = 1$ nM^{-1} min^{-1}, $\tau = 1/K_+ = 10$ min, $K_4 = 10$ nM^{-1} min^{-1}, and $K_5 = 0.18$ nM min^{-1}.

5.2.6   Key observations from each model

Throughout Section 5.2, four models were constructed (with comparable parameter sets) to determine which models can produce sustained oscillations, and proved which models cannot. By completing an initial exploration into these four models, the following key observations are made;

1. A Wnt receptor mechanism which deactivates (rather than deconstructs) destruction complex is capable of generating sustained oscillations.

2. Without a delay in the feedback mechanism, the deconstructor Wnt models do not sustain oscillatory behaviour. This is true and provable for any set of positive parameters.

3. Modelling the feedback delay explicitly or implicitly appears to have minimal effect on the behaviour of the system, although sustained oscillations resulting from an explicit-delay model seem to have a slightly larger amplitude and larger period than the implicit-delay model.

Each of these observations are anecdotal and may be true circumstantially due to the choice of parameters and the simplicity of the model. However, since the models represent the core system structure, they can be analysed. In particular, as mentioned, it was shown explicitly that, in regards to observation (1), the deconstructor model is asymptotically stable for any choice of parameter set. In regards to observation (2), it was proven in Section 5.2.4 that if the delay τ vanishes, so too does the possibility of sustained oscillations. In the following sections, a more detailed analysis will be followed to determine the full set of possible parameters for which sustained oscillations are generated in both the implicit- and explicit-delay deactivator models.

5.3 Results and Discussion

5.3.1 A note comparing implicit- and explicit-delay models

The explicit-delay model outlined in Section 5.2.5 is taken as an approximation to the implicit-delay model in Section 5.2.3, or, depending on how it is looked at, the implicit-delay model is an approximation of the explicit-delay model. Here it will be outlined how this comparison is achieved, and under what circumstances the models behave the same and how they differ.

The implicit-delay model is given by the evolution of the following ODE system

$$\frac{dA}{dt} = K_1 B - K_+ A, \tag{5.29}$$

$$\frac{dB}{dt} = K_2 - K_3 BC, \tag{5.30}$$

$$\frac{dC}{dt} = K_+ A - K_4 CR, \tag{5.31}$$

$$\frac{dR}{dt} = K_5 - K_4 CR. \tag{5.32}$$

A can be written as the power series

$$A = a_0 + \frac{1}{K_+} a_1 + \frac{1}{(K_+)^2} a_2 + \ldots, \tag{5.33}$$

where a_0, a_1, ... are constants. Substitution of (5.33) into (5.29), and matching powers of K_+ gives $a_0 = 0$ and

$$a_i = (-1)^{(i-1)} K_1 \frac{d^{(i-1)} B}{dt^{(i-1)}}. \tag{5.34}$$

Substitution of A as a power series into (5.31) and disregarding A which is now defined in terms of B and its derivatives, the implicit-delay model becomes

$$\frac{dB}{dt} = K_2 - K_3 BC, \tag{5.35}$$

$$\frac{dC}{dt} = -K_4 CR + K_1 \left(\sum_{i=0}^{\infty} \left(\frac{(-1)}{K_+} \right)^i \frac{d^i B}{dt^i} \right), \tag{5.36}$$

$$\frac{dR}{dt} = K_5 - K_4 CR. \tag{5.37}$$

Noting that

$$\sum_{i=0}^{\infty} \left(\frac{(-1)}{K_+} \right)^i \frac{d^i B}{dt^i} = B \left(t - \frac{1}{K_+} \right), \tag{5.38}$$

this gives the explicit-delay model

$$\frac{dB}{dt} = K_2 - K_3 BC, \tag{5.39}$$

$$\frac{dC}{dt} = K_1 B \left(t - \tau \right) - K_4 CR, \tag{5.40}$$

$$\frac{dR}{dt} = K_5 - K_4 CR, \tag{5.41}$$

95

where $\tau = 1/K_+$ is a good approximation of the implicit-delay model under conditions where τ is much smaller than characteristic time-scales for changes in B. The differences, in the two models depends on the parameters of the system but are diminished if τ is reduced. It is interesting to point out though that because the discrepancy that lead to (5.40) depends on time derivatives of B, these two models exhibit the same steady states (whereby B is constant with time). It is not clear, however, what are the differences in the stability of this steady state. The stability of these steady states will be explored in the following sections. As shall be seen, these two models require significant delays in order to induce sustained oscillations, and therefore it can be seen that there are significant differences in the two models when focusing on the conditions for stability of their common steady states.

5.3.2 Stability analysis for the implicit-delay deactivator model

Model stability

The set of four ODEs constituting the implicit-delay model are,

$$\frac{dA}{dt} = K_1 B - K_+ A, \tag{5.42}$$

$$\frac{dB}{dt} = K_2 - K_3 B C, \tag{5.43}$$

$$\frac{dC}{dt} = K_+ A - K_4 C R, \tag{5.44}$$

$$\frac{dR}{dt} = K_5 - K_4 C R. \tag{5.45}$$

The steady state concentrations for this system are,

$$A_0 = \frac{K_5}{K_+}, \quad B_0 = \frac{K_5}{K_1}, \quad C_0 = \frac{K_1 K_2}{K_3 K_5}, \quad R_0 = \frac{K_3 K_5 K_5}{K_1 K_2 K_4}. \tag{5.46}$$

In Sections 5.2.2 and 5.2.4, the stability those simpler models could be easily analysed. However, this is not possible for the implicit-delay model (and also the explicit-delay model). Instead the analysis is significantly simplified by first non-dimensionalising the system of ODEs. The following dimensionless variables and parameters are defined,

$$\overline{A} = \frac{A}{A_0}, \quad \overline{B} = \frac{B}{B_0}, \quad \overline{C} = \frac{C}{C_0}, \quad \overline{R} = \frac{R}{R_0}, \quad \sigma = \frac{K_1 K_2}{K_5} t, \tag{5.47}$$

and,

$$\alpha = \frac{K_4}{K_3}, \quad \beta = \frac{K_+}{(K_1 K_2 K_3)^{1/3}}, \text{ and } \gamma = \frac{K_3 K_5^3}{(K_1 K_2)^2}, \tag{5.48}$$

where deviations from standard non-dimensionalisation has been included to simplify the analysis. The parameters α, β and γ measure the relative magnitudes of K_4, K_+ and K_5

respectively. The non-dimensionalised model becomes

$$\frac{d\overline{A}}{d\sigma} = \gamma^{1/3}\beta\left(\overline{B} - \overline{A}\right), \tag{5.49}$$

$$\frac{d\overline{B}}{d\sigma} = 1 - \overline{B}\,\overline{C}, \tag{5.50}$$

$$\frac{d\overline{C}}{d\sigma} = \gamma\left(\overline{A} - \overline{C}\,\overline{R}\right), \tag{5.51}$$

$$\frac{d\overline{R}}{d\sigma} = \alpha\left(1 - \overline{C}\,\overline{R}\right). \tag{5.52}$$

By linearising around the steady state $\overline{\mathbf{X}}_0 = (1,1,1,1)$, the eigenvalues λ for the Jacobian $\mathbf{J_F}(\overline{\mathbf{X}}_0)$ are determined by

$$|\mathbf{J_F}(\overline{\mathbf{X}}_0) - \lambda\mathbf{I}| = \begin{vmatrix} -\gamma^{1/3}\beta - \lambda & \gamma^{1/3}\beta & 0 & 0 \\ 0 & -1 - \lambda & -1 & 0 \\ \gamma & 0 & -\gamma - \lambda & -\gamma \\ 0 & 0 & -\alpha & -\alpha - \lambda \end{vmatrix} = 0, \tag{5.53}$$

which generates the auxiliary equation,

$$D(\lambda) = \lambda^4 + a\lambda^3 + b\lambda^2 + c\lambda + d = 0, \tag{5.54}$$

where,

$$a = \beta\gamma^{1/3} + \alpha + \gamma + 1, \tag{5.55}$$

$$b = (\alpha + \gamma + 1)\beta\gamma^{1/3} + \alpha + \gamma, \tag{5.56}$$

$$c = \beta\gamma^{1/3}\left(2\gamma + \alpha\right), \tag{5.57}$$

$$d = \beta\gamma^{4/3}\alpha. \tag{5.58}$$

The Routh-Hurwitz criteria for a fourth order polynomial of the form (5.54) with positive coefficients a-d states that $D(\lambda)$ will have roots which lie entirely in the left half plane - meaning the steady state $\overline{\mathbf{X}}_0$ is asymptotically stable - if and only if,

$$ab - c > 0, \quad \text{and } abc - a^2d - c^2 > 0. \tag{5.59}$$

It is clear by inspection that $ab > c$ and therefore the steady state $\overline{\mathbf{X}}_0$ is asymptotically stable if and only if $abc - a^2d - c^2 > 0$. Let $\Theta = \beta\gamma(\alpha^2 + 2\alpha\gamma + 2\gamma^2 + \alpha + 2\gamma) > 0$ and $\Phi = (abc - a^2d - c^2)/\Theta$. In the case, $\Phi < 0$ the steady state is asymptotically unstable and in the case $\Phi > 0$ the steady state $\overline{\mathbf{X}}_0$ is asymptotically stable. The manifold of the bifurcation defined explicitly by $\Phi = 0$ will be investigated. The important quantity Φ can be written as a quadratic in terms of β:

$$\Phi = \beta^2 + 2p\beta + q, \tag{5.60}$$

where

$$p(\alpha, \gamma) = \frac{2\gamma^3 + (3\alpha + 2)\gamma^2 + (2\alpha^2 + 3\alpha + 2)\gamma + \alpha^3 + 2\alpha^2 + \alpha}{2\gamma^{1/3}\left(\alpha^2 + 2\alpha\gamma + 2\gamma^2 + \alpha + 2\gamma\right)}, \quad \text{and} \tag{5.61}$$

$$q(\alpha, \gamma) = \frac{-\left(\alpha + \gamma + 1\right)\left((\alpha - 2)\gamma^2 + \alpha(\alpha - 2)\gamma - \alpha^2\right)}{\gamma^{2/3}\left(\alpha^2 + 2\alpha\gamma + 2\gamma^2 + \alpha + 2\gamma\right)}. \tag{5.62}$$

The bifurcation at $\Phi = 0$ can be written using β as the subject to give

$$\beta = \psi(\alpha, \gamma) = -p(\alpha, \gamma) + \sqrt{p(\alpha, \gamma)^2 - q(\alpha, \gamma)}. \tag{5.63}$$

The negative branch of the root of the quadratic (5.60) is not taken since it is clear from (5.61) that $p > 0$ and thus the negative branch is always negative (whereas β should be positive to obtain asymptotically unstable solutions). Furthermore, if $\psi(\alpha, \gamma)$ as defined by (5.63) is negative for some α and γ, then the steady state for these parameters is asymptotically stable irrespective of the value of β. Thus, (5.63) is defined to be only on the domain that coincides with $\psi(\alpha, \gamma) > 0$. This function shall be explored in the coming sections.

The domain of $\psi(\alpha, \gamma)$

The function ψ which defines the bifurcation points $\beta = \psi(\alpha, \gamma)$ is defined only where $q(\alpha, \gamma) < 0$. Noting that if $K_3 > 0$ and $K_4 > 0$, then $\alpha > 0$. Using (5.62), it is clear that $\alpha > 2$ is necessary for $\psi(\alpha, \gamma)$ to be positive.

Furthermore, if $\alpha > 2$, (5.62) indicates that for small γ, $q(\alpha, \gamma)$ is negative. When γ increases from 0 however, it is clear that $q(\alpha, \gamma)$ goes from positive to negative exactly once (due to the signs of the coefficients in the quadratic part of the numerator in (5.62)). Thus, there is some function $\gamma^*(\alpha)$ with $\alpha > 2$ such that $q = 0$ on $\gamma = \gamma^*(\alpha)$. This curve defines the boundary of the domain of $\psi(\alpha, \gamma)$. It can be found by identifying the positive zero (with respect to γ) of (5.62),

$$\gamma^*(\alpha) = \frac{\alpha}{2} \left(\sqrt{\frac{\alpha + 2}{\alpha - 2}} - 1 \right), \quad \text{for } \alpha > 2. \tag{5.64}$$

Note that $\gamma^* > 1$ for all $\alpha > 2$. The domain for $\psi(\alpha, \gamma)$ is therefore as follows: $\{(\alpha, \gamma) \in (2, \infty) \times (1, \infty) \ s.t. \ \gamma > \gamma^*(\alpha)\}$. On this domain, ψ is positive. It is also smooth because it consists of square roots and polynomial fractions with no cusps or singularities in the domain.

Inside this domain, if β is chosen such that $0 < \beta < \psi$, then sustained oscillations will be observed. However, if $\beta > \psi$, then the steady state of the system will be asymptotically stable. The steady state will be asymptotically stable irrespective of β if outside the domain of ψ.

Therefore, given that $\alpha > 2$ and $\gamma > \gamma^*$, then $K_4 > 2K_3$ and $K_5 > K_5^*$ are necessary conditions in order to have some chance of sustained oscillations where,

$$K_5^{*3} = \frac{K_1^2 K_2^2 K_4}{2K_3^2} \left(\sqrt{\frac{K_4 + 2K_3}{K_4 - 2K_3}} - 1 \right). \tag{5.65}$$

The lower bound on K_5^* means irrespective of the parameter K_+ or K_4, a receptor turnover rate of at least $K_5 = [(K_1 K_2)^2 / K_3]^{1/3}$ is required for sustained oscillations to occur.

Necessary conditions for an instability in the steady state is that $K_4 > 2K_3$ and $K_5 > K_5^*$. Within those parameters, $\psi(\alpha, \gamma)$ is positive and a sufficient condition for asymptotic instability is $0 < \beta < \psi(\alpha, \gamma)$. The functional form of $\psi(\alpha, \gamma)$ is given in (5.63) combined with (5.61) and (5.62). This functional form is not very attractive. In the next subsection, the focus will be on the qualitative and approximate characteristics of $\psi(\alpha, \gamma)$ which can be established.

The shape of $\psi(\alpha, \gamma)$

On the boundary $\gamma = \gamma^*(\alpha)$, $q = 0$ and therefore by (5.63), $\psi = 0$. As $\gamma \to \infty$, it can be seen from (5.61) and (5.62) that $p \sim \gamma^{2/3}/2 + \alpha\gamma^{-1/3} + O(\gamma^{-4/3})$ and $q \sim -\frac{\alpha-2}{2}\gamma^{1/3} + O(\gamma^{-2/3})$. Thus, from (5.63), $\psi \sim \frac{\alpha-2}{2}\gamma^{-1/3} + O(\gamma^{-4/3})$ and as such $\lim_{\gamma\to\infty} \psi(\alpha, \gamma) = 0$. When $\alpha \to \infty$ it gives $p \sim \gamma^{-1/3}\alpha/2 + \gamma^{-1/3}/2 + O(\alpha^{-1})$ and $q \sim -\alpha\gamma^{-2/3}(\gamma-1) + O(\alpha^0)$. Thus, $\psi \sim \gamma^{-1/3}(\gamma-1) + O(\alpha^{-1})$. That is, $\lim_{\alpha\to\infty} \psi(\alpha, \gamma) = \gamma^{-1/3}(\gamma-1)$, a constant with respect to α.

It is possible to prove that $\psi(\alpha, \gamma)$, for any α, on the interval $\gamma \in (\gamma^*, \infty)$, rises from zero at γ^* to a single local maximum and then falls monotonically to zero (asymptotically, as already found, as $\frac{\alpha-2}{2}\gamma^{1/3}$). The following arguments require substantial and careful bookkeeping. The key steps are outlined here, but the details are quite long and not put in print. Local extrema are found by solving

$$\partial\psi/\partial\gamma = 0, \tag{5.66}$$

noting that ψ is a smooth function that can be differentiated everywhere. With careful manipulation, this reduces to finding the zeros of an order 9 polynomial

$$\sum_{i=0}^{9} a_i\gamma^i = 0,$$

where the exact forms of a_i have been omitted here for brevity. It can be shown that

$$\{\text{sgn}(a_i)\}_{i=0}^{9} = \{1, 1, -1, -1, -1, -1, 1, 1, 1, 1\}.$$

The Descartes' rule of signs then states that there are at most two positive solutions to (5.66). Since $\psi(\alpha, \gamma^*(\alpha)) = \psi(\alpha, \infty) = 0$ and in between $\psi > 0$ it is not possible to have an even number of turning points on the interval $\gamma \in (\gamma^*, \infty)$. Thus there is exactly one and it must be a local maximum.

The consequences of the shape are as follows. For all $\alpha > 2$ there exists some minimum time delay $1/K_+^*$ ($1/\beta^*(\alpha)$ in dimensionless variables) below which sustained oscillations will not be possible and above which a single continuous interval/window $\gamma_-(\alpha, \beta) < \gamma < \gamma_+(\alpha, \beta)$ exists in which sustained oscillations will occur. This window monotonically grows in size as the time delay is increased (the rate β is decreased) above the minimum time delay. In practical terms, this means that if $\alpha > 2$ and β is sufficiently small, K_5 which describes the turnover of active receptor complex (and therefore linked to the Wnt signal strength) needs to lie within a single finite window of values such that the model generate sustained oscillations.

Bounds and approximations for $\psi(\alpha, \gamma)$

Figure 5.9 is a surface plot of the function $\beta = \psi(\alpha, \gamma)$ focusing near the boundary of the domain (small α and small γ). The region of parameter space which lies below the surface exhibits sustained oscillations in the model, otherwise the steady state is asymptotically stable.
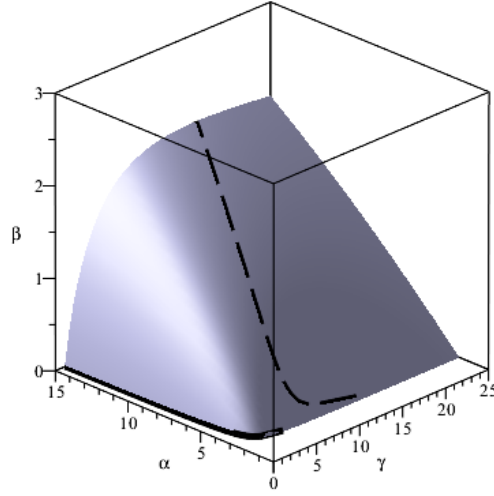
Figure 5.9: A surface plot of $\beta = \psi(\alpha, \gamma)$. The solid line indicates $\gamma^*(\alpha)$ and the dashed line indicates where $\partial\psi/\partial\gamma = 0$.

The full surface $\psi(\alpha, \gamma)$ given by (5.63) provides all of the information required to determine if the implicit model is going to exhibit sustained oscillations. However, (5.63) is not an aesthetically pleasing function. Here, (5.63) is used to report on bounds and approximations for the key characteristic functions (1) $\gamma_-(\alpha, \beta)$, (2) $\gamma_+(\alpha, \beta)$ and, (3) $\beta^*(\alpha)$.

As can be seen in Figure 5.9, ψ rather rapidly increases with respect to γ towards its maximum value before decaying at a much slower rate. It may suit the purposes of the reader to approximate $\gamma_-(\alpha, \beta) \approx \gamma^*(\alpha)$ for each β less than $\beta^*(\alpha)$. More complicated estimates may also be found from power series approximations of ψ but none of these offer a satisfyingly simple closed form.

It was already seen that $\psi \sim \frac{\alpha-2}{2}\gamma^{-1/3}$ as $\gamma \to \infty$. Furthermore, subtracting $\frac{\alpha-2}{2}\gamma^{-1/3}$ explicitly from the full analytic description of $\psi(\alpha, \gamma)$, it can be shown, using $\gamma > \gamma^*(\alpha)$ and $\alpha > 2$, that $\frac{\alpha-2}{2}\gamma^{-1/3} - \psi(\alpha, \gamma) < 0$. Thus, $\frac{\alpha-2}{2}\gamma^{-1/3}$ is not only an asymptotically good approximation for ψ at large values of γ, but it is also an upper bound for the function as a whole. Therefore, the approximation $\gamma_+(\alpha, \beta) = \left(\frac{\alpha-2}{2\beta}\right)^3$ is taken. Both of the approximations for γ_- and γ_+ are outer bounds for the interval (γ_-, γ_+). That is, the true window (γ_-, γ_+) lies entirely within the same window which is estimated using the approximations here.

A formal, but tractable and simple bound for the maximal delay rate (inverse of the minimum delay time) $\beta^*(\alpha)$ is challenging to find. Using dominant balance and heuristic arguments gives,

$$\beta^*(\alpha) \approx \frac{(\alpha-2)^{2/3}(4\alpha-3)}{10\alpha+2}, \tag{5.67}$$

which is a very close approximation to the maximal value of ψ along each line of constant α. The accuracy of this approximation is demonstrated in Figure 5.10 by plotting it alongside the true maximum which is calculated numerically. Indeed, this estimate converges to the true maximum as $\alpha \to \infty$ and suffers the greatest errors for α closer to 2.
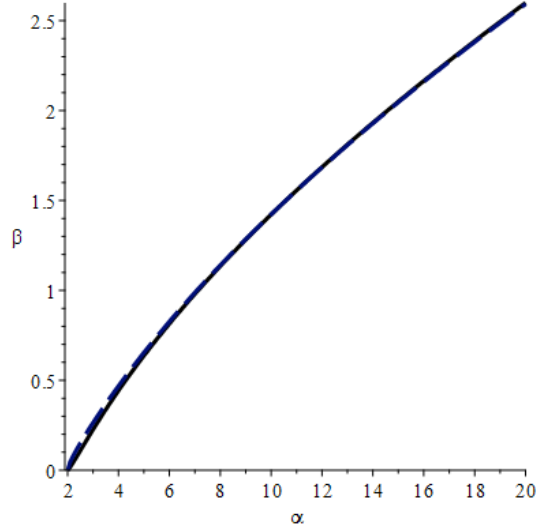
Figure 5.10: A plot of $\beta = \beta^*(\alpha)$, the maximal value of ψ with respect to γ along each line of constant α. The solid line is the true maximum calculated numerically from (5.63) and the dashed line is the approximation (5.67).

In Figure 5.11 a typical cross section of $\beta = \psi(\alpha, \gamma)$ is presented with α set to 8. On this curve, the aforementioned approximations for $\gamma = \gamma_-(\alpha, \beta)$, $\gamma = \gamma_+(\alpha, \beta)$ and $\beta = \beta * (\alpha)$ are plotted. The purpose here is to demonstrate the context of the bounds γ_- and γ_+, and to indicate the importance of β^* in limiting the region of the parameter space which is approximated by these bounds to the true region given by (5.63).
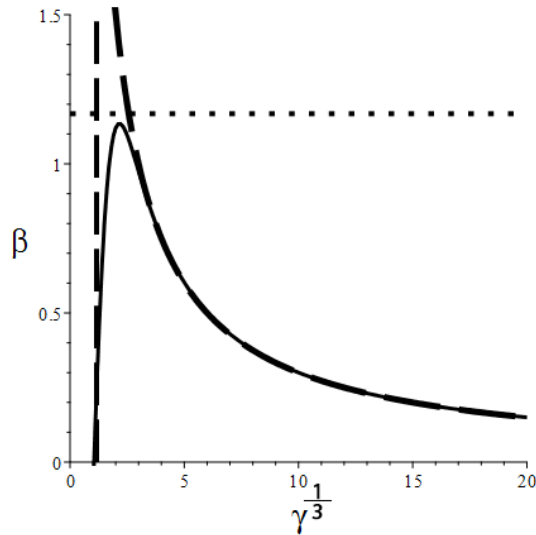

Figure 5.11: A sample plot of $\beta = \psi(\alpha, \gamma)$ for $\alpha = 8$ with γ^3 on the horizontal axis. The solid line is the true function found by plotting (5.63). The two dashed lines represent outer bounds (approximations) on the minimum and maximum values of γ which exhibit sustained oscillations (γ_- and γ_+). The dotted line represents the approximation of the maximum delay rate β^* for this value of α above which sustained oscillations are not possible (see (5.67))

The result of this analysis is as follows. Under the necessary condition $K_4 > 2K_3$, if

101

the delay K_+ satisfies

$$K_+ \lessgtr \left(\frac{K_1 K_2 (K4 - 2K_3)^2}{8K_3} \right)^{1/3} \frac{(4K_4 - 3K_3)}{5K_4 + 2K_3}, \tag{5.68}$$

then sustained oscillations will be observed in a single window of K_5 values contained within $\gamma_- < \gamma < \gamma_+$. This window is contained within the larger window,

$$\left[\frac{K_1^2 K_2^2 K_4}{2K_3^2} \left(\sqrt{\frac{K_4 + 2K_3}{K_4 - 2K_3}} - 1 \right) \right]^{1/3} < K_5 < \frac{K_1 K_2 (K_4 - 2K_3)}{2K_+ K_3}. \tag{5.69}$$

If the value of K_5 is not within its window of values or the necessary conditions are not met, the steady state for the system is asymptotically stable and Wnt signalling simply acts to increase the concentration of β-catenin.

Summary of key results

The analysis of the implicit-delay model indicated that the asymptotically stable steady state associated with static concentrations in a given regime, undergoes a bifurcation into the sustained oscillatory regime, when the inverse of the time delay in the feedback is below a critical value. This critical value depends on the other parameters of the system, and is given by $K_+ < (K_1 K_2 K_3)^{1/3} \psi_I(\alpha, \gamma)$, where $\alpha = K_4/K_3$, $\gamma = K_3 K_5^3/(K_1 K_2)^2$,

$$\psi_I(\alpha, \gamma) = -p(\alpha, \gamma) + \sqrt{p(\alpha, \gamma)^2 - q(\alpha, \gamma)}, \tag{5.70}$$

and

$$p(\alpha, \gamma) = \frac{2\gamma^3 + (3\alpha + 2)\gamma^2 + (2\alpha^2 + 3\alpha + 2)\gamma + \alpha^3 + 2\alpha^2 + \alpha}{2\gamma^{1/3} \left(\alpha^2 + 2\alpha\gamma + 2\gamma^2 + \alpha + 2\gamma \right)}, \quad \text{and} \tag{5.71}$$

$$q(\alpha, \gamma) = \frac{-(\alpha + \gamma + 1) \left((\alpha - 2)\gamma^2 + \alpha(\alpha - 2)\gamma - \alpha^2 \right)}{\gamma^{2/3} \left(\alpha^2 + 2\alpha\gamma + 2\gamma^2 + \alpha + 2\gamma \right)}. \tag{5.72}$$

As complicated/messy as this solution appears, some very interesting conclusions can be demonstrated from it.

1. There is always one and only one positive steady state for the system.

2. The steady state is always asymptotically stable if $K_4 < 2K_3$ (irrespective of the strength of the Wnt stimulus K_5 or the magnitude of negative feedback K_1).

3. The steady state is always asymptotically stable if $K_+ > K_+^*$ (that is, if the feedback delay is sufficiently short), where K_+^* is the maximum allowable K_+ value for asymptotic instability of the steady state. This maximum allowable K_+ is independent of the Wnt signal strength K_5. Whilst it is difficult to write down explicitly what this critical delay is, a good approximation can be found,

$$K_+^* \approx \left(\frac{K_1 K_2 (K_4 - 2K_3)^2}{8K_3} \right)^{1/3} \frac{(4K_4 - 3K_3)}{5K_4 + 2K_3}. \tag{5.73}$$

4. If $K_4 > 2K_3$ and $K_+ < K_+^*$, then there exists a single finite interval of Wnt signal strengths K_5 in which sustained oscillations will occur. That is, there exist a $K_{5\text{min}}$ and a $K_{5\text{max}} > K_{5\text{min}}$ such that sustained oscillations in the signalling pathway occur if and only if $K_{5\text{min}} < K_5 < K_{5\text{max}}$.

The first conclusion is not controversial but important. It can be interpreted as 'in the case of no sustained oscillations, a given Wnt stimulus will result in a uniquely defined static chemical steady state within the cell'. The steady state can also be trivially shown to increase β-catenin levels in response to a Wnt stimulus.

The second conclusion is somewhat profound. It is interpreted as 'cells for which destruction complex ubiquitination of β-catenin is more efficient comparatively than the deactivation efficacy of Wnt stimulation will not exhibit sustained oscillatory behaviour'. This might highlight new roles for Wnt receptor and co-receptor expression rates in the cells response to Wnt.

The third conclusion emphasizes the role of transcriptional delay in producing sustained oscillatory behaviour in Wnt signalling. Beyond that, it is difficult to assess the importance of (5.73) other than to point out that the delay must scale roughly with respect to the intrinsic time-scales of the β-catenin regulation cycle.

Finally, it is an interesting observation that if sustained oscillations can occur in Wnt signalling, this only occurs within a finite window of stimulus values K_5. Phenomenon that rely on Wnt signalling sustained oscillations therefore have to maintain a carefully robust signal strength downstream of the receptor.

5.3.3 Stability analysis for the explicit-delay deactivator model

Model stability

The explicit-delay model from Section 5.2.5 was shown to have at least one case in which the steady state system is asymptotically unstable, and can generate sustained oscillations. In this section, the exact conditions to determine when the steady state system changes its asymptotic stability will be analysed.

The set of three DDEs constituting the explicit-delay model are,

$$\frac{dB}{dt} = K_2 - K_3 BC, \tag{5.74}$$

$$\frac{dC}{dt} = K_1 B \left(t - \frac{1}{K_+} \right) - K_4 CR, \tag{5.75}$$

$$\frac{dR}{dt} = K_5 - K_4 CR. \tag{5.76}$$

As already explained in this chapter, the steady states of this system are the same as that of the implicit-delay model (with the exception of A),

$$B_0 = \frac{K_5}{K_1}, \quad C_0 = \frac{K_1 K_2}{K_3 K_5}, \quad R_0 = \frac{K_3 K_5 K_5}{K_1 K_2 K_4}. \tag{5.77}$$

The same dimensionless variables and parameters that were used in the analysis of the implicit-delay model will be used for the explicit-delay model. These are

$$\overline{B} = \frac{B}{B_0}, \quad \overline{C} = \frac{C}{C_0}, \quad \overline{R} = \frac{R}{R_0}, \quad \sigma = \frac{K_1 K_2}{K_5} t, \tag{5.78}$$

$$\alpha = \frac{K_4}{K_3}, \quad \beta = \frac{K_+}{(K_1 K_2 K_3)^{1/3}}, \quad \text{and} \quad \gamma = \frac{K_3 K_5^3}{(K_1 K_2)^2}. \tag{5.79}$$

Recall that parameters α, β, and γ measure the relative magnitudes of K_4, K_+ and K_5

respectively. The non-dimensionalised model becomes,

$$\frac{d\overline{B}}{d\sigma} = 1 - \overline{B}\,\overline{C}, \tag{5.80}$$

$$\frac{d\overline{C}}{d\sigma} = \gamma\left(\overline{B}\left(\sigma - \overline{\tau}\right) - \overline{C}\,\overline{R}\right), \tag{5.81}$$

$$\frac{d\overline{R}}{d\sigma} = \alpha\left(1 - \overline{C}\,\overline{R}\right), \tag{5.82}$$

where $\overline{\tau} = (\beta\gamma^{1/3})^{-1}$. By linearising around the steady state $\overline{\mathbf{X}}_0 = (1, 1, 1)$, and inspecting the ansatz $\overline{\mathbf{X}}(t) - \overline{\mathbf{X}}_0 = \left(\overline{\mathbf{X}}(0) - \overline{\mathbf{X}}_0\right)\exp(\lambda t)$, it is clear that if $\mathrm{Re}(\lambda) > 0$ and $\mathrm{Im}(\lambda) \neq 0$, the steady state is asymptotically unstable and sustained oscillations will be observed. To find where in parameter space a bifurcation occurs, an attempt is made to find $\mathrm{Re}(\lambda) = 0$, where λ is defined by substitution of the ansatz into the linearised dimensionless model. Specifically,

$$\begin{vmatrix} -1 - \lambda & -1 & 0 \\ \gamma e^{-\lambda\overline{\tau}} & -\gamma - \lambda & -\gamma \\ 0 & -\alpha & -\alpha - \lambda \end{vmatrix} = 0, \tag{5.83}$$

which gives the auxiliary equation,

$$D(\lambda, \overline{\tau}) = \lambda^3 + a\lambda^2 + (b_0 + b_1 e^{-\lambda\overline{\tau}})\lambda + c e^{-\lambda\overline{\tau}} = 0, \tag{5.84}$$

where,

$$a = \alpha + \gamma + 1, \tag{5.85}$$
$$b_0 = \alpha + \gamma, \tag{5.86}$$
$$b_1 = \gamma, \tag{5.87}$$
$$c = \gamma\alpha. \tag{5.88}$$

To investigate the bifurcation of the explicit-delay model from an asymptotically stable steady state into an unstable one, solutions to $\mathrm{Re}(\lambda) = 0$ need to be found. Substitution of $\lambda = \mu + i\nu$ into (5.84) so that the real and imaginary parts of λ are explicit gives,

$$\mathrm{Re}(D) = \mu^3 + a\mu^2 - a\nu^2 - 3\mu\nu^2 + b_0\mu + c e^{-\overline{\tau}\mu}\cos(\overline{\tau}\nu)$$
$$+ b_1 e^{-\overline{\tau}\mu}\left[\mu\cos(\overline{\tau}\nu) + \nu\sin(\overline{\tau}\nu)\right] = 0, \tag{5.89}$$

and,

$$\mathrm{Im}(D) = -\nu^3 + 3\mu^2\nu + 2a\mu\nu + b_0\nu - c e^{-\overline{\tau}\mu}\sin(\overline{\tau}\nu)$$
$$+ b_1 e^{-\overline{\tau}\mu}\left[\nu\cos(\overline{\tau}\nu) - \mu\sin(\overline{\tau}\nu)\right] = 0. \tag{5.90}$$

Note here that, being a solution to the real (5.84), solutions λ should come as complex conjugate pairs and so it is expected that the positive and negative values of ν satisfy (5.89) and (5.90). Setting $\mathrm{Re}(\lambda) = \mu = 0$, (5.89) and (5.90) are simplified to,

$$-a\nu^2 + c\cos(\overline{\tau}\nu) + \nu b_1\sin(\overline{\tau}\nu) = 0, \tag{5.91}$$
$$-\nu^3 + b_0\nu - c\sin(\overline{\tau}\nu) + \nu b_1\cos(\overline{\tau}\nu) = 0. \tag{5.92}$$

To solve these equations simultaneously, first eliminate $\bar{\tau}$ by squaring both sides, and then add the equations together to obtain,

$$\nu^6 + \nu^4(a^2 - 2b_0) + \nu^2(b_0^2 - b_1^2) - c^2 = 0. \tag{5.93}$$

In terms of the dimensionless parameters of the model α and γ, (5.93) is the following cubic equation in ν^2,

$$(\nu^2)^3 + ((\alpha + \gamma)^2 + 1)(\nu^2)^2 + \alpha(\alpha + 2\gamma)(\nu^2) - \gamma^2\alpha^2 = 0. \tag{5.94}$$

For any given $\alpha > 0$ and $\gamma > 0$, it is clear, since each coefficient in the cubic (5.94) is strictly positive except the last term which is strictly negative, that there is exactly one solution for which $\mu = 0$ and v^2 is real and positive, specifically $0 < \nu^2 < \gamma^2\alpha/(\alpha + 2\gamma)$. To obtain the value of $\bar{\tau}$ which coincides with a given α, γ, and $\nu(\alpha, \gamma)^2$ on the bifurcation described by $\mu = 0$, rearrange (5.91) and (5.92) into a matrix equation for $(\cos(\bar{\tau}), \sin(\bar{\tau}))$, then solve and rearrange for $\bar{\tau}$. It was found that

$$\bar{\tau} = \frac{1}{\nu} \arctan\left(\frac{b_0 c + (ab_1 - c)\nu^2}{-b_0 b_1 \nu + ac\nu + b_1\nu^3}\right). \tag{5.95}$$

This expression leads directly to an equivalent explicit-delay version of $\psi(\alpha, \gamma)$ defined in Section 5.3.2 for the implicit-delay model. Written in terms of β (rather than $\bar{\tau}$), α, and γ, then (5.95) becomes

$$\beta = \psi(\alpha, \gamma) = \nu\gamma^{-1/3} \left[\arctan\left(\frac{(\gamma + 1)\nu^2 + \alpha(\alpha + \gamma)}{\nu\left(\nu^2 + \alpha(\alpha + \gamma) - \gamma\right)}\right)\right]^{-1}, \tag{5.96}$$

where $\nu = \nu(\alpha, \beta)$ is given implicitly as the positive solution to (5.94). As already discussed, there is exactly one value of ν^2 for each $\alpha > 0$ and $\gamma > 0$. Both the negative and positive square root of ν^2 give the same value for $\psi(\alpha, \gamma)$, so the convention of only using the positive square root will be adhered to.

As previously for the implicit-delay model, the function $\psi(\alpha, \beta)$ is defined only on the domain in which its definition (5.96) is positive. It is on this domain only where there exists some β which may describe sustained oscillations in the model output.

The domain of $\psi(\alpha, \gamma)$

Based on (5.96), the function $\psi(\alpha, \gamma)$ is positive and therefore defined if $\alpha > 1$ (that is, if $K_4 > K_3$). This is because $\psi(\alpha, \gamma) > 0$ if $\nu^2 + \alpha^2 > (1 - \alpha)\gamma$ given that α and γ are both positive parameters. If $\alpha > 1$, then this statement becomes $\gamma > (\nu^2 + \alpha^2)/(1 - \alpha)$, which is automatically satisfied since the RHS of this inequality is negative whilst $\gamma > 0$. If $\alpha < 1$ then $\psi(\alpha, \gamma)$ is positive only if $\nu^2 > (1 - \alpha)\gamma - \alpha^2$. Therefore, if the LHS of (5.94) is negative when evaluated at $\nu^2 = (1 - \alpha)\gamma - \alpha^2$, then $\psi(\alpha, \gamma)$ is positive, otherwise it is negative. Substituting $\nu^2 = (1 - \alpha)\gamma - \alpha^2$ into (5.94) gives $\psi(\alpha, \gamma) > 0$, and therefore defined if (1) $\alpha > 1$ or (2),

$$H(\alpha, \gamma) = \alpha^4 + (3\gamma + 2)\alpha^3 + (3\gamma^2 + 3\gamma + 1)\alpha^2 + \gamma(\gamma^2 - 1)\alpha - \gamma^3 - \gamma^2 - \gamma > 0. \tag{5.97}$$

Equation (5.97) can be shown to be reducible to $\alpha > \alpha^*(\gamma)$, where α^* is a smooth function between 0 (evaluated at $\gamma = 0$), and 1 (which is approached asymptotically as $\gamma \to \infty$) for all $\gamma \in (0, \infty)$. The proof of this consists of using Descartes' sign rule to establish, for each $\gamma \in (0, \infty)$, the existence of at most one root of the quartic (5.97) for $\alpha > 0$, but zero roots for $\alpha > 1$. Together with the change of sign, this quartic is between $\alpha = 0$ and $\alpha = 1$. Smoothness is assured since H is a polynomial. Thus, (5.97) encapsulates the less strict condition $\alpha > 1$. The domain therefore is simply $\alpha > \alpha^*(\gamma)$ where $\alpha = \alpha^*(\gamma)$ is the solution to (5.97), which lies between 0 and 1.

The shape of $\psi(\alpha, \gamma)$

As $\gamma \to \infty$, it is possible to demonstrate that $\nu(\alpha, \gamma) \sim \sqrt{\alpha}$ by taking the dominant balance between the ν^4 term and ν^0 term in (5.94). Thus, $\psi(\alpha, \gamma) \sim \frac{\sqrt{\alpha}}{\gamma^{1/3}\arctan(\sqrt{\alpha}/(\alpha-1))}$ (which is also an upper bound) for $\alpha > 1$. In the case of $\alpha < 1$, it is trivial to see from the previous subsection that the function $\psi(\alpha, \gamma)$ does not exist in the limit $\gamma \to \infty$ (instead the domain of ψ is bounded above by the implicit curve $H(\alpha, \gamma) = 0$). However, because the boundary $\alpha = \alpha^*(\gamma)$ is generated by a change in the sign of ψ as defined by (5.96), if $\alpha^{*-1}(\alpha)$ is particularly large, $\psi(\alpha, \gamma) \approx -\frac{\sqrt{\alpha}}{\gamma^{1/3}\arctan(\sqrt{\alpha}/(\alpha-1))}$ as the boundary of $\gamma = \alpha^{*-1}(\alpha)$ is approached.

Summary of key results

This analysis indicated that the same set of generalised rules described for the implicit-delay model apply to the explicit-delay model. That being said, the solution for the bifurcation which separates the stable system from the oscillating one is not in the same position as that for the implicit-delay model where $\tau = 1/K_+$, despite having the same steady state under this assumption. As before, the sustained oscillatory regime occurs when the inverse of the time delay in the feedback is below a critical value which depends on the other parameters of the system $K_+ < (K_1K_2K_3)^{1/3}\psi_E(\alpha, \gamma)$, where $\alpha = K_4/K_3$, $\gamma = K_3K_5^3/(K_1K_2)^2$,

$$\psi_E(\alpha, \gamma) = \nu\gamma^{-1/3}\left[\arctan\left(\frac{(\gamma+1)\nu^2 + \alpha(\alpha+\gamma)}{\nu\left(\nu^2 + \alpha(\alpha+\gamma) - \gamma\right)}\right)\right]^{-1}, \qquad (5.98)$$

and $\nu = \nu(\alpha, \beta)$ is the implicit positive solution to the polynomial

$$(\nu^2)^3 + ((\alpha+\gamma)^2 + 1)(\nu^2)^2 + \alpha(\alpha+2\gamma)(\nu^2) - \gamma^2\alpha^2 = 0. \qquad (5.99)$$

Once again, this solution seems rather complex but rigorous conclusions can be made from it. The conclusions for the implicit-delay model are similar to that of the explicit-delay model.

1. The steady state for the explicit-delay model is uniquely defined and is the same as the implicit-delay model (except without the component A).

2. The steady state is always asymptotically stable if $H < 0$, where

$$H = \alpha^4 + (3\gamma + 2)\alpha^3 + (3\gamma^2 + 3\gamma + 1)\alpha^2 + \gamma(\gamma^2 - 1)\alpha - \gamma^3 - \gamma^2 - \gamma. \quad (5.100)$$

3. If the steady state of the implicit-delay model is asymptotically unstable, then so is the explicit-delay model. That is, the region of instability in parameter space for the explicit-delay model completely contains the region of instability for the implicit-delay model.

Whilst the first of these conclusions is important (to ensure that the two models are comparable), it is relatively uninteresting.

The second condition is substantially more complex than the analogous conclusion that was made about the implicit-delay model (that the system requires $K_4 > 2K_3$ for sustained oscillations). However, the message is similar. The bifurcation defined implicitly by $H = 0$ begins at $\gamma = 0$ and $\alpha = 0$, but as α increases, γ increases and asymptotes

rapidly towards $\alpha = 1$. Thus, this condition is really saying that if K_5 is 'not small', then one requires $K_4 \gtrsim K_3$ for sustained oscillations to occur, that is, an inefficient Axin deactivation mechanism will ensure that sustained oscillations will not be generated in the signalling pathway.

The final conclusion is interesting since it demonstrates that a fixed time delay feedback in this context always expands the region of instability and sustained oscillations are always more easily generated in the system as a result. This begs the more mathematical question regarding under what conditions on the network structure (for which Wnt signalling is just one example) does a region of instability stay contained and reduce in size if a delay is changed from being an explicit fixed delay to an exponentially distributed time delay? This question is left unanswered for a more mathematical investigation.

5.3.4 Comparison of the implicit- and explicit-delay deactivator models

Numerical simulations and heat maps

Whilst conclusions were compared about the stability analysis of the implicit- and explicit-delay models, a full analysis of the non-linear problem after the onset of the instability is intractable. For this reason, simulations are run similar to those in Figures 5.5 and 5.8, in which the differences in the amplitude and the period between the two models over a wide range of parameters K_+ and K_5 (fixing the other parameters) are compared. It is noted that the shape of the domain for sustained oscillations with respect to these two parameters has been shown to be similar irrespective of the other parameters. Therefore the data is presented with a focus only on K_+ (the feedback delay rate) and K_5 (the magnitude of the Wnt stimulus).

This result is plotted in Figure 5.12 using a heat map where blue denotes a small amplitude and period, and the colour progresses to red representing a high change in amplitude and period. These heat maps are overlapped with the analytical curves in (5.70) and (5.98). In comparing these models, the simulations support the claims that the explicit-delay model has a larger region in parameter space which generate sustained oscillations, but also that the period and amplitude are larger in the sustained oscillatory regime. Unsurprisingly, the oscillation amplitude gets bigger as the Wnt stimulus K_5 is stronger. However, the period of the oscillations have a curious, difficult to explain, distribution in the parameter space.
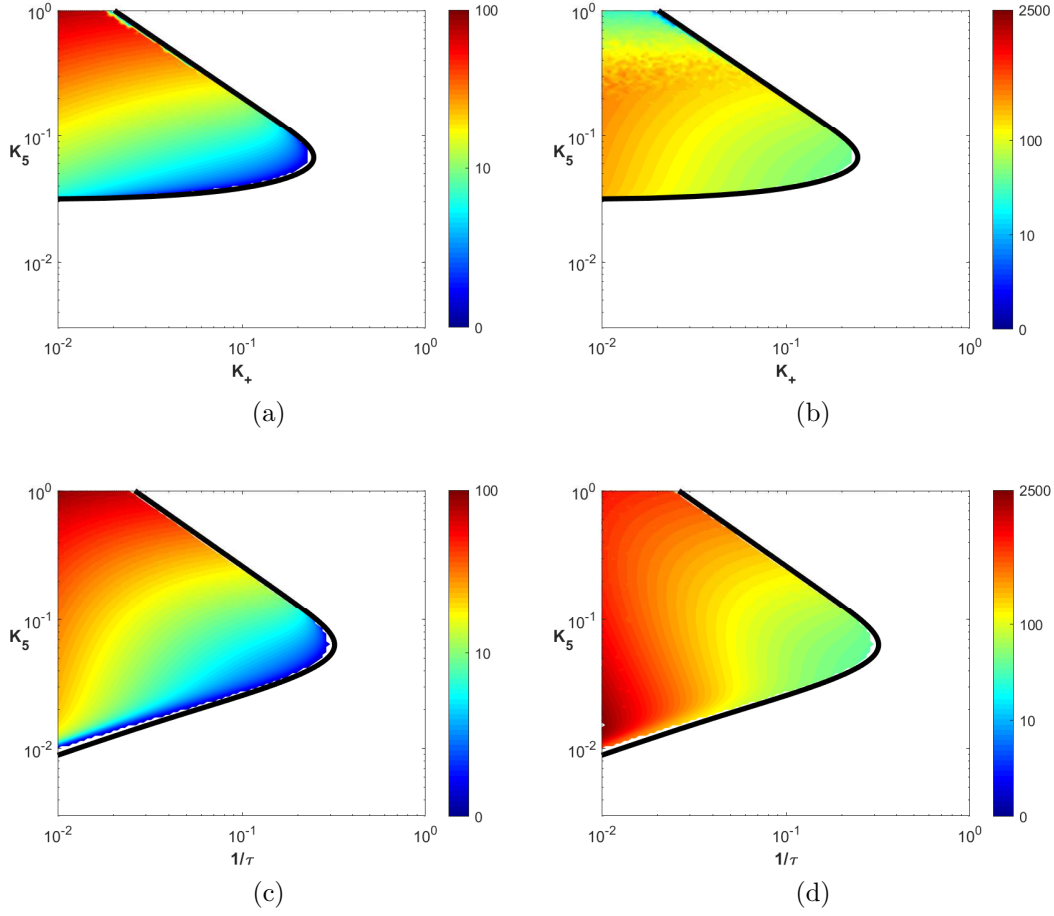
Figure 5.12: Heat map for the implicit-delay model amplitudes (a), periods (b), the explicit-delay model amplitudes (c), and periods (d). The heat maps demonstrate how the size of the amplitude, and the length of the periods between oscillations in β-catenin differ across the parameter space. For the implicit- and explicit-delay models, 10,000 simulations are computed using 100 logarithmically-spaced $K_5 \in (0.001, 1)$, and 100 logarithmically-spaced $K_+ \in (0.01, 1)$ ($\tau = 1/K_+$). The other parameters are held constant as $K_1 = 0.012$ min^{-1}, $K_2 = 0.423$ nM min^{-1}, $K_3 = 1$ nM^{-1} min^{-1}, and $K_4 = 10$ nM^{-1} min^{-1}. Each simulation begins near steady state, and is run up to 10,000 minutes. For each plot, the analytical curves from (5.70) and (5.98) for the implicit (a, b) and the explicit (c, d) models respectively are overlapped. Low values in the heat map for both amplitude and period are coloured blue, whilst high values are coloured red.

A comparison of the analytic derivations of the bifurcations (5.70) and (5.98) is presented in Figure 5.13, which separates the stable regime from the unstable oscillating one using the same parameter sets that were used to generate Figure 5.12. From this plot, it can be seen that there is always an upper and lower bound for K_5 in which sustained oscillations are induced (given the system is in the unstable region). This plot demonstrates that the region of instability for the implicit-delay model is a subset of the region for the explicit-delay model.
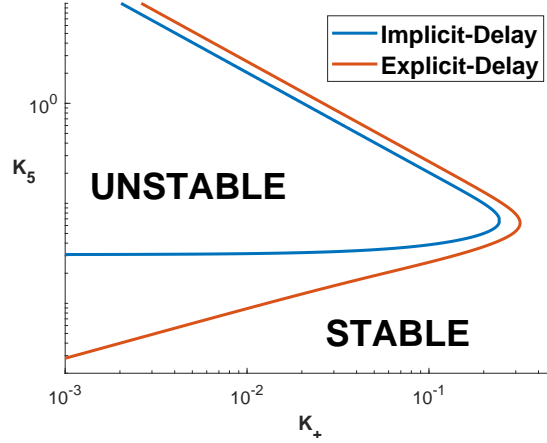
Figure 5.13: Plot of the analytical regions separating the boundary of stability for both the implicit- and explicit-delay models. The rate parameters, $K_1 = 0.012$ min^{-1}, $K_2 = 0.423$ nM min^{-1}, $K_3 = 1$ nM^{-1} min^{-1}, and $K_4 = 10$ nM^{-1} min^{-1} are held constant. Inside the unstable region, sustained oscillations are induced. Outside of this region is when the steady state is asymptotically stable.

Proof that the domain of instability for the implicit-delay model is a subset of the domain of instability for the explicit-delay model

Figure 5.13 suggests that the parameter set region for which sustained oscillations occur in the implicit-delay model is a subset of the domain for the explicit-delay model. Although this appears true for the parameter set chosen, it will be proved in this section that this is always the case regardless of the choice of other parameters.

In this section, the claim that $\psi_E - \psi_I > 0$ will be proved, where ψ_E is defined for the explicit-delay function in (5.96), and ψ_I is defined for the implicit-delay function in (5.63). Both functions are defined in their domain of instability. For this proof, $\alpha > 2$ and $\gamma > 1$ are used, as both ψ_E and ψ_I are positive for these values. $\psi_E(\alpha, \gamma) > \psi_I(\alpha, \gamma)$ can be written as,

$$\gamma^{2/3} \left[\psi_E(\psi_E + 2p) + q\right] > \gamma^{2/3} \left[\psi_E(\psi_I + 2p) + q\right] = 0, \tag{5.101}$$

where p and q are from (5.61) and (5.62), and the right hand side is equal to zero by substitution of (5.63). It is sufficient to show that if the left hand side of (5.101) is greater than zero, then $\psi_E(\alpha, \gamma) > \psi_I(\alpha, \gamma)$.

From (5.96), and using the fact $\arctan(x) < x$ for $x > 0$, gives,

$$\gamma^{2/3} \left[\psi_E(\psi_E + 2p) + q\right] > r(\alpha, \gamma, z)(r(\alpha, \gamma, z) + 2\gamma^{1/3}p) + q\gamma^{2/3}, \tag{5.102}$$

where,

$$r(\alpha, \gamma, z) = \frac{z(z + \alpha(\alpha + \gamma) - \gamma)}{(\gamma + 1)z + \alpha(\alpha + \gamma)}, \tag{5.103}$$

and $z = z(\alpha, \gamma) = v^2(\alpha, \gamma)$ is the solution to,

$$z^3 + ((\alpha + \gamma)^2 + 1)z^2 + \alpha(\alpha + 2\gamma)z - \alpha^2\gamma^2 = 0, \tag{5.104}$$

with the restriction $z > 0$ (which forces v to be a real number). Substitution of the analytic forms of r, p, and q into the right hand side of (5.102) and factorising it gives the following form,

$$\gamma^{2/3} \left[\psi_E(\psi_E + 2p) + q\right] > \Phi_1(\alpha, \gamma, z)\Phi_2(\alpha, \gamma, z), \tag{5.105}$$

where Φ_1 is large, but filled with strictly positive terms in sum and quotient relationships resulting in $\Phi_1 > 0$. On the other hand,

$$z\Phi_2(\alpha, \gamma, z) = z^3 + ((\alpha + \gamma)^2 + 1 - \gamma)z^2 + (2\gamma^2 - \gamma(\gamma - 2)\alpha - (\gamma - 1)\alpha^2)z. \quad (5.106)$$

Subtracting (5.104) from (5.106) simplifies this down to,

$$z\Phi_2(\alpha, \gamma, z) = -\gamma z^2 - \gamma((\alpha - 2)\gamma + \alpha^2)z + \gamma^2\alpha^2. \quad (5.107)$$

Since $\gamma > 1$ and $\alpha > 2$ in the domain of ψ_I, there exists a $z*$ such that for all α and γ in the domain of ψ_I, then

$$\Phi_2(\alpha, \gamma, z) > 0, \quad \text{iff } z < z*, \quad (5.108)$$
$$\Phi_2(\alpha, \gamma, z) < 0, \quad \text{iff } z > z*, \quad (5.109)$$

where $z*$ is the positive zero of (5.107). However from (5.104), it is known that $z < \alpha\gamma/(\sqrt{(\alpha + \gamma)^2 + 1})$. Substitution of z equal to this into $((\alpha + \gamma)^2 + 1)^{3/2}z\Phi_2(\alpha, \gamma, z)$ gives,

$$((\alpha + \gamma)^2 + 1)^{3/2}z\Phi_2 = \sqrt{(\alpha + \gamma)^2 + 1}\gamma\left[\gamma\alpha^2((\alpha + \gamma)^2 - \gamma + 1)\right]$$
$$- \gamma^2\alpha((\alpha - 2)\gamma + \alpha^2)((\alpha + \gamma)^2 + 1). \quad (5.110)$$

Since $\sqrt{(\alpha + \gamma)^2 + 1} > (\alpha + \gamma)$,

$$((\alpha + \gamma)^2 + 1)^{3/2}z\Phi_2 > \gamma^2\alpha\left[2\gamma((\alpha + \gamma)^2 + 1)\alpha\gamma(\alpha + \gamma)\right] > 0, \quad (5.111)$$

for $\alpha > 2$ and $\gamma > 1$. Therefore $\Phi_2 > 0$ which means by (5.108) that,

$$z < \frac{\alpha\gamma}{\sqrt{(\alpha + \gamma)^2 + 1}} < z*, \quad (5.112)$$

or that $\Phi_2(\alpha, \gamma, z) > 0$ for all α and γ in the domain of ψ_I.

Since $\Phi_1 > 0$ and $\Phi_2 > 0$ for all α and γ in the domain of ψ_I, then (5.105) gives,

$$\gamma^{2/3}\left[\psi_E(\psi_E + 2p) + q\right] > 0, \quad (5.113)$$

and therefore, $\psi_E > \psi_I$ within the domain for instability.

5.4 Conclusion

In this chapter, a number of simple models of Wnt signalling were investigated, which contain only the key structures and dynamics postulated in the literature. The rationale for simplifying these models was so dominant biochemical processes can be rigorously analysed, and a deep understanding for how these processes are related could be attained. The chapter focused on what determines if a cell processes a Wnt signal through the canonical pathway by increasing cytosolic β-catenin to a static equilibrium, or if it will drive temporal oscillations in the pathway components. The mechanism for oscillations makes use of the upregulation of Axin2 as a target of β-catenin-dependent transcription - a negative feedback for the Wnt signalling pathway.

The first investigation primarily asked the question 'does the destruction complex inhibitory mechanism of Wnt influence the conditions required for sustained oscillations

in the pathway?'. This question is inspired by the uncertainty with how Wnt receptor complex interacts with the destruction complex. Does the mechanism of interaction even matter from the perspective of Wnt targets? From the perspective of attaining possible sustained oscillatory behaviour in the pathway, this question is very important. It has been shown that introducing heuristic and non-linear kinetics can induce sustained oscillations in the case where the Wnt receptor complex dissociates the destruction complex. It was proved that with a simple model, the mechanism is not capable of producing sustained oscillations. This is opposed to a model whereby the Wnt receptor complex deactivates destruction complex (by removing/sequestering it as active altogether), where sustained oscillations are much more easily generated.

The second investigation focuses on the nature of the delay in the feedback. Since Axin2 is fed back into the system by means of transcription, translation and then complex formation (into active destruction complex), there is a significant delay associated with this feedback. It is not clear what should characterise this delay, whether it is an exponentially distributed delay (dominated by the wait time required for proteins to form a complex in the cytoplasm) or if the delay is a fixed time (more likely associated with the transcription and translation machinery). The changes of each of these descriptions of the delay (a four-species ODE system or an equivalent three-species DDE system respectively) have on the conditions required for sustained oscillatory behaviour were investigated. These models are called the 'implicit-delay' model and the 'explicit-delay' model respectively. In both of these models, Wnt receptor complex deactivates the destruction complex (since no sustained oscillations are possible if it simply dissociates it). For each of these models, analytic solutions were found for the bifurcation of asymptotically stable Wnt signalling into the sustained oscillatory regime. These analytical solutions gave a number of insights into just how these sustained oscillations are generated. The main conclusions are as follows;

- Irrespective of other properties of the system, the Wnt complex must deactivate the destruction complex at a sufficiently fast rate compared to the ubiquitination/-turnover rate of β-catenin by active destruction complex in order for sustained oscillations to occur. For the implicit-delay model, the rate had to be at least twice as fast. For the explicit-delay model, it just had to be faster.

- A delay in the negative feedback loop is essential. For any possible set of parameters, a minimum time delay exists, below which no sustained oscillations can be generated. This is true for both implicit- and explicit-delay models, although the minimum time delay is always lower in the explicit-delay model.

- If sustained oscillations can be driven in the system, then there is always one, and only one, finite window of Wnt stimulus levels which will drive sustained oscillations in the system. That is, if the Wnt stimulus is either too low or too high, no sustained oscillations will occur.

- It was proved that irrespective of the choice of parameters, if sustained oscillations were generated in the implicit-delay model, sustained oscillations were guaranteed in the explicit-delay model (but not the other way around). Whilst it is unclear what is the specific mathematical quality of the Wnt signalling pathway that leads to this property, it does hint that fixed time delays (that may be associated with transcript-based feedback in biochemical systems, for example) have the potential to increase the possibility for sustained oscillations in sub-cellular systems and thus provide a mechanism for encoding information in cells.

Chapter 6

Stochastic oscillations in the Wnt/β-catenin signalling pathway

6.1   Introduction

In this chapter, the role of stochasticity in driving oscillations in regions where they otherwise would normally not occur will be investigated. The Tymchyshyn and Kwiatkowska paper [72] reviewed in Section 2.3.4 suggested that stochasticity can drive oscillations outside the equivalent parameter space required to drive them in a deterministic model. In Chapter 5 it was shown which parameters will induce sustained oscillations deterministically. In this chapter, stochasticity is investigated in the following two ways:

1. Chemical reactions are simulated stochastically using the Gillespie SSA,

2. Diffusion is introduced to investigate how spatio-temporal noise affects oscillations, and the associated reaction-diffusion system is simulated using the Smoldyn algorithm.

Method 1 focuses on any change in behaviour due to the introduction of noise associated with discrete copy numbers in the chemical system. Each simulation using the Gillespie SSA is assumed to be well-mixed so that no spatio-temporal element to the noise in the system is considered. The Gillespie SSA for reaction processes provides an excellent initial exploration into how stochasticity drives oscillations.

Method 2 explores how the introduction of a spatial component (in the form of diffusion) further modifies the model behaviour when compared to the well-mixed system of method 1. This method highlights the differences between meso- and micro-scale simulations, specifically for the implicit-delay model from Chapter 5.

A comment on the choice of simulation volume

The stochastic simulations of the Wnt signalling pathway in Chapter 4 utilised the cell volume of Xenopus oocytes (see Section 4.5.4 for the full details of this model). Xenopus oocytes have a typical cell diameter of 1 mm which translates to an approximate cell volume of 4.2×10^{-9} m^3 [121]. As stated in Section 4.5.4, a cell volume of this size would result in simulating over 100 billion molecules, which would be quite computationally intensive to simulate. Hence, a cubic sub-volume 1 million times smaller than the cell volume ($V = 4.2 \times 10^{-15}$ m^3) was used to overcome this problem.

As this chapter focuses on exploring numerical simulations into stochastic models of the Wnt signalling pathway rather than investigating experimental models of Wnt, the

choice of volume to simulate Wnt accurately is not as important as it was in Chapter 4. For this reason, the simulations start with a volume of $V = 10^{-16}$ m^3, which is smaller than what was used in Chapter 4. It will be shown throughout this chapter that the choice of volume for stochastic models of Wnt will significantly affect the simulation outputs.

6.2 Initial investigation into stochastically driven oscillations

Stochasticity is introduced to the implicit-delay deactivator model developed in Chapter 5. Recalling that the model is the system of ODEs,

$$\frac{dA}{dt} = K_1 B - K_+ A, \tag{6.1}$$

$$\frac{dB}{dt} = K_2 - K_3 BC, \tag{6.2}$$

$$\frac{dC}{dt} = K_+ A - K_4 CR, \tag{6.3}$$

$$\frac{dR}{dt} = K_5 - K_4 CR, \tag{6.4}$$

where A represents Axin, B represents β-catenin, C represents active destruction complex, and R represents the receptor complex. The steady states of (6.1) to (6.4) are,

$$A_0 = \frac{K_5}{K_+}, \quad B_0 = \frac{K_5}{K_1}, \quad C_0 = \frac{K_1 K_2}{K_3 K_5}, \quad R_0 = \frac{K_3 K_5 K_5}{K_1 K_2 K_4}. \tag{6.5}$$

To stochastically simulate the implicit-delay model, the concentrations A, B, C, and R are converted to copy numbers by multiplying each species concentration by the system volume V.

In this chapter, each simulation will start at the steady state of (6.1) to (6.4) rounded to the nearest integer copy number (after the concentration of each species is multiplied by the system volume). Each species starts in a well-mixed distribution (this statement holds for the entire time for the Gillespie simulations).

6.2.1 Gillespie algorithm - Reaction processes

Throughout this chapter, well-mixed reactions are simulated using the Gillespie algorithm defined in Section 3.4.1. The Gillespie algorithms were implemented using custom code in MATLAB.

Using the Gillespie algorithm, two simulations of the implicit-delay model were computed and the results presented in Figure 6.1 alongside the deterministic solutions. The rate parameters used in both simulations were $K_1 = 0.012$ min^{-1}, $K_2 = 0.423$ nM min^{-1}, $K_3 = 1$ nM^{-1} min^{-1}, $K_4 = 10$ nM^{-1} min^{-1}, $K_+ = 0.1$ min^{-1}, and the system volume was set to $V = 10^{-16}$ m^3. The first simulation (Figure 6.1a) uses $K_5 = 0.18$ nM min^{-1} (high Wnt stimulus), whilst the second simulation (Figure 6.1b) uses $K_5 = 0.018$ nM min^{-1} (low Wnt stimulus).

The stochastic simulation (blue curve) in the high Wnt case (see Figure 6.1a) matches well with the deterministic solution (red curve). The β-catenin solutions match closely, whilst the destruction complex simulations have a similar period, but varying amplitude.

It is initially evident that a Gillespie simulation under high Wnt conditions closely matches the deterministic model.

However, the stochastic simulation for the low Wnt case (see Figure 6.1b) shows various peaks and oscillations when the deterministic solution remains at steady state. These simulations certainly validates the claim in Tymchyshyn *et al.* for the implicit-delay model, that the Wnt/β-catenin pathway can exhibit periodic spiking when the Wnt stimulus is low [72].
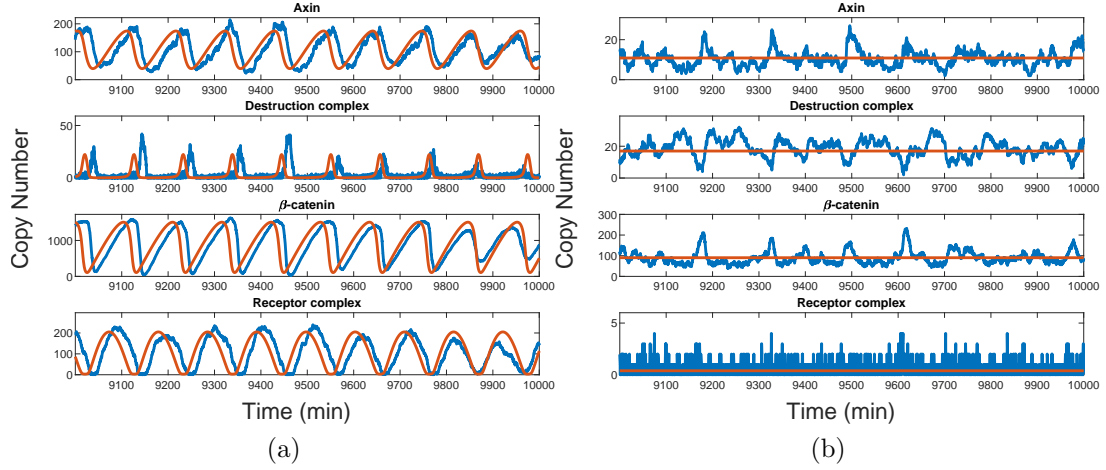

(a)   (b)

Figure 6.1: A comparison of stochastic simulations (blue curves) plotted against the deterministic solutions (red curves) for the implicit-delay model in the presence of (a) high Wnt stimulus, and (b) low Wnt stimulus. For the stochastic simulations, the Gillespie algorithm is used with rate parameters $K_1 = 0.012$ min^{-1}, $K_2 = 0.423$ nM min^{-1}, $K_3 = 1$ nM^{-1} min^{-1}, $K_4 = 10$ nM^{-1} min^{-1}, $K_+ = 0.1$ min^{-1}, and the system volume was set to $V = 10^{-16}$ m^3. The high Wnt case (a) is run with $K_5 = 0.18$ nM min^{-1}, whilst the low Wnt case (b) is run with $K_5 = 0.018$ nM min^{-1}, a 10-fold decrease in the amount of incoming active receptor complex. Simulations are run until $t = 10,000$ minutes, and only the last $1,000$ minutes are plotted.

6.2.2 Smoldyn algorithm - Reaction-diffusion processes

To determine how the introduction of diffusion into the system alters the stochastic behaviour of the model, the Smoldyn algorithm is used. The simulations throughout this chapter which utilise the Smoldyn algorithm are written with custom MATLAB code. To use the Smoldyn algorithm, the first step is to define the diffusion constant D for all four chemical species, and then to define the system boundaries. Simulations in this section use $D = 10^{-12}$ m^2 /s for all four chemical species (a typical diffusion constant for proteins), a volume of $V = 10^{-16}$ m^3, a fixed time-step of $\Delta t = 10^{-4}$ minutes, and the system is scaled such that the domain is a cube of unit length with periodic boundary conditions. These were chosen so that boundary effects do not interfere with model outputs.

Similar to Figure 6.1, two simulations are computed, the first in which K_5 is high, and the second for which it is low. These simulations are plotted against their deterministic counterpart (that is (6.1) to (6.4)) in Figure 6.2. The parameters in this figure are exactly the same as Figure 6.1 with the addition of diffusion. Figure 6.2 demonstrates that periodic spiking occurs under a low Wnt stimulus when using a Smoldyn algorithm. The actual effect of spatial-associated noise is explored in Section 6.4.
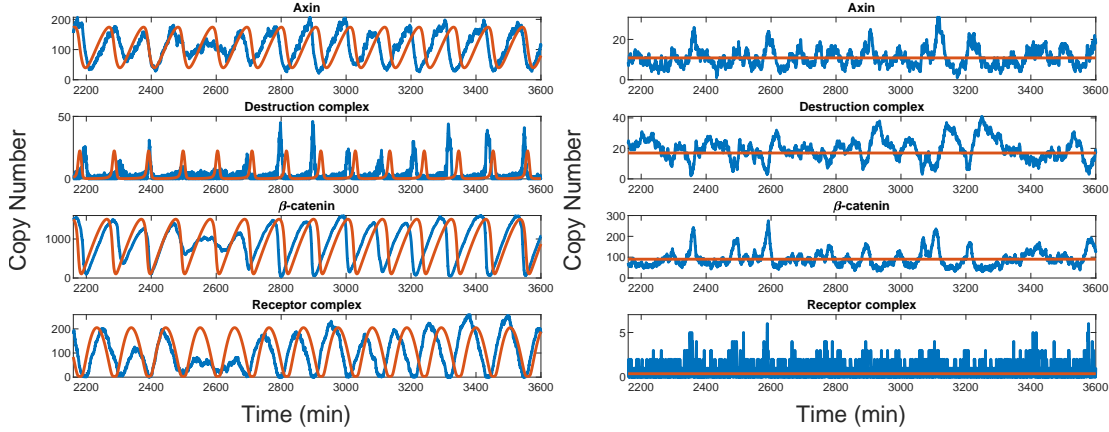
Figure 6.2: Smoldyn plots for (a) high Wnt ($K_5 = 0.18$ nM min^{-1}), and (b) low Wnt ($K_5 = 0.018$ nM min^{-1}). The deterministic solutions are plotted in red, whilst the stochastic simulations are plotted in blue. All simulations use rate parameters $K_1 = 0.012$ min^{-1}, $K_2 = 0.423$ nM min^{-1}, $K_3 = 1$ nM^{-1} min^{-1}, $K_4 = 10$ nM^{-1} min^{-1}, $K_+ = 0.1$ min^{-1}, a volume $V = 10^{-16}$ m^3, time-step $\Delta t = 10^{-4}$ min, and diffusion constant $D = 10^{-12}$ m^2 /s. Similar to the Gillespie plots in Figure 6.1, the Smoldyn simulation for the high Wnt case appears similar to the deterministic solution, and the Smoldyn simulation for the low Wnt case oscillates when the deterministic solution does not.

These initial simulations show that both the Gillespie SSA for chemical reactions, and the Smoldyn algorithm for reaction-diffusion processes can drive oscillations stochastically in a region of parameter space larger than that associated with the model in the absence of noise. Further investigation into these methods is the focus of Sections 6.3 and 6.4.

6.3 The stochastic oscillation parameter regime

6.3.1 The stochastic implicit-delay deactivator model

Results in Section 6.2 confirmed that oscillatory behaviour can occur outside of the oscillatory parameter region defined in Section 5.3.4. A natural question to ask is, how far do stochastic effects extend this region?

To answer this question, a computation is run similar to that presented for the deterministic models in Figure 5.12, where the amplitude and period of oscillations in the stochastic models are computed over a large range of values for K_5 and K_+. However, to create this heat map, a definition of what constitutes 'oscillations' in a noisy time series is required.

Unlike the heat map for the deterministic solutions in Figure 5.12, it is not so straight forward to determine if an oscillation actually occurs under stochastic conditions. The stochastic simulation will never remain at steady state, as there will always be a small amount of noise. Therefore, to determine that an oscillation has occurred, the following criteria must be satisfied (represented visually in Figure 6.3). First, simulations are run up until $t = 10{,}000$ minutes, to ensure the solution is far enough away from any initial transient effects. For this reason also, oscillations are only checked in the second half of the simulation ($t > 5000$ minutes). This domain is then divided into 10 compartments of equal length. The maximum and minimum β-catenin values are recorded for each compartment. These maximums and minimums are then averaged together. An oscillation occurs when

either the average maximum value is 1.3 times greater than the stochastic steady state, or the average minimum value is 0.7 times the steady state. These values were chosen as they are far enough away from steady state such that it can be considered as an oscillation as opposed to noise. The amplitude of the oscillation is then the difference between the average minimum and maximum values.
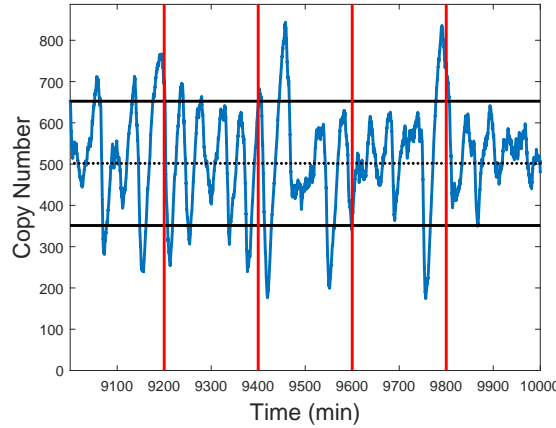

Figure 6.3: Visualisation of the conditions to determine if an oscillation occurs, and what the amplitude of the oscillations are. The evolution of β-catenin in a single sample simulation is shown. The dotted black line represents the steady state of β-catenin under deterministic conditions. The two black lines represent values of 1.3 and 0.7 times the steady state. The domain to check for oscillations is divided up into compartments (in this case 5 compartments). The maximum values are recorded for each compartment, and then the average of these maximums is taken. The same is done for the minimum values. If the average maximum value is more than 1.3 times greater than the steady state value, or if the average minimum value is less than 0.7 times the steady state, then an oscillation is said to occur. The size of the amplitude is then half the difference between the average maximum and average minimum values.

The period of these oscillations is calculated differently to Section 5.3.4 due to the fact that the time between peaks can no longer be used to measure the period as the noise introduces far too many local peaks. Instead, a Fast Fourier Transform is applied to the results, and the dominant frequency is extracted from this. The 'period' is then defined as the inverse of this dominant frequency. A visual description of this is presented in Figure 6.4.
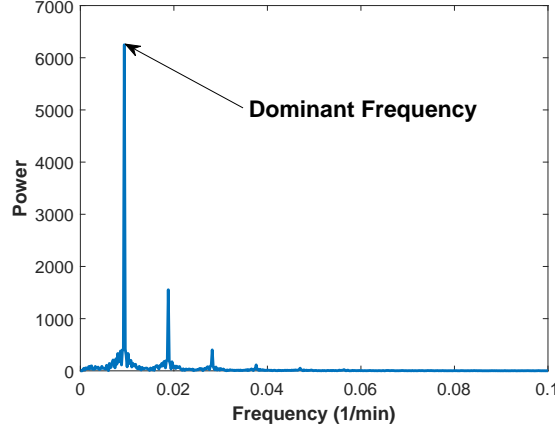
Figure 6.4: An example frequency plot to demonstrate how the period of stochastic oscillations is determined. The frequency spectrum for one simulation is plotted. The dominant frequency in this example occurs at 0.0094 min^{-1}, resulting in a period of 106 minutes.

Similar to the heat maps in Figure 5.12, the simulations in this section are computed over the parameter ranges $0.01 \leqslant K_5 \leqslant 1$, and $0.01 \leqslant K_+ \leqslant 100$, where K_+ is calculated up to 100, as opposed to 1 in the deterministic models. The other four rate parameters are held constant. Both the amplitude and period of the simulations, overlapped with the analytical curve (5.70) (which forms the interface between sustained oscillations and the stable steady state region for the deterministic model), are presented in Figure 6.5.
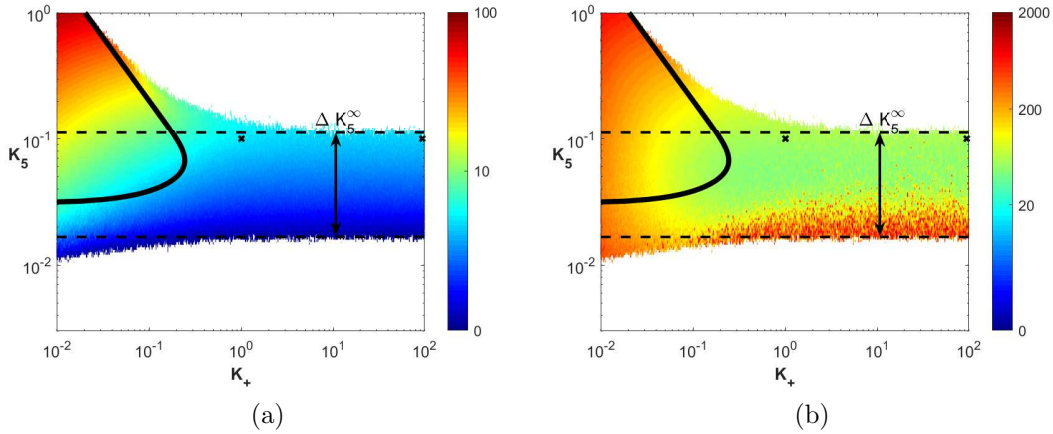

(a)   (b)

Figure 6.5: Heat-maps showing the magnitude of the amplitude (a) and period (b) of oscillations in β-catenin for 10,000 simulations using different combinations of parameters K_5 and K_+. The units for the amplitude plot are in terms of concentration (nM), and the units for the period plot are in minutes. This makes the plots comparable to Figure 5.12. The colour maps operate on a log scale. The volume is set to $V = 10^{-16}$ m^3, and the simulations are computed using the Gillespie algorithm for reactions. Both plots are overlapped with the analytical curve (5.70) which separates the parameter regime into oscillatory and stable regions for the deterministic version of this model. The two black crosses (x) in both plots refers to the choice of parameters for the simulations in Figure 6.6. The range labelled ΔK_5^∞ and bounded by the black dotted lines, refers to a window of K_5 values for which oscillations occur as $K_+ \to \infty$.

These results suggest that β-catenin can exhibit oscillations stochastically outside of

the analytical boundary. Figure 6.5 shows that the oscillatory region appears to extend towards large values of K_+ instead of being limited by an absolute upper limit for K_+ (unlike the deterministic case in Figure 5.12). It appears that there is a window of K_5 values for which the system exhibits oscillations regardless of the value of K_+. The width of this window will be referred to as ΔK_5^∞, and is shown visually in Figure 5.12.

The effect of large K_+

Before explaining the appearance of the ΔK_5^∞ window, it is a good idea to see how the simulation behaves for a set of parameters inside this window. Figure 6.6 compares two instances of the Gillespie simulations, the first with $K_+ = 1$ min^{-1}, the second with $K_+ = 100$ min^{-1}, and both with $K_5 = 0.1$ nM min^{-1}. The volume is set to $V = 10^{-16}$ m^3, and simulations are run until $t = 10,000$ minutes with the last $1,000$ minutes plotted. It is clear in Figure 6.6 that there are oscillations in β-catenin for both plots. The behaviour between the two simulations appear similar, with the exception of Axin, where the copy number of Axin in the second simulation regularly reaches zero. This aligns well with a qualitative understanding of what it means to have large K_+, where any Axin that is produced should almost immediately convert into destruction complex. This type of behaviour appears reminiscent of the zero-delay model introduced in Section 5.2.4. In Section 6.3.2, the limit $K_+ \to \infty$ is taken to reduce the implicit-delay model to the zero-delay model, and then an investigation is completed to see if the zero-delay model can oscillate under stochastic conditions.
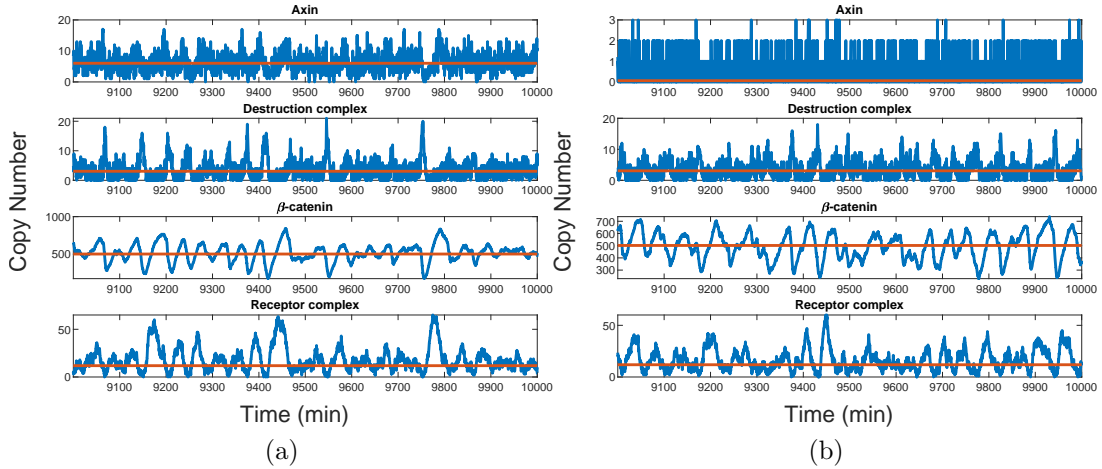

Figure 6.6: Single simulations using parameters of K_5 and K_+ outside of the analytical boundary. For (a), $K_5 = 0.1$ nM min^{-1}, and $K_+ = 1$ min^{-1}. For (b), $K_5 = 0.1$ nM min^{-1} and $K_+ = 100$ min^{-1}. Both simulations use rate parameters $K_1 = 0.012$ min^{-1}, $K_2 = 0.423$ nM min^{-1}, $K_3 = 1$ nM^{-1} min^{-1}, $K_4 = 10$ nM^{-1} min^{-1}, and a volume $V = 10^{-16}$ m^3. Each plot is overlapped with the deterministic curve (which remains at steady state). Simulations are run up to $t = 10,000$ minutes, and only the last $1,000$ minutes are shown.

It is postulated that the ΔK_5^∞ window appears because of the choice of volume. The next section investigates what happens when the volume is increased, and determines at what critical volume does this ΔK_5^∞ window disappear.

The effect of increasing the system volume

The supposedly infinite parameter regime for stochastic oscillations in Figure 6.5, can be explained by investigating the effects of increasing the volume of the system. Increasing the volume increases the number of particles and thus reduces noise. It is expected in the limit $V \to \infty$, that the deterministic results of Figure 5.12 are recaptured.

In Figure 6.7, the same simulations as Figure 6.5 are computed, except with the volume increasing from $V = 10^{-16}$ m^3 to $V = 10^{-15}$ m^3, a 10-fold increase in the volume. Immediately it can be seen that the ΔK_5^∞ window has disappeared.

Despite $V = 10^{-15}$ m^3 being a rather large volume for this model, there is a small difference in the region of parameter space associated with oscillations between Figure 6.7 and the deterministic region from Figure 5.12. The stochastic region for oscillations approximately aligns with the analytical boundary for the deterministic model, except for low K_5 values.
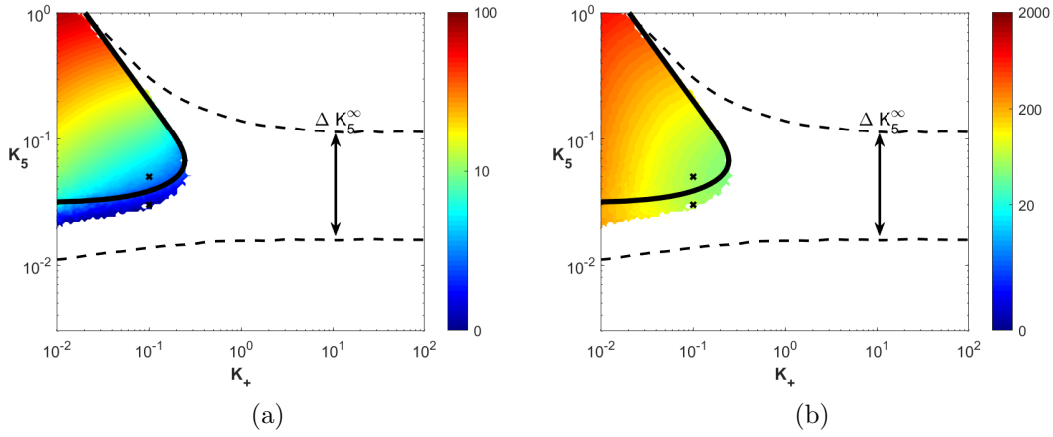

(a)   (b)

Figure 6.7: Heat-maps demonstrating the difference in magnitude over the parameter regime for the amplitude (a), and period (b) of oscillations in β-catenin. This heat-map uses a volume $V = 10^{-15}$ m^3. This heat-map is generated by running Gillespie simulations that vary over $10,000$ combinations of pairs of parameters K_5 and K_+. The analytical curve (5.70) is drawn on both plots to easily compare the stochastic oscillations to the deterministic region. The two black crosses (x) in both plots refers to the choice of parameters for the simulations in Figure 6.8. The dotted black lines represents the upper and lower boundary of the stochastic parameter regime from Figure 6.5 (and the distance between the two for large K_+ values is the ΔK_5^∞ window). These lines allow a direct comparison between changing the volume from $V = 10^{-16}$ m^3 to $V = 10^{-15}$ m^3.

To explain the region outside the analytical boundary which still gives oscillations, simulations are completed where K_5 is just inside the boundary, and when it is just outside. This is done in Figure 6.8 where $K_5 = 0.05$ nM min^{-1} for the high Wnt case, and $K_5 = 0.03$ nM min^{-1} for the low Wnt case. Similar to the simulations in Figure 6.1, the system exhibits oscillations deterministically for just the high Wnt case, but stochastically for both the low and high Wnt cases.
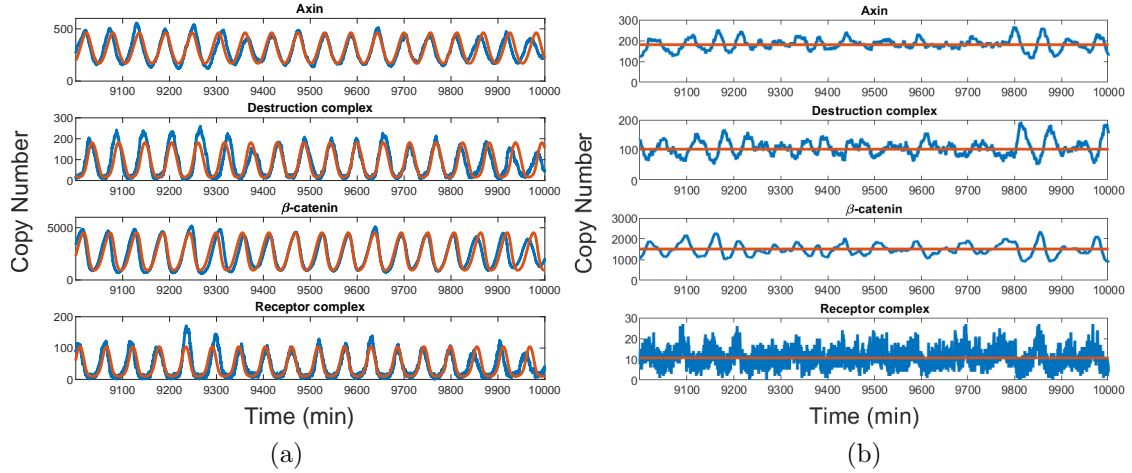
Figure 6.8: (a) One simulation run with $K_5 = 0.05$ nM min^{-1} (high Wnt case). (b) One simulation run with $K_5 = 0.03$ nM min^{-1} (low Wnt case). Both of these simulations use $K_1 = 0.012$ min^{-1}, $K_2 = 0.423$ nM min^{-1}, $K_3 = 1$ nM^{-1} min^{-1}, $K_4 = 10$ nM^{-1} min^{-1}, $K_+ = 0.1$ min^{-1}, and the system volume was set to $V = 10^{-15}$ m^3. Simulations are overlapped with their corresponding deterministic solution.

6.3.2 The stochastic zero-delay deactivator model

An important point to note about Figure 6.5 is that oscillations occur within a window of K_5 even when K_+ is large, but as just demonstrated, this window disappears as the noise is reduced (or volume increased). To investigate the ΔK_5^∞ window which generates oscillations in the limit $K_+ \to \infty$, a stochastic version of the zero-delay model from Section 5.2.4 is simulated. The zero-delay model is the implicit-delay model, in the limit $K_+ \to \infty$,

$$\frac{dB}{dt} = K_2 - K_3 BC, \tag{6.6}$$

$$\frac{dC}{dt} = K_1 B - K_4 CR, \tag{6.7}$$

$$\frac{dR}{dt} = K_5 - K_4 CR. \tag{6.8}$$

It was shown in Section 5.2.4 that this model, without stochasticity, never produces oscillations regardless of the parameter choice. However the stochastic simulation in Figure 6.5 suggests that oscillations may occur under stochastic conditions.

To confirm this, simulations are shown in Figure 6.9, where the period and amplitude is plotted against an increase in K_5 with the volume kept constant at $V = 10^{-16}$ m^3. As can be seen in the figure, there are oscillations in this system until K_5 reaches 0.3, after which, the amplitude sharply decreases and the oscillations disappear.
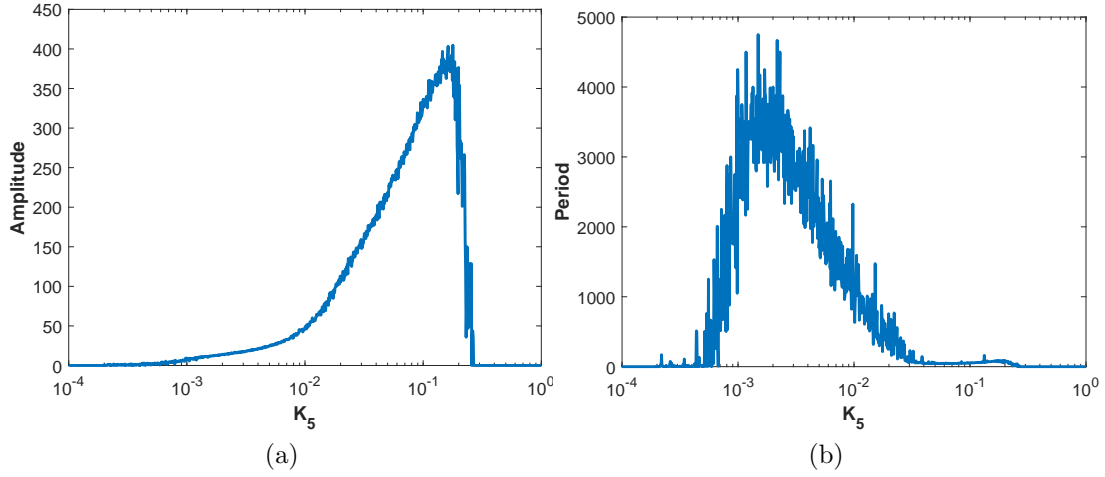
Figure 6.9: Plot of the amplitude (a) and period (b) of oscillations in β-catenin versus K_5 whilst holding the other parameters the same. The K_5 axis is plotted on a log scale. Each point on these plots represent the average of 10 simulations for a particular choice of K_5. A value of zero for either the amplitude or period denotes that no oscillations occurred for that particular choice of K_5.

Effect of volume on the region for oscillations

The main results from Section 6.3.1 suggests that there is a critical volume for stochastic simulations using large K_+ values above which oscillations are impossible (the ΔK_5^∞ window disappears). In this section, there is an attempt to explain the behaviour of the oscillations as the volume varies, and to find the critical volume for which oscillations occur.

Simulations are run for the zero-delay model where the volume is varied from 10^{-18} m^3 to 10^{-15} m^3 with each point logarithmically spaced. The window of K_5 values, ΔK_5^∞, is recorded for which oscillations occur, and this is plotted against volume in Figure 6.10. As can be seen, the window for which oscillations occur stochastically decreases as volume increases following a power law distribution (also plotted in Figure 6.10). This distribution has equation

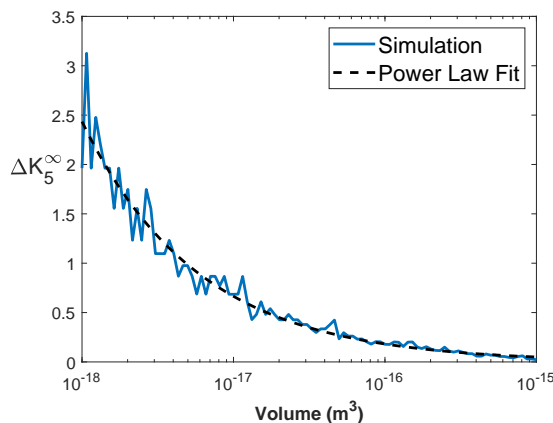$$\Delta K_5^\infty = 1.751 \times 10^{-10} V^{-0.5635}. \tag{6.9}$$

Figure 6.10: Plot of the size of the ΔK_5^∞ window versus an increase in the system volume V. The results are fitted to a power law distribution with equation $\Delta K_5^\infty = 1.751 \times 10^{-10} V^{-0.5635}$. The x-axis is plotted on a log scale. On this scale, the size of the ΔK_5^∞ window decreases logarithmically as V is increased, and appears to reach zero when $V = 10^{-15}$ m^3. Beyond this volume, the zero-delay model will never oscillate (as is the case with the associated deterministic model), and thus the implicit-delay model with a finite K_+ must be used to induce oscillations in β-catenin.

6.4 Spatial effects for stochastic oscillations

In this section, there is an investigation into how introducing spatial effects to the simulation provides different results to the Gillespie SSA. It was shown in Section 6.2.2 that there is a set of parameters where there are no deterministic oscillations, but these oscillations can be driven stochastically.

The models in this section are designed to be strongly diffusion-limited, as opposed to rate-limited for the Gillespie SSA. For this reason, a diffusion constant is chosen in such a way that reducing it any further generates significant inaccuracies in the Smoldyn algorithm. The diffusion constant used is $D = 10^{-15}$ m^2/s (as compared to $D = 10^{-12}$ m^2/s in Section 6.2.2). In this regime, the focus is heavily on the contribution of spatio-temporal noise rather than noise associated simply with small copy numbers, although it is acknowledged that these are intrinsically related.

The rate parameters used are $K_1 = 0.012$ min^{-1}, $K_2 = 0.423$ nM min^{-1}, $K_3 = 1$ nM^{-1} min^{-1}, $K_4 = 10$ nM^{-1} min^{-1}, $K_5 = 0.018$ nM min^{-1}, and $K_+ = 0.01$ min^{-1}. The results from Section 6.3 suggest to use a volume of $V = 10^{-15}$ m^3 in order to avoid oscillations at large K_+. Therefore all simulations in this section utilise $V = 10^{-15}$ m^3.

The first set of simulations is presented in Figure 6.11, where the results of the Smoldyn simulations are compared to the Gillespie SSA, and the corresponding ODE steady state. Each plot compares the copy number of each combination of species for the implicit-delay model. It appears that the copy numbers of A, B, and C, (Axin, β-catenin, and destruction complex respectively) relative to each other, are very similar for both the Smoldyn and Gillespie SSA. However, when comparing these species against R, there is a clear difference. The Smoldyn simulation keeps R at less than 2 molecules whilst the Gillespie SSA regularly reaches values of 18 molecules. This difference is due to the fact that for these rate parameters, and the choice of diffusion constant, the binding radius for reaction 4 (K_4) is over 50% of the size of the system domain. This results in an artificially fast bimolecular reaction, thus suggesting the choice of rate, diffusion, and time-step will produce incorrect results.
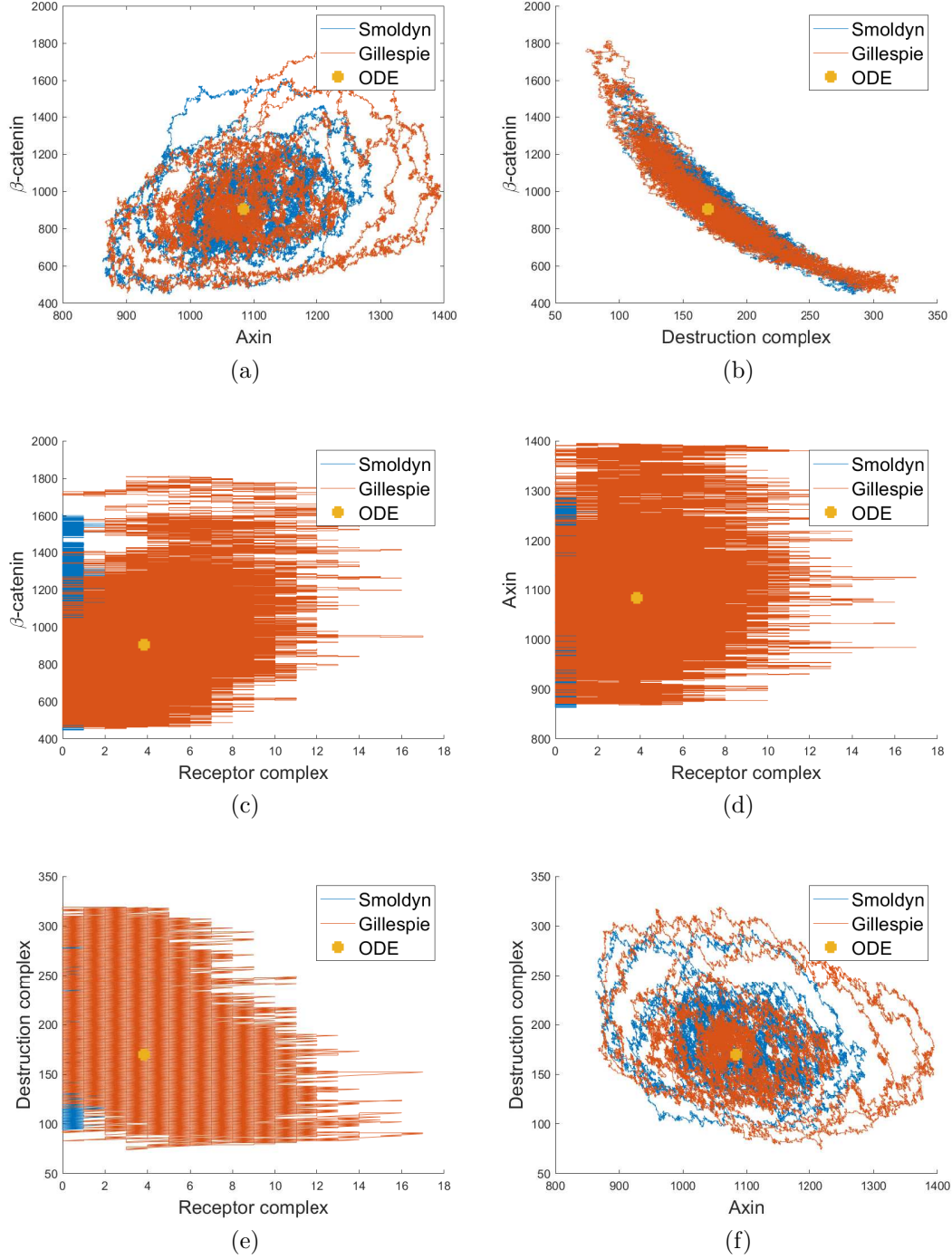
Figure 6.11: Comparison of the phase plane trajectories of the Smoldyn and Gillespie algorithms. Each axes represents the copy numbers of either Axin, β-catenin, destruction complex, or receptor complex. Both simulations use a volume $V = 10^{-15}$ m^3. The Smoldyn simulations has diffusion constant $D = 10^{-15}$ m^2/s, time-step $\Delta t = 10^{-4}$ minutes, and is simulated with periodic boundary conditions.

To address this problem, a second simulation is computed, where K_4 is reduced by a factor of 100 which in turn ensures the binding radius is significantly less than the system domain. Changing K_4 on its own would change the stability of the associated deterministic system. To avoid this, careful attention is taken to ensure that the dimensionless

parameters from (5.48),

$$\alpha = \frac{K_4}{K_3}, \quad \beta = \frac{K_+}{(K_1 K_2 K_3)^{1/3}}, \quad \text{and} \quad \gamma = \frac{K_3 K_5^3}{(K_1 K_2)^2}, \tag{6.10}$$

do not change, resulting in the same analytical curve for stability (see (5.70)). To keep α, β, and γ the same, reducing K_4 by 100 would result in a reduction of K_3 by 100, a reduction of K_+ by $100^{1/3}$, and K_5 is multiplied by a factor of $100^{1/3}$. This scaling does alter the steady states of each species, however this new set of parameters provide a better insight into how spatial effects alter the solution.

Solutions to the Gillespie and Smoldyn simulations using these new parameters are plotted in Figure 6.12. For this set of parameters, there is a visual difference between the range of copy numbers of each species across both types of simulations. In particular for the species Axin, the minimum copy number for the Smoldyn simulation is smaller than the minimum for the Gillespie SSA, and the maximum for the Smoldyn is larger than the maximum for the Gillespie; in other words the range of Axin values is larger in the Smoldyn simulation than the Gillespie SSA, which is due to spatio-temporal effects.
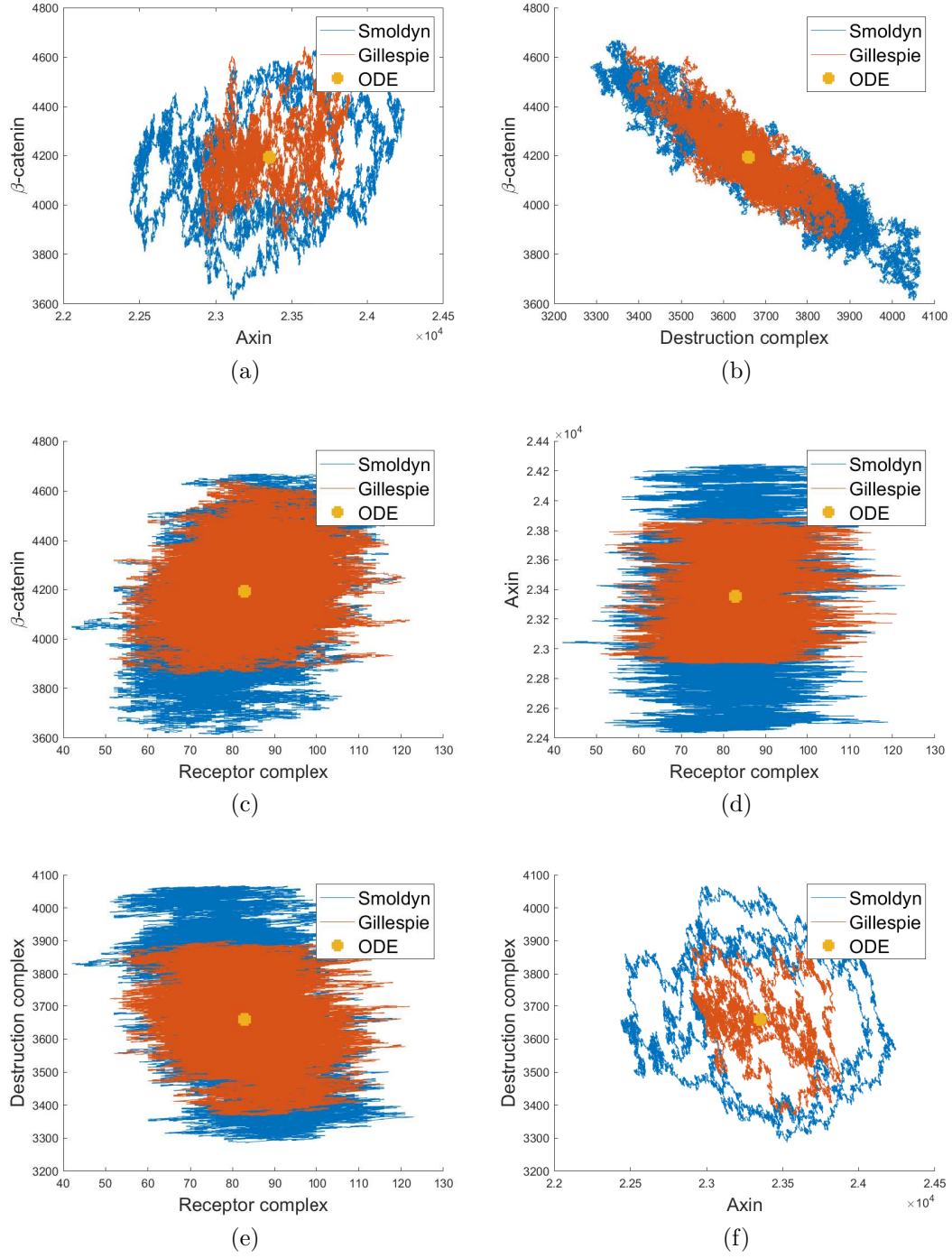
Figure 6.12: Smoldyn simulations plotted against the equivalent Gillespie and ODE solutions, where the rate constant K_4 is reduced by a factor of 100, thus reducing K_3 by 100, K_+ by $100^{1/3}$, and increasing K_5 by a factor of $100^{1/3}$. This simulation has volume $V = 10^{-15}$ m^3, diffusion constant $D = 10^{-15}$ m^2/s, time-step $\Delta t = 10^{-4}$ minutes, and is simulated with periodic boundary conditions. Each axes represents the copy numbers of either Axin, β-catenin, destruction complex, or receptor complex.

6.5 Conclusion

In this chapter, further simulations and analysis of the implicit-delay model were completed by adding stochasticity to the implicit-delay model. The aim of the chapter was to see what unique behaviour arises from stochastic modelling of the implicit-delay model that was not seen in the deterministic model in Chapter 5. Stochasticity was investigated in two different ways: (1) the model was simulated by introducing stochastic noise into the chemical reactions (see Section 6.3), and (2) a spatial component was incorporated into the model (see Section 6.4).

The first, well-mixed model, showed how simply introducing stochasticity could produce unique behaviour not seen with deterministic methods. This was done by setting a finite volume for the system, such that there were a discrete number of molecules in the system. Therefore each reaction would need to be simulated discretely and stochastically. To simulate this system, the Gillespie SSA was utilised.

The purpose of the second model was to see if the behaviour of the system could change if spatial effects were considered. These spatial effects were included by modelling the movement of molecules with diffusion. The Smoldyn algorithm was used to simulate this type of system.

Initial simulations of both the Gillespie SSA and the Smoldyn algorithm showed that there is indeed a region where β-catenin can oscillate stochastically, but not deterministically. This supports the claim from the 2008 Tymchyshyn *et al.* paper [72].

The Gillespie simulations of the implicit-delay model where the volume was chosen to be $V = 10^{-16}$ m^3, showed that the system would continue to oscillate as K_+ increased (delay decreased). This is in direct contradiction to the main findings of Chapter 5, in which a minimum delay was needed to induce oscillations in the deterministic model. This chapter suggests that oscillations can occur stochastically regardless of the delay in the system.

Taking the limit $K_+ \to \infty$, is the same as having zero-delay in the upregulation of destruction complex by β-catenin. That is, it represents the zero-delay model from Section 5.2.4. It was shown in the previous chapter that the zero-delay model can never oscillate deterministically. However, simulations in this chapter identified a parameter regime where the model can exhibit oscillations stochastically, on the condition that the volume of the system was below the critical volume $V = 10^{-15}$ m^3.

By using a volume of $V = 10^{-15}$ m^3, a 10-fold increase, the stochastic oscillations for the zero-delay model disappeared. In fact, the region of oscillations for the stochastic version of the implicit-delay model matched very closely to that of the deterministic model. The only difference between the two modelling approaches, is the stochastic model has a lower limit for K_5 (rate of production of the receptor complex) compared to the deterministic model which supports oscillations.

Simulations of the implicit-delay model with the Smoldyn algorithm were set up to be highly diffusion-limited to emphasise the effect of spatio-temporal noise. However, this presented a computational problem, where the rate of removal of the destruction complex complex by the receptor complex is quite large. This results in an artificially large binding radius that uses over 50% of the reactive volume of the system. To overcome this problem, the rate constants were scaled to ensure the binding radius was significantly smaller than the system volume, whilst ensuring the parameters chosen would keep the system in a stochastically driven oscillatory state.

In comparing both the Smoldyn and Gillespie SSA results, it was shown that there is a larger range of values over which Axin, destruction complex, and β-catenin oscillate in

the Smoldyn simulation. This suggests it is important to model the system with a spatial effect for sparse systems, as simulations showed that the interaction of each molecule in the system depends upon their relative distance to each other.

Suggestions for future experiments to investigate oscillations in the Wnt signalling pathway

Mathematical models are useful tools in helping to design future biological experiments, for which the results from this chapter can act as a great starting point. A major claim from Chapter 5 is that oscillations in the Wnt signalling pathway occur within a finite window of Wnt stimulus values (K_5). Chapter 6 extended this claim to state that oscillations occur stochastically outside of this window. These two points could form the basis of a biological experiment, which would determine how large this window of oscillations would be, and if any periodic spiking occurred outside of this window.

Other interesting questions to answer through experiments include:

- Does inhibiting the Wnt feedback mechanism alter the window of Wnt stimulus for which oscillations are induced?

- Do the claims in this thesis extend to all cell lines, or are they limited to only a few select species?

However, what is suggested in theory may not be good in practice. One major limitation in experiments would be detecting oscillations in the Wnt signalling pathway without interfering with the fundamental behaviour of the cell. Another limitation would be in accurately controlling the amount of Wnt stimulus entering the cell. Overcoming these experimental limitations is something the author leaves to the experimentalists.

Chapter 7

Conclusion

7.1 Thesis summary

The overarching theme of this thesis was on how to improve the modelling of reaction-diffusion processes with a focus on stochastic effects, and how these models provide new insights into the canonical Wnt signalling pathway. Recalling the aims from Chapter 1, research in this thesis was designed to answer the following three questions:

1. How can reactions involving more than two molecules be modelled using the current state-of-the-art framework?

2. What are the fundamental components of the Wnt signalling pathway which give rise to feedback-driven oscillations? What conditions need to be placed on the interactions between these components for oscillatory behaviour to arise?

3. What are the consequences of noise in the Wnt signalling pathway with feedback-driven oscillations?

These questions arose by exploring gaps in the literature for reaction-diffusion processes, and the Wnt signalling pathway. This literature was reviewed in Chapters 2 and 3. Each of the aims formed the basis of the research in Chapters 4 to 6.

Reversible Doi and Smoluchowski kinetics for high-order reactions

The first question proposed in the aims was, 'How can reactions involving more than two molecules be modelled using the current state-of-the-art framework?'. This question was the focus of Chapter 4. In this work, the existing Smoluchowski [110], Doi [115], Lipková [116], and Flegg [118] kinetics were combined into a single framework capable of simulating reversible Nth-order reactions [119].

Smoluchowski kinetics (reviewed in Section 3.5.4) was originally designed to describe two proteins, treated as point particles diffusing freely in space with Brownian motion, that eventually diffuse to within a critical separation distance of each other and instantly react. This separation distance is typically denoted as the binding radius (see Figure 3.1). These kinetics were later developed such that two particles can collide, but not immediately react with each other (see Figure 3.2). This particular model is referred to as Doi kinetics (reviewed in Section 3.5.6).

Lipková kinetics (reviewed in Section 3.5.7) were developed to take Smoluchowski and Doi kinetics, and apply them to reversible bimolecular reactions. These reactions modelled under a Smoluchowski/Doi regime require the use of a second radius called the

unbinding radius (see Figure 3.3). This unbinding radius describes how far apart two particles created from a reverse reaction must be placed. Under a Smoluchowski regime, these particles must be placed further than their binding radius. For Doi kinetics, this rule is relaxed, as particles close to each other do not instantly react, which allows particles the chance to diffuse away from each other.

Flegg kinetics (reviewed in Section 3.5.9) extended the work of Smoluchowski and Doi to apply to reactions involving three or more molecules. These kinetics utilised a new distance metric called Jacobian coordinates, which represent a vector that describes the relative distances of three or more molecules from each other (see Figure 3.4a). If the scaled lengths of these vectors is less than the binding proximity (a binding radius for three or more molecules), then (3.70) is satisfied and a reaction occurs.

The new framework to model reversible N-molecular reactions was developed for two specific cases: (1) the binding proximity is set to be larger than the unbinding proximity (see Section 4.2.1), and (2) the binding proximity is smaller than or equal to the unbinding proximity (see Section 4.2.2). The binding and unbinding proximities are similar to those defined under Lipková kinetics, except they describe the placement of N molecules that react or dissociate (see Figure 4.2).

The kinetics for case (1) in (4.23), although initially derived under the Doi regime, can be simplified to a Smoluchowski framework by making the forward reaction instantaneous (see (4.24)). These kinetics are reducible to the models derived by Flegg, Lipková, Doi, and Smoluchowski, as demonstrated at the end of Section 4.2.1. Therefore these kinetics can be used in place of the other frameworks as opposed to having five different models to work from.

The case (2) kinetics in (4.30) opens itself to a number of interesting modelling choices. For this case, the unbinding proximity can be taken to be zero (molecules produced from reverse reaction are placed at the same point), which reduces the number of parameters to set, and results in the kinetics in (4.31). Additionally, by considering the probability of geminate recombination derived in Section 4.2.3, (4.30) can be further reduced to (4.40). This last relation means the binding proximity can be fully determined by the forward reaction rate constant, the diffusion constants for each molecule, and the probability of geminate recombination.

To simulate these new kinetics, a modified version of the Smoldyn algorithm [81] from Section 3.6 is presented in Section 4.3. A crucial step to modifying the Smoldyn algorithm is solving the PDE in (4.41) using Green's functions. However, analytic Green's functions could not easily be solved for reactions involving an odd number of molecules, resulting in the need for approximate solutions to this PDE. Thus the algorithm has sacrificed some accuracy, but this could be fixed in the future if a usable analytic solution to (4.41) can be found. The modified algorithm was constructed in two parts, the first to build a lookup table relating the binding proximity to the forward reaction rate constant in Section 4.3.1, and the second algorithm described how to find the binding proximity from the constructed lookup table (see Section 4.3.2).

In order to confirm the new framework developed in Chapter 4, simulations were completed for two main examples. The first example applied these kinetics to theoretical simulations of basic second-, third-, and fourth-order reactions. Figure 4.3 visually demonstrated the accuracy of these new kinetics for these three cases. The accuracy was verified by calculating the Kullback-Leibler divergence [120], which were found to be low in each case. This means there is very strong agreement between the simulations and the expected steady-states.

The second of these main examples simulated a modified version of the Lee model [58]

for the Wnt signalling pathway in Section 4.5. This example was intended to demonstrate the power of these new kinetics and algorithm in simulating a complex reaction pathway. The Lee model was one of the first models to comprehensively describe most interactions in the Wnt signalling pathway. In the Lee model, the protein β-catenin, is regulated by a destruction complex consisting of Axin, APC, and GSK3β. The rate at which this destruction complex can regulate β-catenin is heavily influenced by a Wnt receptor complex containing Dishevelled, which in high concentrations, will increase the dissociation rate of destruction complex. Further analysis of the Lee model [59] demonstrated that the pathway operates on three distinct time-scales: (1) a long time-scale on which the degradation of free β-catenin operates, (2) the medium time-scale for which the formation of destruction complex and its dissociation in the presence of high Dishevelled concentration is considered, and (3) the short time-scale which deals with the rapid phosphorylation and degradation of β-catenin via its association with the destruction complex. This demonstrates that a modified version of the Lee model needs to consider these fast-slow kinetics as they can cause issues when simulated under Smoluchowski kinetics (see Section 4.5.5).

Initial simulations of the Lee model used Lipková kinetics to describe a series of two reversible bimolecular reactions in the formation of the destruction complex. This simulation was compared to a reactive-only system of the Lee model simulated by the Gillespie SSA in Figure 4.5. By comparing the two simulations, it is clear that simulating the Lee model using bimolecular reactions for the formation of the destruction complex produces inaccurate results. This inaccuracy is due to an issue with the fundamental nature of Smoluchowski kinetics when simulating fast-slow reactions. In particular, a fast reaction can result in a large reaction proximity which artificially inflates the simulated reaction rate (demonstrated visually in Figure 4.6).

This issue is solved by modifying the Lee model further by treating the formation of destruction complex as a single trimolecular reaction. The system is then simulated using the kinetics derived in this thesis in Section 4.2 and the algorithm in Section 4.3. Figure 4.8 demonstrates that this new method produces results with excellent agreement to the equivalent Gillespie style simulation. This small change in the model suggests reversible Nth-order reaction kinetics is more accurate and computationally faster than using the standard Smoluchowski kinetics for a series of bimolecular reactions involving fast-slow kinetics.

Although these simulations were more accurate, they are still susceptible to stochastic effects, in particular stochastic focusing. This behaviour was demonstrated visually in Figure 4.9, where simulations focusing on the destruction complex regulating β-catenin were carried out. As the phosphorylation and degradation of β-catenin is quite rapid, these results suggested that stochastic models of Wnt need to treat this particular process as instantaneous.

Delay-driven oscillations via Axin2 feedback in the Wnt/β-catenin signalling pathway

The second questions of the aims were, 'What are the fundamental components of the Wnt signalling pathway which give rise to feedback-driven oscillations? What conditions need to be placed on the interactions between these components for oscillatory behaviour to arise?'. These questions were researched in Chapter 5.

An important part of Wnt signalling is the effect of Axin2 feedback in the system. Axin2 creates a negative feedback loop which leads to oscillatory behaviour in the total concentration of β-catenin. Current models for Wnt signalling [68, 71, 72] can simu-

late these oscillations. However these models are far too complex to develop analytical relationships that can describe the exact conditions for which sustained oscillations occur.

This problem is addressed by simplifying the Tymchyshyn model from Section 2.3.4 to create two new models. Central to the Tymchyshyn model is the deactivation (removal) of destruction complex by a Wnt receptor complex, a behaviour that is necessary to induce sustained oscillations.

The first simplified model is called the implicit-delay deactivator model (see Figure 5.4), where only the four components, Axin, destruction complex, β-catenin, and a Wnt receptor complex are considered. The interactions in this model are described by (5.15) to (5.18) which represent a system of four ordinary differential equations. In this model, Axin is produced from β-catenin, and acts as an 'implicit' delay in the production of destruction complex. This delay in producing destruction complex causes a delay in both the removal of destruction complex with receptor complex, and the degradation of β-catenin by destruction complex.

The asymptotic stability of the implicit-delay deactivator model was determined in Section 5.3.2. Equation (5.70) describes the bifurcation curve for this model, in which sustained oscillations are obtained when (5.70) is positive. This bifurcation line leads to a number of conclusions about Axin2 feedback in Wnt signalling. Each of these statements provides necessary conditions for sustained oscillations to be induced in this model:

1. A delay in destruction complex production is necessary.

2. The delay in destruction complex production must be greater than some minimum value.

3. The rate at which Wnt receptor complex removes destruction complex must be greater than the rate at which destruction complex can phosphorylate and degrade β-catenin.

4. The influx rate of Wnt receptor complex must lie within a finite window of Wnt stimulus levels for which oscillations can occur.

All of these statements must be satisfied in order to induce sustained oscillations in the implicit-delay model.

The second model produced in Chapter 5 is the explicit-delay deactivator model (see Section 5.2.5). This model simplifies the implicit-delay model by replacing the delay in destruction complex production with a single fixed time delay. The new model is the system of delay differential equations described by (5.26) to (5.28).

Analysis of the explicit-delay model resulted in the bifurcation line described by (5.96). Similar to the implicit-delay model, this bifurcation line needs to be positive to produce sustained oscillations. All the statements that need to be satisfied in the implicit-delay model in order for sustained oscillations to occur also hold true for the explicit-delay model. The only difference is that the explicit-delay model has a larger region of parameters for which sustained oscillations can be induced.

Equations (5.70) and (5.96) are presented visually in Figures 5.12 and 5.13. The first figure describes the strength of the amplitude and period of sustained oscillations. The second compares the stability region for both models. From Figure 5.13, it can be seen that the region of stability for the explicit-delay model is larger than that of the implicit-delay model.

It was not determined in Chapter 5 which model should be used. Instead, that choice is left to the modeller. Both models have advantages and disadvantages. The implicit-delay model allows a modeller to adjust all the rate constants. This is advantageous if

the experimental data is provided in terms of reaction rate constants. The explicit-delay model has less components, and allows for the ability to specify an exact time for the delay in destruction complex production. However it is more computationally intensive to solve, which can be a major problem when simulating a large number of systems, for example, for parameter estimation purposes.

Stochastic oscillations in the Wnt/β-catenin signalling pathway

The final question of the aims was, 'What are the consequences of noise in the Wnt signalling pathway with feedback-driven oscillations?'. This was researched in Chapter 6, by taking the implicit-delay model from Section 5.2.3, and simulating it stochastically using the Gillespie SSA from Section 3.4.1 and the Smoldyn algorithm from Section 3.6.

The Gillespie SSA determined how noise associated with discrete chemical copy numbers alters the stability of the implicit-delay model. Initial simulations using the Gillespie SSA demonstrated that under a Wnt stimulus, oscillations can still occur stochastically when they would not occur deterministically. This claim also holds true for spatio-temporal systems simulated using the Smoldyn algorithm.

The region of parameter space for which stochastic models induce oscillations (with a small enough volume) is significantly larger than that for deterministic models (see Figure 6.5). In particular, given a small volume ($V < 10^{-15}$ m^3) and if the delay in destruction complex production is taken to be infinitely small, then there is a finite window of Wnt stimulus values for which oscillations will occur stochastically.

This phenomenon results in stochastic oscillations in the zero-delay model from Section 5.2.4. Although this model can never generate sustained oscillations deterministically, it can when simulated under stochastic conditions. However, by increasing the system volume, the zero-delay model reaches a critical volume at which oscillations cease (see Figure 6.10).

In using a volume larger than the critical volume, the region of parameters for which stochastic oscillations can be induced is smaller than if a value less than the critical volume is used. The resulting region is presented in Figure 6.7. Solutions from this region of parameter space can still oscillate stochastically for low values of Wnt stimulus.

By simulating the implicit-delay model using spatio-temporal simulations (reaction-diffusion model), new behaviour arises. Under highly diffusion-limited conditions, the range of values for which β-catenin and Axin oscillate over increases. However, care needs to be taken to ensure the parameters for the Smoldyn algorithm do not result in artificially large reaction radii (see Figures 6.11 and 6.12).

7.2 Open problems

The main results from this thesis lead to a number of open problems to solve. In this section, four main research questions are proposed.

What other algorithms can be modified to simulate reversible Nth-order reactions?

The kinetics for the reversible Nth-order reaction developed in Chapter 4, were simulated by a modified version of the Smoldyn algorithm. The Smoldyn algorithm was chosen as it is simple to implement, and is relatively efficient for dense micro-scale systems. However, for sparse micro-scale systems, an event-driven algorithm, such as eGFRD [83], would

be far more computationally efficient than Smoldyn. The eGFRD algorithm was briefly reviewed in Section 3.2.4. The core component of this algorithm is the placement of protective boundaries around either a single molecule, or a pair of molecules that have the potential to react together. The time taken until a single molecule or pair of molecules diffuses outside the protective boundary, or the molecules react, is calculated and placed in a list ordered from the shortest time to the longest time. The algorithm proceeds through this list, executing one event at a time, and updating the list as each event occurs.

To derive the eGFRD algorithm to simulate reversible Nth-order reactions, there are two main mathematical problems to solve. The first is to determine how protective boundaries should be placed around a set of N-molecules. The kinetics for Nth-order reactions require the binding proximity to operate in $3(N-1)$-dimensional space to determine what is the closest set of N molecules that can react together.

The second problem to solve, is finding an exact solution to the partial differential equation (PDE) which governs when N molecules react together. This PDE would be similar to the diffusion equation in the paper by Takahashi *et al.* [83], except it would be modified to describe the diffusion of N molecules, as opposed to only two. There is no guarantee that there are analytical solutions to this PDE. If this was the case, then approximate solutions would need to be used, and the eGFRD would no longer produce 'exact' results.

How would the kinetics for reversible Nth-order reactions be constructed under a Collins-Kimball framework?

The Collins-Kimball model [114] (reviewed in Section 3.5.5) is based on the Smoluchowski approach to modelling bimolecular reactions, except that reactions are activation-limited as opposed to diffusion-limited. This type of approach increases both the mathematical and computational complexity of resolving reactions, however the Smoldyn software provides a way to overcome these issues [81]. Just as Chapter 4 asked the question about how Smoluchowski kinetics could be extended to model reversible Nth-order reactions, the same can be asked of the Collins-Kimball model. The derivation of the Collins-Kimball model for reversible Nth-order reactions would likely follow a similar approach to that of Section 4.2, with the modification of how boundary conditions are implemented to ensure the reactions become activation-limited.

How can models of Wnt with crosstalk between other pathways such as Notch and FGF signalling be simplified, and how does this crosstalk affect oscillations in the Wnt signalling pathway?

The implicit- and explicit-delay models developed in Chapter 5 were simplifications of the oscillatory Wnt pathway. These models beg the question, can other oscillating signalling pathways, such as that of Notch and fibroblast growth factor (FGF), be simplified in a similar way for the purposes of analysis? Once these models are simplified (if it is possible to do so), then it would be interesting to simulate the crosstalk between simplified models of Wnt, Notch, and FGF signalling. This coupled pathway could then be compared to the implicit- and explicit-delay models, to determine how the induction of sustained oscillations differs between the models.

How can the conditions required to induce oscillatory behaviour in Wnt signalling be validated through biological experiments?

An important part of modelling biological processes, is to develop models that can influence and design future biological experiments. A key outcome of Chapter 5 were the conditions needed to induce oscillations in both the implicit- and explicit-delay models. In Chapter 6, it was shown that stochastic models have a larger region of Wnt influx for which periodic spiking is induced. A number of observations were identified as by-products of simulating a simple model of Wnt signalling. These observations would require experimental validation before being considered as accepted scientific theory.

7.3 Concluding remarks

The quantity of research in mathematical biology has increased due to the advancement of mathematical and algorithmic techniques in simulating biological systems. The work in this thesis has contributed to these advancements in the following way:

- Kinetics for reactions involving more than two molecules were created. These kinetics overcome issues in simulating a series of fast-slow reactions in a biological pathway.

- Simplified pathways for an oscillating Wnt system were developed. This simplification provides greater insight into the exact conditions required to induced sustained oscillations.

- Observations into stochastically modelling the Wnt signalling pathway were made. These observations highlighted behaviour that could drive future biological experiments.

A barrier in mathematical biology is to design software that can efficiently simulate biological systems without sacrificing accuracy. Current software handle this problem well [96]. However as these methods become more efficient, a natural step is to then define them for smaller scales. If future models can describe the underlying molecular and atomic dynamics of biological systems, and can simulate these efficiently, then the quality of research in mathematical biology will improve drastically. Until this time, it is important to design simpler models of biological systems, and to improve the algorithms used to simulate them.

Bibliography

[1] C. W. Tan, B. S. Gardiner, Y. Hirokawa, M. J. Layton, D. W. Smith, and A. W. Burgess, "Wnt Signalling Pathway Parameters for Mammalian Cells," *PLOS ONE*, vol. 7, no. 2, pp. 1–16, 2012.

[2] J. Gerhart, "1998 Warkany Lecture: Signaling Pathways in Development," *Teratology*, vol. 60, no. 4, pp. 226–239, 1999.

[3] R. H. Giles, J. H. van Es, and H. Clevers, "Caught up in a Wnt storm: Wnt signaling in cancer," *Biochimica et Biophysica Acta (BBA) - Reviews on Cancer*, vol. 1653, no. 1, pp. 1–24, 2003.

[4] R. Nusse and H. E. Varmus, "Many tumors induced by the mouse mammary tumor virus contain a provirus integrated in the same region of the host genome," *Cell*, vol. 31, no. 1, pp. 99–109, 1982.

[5] S. Munemitsu, I. Albert, B. Souza, and P. Rubinfeld, B.and Polakis, "Regulation of intracellular beta-catenin levels by the adenomatous polyposis coli (APC) tumor-suppressor protein," *Proceedings of the National Academy of Sciences*, vol. 92, no. 7, pp. 3046–3050, 1995.

[6] B. Rubinfeld, D. A. Tice, and P. Polakis, "Axin-dependent Phosphorylation of the Adenomatous Polyposis Coli Protein Mediated by Casein Kinase 1ϵ," *Journal of Biological Chemistry*, vol. 276, no. 42, pp. 39037–39045, 2001.

[7] A. Kikuchi, "Roles of Axin in the Wnt Signalling Pathway," *Cellular Signalling*, vol. 11, no. 11, pp. 777–788, 1999.

[8] H. Yamamoto, S. Kishida, M. Kishida, S. Ikeda, S. Takada, and A. Kikuchi, "Phosphorylation of Axin, a Wnt Signal Negative Regulator, by Glycogen Synthase Kinase-3β Regulates Its Stability," *Journal of Biological Chemistry*, vol. 274, no. 16, pp. 10681–10684, 1999.

[9] E. Lee, A. Salic, and M. W. Kirschner, "Physiological regulation of β-catenin stability by Tcf3 and CK1ϵ," *The Journal of Cell Biology*, vol. 154, no. 5, pp. 983–994, 2001.

[10] B. Lloyd-Lewis, A. G. Fletcher, T. C. Dale, and H. M. Byrne, "Toward a quantitative understanding of the Wnt/β-catenin pathway through simulation and experiment," *Wiley Interdisciplinary Reviews: Systems Biology and Medicine*, vol. 5, no. 4, pp. 391–407, 2013.

[11] J. R. Miller, "The Wnts," *Genome Biology*, vol. 3, no. 1, pp. 1–15, 2001.

[12] R. van Amerongen, "Alternative Wnt Pathways and Receptors," *Cold Spring Harbor Perspectives in Biology*, vol. 4, no. 10, pp. 1–18, 2012.

[13] A. De, "Wnt/Ca^{2+} signaling pathway: A brief overview," *Acta Biochimica et Biophysica Sinica*, vol. 43, no. 10, pp. 745–756, 2011.

[14] H. Clevers, "Wnt/β-Catenin Signaling in Development and Disease," *Cell*, vol. 127, no. 3, pp. 469–480, 2006.

[15] H. A. Kestler and M. Kühl, "From individual Wnt pathways towards a Wnt signalling network," *Philosophical Transactions of the Royal Society B: Biological Sciences*, vol. 363, no. 1495, pp. 1333–1347, 2008.

[16] Q. Tian, H. Jin, Y. Cui, C. Guo, and X. Lu, "Regulation of Wnt gene expression," *Development, Growth & Differentiation*, vol. 47, no. 5, pp. 273–281, 2005.

[17] J.-L. Teo and M. Kahn, "The Wnt signaling pathway in cellular proliferation and differentiation: A tale of two coactivators," *Advanced Drug Delivery Reviews*, vol. 62, no. 12, pp. 1149–1155, 2010.

[18] V. L Church and P. Francis-West, "Wnt signalling during limb development," *The International Journal of Developmental Biology*, vol. 46, no. 7, pp. 927–936, 2002.

[19] A. Aman and T. Piotrowski, "Wnt/β-Catenin and Fgf Signaling Control Collective Cell Migration by Restricting Chemokine Receptor Expression," *Developmental Cell*, vol. 15, no. 5, pp. 749–761, 2008.

[20] A. Tian, H. Benchabane, Z. Wang, and Y. Ahmed, "Regulation of Stem Cell Proliferation and Cell Fate Specification by Wingless/Wnt Signaling Gradients Enriched at Adult Intestinal Compartment Boundaries," *PLOS Genetics*, vol. 12, no. 2, pp. 1–31, 2016.

[21] H. Hikasa and S. Y. Sokol, "Wnt Signaling in Vertebrate Axis Specification," *Cold Spring Harbor Perspectives in Biology*, vol. 5, no. 1, pp. 1–20, 2013.

[22] A. Kusserow, K. Pang, C. Sturm, M. Hrouda, J. Lentfer, H. A. Schmidt, U. Technau, A. von Haeseler, B. Hobmayer, M. Q. Martindale, and T. W. Holstein, "Unexpected complexity of the Wnt gene family in a sea anemone," *Nature*, vol. 433, no. 7022, pp. 156–160, 2005.

[23] A. P. McMahon and R. T. Moon, "Ectopic expression of the proto-oncogene int-1 in Xenopus embryos leads to duplication of the embryonic axis," *Cell*, vol. 58, no. 6, pp. 1075–1084, 1989.

[24] K. Willert, C. Logan, A. Arora, M. Fish, and R. Nusse, "A Drosophila Axin homolog, Daxin, inhibits Wnt signaling," *Development*, vol. 126, no. 18, pp. 4165–4173, 1999.

[25] R. Nusse and H. Clevers, "Wnt/β-Catenin Signaling, Disease, and Emerging Therapeutic Modalities," *Cell*, vol. 169, no. 6, pp. 985–999, 2017.

[26] C. Y. Logan and R. Nusse, "The Wnt Signaling Pathway in Development and Disease," *Annual Review of Cell and Developmental Biology*, vol. 20, no. 1, pp. 781–810, 2004.

[27] K.-H. Cho, S. Baek, and M.-H. Sung, "Wnt pathway mutations selected by optimal β-catenin signaling for tumorigenesis," *FEBS letters*, vol. 580, no. 15, pp. 3665–3670, 2006.

[28] C.-M. Yang, S. Ji, Y. Li, L.-Y. Fu, and F.-D. Jiang, Taoand Meng, "β-Catenin promotes cell proliferation, migration, and invasion but induces apoptosis in renal cell carcinoma," *OncoTargets and Therapy*, vol. 10, pp. 711–724, 2017.

[29] N.-C. Ha, T. Tonozuka, J. L. Stamos, H.-J. Choi, and W. I. Weis, "Mechanism of Phosphorylation-Dependent Binding of APC to β-Catenin and Its Role in β-Catenin Degradation," *Molecular Cell*, vol. 15, no. 4, pp. 511–521, 2004.

[30] K. Aoki and M. M. Taketo, "Adenomatous polyposis coli (APC): a multi-functional tumor suppressor gene," *Journal of Cell Science*, vol. 120, no. 19, pp. 3327–3335, 2007.

[31] E. Beurel, S. F. Grieco, and R. S. Jope, "Glycogen synthase kinase-3 (GSK3): Regulation, actions, and diseases," *Pharmacology & Therapeutics*, vol. 148, pp. 114–131, 2015.

[32] P. Seshacharyulu, P. Pandey, K. Datta, and S. K. Batra, "Phosphatase: PP2A structural importance, regulation and its aberrant expression in cancer," *Cancer Letters*, vol. 335, no. 1, pp. 9–18, 2013.

[33] B. Schittek and T. Sinnberg, "Biological functions of casein kinase 1 isoforms and putative roles in tumorigenesis," *Molecular Cancer*, vol. 13, no. 1, pp. 231–244, 2014.

[34] R. Dajani, E. Fraser, S. M. Roe, M. Yeo, V. M. Good, V. Thompson, T. C. Dale, and L. H. Pearl, "Structural basis for recruitment of glycogen synthase kinase 3β to the axin-APC scaffold complex," *The EMBO Journal*, vol. 22, no. 3, pp. 494–501, 2003.

[35] C. Liu, Y. Li, M. Semenov, C. Han, G.-H. Baeg, Y. Tan, Z. Zhang, and X. Lin, Xinhuaand He, "Control of β-Catenin Phosphorylation/Degradation by a Dual-Kinase Mechanism," *Cell*, vol. 108, no. 6, pp. 837–847, 2002.

[36] K. Orford, C. Crockett, J. P. Jensen, A. M. Weissman, and S. W. Byers, "Serine Phosphorylation-regulated Ubiquitination and Degradation of β-Catenin," *Journal of Biological Chemistry*, vol. 272, no. 40, pp. 24735–24738, 1997.

[37] C. Y. Janda, D. Waghray, A. M. Levin, C. Thomas, and K. C. Garcia, "Structural Basis of Wnt Recognition by Frizzled," *Science*, vol. 337, no. 6090, pp. 59–64, 2012.

[38] K. I. Pinson, J. Brennan, S. Monkley, B. J. Avery, and W. C. Skarnes, "An LDL-receptor-related protein mediates Wnt signalling in mice," *Nature*, vol. 407, no. 6803, pp. 535–538, 2000.

[39] N. S. Tolwinski, M. Wehrli, A. Rives, N. Erdeniz, S. DiNardo, and E. Wieschaus, "Wg/Wnt Signal Can Be Transmitted through Arrow/LRP5,6 and Axin Independently of Zw3/Gsk3β Activity," *Developmental Cell*, vol. 4, no. 3, pp. 407–418, 2003.

[40] A. Salic, E. Lee, L. Mayer, and M. W. Kirschner, "Control of β-Catenin Stability: Reconstitution of the Cytoplasmic Steps of the Wnt Pathway in Xenopus Egg Extracts," *Molecular Cell*, vol. 5, no. 3, pp. 523–532, 2000.

[41] A. J. Mikels and R. Nusse, "Purified Wnt5a Protein Activates or Inhibits β-Catenin–TCF Signaling Depending on Receptor Context," *PLOS Biology*, vol. 4, no. 4, pp. 570–582, 2006.

[42] J. Y. Leung, F. T. Kolligs, R. Wu, Y. Zhai, R. Kuick, S. Hanash, K. R. Cho, and E. R. Fearon, "Activation of AXIN2 Expression by β-Catenin-T Cell Factor. A feedback repressor pathway regulating Wnt signaling," *The Journal of Biological Chemistry*, vol. 277, no. 24, pp. 21657–21665, 2002.

[43] J. Behrens, B.-A. Jerchow, M. Würtele, J. Grimm, C. Asbrand, R. Wirtz, M. Kühl, D. Wedlich, and W. Birchmeier, "Functional Interaction of an Axin Homolog, Conductin, with β-Catenin, APC, and GSK3β," *Science*, vol. 280, no. 5363, pp. 596–599, 1998.

[44] E.-h. Jho, T. Zhang, C. Domon, C.-K. Joo, J.-N. Freund, and F. Costantini, "Wnt/β-Catenin/Tcf Signaling Induces the Transcription of Axin2, a Negative Regulator of the Signaling Pathway," *Molecular and Cellular Biology*, vol. 22, no. 4, pp. 1172–1183, 2002.

[45] I. M. van Leeuwen, H. M. Byrne, O. E. Jensen, and J. R. King, "Elucidating the interactions between the adhesive and transcriptional functions of β-catenin in normal and cancerous cells," *Journal of Theoretical Biology*, vol. 247, no. 1, pp. 77–102, 2007.

[46] F. Cong, L. Schweizer, M. Chamorro, and H. Varmus, "Requirement for a Nuclear Function of β-Catenin in Wnt Signaling," *Molecular and Cellular Biology*, vol. 23, no. 23, pp. 8462–8470, 2003.

[47] T. J. Harris and M. Peifer, "Decisions, decisions: β-catenin chooses between adhesion and transcription," *Trends in Cell Biology*, vol. 15, no. 5, pp. 234–237, 2005.

[48] L. Brunt and S. Scholpp, "The function of endocytosis in Wnt signaling," *Cellular and Molecular Life Sciences*, vol. 75, no. 5, pp. 785–795, 2018.

[49] A. Cliffe, F. Hamada, and M. Bienz, "A Role of Dishevelled in Relocating Axin to the Plasma Membrane during Wingless Signaling," *Current Biology*, vol. 13, no. 11, pp. 960–966, 2003.

[50] C. Gao and Y.-G. Chen, "Dishevelled: The hub of Wnt signaling," *Cellular Signalling*, vol. 22, no. 5, pp. 717–727, 2010.

[51] M. Fiedler, C. Mendoza-Topaz, T. J. Rutherford, J. Mieszczanek, and M. Bienz, "Dishevelled interacts with the DIX domain polymerization interface of Axin to interfere with its function in down-regulating β-catenin," *Proceedings of the National Academy of Sciences*, vol. 108, no. 5, pp. 1937–1942, 2011.

[52] A. Yu, J.-F. Rual, K. Tamai, Y. Harada, M. Vidal, X. He, and T. Kirchhausen, "Association of Dishevelled with the Clathrin AP-2 Adaptor Is Required for Frizzled Endocytosis and Planar Cell Polarity Signaling," *Developmental Cell*, vol. 12, no. 1, pp. 129–141, 2007.

[53] A. Yu, Y. Xing, S. C. Harrison, and T. Kirchhausen, "Structural Analysis of the Interaction between Dishevelled2 and Clathrin AP-2 Adaptor, A Critical Step in Noncanonical Wnt Signaling," *Structure*, vol. 18, no. 10, pp. 1311–1320, 2010.

[54] A. I. H. Hagemann, J. Kurz, S. Kauffeld, Q. Chen, P. M. Reeves, S. Weber, S. Schindler, G. Davidson, T. Kirchhausen, and S. Scholpp, "In vivo analysis of formation and endocytosis of the Wnt/β-Catenin signaling complex in zebrafish embryos," *Journal of Cell Science*, vol. 127, no. 18, pp. 3970–3982, 2014.

[55] E. Cocucci, F. Aguet, S. Boulant, and T. Kirchhausen, "The First Five Seconds in the Life of a Clathrin-Coated Pit," *Cell*, vol. 150, no. 3, pp. 495–507, 2012.

[56] M. V. Gammons, M. Renko, C. M. Johnson, T. J. Rutherford, and M. Bienz, "Wnt Signalosome Assembly by DEP Domain Swapping of Dishevelled," *Molecular Cell*, vol. 64, no. 1, pp. 92–104, 2016.

[57] S.-E. Kim, H. Huang, M. Zhao, X. Zhang, A. Zhang, M. V. Semonov, B. T. MacDonald, X. Zhang, J. G. Abreu, L. Peng, and X. He, "Wnt Stabilization of β-Catenin Reveals Principles for Morphogen Receptor-Scaffold Assemblies," *Science*, vol. 340, no. 6134, pp. 867–870, 2013.

[58] E. Lee, A. Salic, R. Krüger, R. Heinrich, and M. W. Kirschner, "The Roles of APC and Axin Derived from Experimental and Theoretical Analysis of the Wnt Pathway," *PLOS Biology*, vol. 1, no. 1, pp. 116–132, 2003.

[59] G. R. Mirams, H. M. Byrne, and J. R. King, "A multiple timescale analysis of a mathematical model of the Wnt/β-catenin signalling pathway," *Journal of Mathematical Biology*, vol. 60, no. 1, pp. 131–160, 2010.

[60] R. Krüger and R. Heinrich, "Model Reduction and Analysis of Robustness for the Wnt/β-Catenin Signal Transduction Pathway," *Genome Informatics*, vol. 15, no. 1, pp. 138–148, 2004.

[61] J. Lewis, "Autoinhibition with Transcriptional Delay: A Simple Mechanism for the Zebrafish Somitogenesis Oscillator," *Current Biology*, vol. 13, no. 16, pp. 1398–1408, 2003.

[62] D. M. Ornitz and N. Itoh, "The Fibroblast Growth Factor signaling pathway," *Wiley Interdisciplinary Reviews. Developmental Biology*, vol. 4, no. 3, pp. 215–266, 2015.

[63] A. Aulehla, C. Wehrle, B. Brand-Saberi, R. Kemler, A. Gossler, B. Kanzler, and B. G. Herrmann, "Wnt3a Plays a Major Role in the Segmentation Clock Controlling Somitogenesis," *Developmental Cell*, vol. 4, no. 3, pp. 395–406, 2003.

[64] A. Aulehla and O. Pourquié, "Oscillating signaling pathways during embryonic development," *Current Opinion in Cell Biology*, vol. 20, no. 6, pp. 632–637, 2008.

[65] H.-Y. Wang, Y.-X. Huang, L.-H. Zheng, Y.-L. Bao, L.-G. Sun, Y. Wu, C.-L. Yu, Z.-B. Song, Y. Sun, G.-N. Wang, Z.-Q. Ma, and Y.-X. Li, "Modelling Coupled Oscillations in the Notch, Wnt, and FGF Signaling Pathways during Somitogenesis: A Comprehensive Mathematical Model," *Computational Intelligence and Neuroscience*, vol. 2015, 2015.

[66] D. Kim, O. Rath, W. Kolch, and K.-H. Cho, "A hidden oncogenic positive feedback loop caused by crosstalk between Wnt and ERK Pathways," *Oncogene*, vol. 26, pp. 4571–4579, 2007.

[67] A. Goldbeter and O. Pourquié, "Modeling the segmentation clock as a network of coupled oscillations in the Notch, Wnt and FGF signaling pathways," *Journal of Theoretical Biology*, vol. 252, no. 3, pp. 574–585, 2008.

[68] C. Wawra, M. Kühl, and H. A. Kestler, "Extended analyses of the Wnt/β-catenin pathway: Robustness and oscillatory behaviour," *FEBS Letters*, vol. 581, no. 21, pp. 4043–4048, 2007.

[69] M. V. Semënov, K. Tamai, B. K. Brott, M. Kühl, S. Sokol, and X. He, "Head inducer Dickkopf-1 is a ligand for Wnt coreceptor LRP6," *Current Biology*, vol. 11, no. 12, pp. 951–961, 2001.

[70] A. Niida, T. Hiroko, M. Kasai, Y. Furukawa, Y. Nakamura, Y. Suzuki, S. Sugano, and T. Akiyama, "DKK1, a negative regulator of Wnt signaling, is a target of the β-catenin/TCF pathway," *Oncogene*, vol. 23, pp. 8520–8526, 2004.

[71] P. B. Jensen, L. Pedersen, S. Krishna, and M. H. Jensen, "A Wnt Oscillator Model for Somitogenesis," *Biophysical Journal*, vol. 98, no. 6, pp. 943–950, 2010.

[72] O. Tymchyshyn and M. Kwiatkowska, "Combining Intra- and Inter-cellular Dynamics to Investigate Intestinal Homeostasis," *Formal Methods in Systems Biology*, vol. 5054, pp. 63–76, 2008.

[73] A. Regev and E. Shapiro, *The π-calculus as an Abstraction for Biomolecular Systems*. Berlin, Heidelberg: Springer, 2004.

[74] C. Priami, "Stochastic π-Calculus," *The Computer Journal*, vol. 38, no. 7, pp. 578–589, 1995.

[75] D. T. Gillespie, "Exact stochastic simulation of coupled chemical reactions," *The Journal of Physical Chemistry*, vol. 81, no. 25, pp. 2340–2361, 1977.

[76] C. B. Muratov, E. Vanden-Eijnden, and W. E, "Self-induced stochastic resonance in excitable systems," *Physica D: Nonlinear Phenomena*, vol. 210, no. 3-4, pp. 227–240, 2005.

[77] J. Schnakenberg, "Simple chemical reaction systems with limit cycle behaviour," *Journal of Theoretical Biology*, vol. 81, no. 3, pp. 389–400, 1979.

[78] D. T. Gillespie, "Approximate accelerated stochastic simulation of chemically reacting systems," *The Journal of Chemical Physics*, vol. 115, no. 4, pp. 1716–1733, 2001.

[79] J. Stiles and T. Bartol, *Monte Carlo Methods for Simulating Realistic Synaptic Microphysiology Using MCell*, pp. 87–127. Boca Raton: CRC Press, 2001.

[80] R. Kerr, T. Bartol, B. Kaminsky, M. Dittrich, J. Chang, S. Baden, T. Sejnowski, and J. Stiles, "Fast Monte Carlo Simulation Methods for Biological Reaction-Diffusion Systems in Solution and on Surfaces," *SIAM Journal on Scientific Computing*, vol. 30, pp. 3126–3149, 2008.

[81] S. S. Andrews and D. Bray, "Stochastic simulation of chemical reactions with spatial resolution and single molecule detail," *Physical Biology*, vol. 1, no. 3, pp. 137–151, 2004.

[82] J. S. van Zon and P. R. ten Wolde, "Green's-function reaction dynamics: A particle-based approach for simulating biochemical networks in time and space," *The Journal of Chemical Physics*, vol. 123, no. 23, p. 234910, 2005.

[83] K. Takahashi, S. Tănase-Nicola, and P. R. ten Wolde, "Spatio-temporal correlations can drastically change the response of a MAPK pathway," *Proceedings of the National Academy of Sciences*, vol. 107, no. 6, pp. 2473–2478, 2010.

[84] T. R. Sokolowski, J. Paijmans, L. Bossen, T. Miedema, M. Wehrens, N. B. Becker, K. Kaizu, K. Takahashi, M. Dogterom, and P. R. ten Wolde, "eGFRD in all dimensions," *The Journal of Chemical Physics*, vol. 150, no. 5, p. 054108, 2019.

[85] K. R. Sanft, S. Wu, M. Roh, J. Fu, R. K. Lim, and L. R. Petzold, "StochKit2: software for discrete stochastic simulation of biochemical systems with events," *Bioinformatics*, vol. 27, no. 17, pp. 2457–2458, 2011.

[86] B. Drawert, S. Engblom, and A. Hellander, "URDME: a modular framework for stochastic simulation of reaction-transport processes in complex geometries," *BMC Systems Biology*, vol. 6, no. 1, p. 76, 2012.

[87] S. A. Isaacson, "A convergent reaction-diffusion master equation," *The Journal of Chemical Physics*, vol. 139, no. 5, p. 054101, 2013.

[88] J. Hattne, D. Fange, and J. Elf, "Stochastic reaction-diffusion simulation with MesoRD," *Bioinformatics*, vol. 21, no. 12, pp. 2923–2924, 2005.

[89] B. Drawert, A. Hellander, B. Bales, D. Banerjee, G. Bellesia, B. J. Daigle, Jr., G. Douglas, M. Gu, A. Gupta, S. Hellander, C. Horuk, D. Nath, A. Takkar, S. Wu, P. Lötstedt, C. Krintz, and L. R. Petzold, "Stochastic Simulation Service: Bridging the Gap between the Computational Expert and the Biologist," *PLOS Computational Biology*, vol. 12, no. 12, pp. 1–15, 2016.

[90] J. Elf and M. Ehrenberg, "Spontaneous separation of bi-stable biochemical systems into spatial domains of opposite phases," *Systems Biology*, vol. 1, no. 2, pp. 230–236, 2005.

[91] S. S. Andrews, N. J. Addy, R. Brent, and A. P. Arkin, "Detailed Simulations of Cell Biology with Smoldyn 2.1," *PLOS Computational Biology*, vol. 6, no. 3, pp. 1–10, 2010.

[92] D. Gladkov, S. Alberts, R. D'Souza, and S. Andrews, "Accelerating the Smoldyn spatial stochastic biochemical reaction network simulator using GPUs," *Proceedings of the 19th High Performance Computing Symposia*, pp. 151–158, 2011.

[93] L. Dematte, "Smoldyn on Graphics Processing Units: Massively Parallel Brownian Dynamics Simulations," *IEEE/ACM Transactions on Computational Biology and Bioinformatics*, vol. 9, no. 3, pp. 655–667, 2012.

[94] M. I. Stefan, T. M. Bartol, T. J. Sejnowski, and M. B. Kennedy, "Multi-state Modeling of Biomolecules," *PLOS Computational Biology*, vol. 10, no. 9, pp. 1–9, 2014.

[95] G. Maruyama, "Continuous Markov processes and stochastic equations," *Rendiconti del Circolo Matematico di Palermo*, vol. 4, no. 1, pp. 48–90, 1955.

[96] S. S. Andrews, *Particle-Based Stochastic Simulators*, pp. 1–5. Springer New York, 2018.

[97] C. A. Yates and M. B. Flegg, "The pseudo-compartment method for coupling partial differential equation and compartment-based models of diffusion," *Journal of The Royal Society Interface*, vol. 12, no. 106, 2015.

[98] B. Franz, M. B. Flegg, S. J. Chapman, and R. Erban, "Multiscale Reaction-Diffusion Algorithms: PDE-Assisted Brownian Dynamics," *SIAM Journal on Applied Mathematics*, vol. 73, no. 3, pp. 1224–1247, 2013.

[99] M. B. Flegg, S. J. Chapman, and R. Erban, "The two-regime method for optimizing stochastic reaction-diffusion simulations," *Journal of the Royal Society Interface*, vol. 9, no. 70, pp. 859–868, 2012.

[100] M. Robinson, M. Flegg, and R. Erban, "Adaptive two-regime method: Application to front propagation," *The Journal of Chemical Physics*, vol. 140, no. 12, p. 124109, 2014.

[101] A. Hellander, S. Hellander, and P. Lötstedt, "Coupled mesoscopic and microscopic simulation of stochastic reaction-diffusion processes in mixed dimensions," *Multiscale Modeling & Simulation*, vol. 10, no. 2, pp. 585–611, 2012.

[102] M. B. Flegg, S. Hellander, and R. Erban, "Convergence of methods for coupling of microscopic and mesoscopic reaction–diffusion simulations," *Journal of Computational Physics*, vol. 289, pp. 1–17, 2015.

[103] M. Robinson, S. S. Andrews, and R. Erban, "Multiscale reaction-diffusion simulations with Smoldyn," *Bioinformatics*, vol. 31, no. 14, pp. 2406–2408, 2015.

[104] B. M. Slepchenko, J. C. Schaff, I. Macara, and L. M. Loew, "Quantitative cell biology with the Virtual Cell," *Trends in Cell Biology*, vol. 13, no. 11, pp. 570–576, 2003.

[105] M. Klann, A. Ganguly, and H. Koeppl, "Hybrid spatial Gillespie and particle tracking simulation," *Bioinformatics*, vol. 28, no. 18, pp. i549–i555, 2012.

[106] R. Erban, J. Chapman, and P. Maini, "A practical guide to stochastic simulations of reaction-diffusion processes," *arXiv e-prints*, p. arXiv:0704.1908, 2007.

[107] R. Erban and S. J. Chapman, "Stochastic modelling of reaction–diffusion processes: algorithms for bimolecular reactions," *Physical Biology*, vol. 6, no. 4, p. 046001, 2009.

[108] M. A. Gibson and J. Bruck, "Efficient Exact Stochastic Simulation of Chemical Systems with Many Species and Many Channels," *The Journal of Physical Chemistry A*, vol. 104, no. 9, pp. 1876–1889, 2000.

[109] R. Brown, "XXVII. A brief account of microscopical observations made in the months of June, July and August 1827, on the particles contained in the pollen of plants; and on the general existence of active molecules in organic and inorganic bodies," *The Philosophical Magazine*, vol. 4, no. 21, pp. 161–173, 1828.

[110] M. Smoluchowski, "Versuch einer mathematischen Theorie der Koagulationskinetik kolloider Lösungen," *Zeitschrift für Physikalische Chemie, XCII*, vol. 92, no. 40, pp. 129–168, 1917.

[111] A. D. Fokker, "Die mittlere Energie rotierender elektrischer Dipole im Strahlungsfeld," *Annalen der Physik*, vol. 348, no. 5, pp. 810–820, 1914.

[112] A. Kolmogoroff, "Über die analytischen methoden in der wahrscheinlichkeitsrechnung," *Mathematische Annalen*, vol. 104, no. 1, pp. 415–458, 1931.

[113] H. C. Berg, *Random Walks in Biology*. Princeton University Press, 1993.

[114] F. C. Collins and G. E. Kimball, "Diffusion-controlled reaction rates," *Journal of Colloid Science*, vol. 4, no. 4, pp. 425–437, 1949.

[115] M. Doi, "Stochastic theory of diffusion-controlled reaction," *Journal of Physics A: Mathematical and General*, vol. 9, no. 9, pp. 1479–1495, 1976.

[116] J. Lipková, K. C. Zygalakis, S. J. Chapman, and R. Erban, "Analysis of Brownian Dynamics Simulations of Reversible Bimolecular Reactions," *SIAM Journal on Applied Mathematics*, vol. 71, no. 3, pp. 714–730, 2011.

[117] S. S. Andrews, "Serial rebinding of ligands to clustered receptors as exemplified by bacterial chemotaxis," *Physical Biology*, vol. 2, no. 2, pp. 111–122, 2005.

[118] M. B. Flegg, "Smoluchowski Reaction Kinetics for Reactions of Any Order," *SIAM Journal on Applied Mathematics*, vol. 76, no. 4, pp. 1403–1432, 2016.

[119] J. Cavallo and M. Flegg, "Reversible Doi and Smoluchowski Kinetics for High-Order Reactions," *SIAM Journal on Applied Mathematics*, vol. 79, no. 2, pp. 594–618, 2019.

[120] S. Kullback and R. A. Leibler, "On Information and Sufficiency," *The Annals of Mathematical Statistics*, vol. 22, no. 1, pp. 79–86, 1951.

[121] Y. Lin-Moshier and J. S. Marchant, "The Xenopus Oocyte: A Single-Cell Model for Studying Ca^{2+} Signaling," *Cold Spring Harbor Protocols*, vol. 2013, no. 3, pp. 185–191, 2013.

[122] J. Paulsson, O. G. Berg, and M. Ehrenberg, "Stochastic focusing: Fluctuation-enhanced sensitivity of intracellular regulation," *Proceedings of the National Academy of Sciences*, vol. 97, no. 13, pp. 7148–7153, 2000.

[123] A. Mahmutovic, D. Fange, O. G. Berg, and J. Elf, "Lost in presumption: stochastic reactions in spatial models," *Nature Methods*, vol. 9, no. 12, pp. 1163–1166, 2012.

[124] K. F. Sonnen, V. M. Lauschke, J. Uraji, H. J. Falk, Y. Petersen, M. C. Funk, M. Beaupeux, P. François, C. A. Merten, and A. Aulehla, "Modulation of Phase Shift between Wnt and Notch Signaling Oscillations Controls Mesoderm Segmentation," *Cell*, vol. 172, no. 5, pp. 1079–1090, 2018.